

Politecnico di Torino

Laurea magistrale in Ingegneria per l'Ambiente e il Territorio

Gestione dei Rischi Naturali

A.a. 2025/2026

Sessione di Laurea Luglio 2026

Combining remote sensing technologies with subsurface deformation measurements to analyse Deep-seated Gravitational Slope Deformations

Relatori:

Prof. Federico Vagnon

Prof. Roberto Tomás Jover

Dott.ssa Roberta Narcisi

Dott. Luca Maria Lanteri

Dott. Davide Tiranti

Candidata:

Vittoria Maria Adela Giordano

Abstract

This thesis analyses the movement of two Deep-seated Gravitational Slope Deformations (DsGSDs): the Grangesises and Thuras landslides, located in the Susa Valley (Western Alps, Italy). The study combines ground-based and satellite-based monitoring techniques to characterise displacement patterns across the two areas in terms of intrinsic and seasonal movements. The analysis has proven effective in characterising both landslides kinematics and provides a complete overview, better than either technique alone. The work is structured as an introduction to the discussed topics, a geological and geographical setting of the two landslides, a presentation of methodology, and its application to the two case studies. The methodology includes a primary data gathering entailing Sentinel-1 EGMS (European Ground Motion Service) time series, meteorological data (temperature, precipitation, and snow depth) from the Arpa Sestriere weather station, and readings from fixed and manual inclinometers, and piezometers from the Arpa Regional Landslide Monitoring Network (ReRCoMF). The data analysis begins with a validation of EGMS data against manual inclinometer readings and a subsequent analysis of inclinometers' trends. Subsequently, EGMS data is examined in terms of Permanent Scatterers (PS) density and displacement stability across three land cover classes (urbanised, exposed soil, and forest). A Norton linear creep model is then applied to the EGMS displacement datasets to define the landslides' intrinsic, long-term component of movement. The EGMS subsets (distinguished by land cover) are plotted against the potential triggering factors to define seasonal trends. A cross-wavelet analysis is conducted to define the time periods of significant coherence between displacement and each forcing factor, and to estimate the associated phase delay. Results indicate land-cover-dependent displacement responses, with freeze-thaw cycles affecting exposed soil areas and thermal expansion affecting urbanised areas. These findings are discussed in relation to the underlying deformation mechanisms of the two landslides, along with the limitations of the datasets and methods employed.

Un faggio, più dritto o più storto, sempre da faggio crescerà.
(Stefano Mancuso)

Contents

1 Introduction **11**
- 1.1 Deep-seated Gravitational Slope Deformations (DsGSDs) . . . 11
  - 1.1.1 Overview . . . 11
  - 1.1.2 Evidence . . . 13
  - 1.1.3 Mechanism . . . 16
- 1.2 Synthetic Aperture Radar (SAR) Interferometry . . . 18
  - 1.2.1 Overview . . . 18
  - 1.2.2 SAR acquisition . . . 21
  - 1.2.3 Interferometric Synthetic Aperture Radar (InSAR) . . . 24
  - 1.2.4 Multi-interferogram techniques . . . 26
  - 1.2.5 The European Ground Motion Service (EGMS) . . . 27

2 Geographical and geological setting **30**
- 2.1 Geographical setting . . . 30
  - 2.1.1 Overview . . . 30
- 2.2 Geological setting . . . 35
  - 2.2.1 Overview . . . 35
  - 2.2.2 Grangesises landslide geological and geo-morphological setting . . . 37
  - 2.2.3 Thuras landslide geological and geo-morphological setting . . . 39

3 Methodology **44**
- 3.1 Overview . . . 44
- 3.2 Data gathering . . . 44
  - 3.2.1 InSAR . . . 44
  - 3.2.2 ReRCoMF . . . 45
  - 3.2.3 Arpa weather stations . . . 45
- 3.3 Data analysis . . . 46

4 Case study 1: the Grangesises landslide **51**
- 4.1 Data gathering . . . 51
  - 4.1.1 EGMS . . . 51
  - 4.1.2 ReRCoMF . . . 52
  - 4.1.3 Arpa weather stations . . . 55
- 4.2 Data analysis . . . 56
  - 4.2.1 EGMS data validation . . . 56
  - 4.2.2 Inclinometers . . . 57
  - 4.2.3 EGMS . . . 68
  - 4.2.4 Triggering factors analysis . . . 74

5 Case study 2: the Thuras landslide **85**
- 5.1 Data gathering . . . 85
  - 5.1.1 EGMS . . . 85

5.1.2 ReRCoMF 85
5.1.3 Arpa weather stations 88
5.2 Data analysis 88
5.2.1 EGMS data validation 88
5.2.2 Inclinometers 88
5.2.3 EGMS 92
5.2.4 Triggering factors analysis 96

6 Conclusions **105**

A Chapter 4 appendix **109**

B Chapter 5 appendix **142**

Bibliography **165**

List of Figures

1.1 "Mechanisms of large-scale rock-slope failures" (Agliardi et al., 2012, p.208) 14
1.2 Possible kinematics and morpho-structures: "*1) head scarp, 2) scarps, 3) trenches, 4) basal shear surface, 5) counterscarp, 6) toe, 7) nested landslide*" (Crippa, 2021, p.15) 14
1.3 Simplified scheme of main processes acting on a slope (Jaboyedoff et al., 2013) . . 15
1.4 Morpho-structural features typical of DsGSDs (Agliardi et al., 2012) 15
1.5 Conceptual glacial to postglacial slope evolution (Riva et al., 2018) 17
1.6 The electromagnetic spectrum (NASA, 2026) 19
1.7 SAR wavelengths penetration (Meyer, 2019) 21
1.8 SAR missions and relative revisiting times (TREAltamira, 2026) 22
1.9 SAR orbits (TREAltamira, 2026) 23
1.10 Radar acquisition geometry (Crippa, 2021) 23
1.11 SAR azimuth resolution geometry (EGMS, 2025a) 24
1.12 SAR geometrical distortions (Crippa, 2021) 25
1.13 PSInSAR method representation (TREAltamira, 2026) 27
1.14 Sentinel-1 IW acquisition mode: 3 sub-swaths with 9 bursts each (EGMS, 2025a) . 28

2.1 Geographic setting - overview 31
2.2 Geographic setting - Susa Valley 31
2.3 Geographic setting - municipalities 32
2.4 Grangesises and Thuras landslides 32
2.6 Grangesises landslide - topography and water courses 32
2.7 Grangesises landslide - roads 32
2.5 Grangesises landslide - urban settlements 33
2.8 Grangesises landslide - land and use distribution 33
2.9 Thuras landslide - urban settlements 34
2.10 Thuras landslide - location (Alberto et al., 2008) 34
2.11 Thuras landslide - topography and water courses 34
2.12 Thuras landslide - roads 34
2.18 T geological classification 40
2.19 T landslide - geologic and geomorphologic sketch (modified from Alberto et al., 2008) 40
2.13 Cesana Torinese Sheet - simplified geological scheme (Fioraso & Mosca, 2014) . . . 41
2.14 GS geological classification (Agenzia Regionale per la Protezione dell'Ambiente del Piemonte, 2025a) 42
2.15 GS landslide classification (Agenzia Regionale per la Protezione dell'Ambiente del Piemonte, 2015) 42
2.16 GS landslide sectors (Agenzia Regionale per la Protezione dell'Ambiente del Piemonte, 2012) 43
2.17 T landslide classification (Agenzia Regionale per la Protezione dell'Ambiente del Piemonte, 2015) 43

3.1 Analysis part 1 workflow 47
3.2 Wavelet phase description (Roesch & Schmidbauer, 2018) 50

3.3 Wavelet phase angle interpretation 50

4.1 GS datasets' names conversion 52
4.2 GS ReRCoMF instruments 53
4.3 GS Arpa weather stations 55
4.4 GS EGMS data validation 58
4.5 GS fixed inclinometers location 59
4.6 GS fixed inclinometers: Cumulative displacement vs cumulative precipitation . . . 60
4.7 GS manual inclinometers location 61
4.8 GS manual inclinometers elevation and group division 62
4.9 GS manual inclinometers: possible shear surfaces depths 62
4.10 GS manual inclinometers: possible shear surfaces profiles 63
4.11 GS manual inclinometers, Group 1 and 3: cumulative azimuth and resultant displacement 64
4.12 GS manual inclinometers, Group 2: cumulative azimuth and resultant displacement 65
4.13 GS manual inclinometers - latest cumulative displacement and azimuth 67
4.14 GS 2015 - 2022: EGMS PS, mean velocity distribution 69
4.15 GS 2019 - 2024: EGMS PS, mean velocity distribution 70
4.16 GS: Norton model applied to *horizontal* and *vertical* datasets 72
4.17 Norton model applied to *ascending* and *descending* datasets 73
4.18 Example: GS 2015 - 2022, EGMS and triggering factors 75
4.19 GS - triggering factors period occurrence 77
4.20 Freeze-thaw mechanism: uplift values (blue) caused by freezing and subsidence values (red) caused by thaw process (H. Chen et al., 2025) 82

5.1 T ReRCoMF instruments 86
5.2 T EGMS data validation 89
5.3 T fixed inclinometers: Cumulative displacement vs cumulative precipitation 90
5.4 T manual inclinometer: cumulative displacement vs depth 91
5.5 T manual inclinometer: cumulative azimuth and resultant displacement 91
5.8 T: Norton model applied to *horizontal* and *vertical* datasets 94
5.9 T: Norton model applied to *ascending* and *descending* datasets 95
5.10 T - triggering factors period occurrence 98
5.6 T 2015 - 2022: EGMS PS, mean velocity distribution 103
5.7 T 2019 - 2024: EGMS PS, mean velocity distribution 104

A1 GS data validation 1 109
A2 GS data validation 2 110
A3 GS data validation 3 110
A4 GS data validation 4 111
A5 GS data validation 5 111
A6 GS data validation 6 112
A7 GS manual inclinometers 1 113
A8 GS manual inclinometers 2 114
A9 GS manual inclinometers 3 114
A10 GS creep models 1 115
A11 GS creep models 2 116
A12 GS creep models 3 116
A13 GS creep models 4 117
A14 GS triggers 1 118
A15 GS triggers 2 119
A16 GS triggers 3 119
A17 GS triggers 4 120
A18 GS triggers 5 120
A19 GS triggers 6 121
A20 GS triggers 7 121

A21 GS triggers 8 . . . 122
A22 GS triggers 9 . . . 122
A23 GS triggers 10 . . . 123
A24 GS triggers 11 . . . 123
A25 GS triggers 12 . . . 124
A26 GS triggers 13 . . . 124
A27 GS triggers 14 . . . 125
A28 GS triggers 15 . . . 125
A29 GS triggers 16 . . . 126
A30 GS wavelet analysis 1 . . . 127
A31 GS wavelet analysis 2 . . . 128
A32 GS wavelet analysis 3 . . . 128
A33 GS wavelet analysis 4 . . . 129
A34 GS wavelet analysis 5 . . . 129
A35 GS wavelet analysis 6 . . . 130
A36 GS wavelet analysis 7 . . . 130
A37 GS wavelet analysis 8 . . . 131
A38 GS wavelet analysis 9 . . . 131
A39 GS wavelet analysis 10 . . . 132
A40 GS wavelet analysis 11 . . . 132
A41 GS wavelet analysis 12 . . . 133
A42 GS wavelet analysis 13 . . . 133
A43 GS wavelet analysis 14 . . . 134
A44 GS wavelet analysis 15 . . . 134
A45 GS wavelet analysis 16 . . . 135
A46 GS wavelet analysis 17 . . . 135
A47 GS wavelet analysis 18 . . . 136
A48 GS wavelet analysis 19 . . . 136
A49 GS wavelet analysis 20 . . . 137
A50 GS wavelet analysis 21 . . . 137
A51 GS wavelet analysis 22 . . . 138
A52 GS wavelet analysis 23 . . . 138
A53 GS wavelet analysis 24 . . . 139

B1 T creep models 1 . . . 142
B2 T creep models 2 . . . 143
B3 T creep models 3 . . . 143
B4 T creep models 4 . . . 144
B5 T triggers 1 . . . 145
B6 T triggers 2 . . . 146
B7 T triggers 3 . . . 146
B8 T triggers 4 . . . 147
B9 T triggers 5 . . . 147
B10 T triggers 6 . . . 148
B11 T triggers 7 . . . 148
B12 T triggers 8 . . . 149
B13 T triggers 9 . . . 149
B14 T triggers 10 . . . 150
B15 T triggers 11 . . . 150
B16 T triggers 12 . . . 151
B17 T triggers 13 . . . 151
B18 T triggers 14 . . . 152
B19 T triggers 15 . . . 152
B20 T triggers 16 . . . 153
B21 T wavelet analysis 1 . . . 154

B22 T wavelet analysis 2 155
B23 T wavelet analysis 3 155
B24 T wavelet analysis 4 156
B25 T wavelet analysis 5 156
B26 T wavelet analysis 6 157
B27 T wavelet analysis 7 157
B28 T wavelet analysis 8 158
B29 T wavelet analysis 9 158
B30 T wavelet analysis 10 159
B31 T wavelet analysis 11 159
B32 T wavelet analysis 12 160
B33 T wavelet analysis 13 160
B34 T wavelet analysis 14 161
B35 T wavelet analysis 15 161
B36 T wavelet analysis 16 162

List of Tables

1.1 Abbreviated Classification of Slope Movements (Cruden & Varnes, 1996, p.38) . . 12
1.2 SAR bands: frequencies, wavelengths, and typical applications (NASA, 2026) . . . 20

4.1 GS ReRCoMF instruments 54
4.2 GS Arpa weather stations' details 56
4.3 GS: EGMS and manual inclinometer average velocities 57
4.4 GS - PS density (PS/km^2) based on land cover class and EGMS component 71
4.5 GS 2015–2022: Average cross-wavelet power at period=365 d 78
4.6 GS 2019–2024: Average cross-wavelet power at period=365 d 79
4.7 GS 2019–2024: Phase angles at period=365 d (filtered by power ≥ 0.7) 81
4.8 GS 2019–2024: Phase delays at period=365 d (filtered by power ≥ 0.7) 84

5.1 GS ReRCoMF instruments 87
5.2 T - PS density (PS/km^2) based on land cover class and EGMS component 93
5.3 T 2015–2022: Average cross-wavelet power at period=365 d 99
5.4 T 2019–2024: Average cross-wavelet power at period=365 d 100
5.5 T 2019–2024: Phase angles at period=365 d (filtered by power ≥ 0.7) 101
5.6 T 2019–2024: Phase delays at period=365 d (filtered by power ≥ 0.7) 102

A1 GS 2015-2022 wavelet analysis: periods, phase angles, and phase delays 140
A2 GS 2019-2024 wavelet analysis: periods, phase angles, and phase delays 141

B1 T 2015-2022 wavelet analysis: periods, phase angles, and phase delays 163
B2 T 2019-2024 wavelet analysis: periods, phase angles, and phase delays 164

Acronyms

DEM Digital Elevation Model.

DInSAR Differential Interferometric Synthetic Aperture Radar.

DsGSDs Deep-seated Gravitational Slope Deformations.

EGMS European Ground Motion Service.

GS Grangesises.

InSAR Interferometric Synthetic Aperture Radar.

LLs Large Landslides.

LOS Line of sight.

MP Measurement Point.

PS Permanent Scatterers.

PSInSAR Permanent Scatterers Interferometric Synthetic Aperture Radar.

RAR Real Aperture Radar.

SAR Synthetic Aperture Radar.

T Thuras.

Chapter 1

Introduction

1.1 Deep-seated Gravitational Slope Deformations (DsGSDs)

1.1.1 Overview

Deep-seated Gravitational Slope Deformations (DsGSDs) represent a complex geological phenomenon which has been studied since the 1940s. These slope movements have distinct definitions across the literature, reflecting the different approaches and hypotheses made on their evolutionary mechanisms (Agliardi et al., 2001; Ambrosi & Crosta, 2006; Barla et al., 2010; Pánek & Klimeš, 2016; Cignetti et al., 2020). In essence, DsGSDs can be defined as large-scale, gravity-induced mass movements that affect entire high-relief hill-slopes (Agliardi et al., 2001; Pánek & Klimeš, 2016; Crippa, 2021; Cannarozzi, 2023).

They typically extend from the toe to the ridge, reaching up to *200 - 300 m* in depth, consequently involving rock volumes up to hundreds of millions of cubic metres with relatively minor displacements compared to the overall slope dimensions (Agliardi et al., 2001; Crosta et al., 2013; Pánek & Klimeš, 2016). However, they are usually characterised by poorly defined boundaries (Crosta et al., 2013; Pánek & Klimeš, 2016). These phenomena have a *very slow* velocity (*mm-cm/year*) over large periods of time (10^3 – 10^4 years), primarily through creep mechanisms (Chigira, 1992; Cruden & Varnes, 1996; Pánek & Klimeš, 2016; Crippa, 2021). Such mechanism is commonly divided into three stages: primary, secondary (steady-state), and tertiary (accelerated), eventually leading to failure (Aydan et al., 2014). While creep is a primary long-term trend, it is often combined with seasonal accelerations triggered by external events like heavy rainfall, snow cover and changes in temperature (Pánek & Klimeš, 2016).

According to Varnes' widely adopted landslide classification represented in Table 1.1, all types of slope movements are classified depending on *"the type of movement, kind of*

material, rate of movement, geometry of the area of failure and the resulting deposit, age, causes, degree of disruption of the displacement mass, relation or lack of relation of slide geometry to geologic structure, degree of development, geographic location of type examples, and state activity" (Varnes, 1978, p.11). The main factors defining these phenomena are the type of movement and the type of materials involved. The former includes five possibilities: *falls, topples, slides, spreads, flows*, while the latter is divided in *rock, debris and earth* (Cruden & Varnes, 1996). It is also possible to define a *"complex landslide"* in the case of a combination of at least two of the five principal types of movement previously defined (Varnes, 1978; Cruden & Varnes, 1996).

Table 1.1. Abbreviated Classification of Slope Movements (Cruden & Varnes, 1996, p.38)

TYPE OF MOVEMENT	**TYPE OF MATERIAL**		
	Bedrock	**Engineering soils**	
		Predominantly Coarse	**Predominantly Fine**
Fall	Rock fall	Debris fall	Earth fall
Topple	Rock topple	Debris topple	Earth topple
Slide	Rock slide	Debris slide	Earth slide
Spread	Rock spread	Debris spread	Earth spread
Flow	Rock flow	Debris flow	Earth flow

Based on the criteria mentioned above, DsGSDs' movement classification has always been challenging (Pánek & Klimeš, 2016). In the past, many authors distinguished *DsGSDs* from conventional *landslides* due to their unique characteristics and the apparent lack of a well-defined *continuous sliding surface* (Dramis & Sorriso-Valvo, 1994; Ambrosi & Crosta, 2006; Crippa, 2021). However, subsequent and more accurate studies using geotechnical and geophysical methods have proven most DsGSDs to have an extremely deep (hundreds of meters) *basal shear zone* below the surface, confirming that this phenomenon is just another category of *landslides* (Barla et al., 2010; Crosta et al., 2013; Crippa, 2021).

DsGSDs are commonly located in mountain ranges worldwide, particularly in Alpine environments characterised by high-relief energy (Dramis & Sorriso-Valvo, 1994; Ambrosi & Crosta, 2006; Crosta et al., 2013; Materazzi et al., 2014; Cignetti et al., 2020). Their slow, non-impulsive yet cumulative displacement can nonetheless damage both superficial and underground infrastructure including roads, buildings, pipelines and tunnels, thus representing a valid natural hazard, potentially affecting settlements and their population (Ambrosi & Crosta, 2006; Frattini et al., 2013; Pánek & Klimeš, 2016; Cignetti et al., 2020; Crippa, 2021). The structural and mechanical changes induced by DsGSDs'

evolution can also trigger secondary nested rapidly-evolving landslides such as rock falls, rotational and translational slides, usually occurring in the middle and lower sections of the landslide body which are intertwined with external factors such as temperature, rainfall and snowmelt (Agliardi et al., 2013; Crosta et al., 2013; Pánek et al., 2018; Cignetti et al., 2020; Crippa, 2021; Albano et al., 2023).

Slow rock slope deformations can be divided in two macro-classes: Deep-seated Gravitational Slope Deformations (DsGSDs) and Large Landslides (LLs) depending on their size, surface type and strain accumulation (Agliardi et al., 2012, 2013; Crosta et al., 2013; Crippa, 2021). On one hand, DsGSDs affect entire slope flanks, typically with size over *6 - 10* km^2 and involving volumes larger than *0.5* km^3, with deep basal shear zones and ill-defined lateral boundaries (Agliardi et al., 2001; Agliardi et al., 2012; Crippa, 2021). They are characterised by complex kinematics and heterogeneous strain fields, typically triggered by inherited geological structures (Agliardi et al., 2001; Crosta et al., 2013). On the other hand, LLs entail smaller areas (usually less than 6 km^2) and volumes and have a more elongated shape (Agliardi et al., 2012; Crippa, 2021). They are usually found on middle-lower slope sectors and show a higher likelihood to collapse given their more intense internal strain, their more pronounced morpho-structures and their overall greater instability compared to DsGSDs (Agliardi et al., 2012; Crosta et al., 2013; Crippa, 2021).

Rock slope stability fundamentally depends on lithology and the spatial arrangement of structural discontinuities as shown in Figure 1.1 (Agliardi et al., 2012; Crippa, 2021). Sparse, widely-separated fracture sets favour intact rock strength, with individual discontinuities dictating failures' location and kinematics (Agliardi et al., 2012). However, pervasive closely-spaced discontinuities produce continuum-like rock mass behaviour where overall strength reflects both intact material and fracture network properties eventually resulting in diverse types of failure geometries (Agliardi et al., 2012).

Depending on the shape of the basal shear surface of slow rock slope deformations, it is possible to have a *curved* (Figure 1.2 (a)), *planar* (Figure 1.2 (b)) or *compound* (Figure 1.2 (c)) failure surface (Agliardi et al., 2012; Crippa, 2021).

1.1.2 Evidence

From a geomorphological point of view, DsGSDs are characterised by unique patterns of linear extensional and compressional morpho-structural features as shown in Figure 1.4 that reflect their heterogeneity and the segmented deformation they induce, thus it is common to find evidence of DsGSDs' long-term activity in the cumulated deformations they show (Crosta et al., 2013; Cignetti et al., 2020; Crippa, 2021; Cannarozzi, 2023).

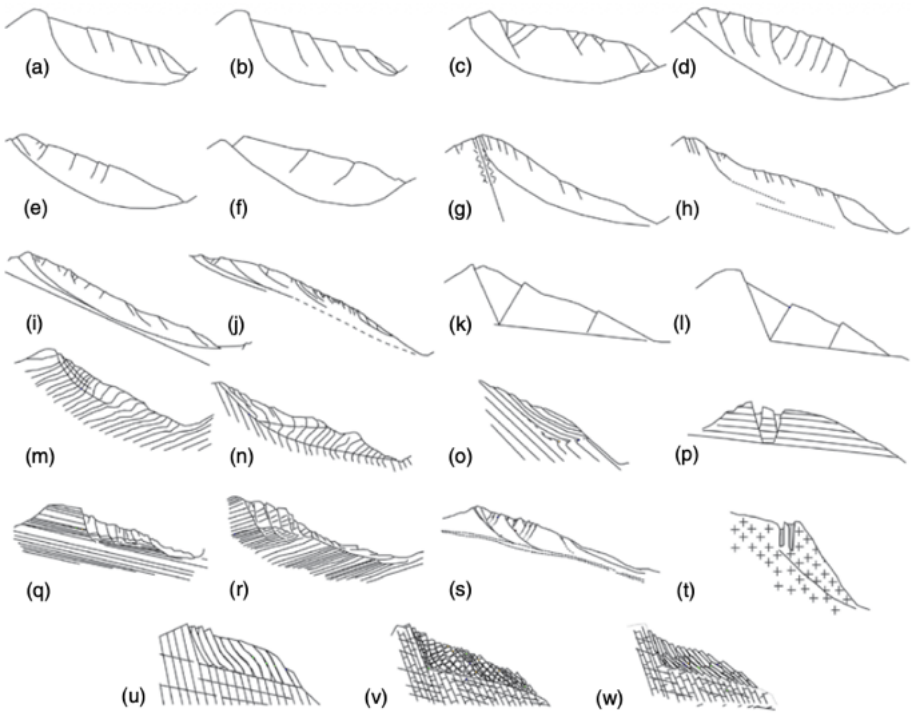


Figure 1.1. "Mechanisms of large-scale rock-slope failures" (Agliardi et al., 2012, p.208)

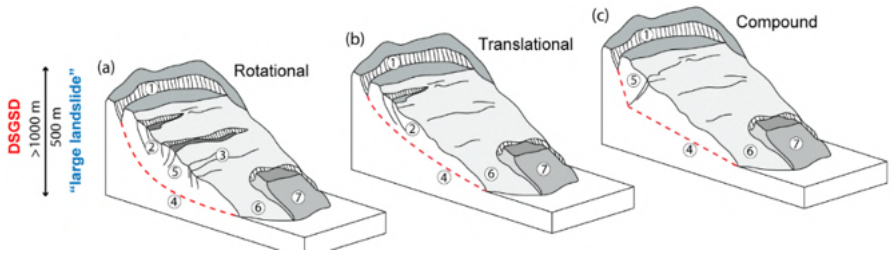


Figure 1.2. Possible kinematics and morpho-structures: "*1) head scarp, 2) scarps, 3) trenches, 4) basal shear surface, 5) counterscarp, 6) toe, 7) nested landslide*" (Crippa, 2021, p.15)

In the upper slope sectors, there typically is an overall extensional to mixed deformation regime expressed by *scarps*, *open* or *infilled trenches*, *graben-like ridge-top depressions*, *double or multiple ridges*, and *counterscarps (uphill-facing or antislope scarps)*, as well as *open tension cracks* and *downthrown blocks* (Dramis & Sorriso-Valvo, 1994; Barla et al., 2010; Agliardi et al., 2013; Crosta et al., 2013; Pánek et al., 2018; Cignetti et al., 2020). Towards the middle and lower slope sectors, the deformation tends to a compressive mechanism, commonly resulting in *toe bulging*, *buckling folds*, *intensely fractured rock masses* and, in some cases, *displacement of valley floors* when the DsGSDs' toe extends across the valley bottom (Chigira, 1992; Dramis & Sorriso-Valvo, 1994; Agliardi et al., 2013; Crosta et al., 2013; Pánek et al., 2018; Cignetti et al., 2020).

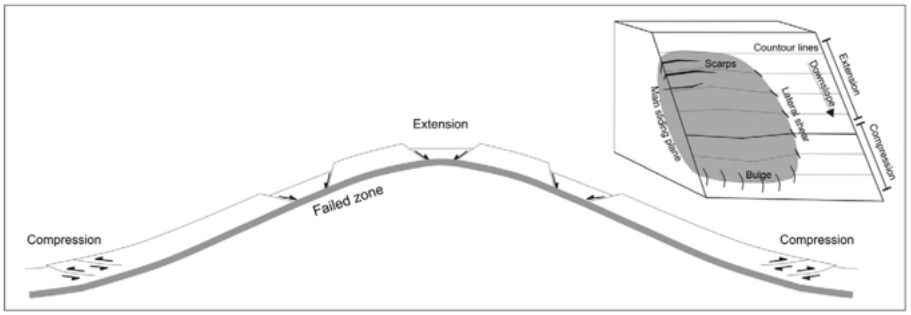


Figure 1.3. Simplified scheme of main processes acting on a slope (Jaboyedoff et al., 2013)

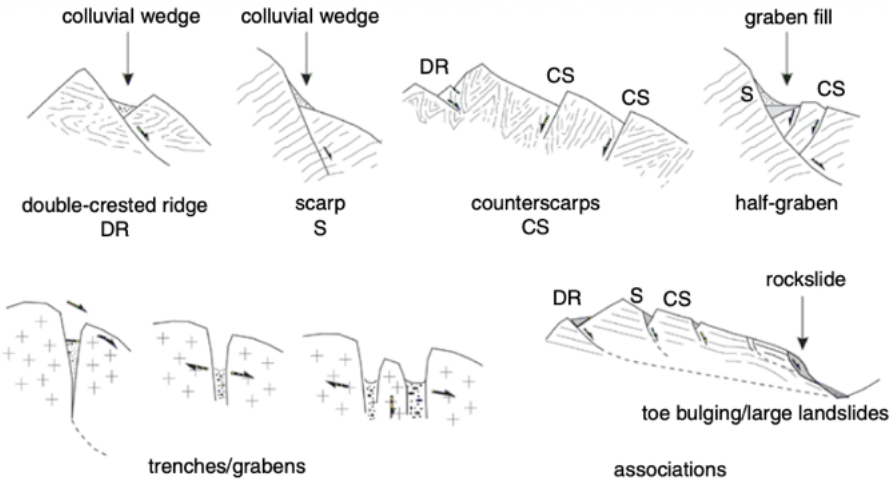


Figure 1.4. Morpho-structural features typical of DsGSDs (Agliardi et al., 2012)

Morpho-structural features associated with DsGSDs are predominantly linear and typically follow pre-existing tectonic elements such as *faults, joints* and *foliation* or *stratigraphic boundaries* as lithological contacts (Crosta et al., 2013). These gravity-driven structures remain confined within DsGSDs' boundaries and significantly affect key slope processes such as failure kinematics, rock mass fragmentation, mechanical degradation, and water circulation (Crosta et al., 2013). As a matter of fact, the presence of counterscarps or transversal features can affect and redirect surface runoff and groundwater flow, eventually triggering secondary slope movements (Crosta et al., 2013; Jaboyedoff et al., 2013; Crippa, 2021).

DsGSDs are widespread globally, particularly in Alpine regions, where inventories document over 1,000 occurrences with preferential clustering along major regional tectonic features such as large shear zones and nappe boundaries (Agliardi et al., 2013; Crosta et al., 2013; Crippa, 2021). They mainly develop in moderately strong anisotropic rock masses including phyllites, micaschists, paragneisses, orthogneisses, flysch-type units (sandstones, marls) and volcanic rocks, while carbonates and granitoids are rarely affected (Agliardi

et al., 2013; Crosta et al., 2013; Crippa, 2021).

1.1.3 Mechanism

A clear definition of the mechanisms behind DsGSDs remains unresolved as a cause of the phenomena's complexity and extremely long lifespan (Crosta et al., 2013). Nonetheless, according to Crosta et al., 2013 many influencing factors have been proposed, divided between *predisposing factors* (lithology, rock mass properties, slope geometry, tectonic inheritance), *preparatory processes* (deglaciation, topographic stress evolution, fluvial incision), and *potential triggers* (seismicity, heavy rainfall, erosion (Crosta et al., 2013, p.15).

One of the key aspects affecting DsGSDs is given by topographic stresses as they can generate compressive stresses at ridge crests and tensile ones along valley bottoms, interacting with tectonic loading, exhumation processes and glacial cycles (Crosta et al., 2013). Topographic stresses are strongly controlled by local topography and geological structures and they can be in turn heavily influenced by other factors such as deglaciation (Crosta et al., 2013).

In Alpine environments, Pleistocene deglaciation is the dominant preparatory mechanism for DsGSDs as it entails a number of processes that cause a progressive rock degradation (Ambrosi & Crosta, 2006; Agliardi et al., 2013; Crosta et al., 2013; Pánek & Klimeš, 2016; Riva et al., 2018; Cignetti et al., 2020). These include the over-steepening of valley walls due to rapid ice debuttressing, the unloading-induced fracturing, the increased topographic relief contrasts and the groundwater regime alterations, overall resulting in a significant change of the topography of the area (Agliardi et al., 2013; Crosta et al., 2013; Pánek & Klimeš, 2016).

Generally, large rock slope failures are not immediate consequences of deglaciation, but rather the result of progressive damage accumulation under subcritical stress conditions (Chigira, 1992; Riva et al., 2018; Crippa, 2021). On the contrary, rockfalls are frequently triggered right after deglaciation by unloading-induced stress redistribution, weathering, and erosion (Riva, 2017, p.10).

As shown in Figure 1.5, glacial cycles initially carve deep valley flanks, consequently modifying the gravitational stress distribution (Crosta et al., 2013; Ballantyne et al., 2014; Grämiger et al., 2017; Riva et al., 2018). Additionally, the glacier retreat triggers paraglacial destabilisation through crack damage, rock mass weakening, enhanced weathering and hydrological perturbations (Crosta et al., 2013; Ballantyne et al., 2014; Grämiger et al., 2017; Riva et al., 2018). The initial long and gentle slopes are dissected

and steepened following ice retreat and are further enhanced by external seasonal triggers as precipitation, change in temperature and snowmelt (Crosta et al., 2013; Riva et al., 2018).

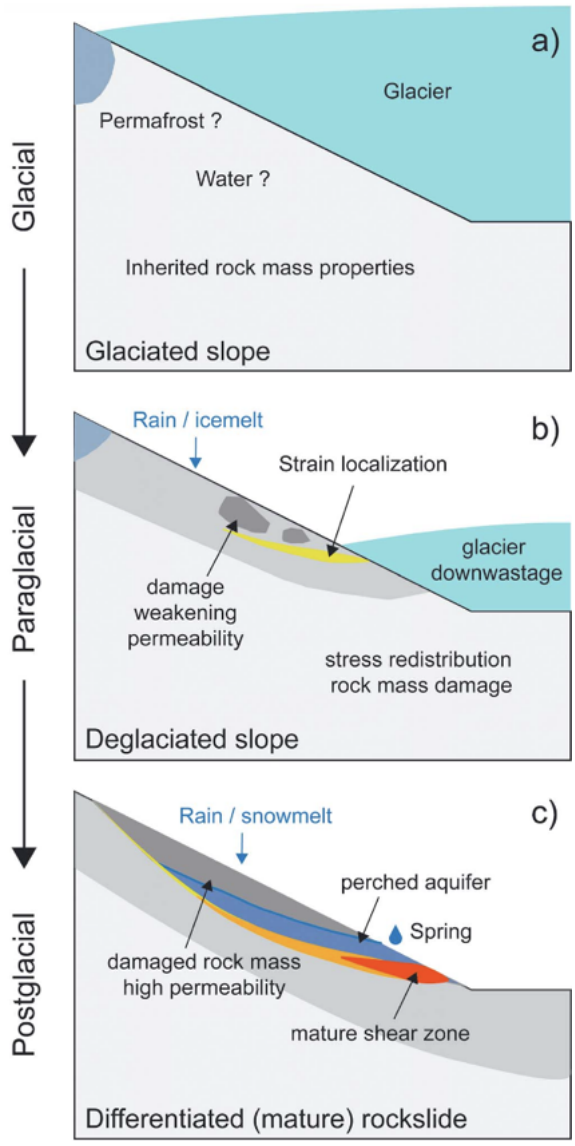


Figure 1.5. Conceptual glacial to postglacial slope evolution (Riva et al., 2018)

Among the differente cyclic loading mechanisms affecting DsGSDs, seismic activity can heavily contribute to the progressive deterioration of the rock mass through ground shaking and coseismic displacements (Ambrosi & Crosta, 2006; Agliardi et al., 2013; Crosta et al., 2013; Jaboyedoff et al., 2013; Cignetti et al., 2020; Albano et al., 2023). In seismically active regions with no presence of deglaciation, seismic events can trigger instabilities along rapid fluvial incisions on high-energy slopes, particularly in layered sedimentary or weak rock masses (Crippa, 2021).

According to Agliardi et al., 2020, mature large rockslides typically maintain slow,

steady creep rates for extended periods of time under drained hydrological conditions. However, in differentiated rockslides dominated by frictional processes along basal shear zones, changes in pore pressure can significantly modify the internal stress state (Agliardi et al., 2020; Crippa, 2021). As a matter of fact, such shift can cause immediate or delayed accelerations, extended phases of constant displacement and eventually rapid catastrophic failure (Agliardi et al., 2020).

Overall, defining the activity of DsGSDs remains extremely challenging due to their complex behaviour spanning thousands of years. A multi-method approach is therefore needed, integrating local measurements from geotechnical and geophysical instruments with wide-area, millimetre-scale surface deformation monitoring provided by spaceborne Differential Interferometric Synthetic Aperture Radar (DInSAR) techniques.

1.2 Synthetic Aperture Radar (SAR) Interferometry

1.2.1 Overview

"Radar" stands for Radio Detection And Ranging and such technology has been of use in several different fields, making actions such as *"imaging, guidance, remote sensing* and *global positioning"* possible (Chan & Koo, 2008). Radar systems have been further developed over time as a tool for detecting ships and aircrafts and they have more recently evolved into a key asset for Earth observation and deformation monitoring (Ferretti et al., 2007; Chan & Koo, 2008; Crippa, 2021; NASA, 2026).

Radar technologies work within the microwave domain of the electromagnetic spectrum with wavelengths ranging from *1 mm to 1 m* as shown in Figure 1.6 (Ferretti et al., 2007; Crippa, 2021; EGMS, 2025a; NASA, 2026). They are considered an active remote sensing technique as they function by emitting microwave energy pulses towards a target and measuring the distance and properties of such through the time-delay and strength of the returned signal (Ferretti et al., 2007; Chan & Koo, 2008; Crippa, 2021; EGMS, 2025a; NASA, 2026). Given the wavelengths used, radar systems have the capability of penetrating through clouds, fog and dust and additionally can operate independently of sunlight as they solely rely on their own illumination (Ferretti et al., 2007; Chan & Koo, 2008; Crippa, 2021; EGMS, 2025a; NASA, 2026).

A radar instrument is usually made of five components: a *transmitter*, an *antenna*,

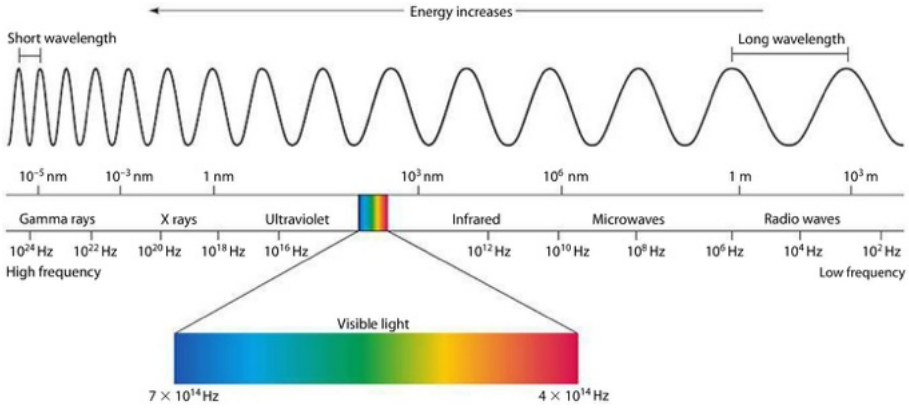


Figure 1.6. The electromagnetic spectrum (NASA, 2026)

a *receiver*, a *switching unit* and a *data recorder* (Chan & Koo, 2008; EGMS, 2025a). In monostatic radar systems, as the one of Copernicus Sentinel-1, the radar antenna works as both the transmitter and the receiver (EGMS, 2025a). These use modern radar technologies that not only measure the signal strength but also record its phase, defined by the path followed by the wave between the sensor and the target (EGMS, 2025a).

Real Aperture Radar (RAR) systems only capture the returning signal amplitude and their spatial resolution solely depends on the physical size of the antenna: the larger the antenna, the larger the resolution, thus a better identification of smaller targets on the ground (Crippa, 2021; EGMS, 2025a; NASA, 2026). In other words, in order to have a very accurate resolution, an extremely large and not practical antenna would be needed (Chan & Koo, 2008; Crippa, 2021; EGMS, 2025a; NASA, 2026). To overcome this issue, Synthetic Aperture Radar (SAR) computationally synthesises an extended antenna through the combination of successive echoes collected by a compact antenna moving along a platform or orbital path in different frequency bands as shown in Table 1.2 (Chan & Koo, 2008; Crippa, 2021; EGMS, 2025a; NASA, 2026).

Table 1.2. SAR bands: frequencies, wavelengths, and typical applications (NASA, 2026)

Band	**Frequency [GHz]**	**Wavelength [cm]**	**Typical Application**
Ka	27–40	1.1–0.8	Rarely used
K	18–27	1.7–1.1	Rarely used
Ku	12–18	2.4–1.7	Rarely used
X	8–12	3.8–2.4	High resolution; urban, ice and snow; low vegetation penetration
C	4–8	7.5–3.8	Global mapping and change detection; moderate vegetation penetration; ice and ocean monitoring
S	2–4	15–7.5	Earth observation and agriculture; better performance in vegetated areas
L	1–2	30–15	Geophysical monitoring; good vegetation penetration; suitable for interferometry
P	0.3–1	100–30	Biomass estimation; dense vegetation; experimental band

The different wavelengths entailed by the possible frequencies define the signal interaction with the surface and the extent of penetration depending on the nature of the observed target (Crippa, 2021; EGMS, 2025a; NASA, 2026). Short wavelengths provide limited penetration and mainly interact with the upper layers of vegetation, whereas longer wavelengths can easily interact with deeper layers of vegetation, dry soils and ice as shown in Figure 1.7 but show a lower sensitivity to small variations of the surface conditions over time (Ferretti et al., 2007; Wempen & McCarter, 2017; Crippa, 2021; EGMS, 2025a; NASA, 2026).

In addition to frequency, polarisation plays a key role too in defining the interaction between the SAR signal and the target. Polarisation, which can be horizontal (H) or vertical (V), describes the propagation direction of the electromagnetic wave emitted and can be adjusted depending on the specific case (Ferretti et al., 2007; Wempen & McCarter, 2017; Crippa, 2021; EGMS, 2025a; NASA, 2026). Polarisation is defined by the transmitted and received signals: single polarisation (HH or VV) occurs when the configuration remains invariate in both cases, while cross-polarisation (HV or VH) involves a change between transmission and reception (Ferretti et al., 2007; Wempen & McCarter, 2017; Crippa, 2021; EGMS, 2025a; NASA, 2026). Different polarisations emphasise different scattering mechanisms. VV polarisation is usually more sensitive to surface scatterings

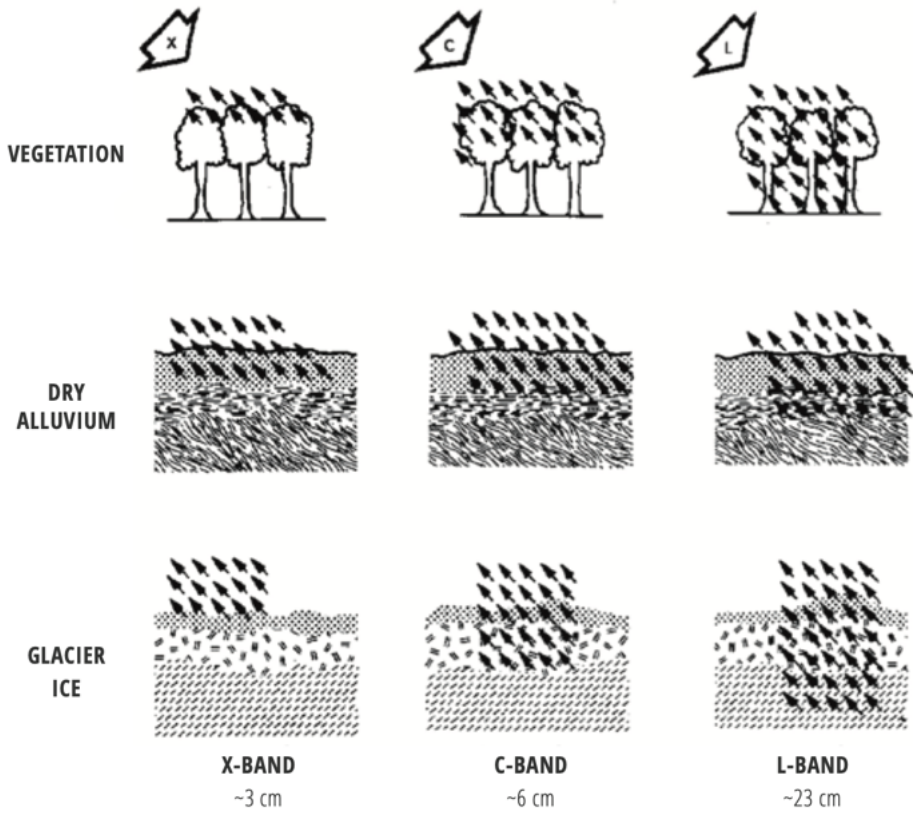


Figure 1.7. SAR wavelengths penetration (Meyer, 2019)

typical of bar soils or water surfaces, while HH polarisation results effective for double-bouncing scattering caused by vertical structures such as buildings, tree trunks or flooded vegetation (Ferretti et al., 2007; Wempen & McCarter, 2017; Crippa, 2021; EGMS, 2025a; NASA, 2026). In contrast, HV or VH configurations usually capture volume scattering associated with vegetation covers (Wempen & McCarter, 2017; Crippa, 2021; EGMS, 2025a; NASA, 2026).

1.2.2 SAR acquisition

SAR systems observe the same area over time, acquiring data regardless of illumination and atmospheric conditions and thus enabling a continuous monitoring and detection of surface displacements, ultimately resulting extremely useful for ground deformation analyses (Crippa, 2021; TREAltamira, 2026). SAR satellites are found in near-polar, sun-synchronous orbits at altitudes between *500* and *800 km* (Ferretti et al., 2007; Crippa, 2021; TREAltamira, 2026). The interval between two successive observations of the same location, which enables a more or less dense temporal sampling, is defined as *revisiting time* and it depends on the satellite mission as shown in Figure 1.8 (Ferretti et al., 2007; Crippa, 2021; TREAltamira, 2026).

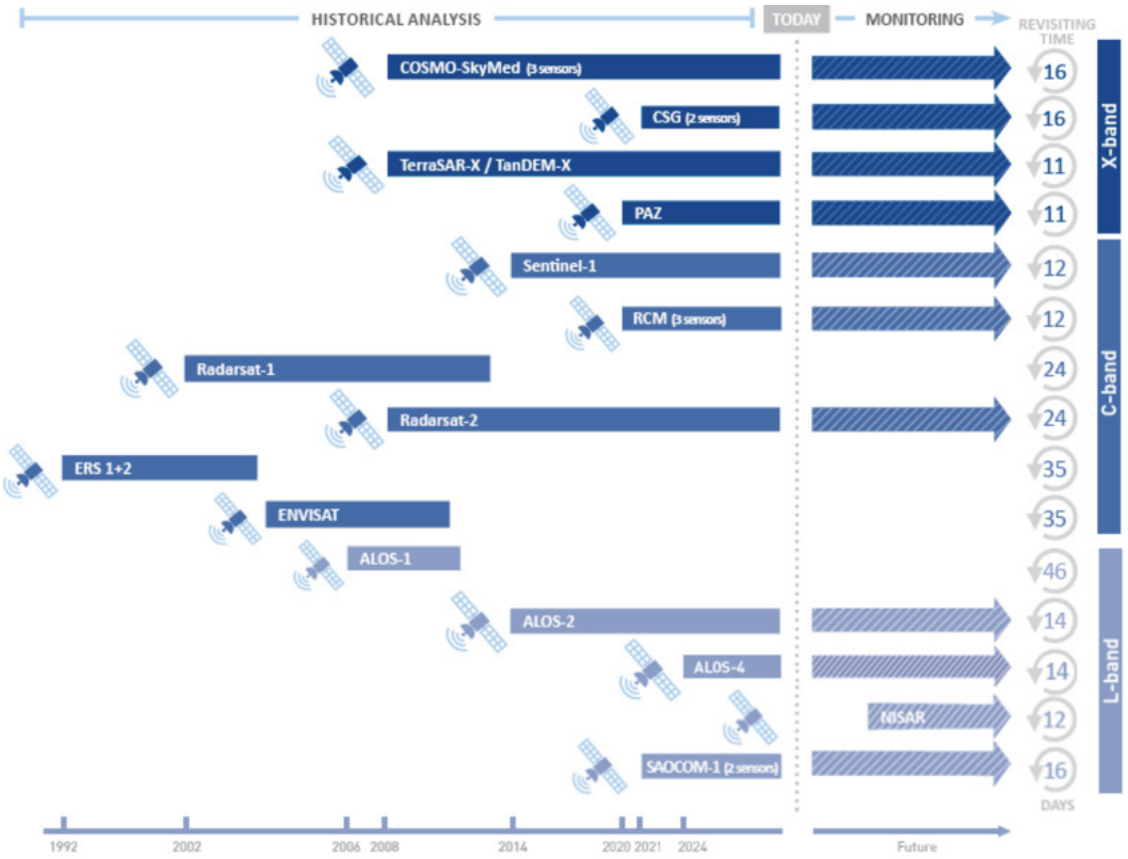


Figure 1.8. SAR missions and relative revisiting times (TREAltamira, 2026)

All SAR satellites follow two orbits while collecting imagery of the same area: an *ascending* one when the satellite moves from the south pole to the north pole and a *descending* one when the satellite travels from the north pole towards the south pole (Figure 1.9 (Ferretti et al., 2007; Crippa, 2021; TREAltamira, 2026). During acquisition, the SAR sensors move along the flight direction, known as the *azimuth* or the *along track direction*, while the perpendicular direction on the ground is referred to as *ground range* or *across track* (Ferretti et al., 2007; Crippa, 2021; TREAltamira, 2026). Targets are located by their distance from the sensor which is defined as the *slant range*, that corresponds to the Line of sight (LOS) direction of the satellite (Ferretti et al., 2007; Crippa, 2021; EGMS, 2025a; TREAltamira, 2026). The illuminated portion of the Earth's surface is defined by the *swath*, which corresponds to the width of the imaged scene, measured either in ground range or in slant range (Ferretti et al., 2007; Baumgartner & Krieger, 2014; EGMS, 2025a).

SAR systems operate in a *side-looking* geometry, where the antenna is oriented at an angle with respect to the *nadir* (the point directly below the satellite), also known as the *off-nadir*, which typically ranges from *20° to 50°* (Ferretti et al., 2007; Crippa, 2021; EGMS, 2025a; TREAltamira, 2026). Due to the Earth's curvature, the *incidence*

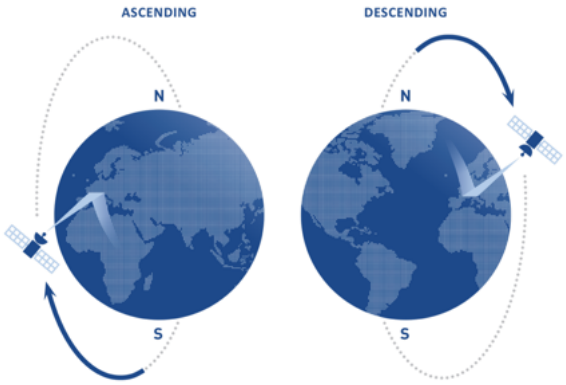


Figure 1.9. SAR orbits (TREAltamira, 2026)

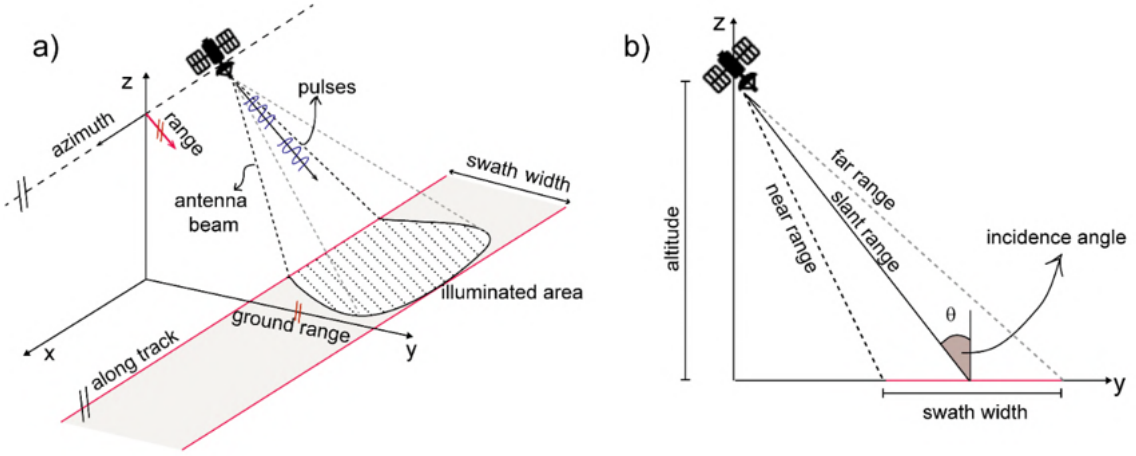


Figure 1.10. Radar acquisition geometry (Crippa, 2021)

angle, defined by the angle between the LOS and the normal to the surface, is generally slightly larger than the *off-nadir* angle over flat terrain (EGMS, 2025a). Because of SAR's side-looking geometry, the satellite's orbit direction affects its sensitivity to topography, making east-facing slopes more easily observable from ascending orbits and west-facing slopes better suited for descending orbits (Ferretti et al., 2007; Crippa, 2021). In terms of imaging quality, the spatial resolution in the azimuth direction depends on the SAR system characteristics shown in Figure 1.11: it is directly proportional to the sensor wavelength (λ) and to the distance between the sensor and the target (R_0), but it is inversely proportional to the size of the antenna (D): $L \approx \frac{R_0 \lambda}{D}$ (EGMS, 2025a).

SAR imaging can also be affected by geometric distortions, especially when observing areas with complex topography or urban structures (EGMS, 2025a). The main distortions include: *foreshortening*, *layover* and *shadowing* which all derive from SAR's side-looking geometry and thus the interaction between the radar beam and the terrain as shown in Figure 1.12 (Ferretti et al., 2007; Crippa, 2021; EGMS, 2025a).

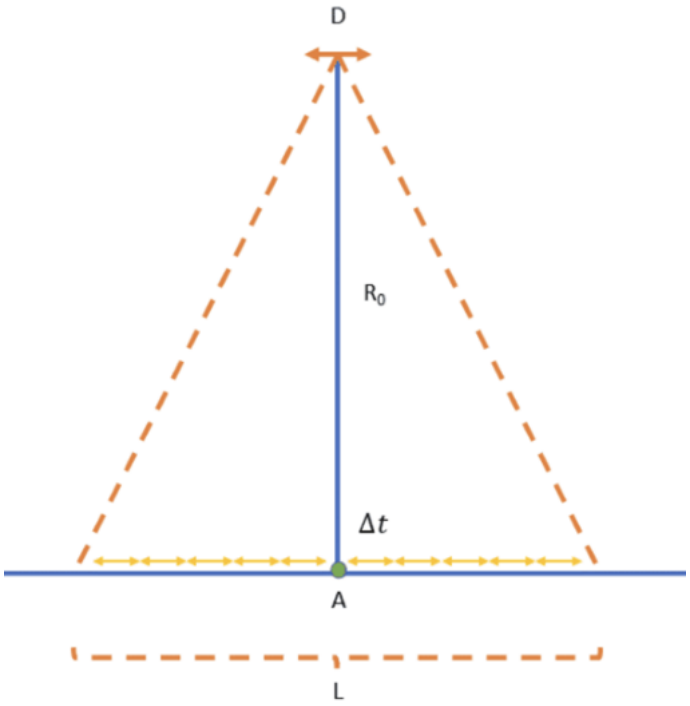


Figure 1.11. SAR azimuth resolution geometry (EGMS, 2025a)

Foreshortening and layover occur when the radar signal reaches different parts of a slope at slightly different times (EGMS, 2025a). The former occurs when the observed slopes face the sensor and the different portions of the slope are compressed in a small number of pixels along the range direction, resulting in shortened slopes in the radar image (Ferretti et al., 2007; Crippa, 2021; EGMS, 2025a). The latter is just an an extreme case of the former, occurring on very steep slopes or tall features where the radar signal reaches its top before the base, thus misrepresenting the actual topography as the top "lays over" the base (Ferretti et al., 2007; Crippa, 2021; EGMS, 2025a). Differently, *shadowing* takes place when observing slopes facing away from the sensor or behind tall structures, where the radar beam cannot reach the ground and thus records such regions with no backscatter as they are not illuminated by the radar (Ferretti et al., 2007; Crippa, 2021; EGMS, 2025a).

1.2.3 Interferometric Synthetic Aperture Radar (InSAR)

Synthetic Aperture Radar (SAR) Interferometry is a technique based on the comparison of phase values collected by repeated acquisitions of the same area of interest over different periods of time and/or from slightly different viewing angles, which ultimately leads to the detection of surface deformations (Crippa, 2021; EGMS, 2025a; TREAltamira, 2026). Although the phase information of single pixels is not directly meaningful, the difference between the phases of two acquisitions, called *interferogram* is of great relevance

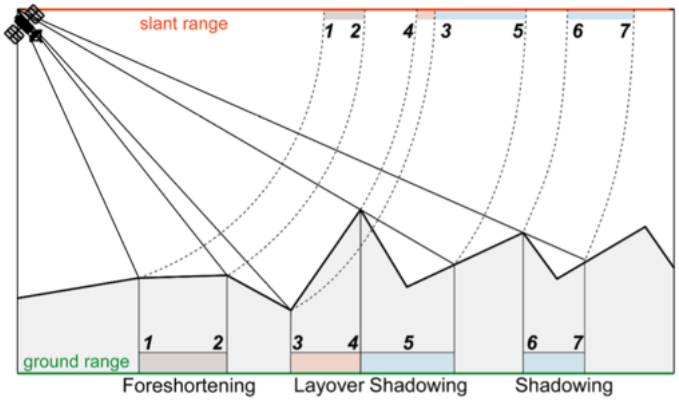


Figure 1.12. SAR geometrical distortions (Crippa, 2021)

(Ferretti et al., 2007; Crippa, 2021; EGMS, 2025a).

The interferometric phase difference $\Delta\phi_i$, which ranges from 0 to 2π, derives from different components related to *displacement*, *atmosphere*, *topography* and overall *noise* (Ferretti et al., 2007; Crippa, 2021; EGMS, 2025a; TREAltamira, 2026). The displacement component reflects changes in the target's position, while the atmospheric component entails variations in the signal's propagation speed caused by water vapour, temperature, pressure and ionospheric effects (Ferretti et al., 2007; Crippa, 2021; EGMS, 2025a; TREAltamira, 2026). The topographic component derives from differences in the acquisition geometry or elevation, while the noise component combines geometric decorrelations with temporal decorrelations such as changes in vegetation or building demolitions (Ferretti et al., 2007; Crippa, 2021; EGMS, 2025a; TREAltamira, 2026).

Diffrential SAR Interferometry (DInSAR) is based on standard SAR Interferometry and uses interferograms obtained from the comparison of pairs of SAR images acquired at different times to detect surface deformation patterns (Ferretti et al., 2007; Crippa, 2021; Crosetto et al., 2021; TREAltamira, 2026).

In order to obtain an accurate result, phase contributions related to topography, atmosphere and other systematic factors are removed from the interferograms usually by subtracting the topographic phase computed from a Digital Elevation Model (DEM) of the area of interest (Ferretti et al., 2007; Crosetto et al., 2016; Crippa, 2021; Crosetto et al., 2021; TREAltamira, 2026). This process consequently provides a residual phase that is primarily sensitive to the surface deformation taking place along the LOS between the two acquisition dates (Crippa, 2021).

The precision of the mean displacement rates estimated through DInSAR techniques is subject to the radar wavelength (shorter wavelengths being more sensitive to small deformations), the spatial resolution (which affects the level of phase noise), and

the number of SAR acquisitions collected over the time span observed (revisiting time) (Bovenga et al., 2018; Crippa, 2021; Crosetto et al., 2021; TREAltamira, 2026). DInSAR is not suited for highly accurate displacement measurements as it has been proven not to be able to successfully detect displacements that exceed the *"velocity of ambiguity"* between two acquisitions, but it can surely be considered an effective method to identify the spatial footprint and approximate magnitude of progressing surface movements over large areas (Crippa, 2021; TREAltamira, 2026).

1.2.4 Multi-interferogram techniques

Although a single interferogram can detect millimetre-scale surface changes, its performance is often limited by ambiguities associated with the previously mentioned factors that constitute the interferometric phase difference (displacement, atmosphere, topography and general noise) (EGMS, 2025a). In slow deformation processes, these error components can be much larger than the actual ground motion, causing the signal to be hidden by noise if the time period considered is not sufficiently long (Crippa, 2021).

Atmospheric artefacts are typically spatially correlated within a single acquisition but vary randomly in time, whereas ground deformation tends to be temporally coherent and may show spatial correlation at some degree (EGMS, 2025a). Such different behaviour suggests the use of multiple interferograms instead of a single one in order to successfully detect slope deformations and to filter errors (Crippa, 2021; EGMS, 2025a).

Several multi-interferogram methods have been developed over time, such as the Persistent/Permanent Scatterers (PS) technique, the SqueeSAR technique, the Small Baseline Subset technique (SBAS) and the Multiple Aperture SAR Interferometry (MAI) (Ferretti et al., 2001, 2007; Crippa, 2021; EGMS, 2025a). Among these, the PS method focuses on highly coherent point-like targets (Permanent Scatterers) whose phase behaviour remains stable over time and is weakly affected by temporal and geometric decorrelations (Ferretti et al., 2007; Crippa, 2021; EGMS, 2025a). All the mentioned methods follow different hypotheses and mechanisms, yet they all share the same objective of gathering consistent displacement information from incoherent backgrounds by assessing phase coherence across multiple acquisitions (Crippa, 2021; EGMS, 2025a).

Permanent Scatterers Interferometric Synthetic Aperture Radar (PSInSAR)

Permanent Scatterer Interferometry represents a specific category of DInSAR (Crosetto et al., 2016). PSInSAR is a technique developed by Politecnico di Milano in the late 1990s to overcome the main limitations of conventional SAR Interferometry, enabling the achievement of millimetre accuracy in the monitoring of relative surface displacements

(Perissin & Ferretti, 2007; TREAltamira, 2026). Such technique focuses on the detection of the most coherent radar targets within a given area of interest (Permanent Scatterers) that have a stable phase and amplitude behaviour, thus emit a constant electromagnetic backscattered signal (Figure 1.13) (Perissin & Ferretti, 2007; Crippa, 2021). PS commonly are anthropic infrastructures such as buildings and bridges and natural features as exposed soil and bare rock (Crippa, 2021; EGMS, 2025a; TREAltamira, 2026).

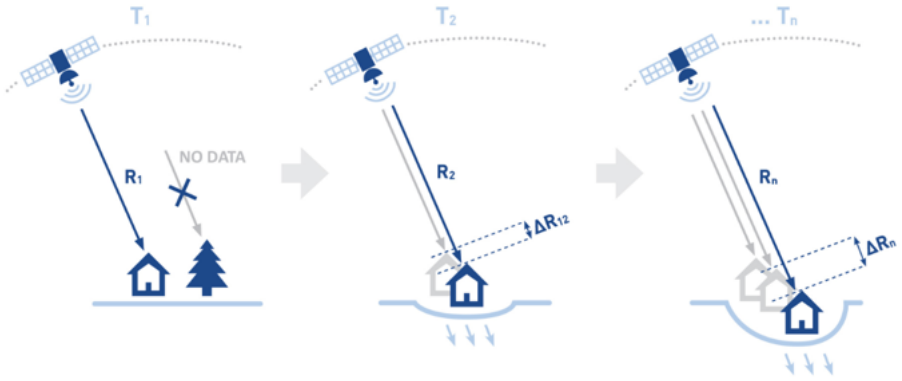


Figure 1.13. PSInSAR method representation (TREAltamira, 2026)

The PS method consists of a number of steps in order to define which PS to use. SAR images are firstly co-registerd to a common master that is set to maximise coherence and minimise temporal and geometric decorrelations and consequently a set of differential interferograms is generated between the different SAR acquisitions and the chosen master one (Crippa, 2021). After a preliminary correction of atmospheric effects, possible PS are identified and only those satisfying determined criteria as respecting specific velocity or amplitude thresholds are kept for the time-series analysis(Crippa, 2021).

The PSInSAR technique results deeply valuable as it generates displacement time series for individual points instead of relaying on spatially-averaged estimates. In this way, it is possible to conduct a more detailed analysis of slope deformations as PS can highlight the kinematics along the ground surface.

1.2.5 The European Ground Motion Service (EGMS)

The EGMS is an integral component of the Copernicus Land Monitoring Service (implemented by the European Environment Agency (EEA)) and it is the largest wide-area ground deformation monitoring service based on PSInSAR technologies (Crosetto et al., 2021, 2025, 2026). It applies advanced multi-interferogram InSAR techniques to full-resolution Sentinel-1 SAR data acquired in both ascending and descending passes to obtain displacement time series and average velocities at Measurement Point (MP)s with a

precision of few millimetres per year (Crosetto et al., 2021; EGMS, 2022; Shahbazi et al., 2024; EGMS, 2026a). The EGMS covers the 30 Copernicus Participating States, providing consistent, standardised, and harmonised information on natural and anthropogenic ground motion phenomena across Europe, with products available on a full, open, and free-access basis (EGMS, 2022; Crosetto et al., 2025, 2026; EGMS, 2026a).

The EGMS offers three types of products: *Basic*, *Calibrated* and *Ortho*. The *Basic* product (*Level 2a*) provides LOS displacement and velocity time series for every MP, having each frame referred to a local reference point and resulting suitable for local-scale deformation analysis (Crosetto et al., 2021; EGMS, 2022). The *Calibrated* product (*Level 2b*) shares the same LOS structure as the previous one but it references the measurements to a deformation model derived from GNSS data, thus ensuring absolute measurements that are consistent across adjacent areas and frames (Crosetto et al., 2021; EGMS, 2022; Crosetto et al., 2025). The *Ortho* product (*Level 3*) is referenced to the same GNSS model but further divides the detected motion into an *east-west horizontal* and an *up-down vertical* component, resampled to a 100 m grid, making it possible to have a ground displacement analysis independent of the radar acquisition geometry, yet maintaining compatibility with other Copernicus Land Monitoring Service datasets (Crosetto et al., 2021; EGMS, 2022, 2026a).

The three products all derive from Level-1 SLC data from the Sentinel-1 satellites, operating in C-band at an Interferometric Wide (IW) mode with a spatial resolution of about 5 m in range and 20 m in azimuth (EGMS, 2022, 2025a). Images acquired in the IW mode are made of three sub-swaths, each formed by a sequence of nine bursts stacked in the azimuth direction as shown in Figure 1.14 (EGMS, 2025a).

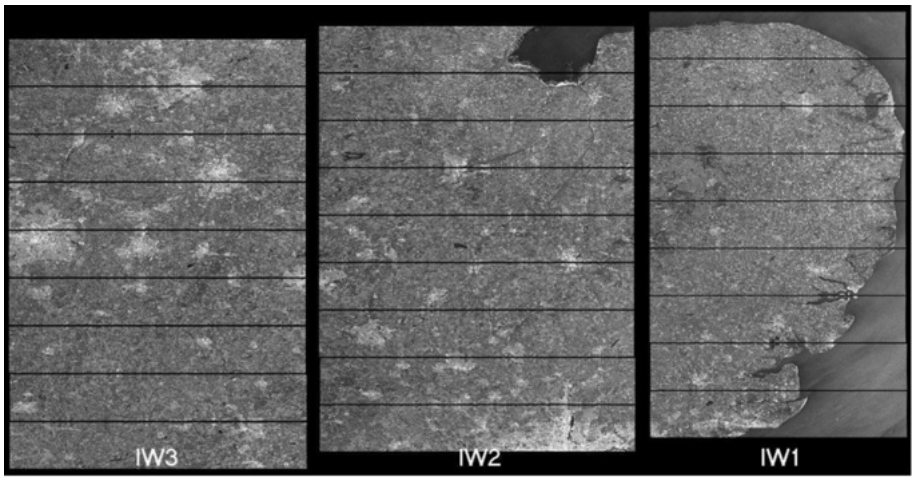


Figure 1.14. Sentinel-1 IW acquisition mode: 3 sub-swaths with 9 bursts each (EGMS, 2025a)

Each burst covers an area of approximately 80 km in range and 20 km in azimuth,

thus completing scene with a total size of about *250 km by 180 km* (EGMS, 2025a). The common revisiting time is of 6 days when both Sentinel-1A and Sentinel-1B are operational, and 12 days when just one of the two is working (EGMS, 2022). The service is updated annually, with a baseline product ranging from 2015 to 2020 and subsequent updates (EGMS, 2022; Crosetto et al., 2025). Internal quality control and external validation based on GNSS, levelling and other ground data ensure the precision and reliability of the deformation estimates (Crosetto et al., 2021; EGMS, 2025c, 2026a).

Chapter 2

Geographical and geological setting

2.1 Geographical setting

2.1.1 Overview

The analyses carried out in this thesis cover an area located in north-western Italy, in Piedmont. Such area of interest lies within the Susa Valley, part of the Cottian Alps, which is formed by 39 municipalities all belonging to the Metropolitan City of Torino, with Bardonecchia, Cesana Torinese, Oulx, and Sauze di Cesana being the most important ones (Alte Valli - Hautes Vallées, 2026). Based on these municipalities' altimetric bands, 32 of them are classified as *mountain* and 7 as *hill* by ISTAT, 2023. Overall, the Susa Valley extends for an area of 1126.82 km^2, representing 16.50 % of the Torino province.

The study area falls within the Cesana Torinese Sheet (F.171) of the Geological Map of Italy at a scale of 1:50.000 (Fioraso & Mosca, 2014). This sheet is based on the geological survey of nine sections of the Piedmont Region's technical map at a 1:10.000 scale and it covers an area of 295.6 km^2 within the Torino province, including most of the Dora di Cesana river basin (municipalities of Oulx, Cesana Torinese, Claviere, Sauze di Cesana, and Sestriere) which defines this work's area of interest (Fioraso & Mosca, 2014). The two DsGSDs that are analysed in this thesis are the Grange Sises (GS) and Thuras (T) landslides as shown in Figure 2.4. They are found where Cesana Torinese, Sestriere and Sauze di Cesana meet as shown in Figure 2.3.

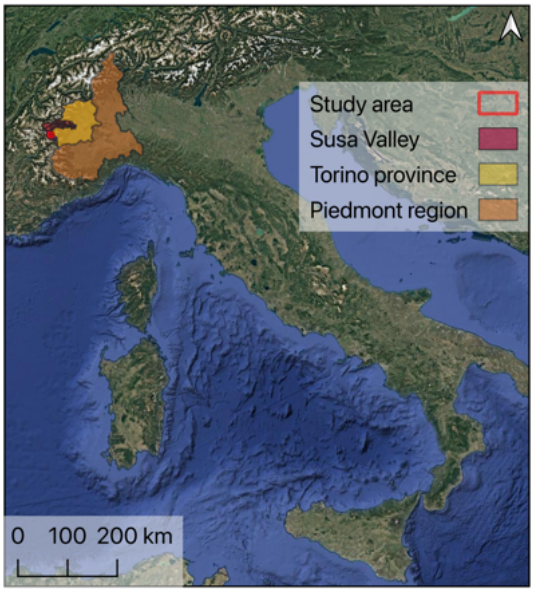


Figure 2.1. Geographic setting - overview

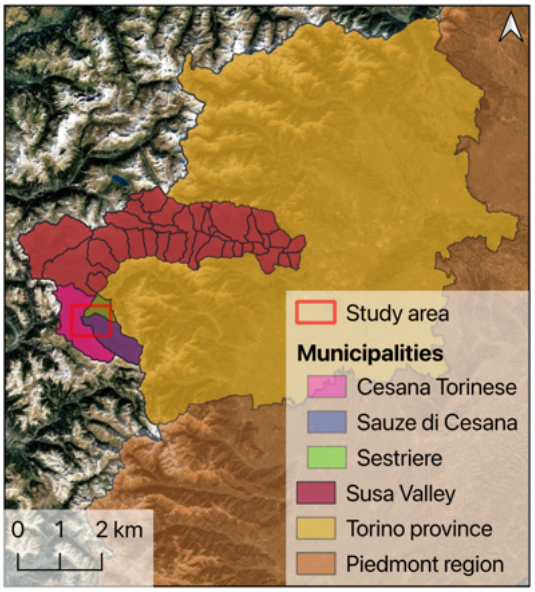


Figure 2.2. Geographic setting - Susa Valley

Grangesises

The Grangesises landslide is located on the right-hand side of the Argentera Valley, also known as the Ripa Valley. It extends from Mount Sises, at 2.657 m a.s.l. down to the municipality of Sauze di Cesana, at an elevation of about 1.540 m a.s.l.. The area also includes other peaks, such as Mount Alpette and Mount Querellert, which reach 2.298 m and 2.722 m a.s.l., respectively. The slope faces west. The landslide area also includes some small settlements, namely Grangesises, Bessen Haut, and Bessen Basse, and reaches the northeastern edge of Sauze di Cesana.

Several water courses cross the area, the main ones being Rio Sises and Rio Ciagrassa, both tributaries of the Ripa Torrent at the valley floor. The Grangesises landslide is crossed by Provincial Road SP215, which connects Grangesises and Bessen Basse with Sestriere and Sauze di Cesana, while Bessen Haut is linked only by the road known as "Strada per Bessen Alto," which leads to Sestriere. The landslide is also close to the Sestriere ski area, with ski lifts extending to both Mount Sises and Mount Alpette.

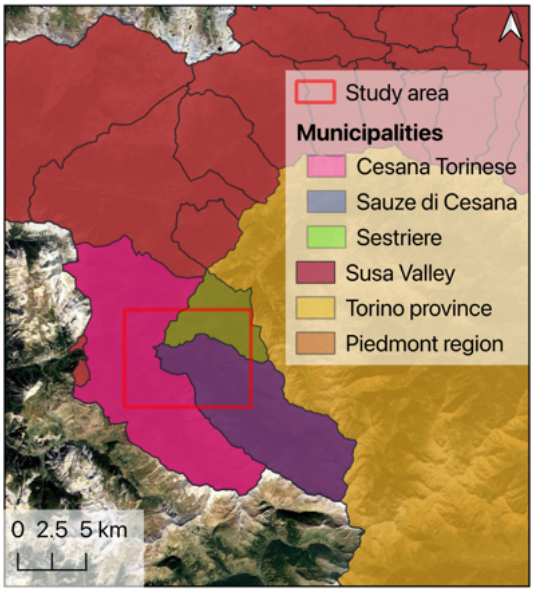


Figure 2.3. Geographic setting - municipalities

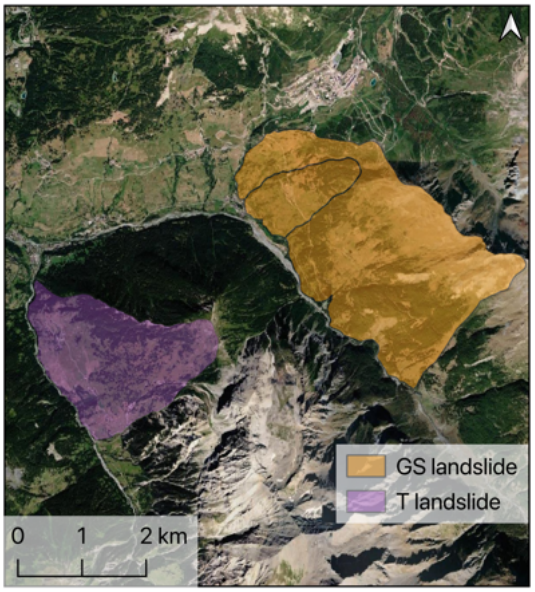


Figure 2.4. Grangesises and Thuras landslides

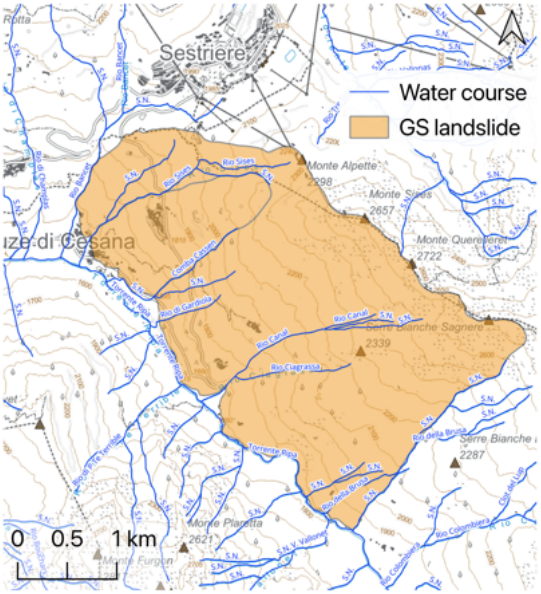


Figure 2.6. Grangesises landslide - topography and water courses

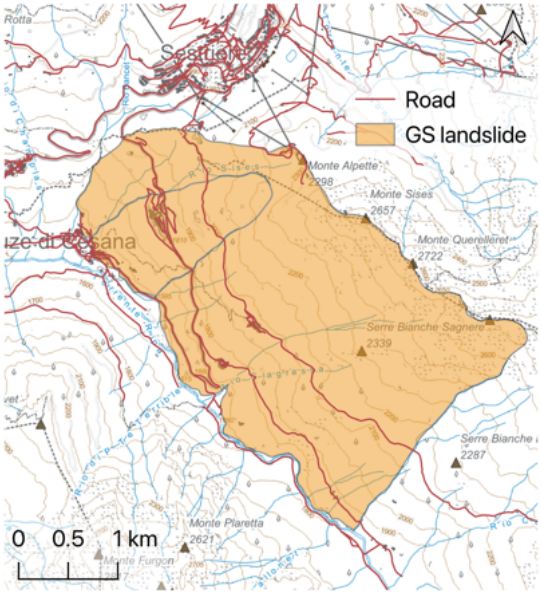


Figure 2.7. Grangesises landslide - roads

The landslide area is predominantly covered by woodland, which accounts for approximately 79% of the total surface as shown in Figure 2.8. Bare rock outcrops make up about 17% of the area and are mainly concentrated in the upper part of the slope, near Mount Querellert. The remaining surface is divided amongst agricultural areas, urbanised areas, and water courses.

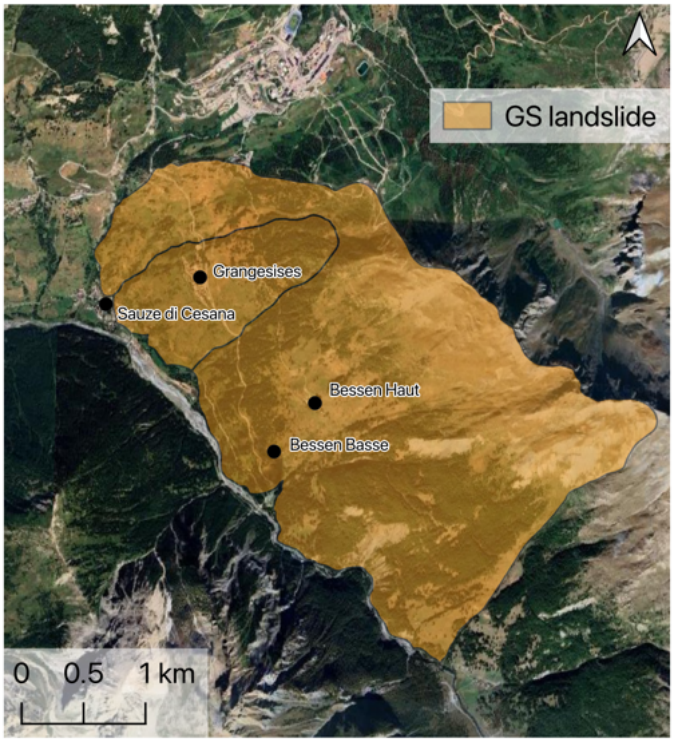


Figure 2.5. Grangesises landslide - urban settlements

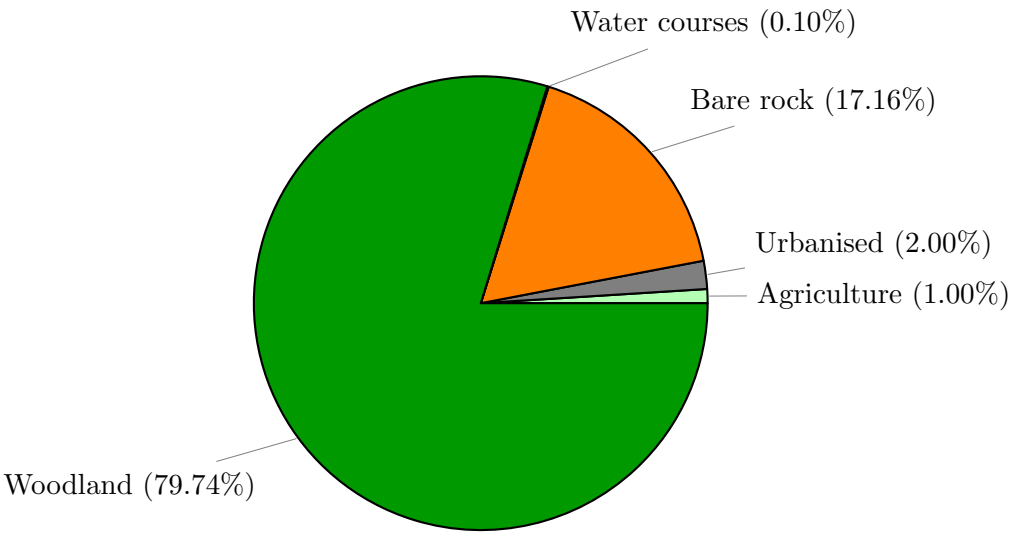


Figure 2.8. Grangesises landslide - land and use distribution

Thuras

The Thuras landslide, also known as the Cima Bosco landslide, is located on the right-hand side of the Thuras Valley. It extends from Mount Cima Bosco down to the Thuras urbanisation at the valley floor, from about 2.370 m a.s.l. to 1.530 m a.s.l. and has

a west-facing aspect. The village of Thuras is the largest settlement within the landslide area, but several very small hamlets are also present, including Champ Quartier, Thuras Gorlier and Rhuilles.

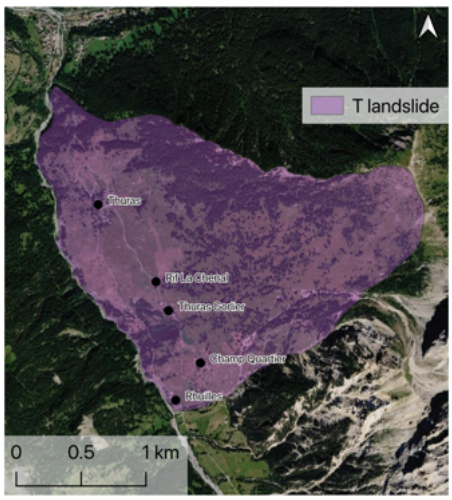


Figure 2.9. Thuras landslide - urban settlements

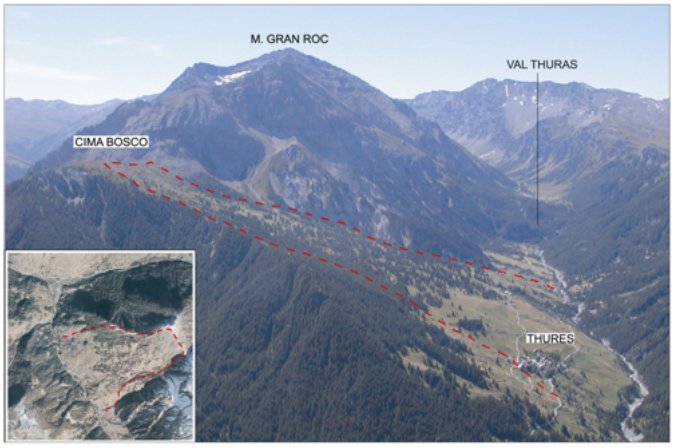


Figure 2.10. Thuras landslide - location (Alberto et al., 2008)

The area is crossed by several water courses, the two main ones being Rio Nortaud and Rio Bouchars, both merging with the Thuras Torrent located at the valley floor. A local road, known as Frazione Thuras, connects the different settlements and links them to the rest of the valley through Bousson and the crossing of the Thuras Torrent.

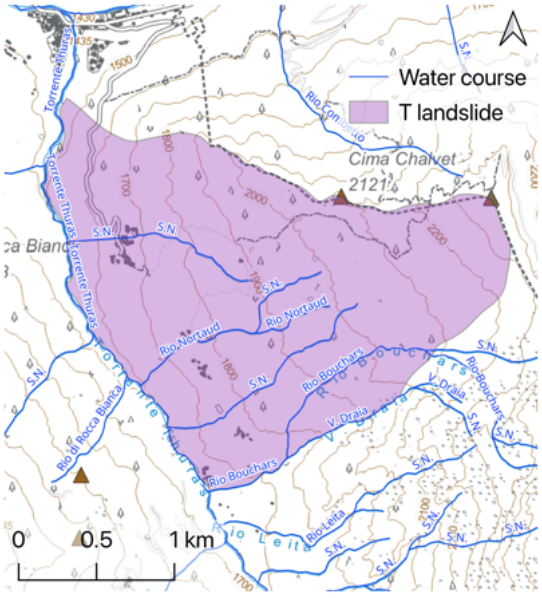


Figure 2.11. Thuras landslide - topography and water courses

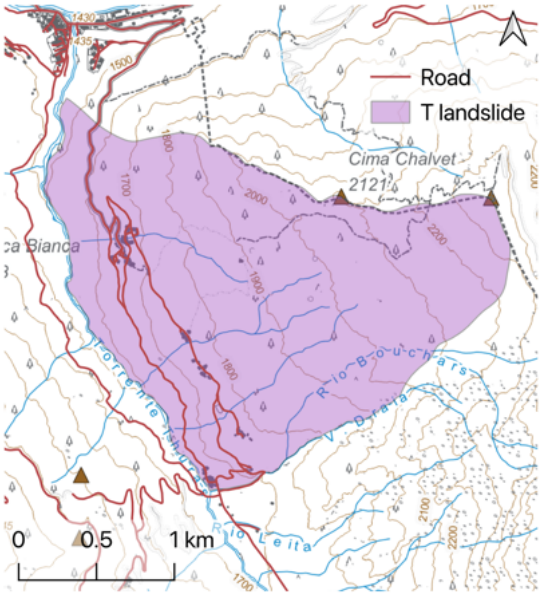


Figure 2.12. Thuras landslide - roads

The landslide area is mainly covered by woodland, which accounts for 94.6% of the total area. Agricultural land covers 3%, while bare rock accounts for 1.21%. The remaining small portion is divided between urbanised areas and water courses.

2.2 Geological setting

2.2.1 Overview

The western sector of the Alpine chain, where the Cesana Torinese Sheet is located, originates from the convergence between the European and the Adriatic plates in the Cretaceous (Fioraso & Mosca, 2014). Such movement triggered a long and complex geo-dynamic evolution that led to the partial subduction and consequent closure of the oceanic domain (the *Ligurian-Piedmontese Basin*), which originally separated the two plates, ultimately resulting in continental collision (Fioraso & Mosca, 2014).

The area entailed by the Cesana Torinese Sheet belongs to the axial zone of the Alpine belt, which is characterised by tectonic units that underwent tectono-metamorphic processes associated with subduction and continental collision during the Alpine orogeny (Fioraso & Mosca, 2014). This area lies between the Insubric Line and the Penninic Front and it encompasses both oceanic (*Ligurian-Piedmontese*) and continental (*Penninic and Austroalpine*) nappes (Fioraso & Mosca, 2014).

The Cesana Torinese Sheet mainly features *Ligurian-Piedmontese* and *distal continental margin* units, such as *Piedmontese units* (Fioraso & Mosca, 2014). The former represent the development of the Mesozoic ocean basin once located between the Adriatic and European plates, while the latter, shown in the carbonate successions of the Gran Roc and in the eastern slopes of Monte Chaberton suggests the crustal stretching and continental rifting that led to the original opening of the Ligurian-Piedmontese ocean (Fioraso & Mosca, 2014).

Ligurian-Piedmontese Units

The sequences within the Ligurian-Piedmontese Units reflect the evolution of the Middle-to-Late Jurassic ocean basin that separated the Adriatic and European plates (Fioraso & Mosca, 2014). According to their lithostratigraphic characteristics, these units are traditionally divided into two categories: *ophiolitic* and *incertae sedis* units (Fioraso & Mosca, 2014).

The *ophiolitic* units consist of fragments of the ancient oceanic basement and its associated sedimentary cover (Fioraso & Mosca, 2014). Such cover is mainly composed of *calc-schists* and often includes portions of the oceanic crust (Fioraso & Mosca, 2014). Those units showing very thick *calc-schists* sequences and scattered ophiolitic elements are interpreted as trench deposits or as sectors where the oceanic crust was consumed during subduction (Fioraso & Mosca, 2014).

The *incertae sedis* units include carbonate metasedimentary successions that lack ophiolitic rocks and often contain a significant soil components (Fioraso & Mosca, 2014). It is thought that these units have been deposited within the subduction trench or along the distal continental margins (Fioraso & Mosca, 2014).

Piedmontese Units

The *Piedmontese* units originate from the distal sectors of the continental margin and they are characterised by a stratigraphic succession that begins with Triassic dolostones and evolves into a calcareous-marly sequence extending into the Cretaceous. In the Cesana Torinese Sheet, this domain is primarily found in the Chaberton - Grand Hoche - Grand Argentier tectono-stratigraphic unit.

The lithostratigraphic evolution of this unit begins with a significant succession of Upper Triassic platform dolostones, followed by Rhaetian-Hettangian alternations of pelites, calcareous schists and limestones (Fioraso & Mosca, 2014). Subsequently, there is evidence of a Sinemurian unconformity, locally marked by discontinuous layers of calcareous-dolomitic breccia which separate earlier deposits from a series of Lower-to-Middle Jurassic calc-schists that still show evidence of continental detrital input (Fioraso & Mosca, 2014). The progressive deepening of the basin is subsequently shown by a Middle-to-Upper Jurassic siliceous horizon which is correlated with the radiolarites found in oceanic units (Fioraso & Mosca, 2014). Finally, the succession ends in the Cretaceous with a dominance of calcareous schists containing dark pelitic layers which are comparable to black shales, showing the margin's definitive transition into a deep pelagic environment (Fioraso & Mosca, 2014).

Quaternary glacial evolution and deposits

The geological understanding of the Quaternary successions in the area originates from the 1911 Cesana Torinese Sheet (F. 66) (Fioraso & Mosca, 2014). Such mapping classified alluvial, lacustrine and glacial deposits, ranging from Würmian to recent moraines, yet it failed to recognise the extensive landslide bodies that characterise the calc-schist slopes of this region (Fioraso & Mosca, 2014).

A more detailed glaciological framework was defined by the geologist Federico

Sacco, who focused on the post-Würmian dynamics of the Dora di Cesana basin (Fioraso & Mosca, 2014). His observations in the Chisonetto Valley highlighted the Borgata glacial complex, characterised by three sub-parallel morainic ridges (Fioraso & Mosca, 2014). Additionally, Sacco found evidence of a massive glacial body occupying the Sestriere Pass which fed both the Val Chisone and the Susa Valley systems (Fioraso & Mosca, 2014).

2.2.2 Grangesises landslide geological and geo-morphological setting

The Grangesises landslide is located within the Piedmontese unit of calc-schists with greenstones (Agenzia Regionale per la Protezione dell'Ambiente del Piemonte, 2012).

According to the Geological Map of Italy, the bedrock mainly consists of highly heterogeneous calc-schists, ranging from carbonaceous and phyllitic to albitic varieties (Agenzia Regionale per la Protezione dell'Ambiente del Piemonte, 2012). These are locally covered by Quaternary deposits, including Würmian to recent moraines and scree deposits (Agenzia Regionale per la Protezione dell'Ambiente del Piemonte, 2012).

From a litho-mechanical perspective, the calc-schists that originate from the low-grade metamorphism of calcareous-marly sediments can be classified into three main lithotypes in the study area:

- *phyllitic calc-schists* with high mica and carbonaceous content, a well-defined schistosity, and advanced weathering,
- *banded calc-schists* showing folds of alternating layers and calcitic veins,
- *massive carbonate calc-schists* with low schistosity (Agenzia Regionale per la Protezione dell'Ambiente del Piemonte, 2012).

Glacial deposits are found at lower elevations and they often appear displaced or altered by slope processes. Scree deposits are way more limited compared to what is shown in the Geological Map of Italy (Agenzia Regionale per la Protezione dell'Ambiente del Piemonte, 2012).

Detailed analyses conducted since the 1980s have revealed that the entire slope is characterised by several geomorphological indicators of deep-seated instability such as scarps, trenches, open fractures, and elongated depressions (Agenzia Regionale per la Protezione dell'Ambiente del Piemonte, 2012). These all share a E-W and ESE-WNW orientation that aligns with the regional discontinuity systems, thus suggesting a direct connection between the failure mechanisms and the intrinsic structure of the bedrock (Agenzia Regionale per la Protezione dell'Ambiente del Piemonte, 2012).

The Piedmont Landslide Information System (SIFRAP) provides a general overview of the different slope processes affecting the area: the main body is classified as a DsGSD and it shows several superficial movements, mainly classified as complex landslides, rock-falls and toppling (Agenzia Regionale per la Protezione dell'Ambiente del Piemonte, 2015).

Agenzia Regionale per la Protezione dell'Ambiente del Piemonte, 2012 was able to further integrate the initial studies of the area through photo-interpretation and subsequently divided the landslide area into five main sectors that are characterised by specific morphology, deformation style, evolutionary stage, and involved materials as shown in Figure 2.17.

Sector 1 is defined as a DsGSD and it includes the middle-upper slope, extending from Monte Sises to Piano San Giacomo (Agenzia Regionale per la Protezione dell'Ambiente del Piemonte, 2012). It is featured by scarps and discontinuities mainly developing in bedrock with local displacements and fractures that induce a stepped morphology (Agenzia Regionale per la Protezione dell'Ambiente del Piemonte, 2012). The upper part of this section shows clear counter-slopes, trenches, transverse depressions and double ridges (Agenzia Regionale per la Protezione dell'Ambiente del Piemonte, 2012). In the middle and lower portions, the slope has a pronounced convex profile caused by large debris accumulations, warping and swelling (Agenzia Regionale per la Protezione dell'Ambiente del Piemonte, 2012).

Sector 1b is found between Rio Merdarello and Rio Comba Cassen, near Grange Sises and it shows a similar pattern to the first sector, yet with more subtle geomorphic features suggesting an intermediate evolutionary stage (Agenzia Regionale per la Protezione dell'Ambiente del Piemonte, 2012). Both loose deposits and fractured rock are present and a slow rock flow affects the area just below the Grange Sises settlement (Agenzia Regionale per la Protezione dell'Ambiente del Piemonte, 2012).

Sector 2 is a superficially unstable area that corresponds to the Rio Merdarello basin (Agenzia Regionale per la Protezione dell'Ambiente del Piemonte, 2012). This slope shows deep incisions and local instability especially near the stream, where notable morphological changes occurred over a period of about 25 years (Agenzia Regionale per la Protezione dell'Ambiente del Piemonte, 2012). The overall behaviour is composite: the upper part is mainly affected by sliding, while the middle and lower parts show slow flow-like movements, thus this sector is classified as a complex landslide (Agenzia Regionale per la Protezione dell'Ambiente del Piemonte, 2012).

Sectors 3 and 4 are classified as complex landslides too as they share a similar behaviour with *sector 2*, yet showing a more rigid mass movement, with sliding rather than visco-plastic flow (Agenzia Regionale per la Protezione dell'Ambiente del Piemonte,

2012). These sectors respectively correspond to the area of Bessen Bas and Bessen Haut and to the Coste Rugne area (Agenzia Regionale per la Protezione dell'Ambiente del Piemonte, 2012). Additionally, a smaller translational/rotational slide has been identified immediately east of Bessen Bas (Agenzia Regionale per la Protezione dell'Ambiente del Piemonte, 2012).

The overall area is covered by a thick sequence of gravitational deposits defined by the progressive disintegration of the rock mass (Agenzia Regionale per la Protezione dell'Ambiente del Piemonte, 2012). Such deposits mainly consist of a sandy-silty matrix that embeds intensely crushed calc-schist blocks and lay upon a highly fractured and weathered bedrock, which shows significant structural degradation extending at least 100 meters below the ground surface (Agenzia Regionale per la Protezione dell'Ambiente del Piemonte, 2012). The displacement dynamics takes place along the line of maximum slope and shows an acceleration towards the valley floor, with velocities in the middle sector ranging from 5 to 20 mm/year (Agenzia Regionale per la Protezione dell'Ambiente del Piemonte, 2012).

2.2.3 Thuras landslide geological and geo-morphological setting

The Thuras landslide is entirely developed within calc-schists belonging to the Piedmont Oceanic Units which show a well-defined schistosity dipping downslope and that are extensively fractured and locally loosened (Alberto et al., 2008). The upper sector of the landslide is divided in a more superficial thick (*10 - 20 m*) layer made of bedrock, eluvio-colluvial materials and glacial deposits that is affected by multiple rotational landslides of recent evolution independent from the deeper body (Alberto et al., 2008). The observed recent and ongoing movements within the shallow portion of the Thuras landslide can be mainly attributed to widespread and disordered water circulation network, as well as to the progressive retreat of the main scarp (Alberto et al., 2008).

Differently, the deeper sector shows evidence of an earlier evolutionary stage consistent with a DsGSD, yet it lacks signs of recent activity (Alberto et al., 2008). This classification is supported by the evidence of the main features typical of this type of phenomenon, including trenches in the upper convex part of the slope, a significant degree of rock mass disaggregation while still preserving its internal structural framework and the presence of glacial deposits showing their original yet deformed morphological characteristics(Alberto et al., 2008).

The SIFRAP Inventory provides a general overview of the different slope processes affecting the area: the main body is classified as a DsGSD and it shows other sreduced superficial movements, mainly classified as complex landslides and rotational/translational

slides (Agenzia Regionale per la Protezione dell'Ambiente del Piemonte, 2015).

The Thuras Valley is carved into several tectono-metamorphic units all belonging to the Penninic Complex:

- *Calc-schist Unit* without ophiolites predominantly consisting of a thick succession of calc-schists,
- *Lago Nero Oceanic Unit* characterised by a serpentinite basement covered by a Ligurian-type sedimentary cover with detrital intercalations,
- *Chenaillet Oceanic Unit* made up of a well-preserved oceanic basement, lacking sedimentary cover and only slightly affected by Alpine metamorphism,
- *Mesozoic Continental Margin Unit* consisting of a thick dolomitic succession,
- *Gypsum-bearing formations* composed of evaporitic rocks that are thought to have contributed to the transformation of part of the dolomitic succession into Pliocene – Quaternary carbonate breccias (Alberto et al., 2008).

The Geological Map of Italy classifies the area as mainly made of schists and mica-schist (Figure 2.18), but a further detailed map shows where the previously mentioned units are observed (Figure 2.19) (Alberto et al., 2008; Agenzia Regionale per la Protezione dell'Ambiente del Piemonte, 2012).

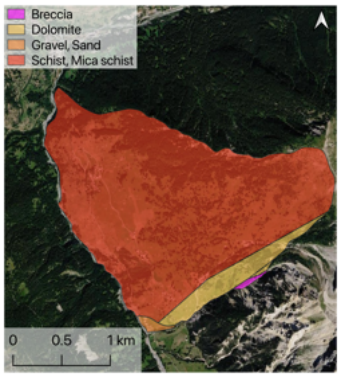


Figure 2.18. T geological classification

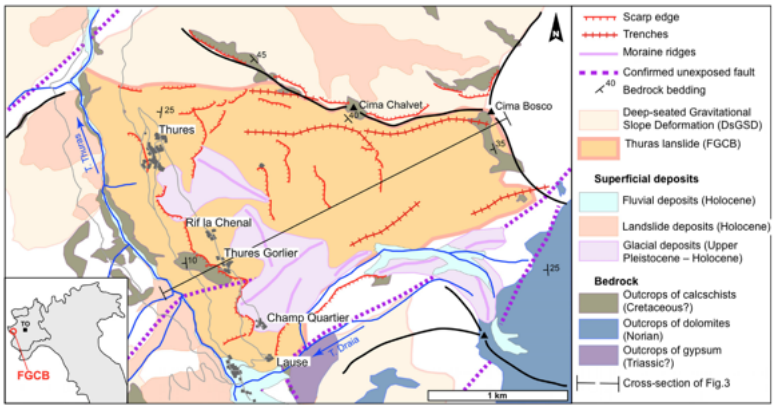


Figure 2.19. T landslide - geologic and geomorphologic sketch (modified from Alberto et al., 2008)

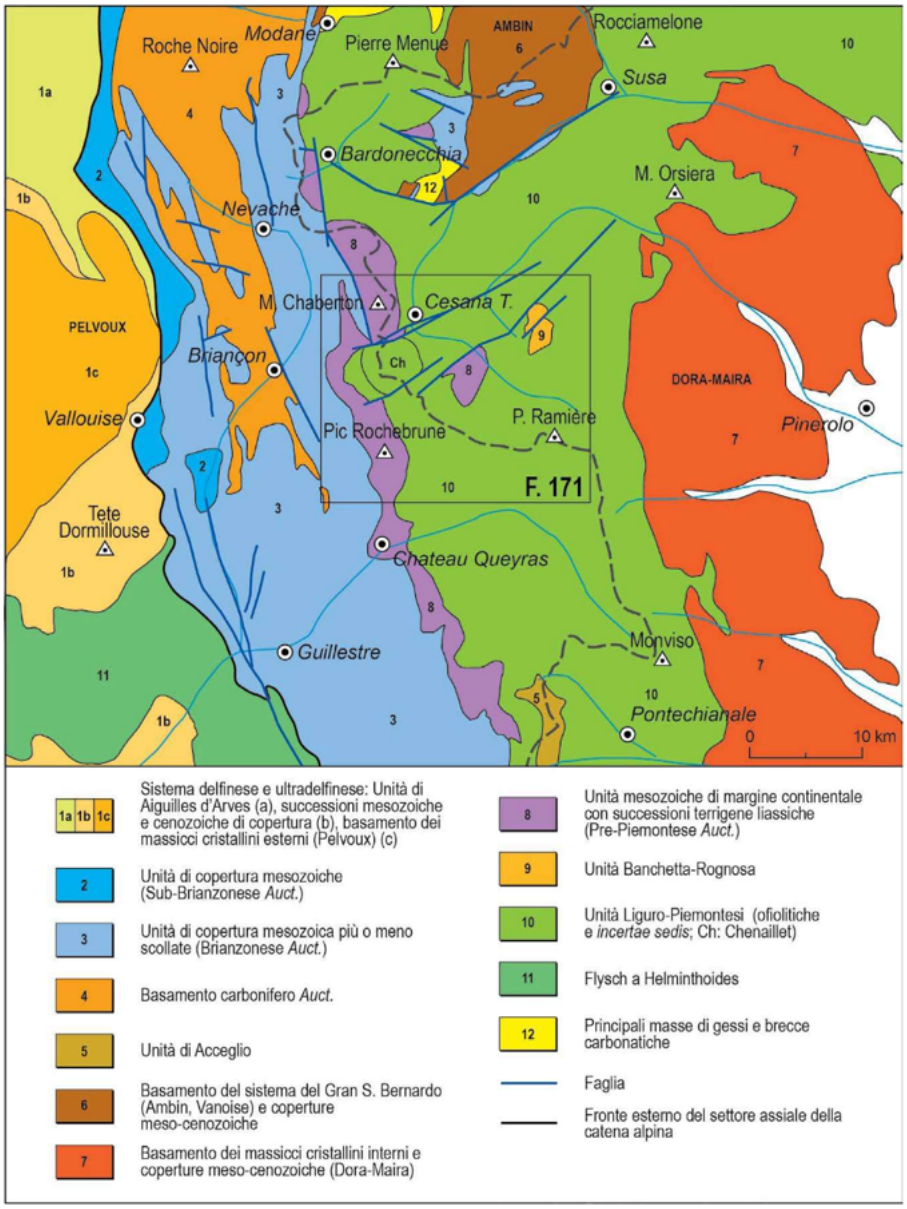


Figure 2.13. Cesana Torinese Sheet - simplified geological scheme (Fioraso & Mosca, 2014)

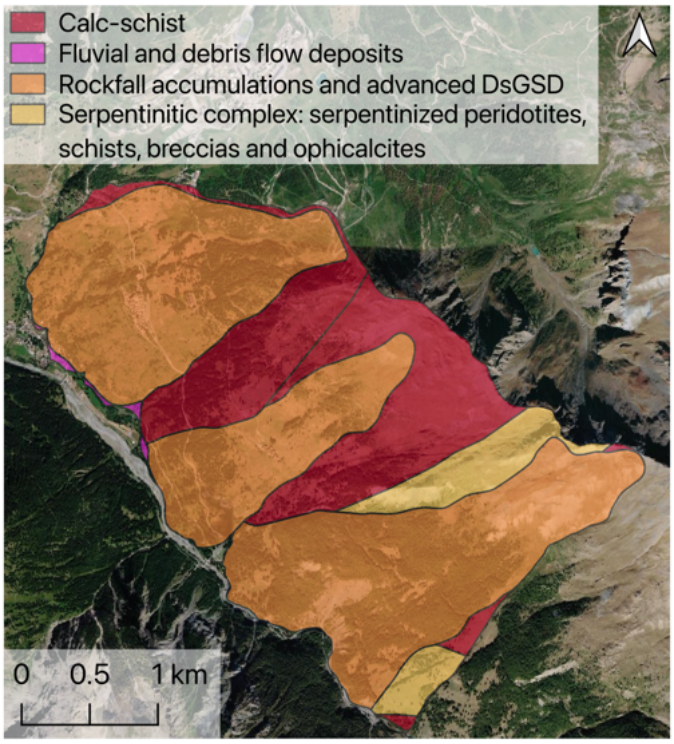


Figure 2.14. GS geological classification (Agenzia Regionale per la Protezione dell'Ambiente del Piemonte, 2025a)

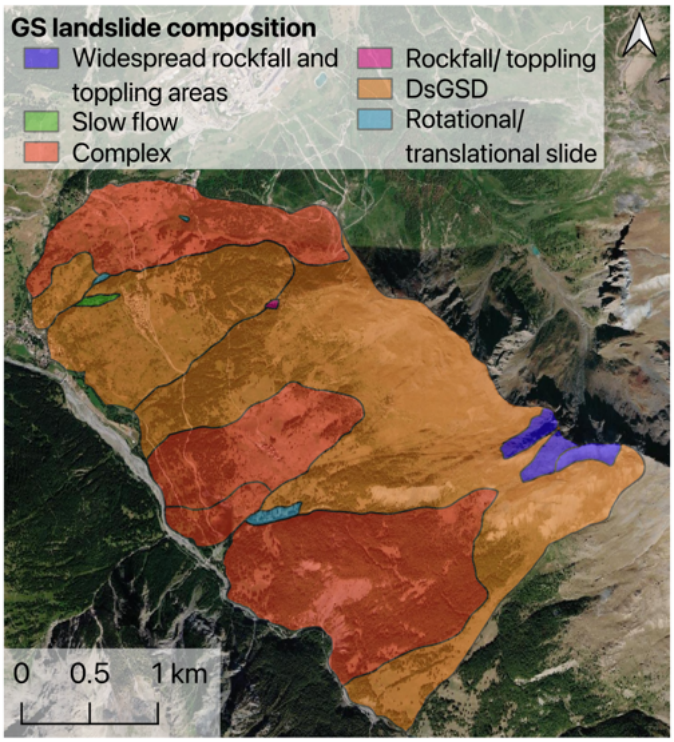


Figure 2.15. GS landslide classification (Agenzia Regionale per la Protezione dell'Ambiente del Piemonte, 2015)

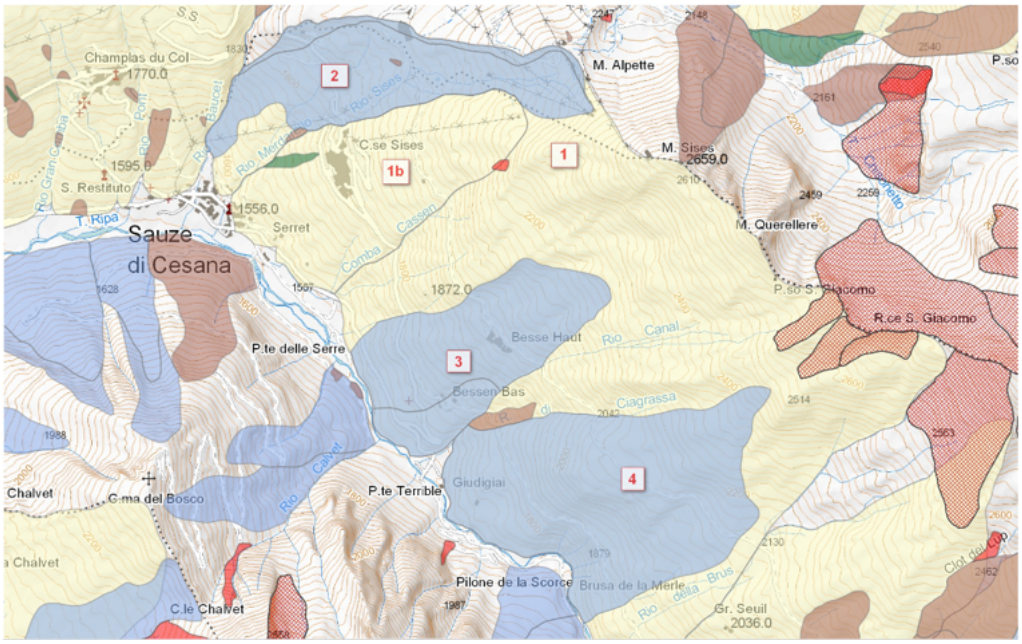


Figure 2.16. GS landslide sectors (Agenzia Regionale per la Protezione dell'Ambiente del Piemonte, 2012)

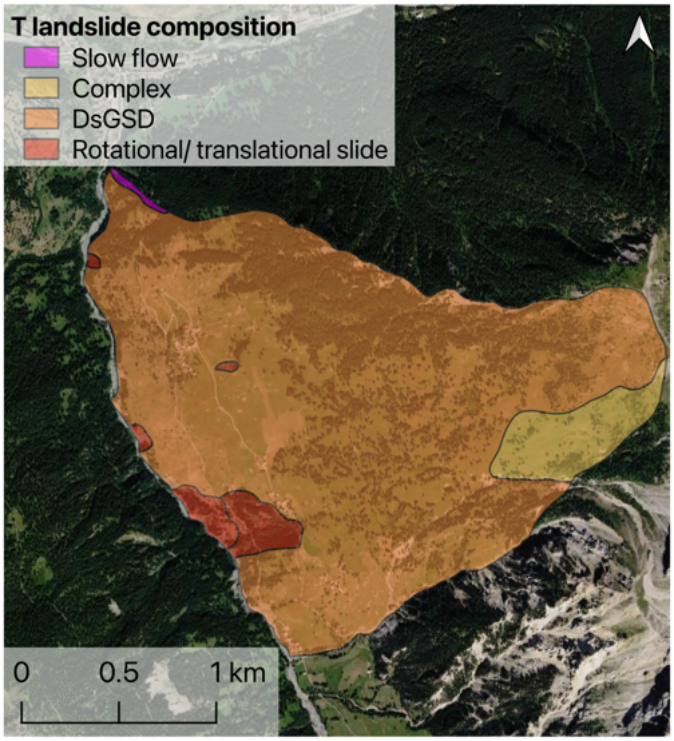


Figure 2.17. T landslide classification (Agenzia Regionale per la Protezione dell'Ambiente del Piemonte, 2015)

Chapter 3

Methodology

3.1 Overview

This thesis analyses the movement of two DsGSDs: the Grangesises and Thuras landslides. The analysis is based on a comparison between interferometric data and data collected by *in situ* instruments, including inclinometers, piezometers and weather stations. The methodology is structured in two main steps: first, data collection and second, data analysis and interpretation.

3.2 Data gathering

3.2.1 InSAR

InSAR data used in this analysis is all gathered from EGMS Stream (EGMS, 2026b). The data is divided in two datasets: one directly available on EGMS Stream website that ranges from January 2019 to December 2023, later referred to as *2019_2024* and one that is obtained under request that goes from January 2015 to December 2021, later named as *2015_2022*. The datasets that are obtained for the overall study area are relatively clipped to the Thuras and Grangesises landslides, obtaining four datasets for each landslide: two ortho layers, one calibrated ascending and one calibrated descending.

The datasets are provided in tabular format, where each row corresponds to a single MP. The first columns contain spatial reference and identification fields, including

coordinates, point ID, and elevation information. Other fields report quality and geometric parameters, such as temporal coherence, amplitude dispersion, incidence angle, track angle, and the components of the line-of-sight vector. The dataset also includes kinematic indicators, such as mean velocity, acceleration, and their relative standard deviations. Finally, the time-series columns contain cumulative displacement values, in *mm*, for each acquisition date.

3.2.2 ReRCoMF

Arpa Piemonte manages the Regional Landslide Monitoring Network (ReRCoMF) which was established in the 1990s and now includes around 210 monitoring sites across Piedmont (Agenzia Regionale per la Protezione dell'Ambiente del Piemonte, 2025b). The network combines superficial measurements, such as topographic benchmarks monitored by total station or GPS, with deep instruments, including manual and fixed inclinometers, automated piezometers and multiparametric borehole columns (Agenzia Regionale per la Protezione dell'Ambiente del Piemonte, 2025b). In some sites, additional devices such as automated GPS, automated total stations and extensometers are also installed (Agenzia Regionale per la Protezione dell'Ambiente del Piemonte, 2025b). This monitoring system is especially suited to slow-moving landslides, since its instruments and acquisition frequency are not designed for direct early warning (Agenzia Regionale per la Protezione dell'Ambiente del Piemonte, 2025b). In the landslides analysed, three types of instruments are present: manual inclinometers, fixed inclinometers, and piezometers.

For what it concerns fixed inclinometers, the data obtained includes the date, the measured displacement and the corresponding direction of movement at a specific depth. Manual inclinometers provide instead displacement measurements at different depths at different times. For every investigated depth (every 0.5 m), the dataset reports both incremental and cumulative displacements that are expressed through two orthogonal vector components, together with their corresponding resultant magnitude and azimuth. Piezometer datasets report, for each date, the corresponding groundwater level measured by the instrument, expressed in metres relative to a reference level.

3.2.3 Arpa weather stations

The regional hydro-meteorological network managed by ARPA Piemonte consists of over 400 stations, reaching an average density of one station per 100 km^2. The network is operational since 1988 and includes meteorological, thermo-pluviometric, snow monitoring and hydrometric stations recording water levels of the main rivers across Piedmont.

In this work, daily measurements of temperature, precipitation and snow depth are used. Minimum, maximum and mean temperatures are provided in degrees Celsius, precipitation is collected by rain gauges and expressed in millimetres. Snow depth measurements in centimetres are manually collected with snow measuring poles by trained technicians every morning at 8:00 local time.

Every Arpa weather station is provided with its metadata attributes including name, location, administrative information, geographic coordinates, elevation above sea level, operational period and aspect. In this research, elevation and aspect are used as the primary criteria for selecting the most relevant stations for the study area.

3.3 Data analysis

The first part of the data analysis carried out is summarised in the workflow shown in Figure 3.1.

The first preliminary step is to do the EGMS data validation. This is performed by comparing the horizontal surface displacement derived from manual inclinometers with the EGMS horizontal dataset. Practically, the cumulative displacement measured at the most superficial depth ($0.5\ m$) of each manual inclinometer is projected onto the horizontal plane and compared with the EGMS horizontal displacement values extracted within a $100\ m$ buffer around each inclinometer location. In cases where no permanent scatterers fall within the buffer, those points with the minimum distance to the inclinometer were used instead.

Secondly, graphs are produced for both fixed and manual inclinometers in order to interpret the evolution of ground deformation within each landslide area and to better understand the kinematics of the movement. For the fixed inclinometers, cumulative displacement is plotted over time to identify possible acceleration phases and trends. For the manual inclinometers instead, cumulative displacement values are plotted along different depths for all available survey dates in order to identify the depth intervals affected by deformation and potentially detect where the shear surfaces take place.

Additionally, the temporal evolution of displacement is further investigated by analysing the cumulative azimuth and the cumulative resultant displacement derived from the two orthogonal inclinometer components. The cumulative azimuth provides informa-

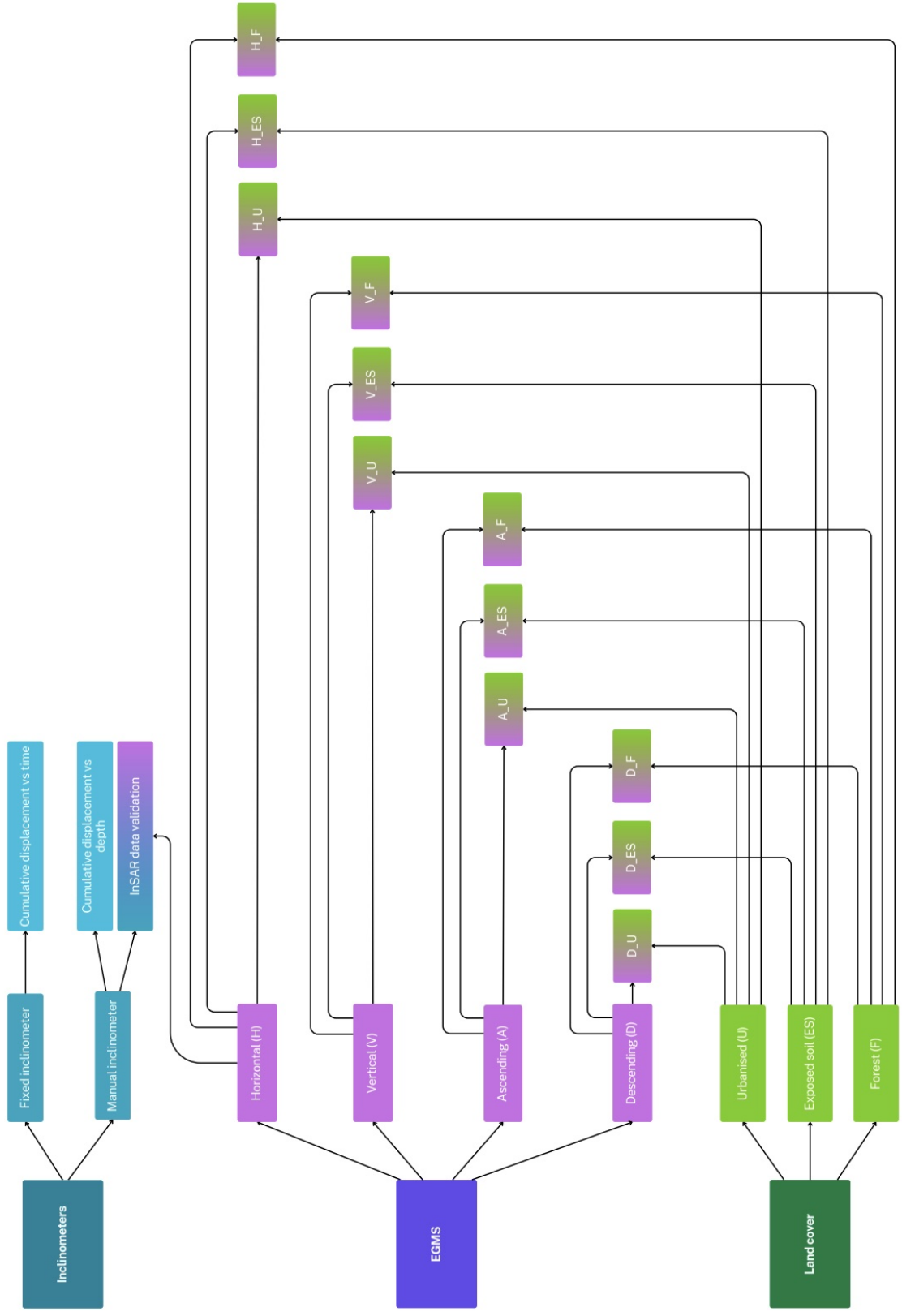


Figure 3.1. Analysis part 1 workflow

tion on the direction of movement with respect to the north, while the cumulative resultant displacement represents the overall magnitude of displacement. These parameters are evaluated over time using the most superficial measurements (*0.5 m*), which are more representative of ground surface kinematics.

Subsequently, in order to examine the overall slope stability and assess whether displacement rates vary across different sectors of the slope, the velocities detected for each PS within the landslide area are presented. To define the stability threshold adopted in this study, the standard deviation of the velocities measured in the downslope points, assumed to be stable, was used as an empirical estimate of measurement uncertainty. Consequently, the stability threshold was expressed as a multiple of this standard deviation.

For the fourth step, the initial inputs are the eight EGMS datasets and the Piedmont Land Cover (LCP) layer shared by the Piedmont Region (Regione Piemonte, 2024). The LCP was reclassified into three categories based on the different polygons' details and photo-interpretation: *urbanised (U)*, *exposed soil (ES)* and *forest (F)*.

The *U* category entails urban settlements and roads. The *ES* includes bare rocks, grasslands and agricultural areas characterised by no or low vegetation cover. Finally, the *F* category follows the definition provided by the Piedmont regional legislation (L.r. 4/2009), which classifies as forest an area with a minimum canopy cover of 20% (Regione Piemonte, 2026). Each of the three land cover categories was then intersected with the four EGMS datasets, resulting in 12 subsets that form the basis of the subsequent analysis.

Since PS are mainly detected in areas characterised by stable reflectors such as bare surfaces, rocky outcrops, urbanised areas or sparsely vegetated terrains, their spatial distribution is not uniform across the different land cover types. In particular, areas with dense vegetation such as forests and woodlands tend to exhibit a lower PS density. For this reason, the PS density is calculated separately for each of the three land cover classes in order to highlight the level of significance that each subset provides.

To model the creep movement characterising DsGSDs, three empirical creep models are fitted to each time series component : the linear Norton's law, the Modified Lomnitz law, and the Aydan model. These models are selected as they are all applicable to the secondary steady stage, matching the most common deformation regime of this type of ground movements (Aydan et al., 2014). The best-fitting model is selected based on the R^2 value and retained for all datasets. For each EGMS time series, the mean of the three fitted curves (*U, ES, F*) is then computed to assess the difference in displacement rates across land cover classes.

In a subsequent phase, the 12 subsets are compared with potential triggering

factors: depth to groundwater, mean temperature, precipitation and snow depth, in order to evaluate correlations in their temporal trends. Since EGMS displacement time series can be noisy, a *wavelet* analysis performed in R using the `WaveletComp` package (Roesch & Schmidbauer, 2018) is applied to identify potential correlations that would otherwise be hidden by noise.

Wavelet analysis makes it possible to examine a time series simultaneously in the time and frequency domains, being an extremely useful tool for non-stationary signals such as the ones analysed (Roesch & Schmidbauer, 2018). In this study, a cross-wavelet approach is used to compare two time series at the time (displacement and a triggering factor), by identifying shared periodic components and assessing how their relationship changes over time (Roesch & Schmidbauer, 2018). The similarities in their trends are quantified through cross-wavelet power,, which measures the intensity of common oscillations at different time scales and periods (Roesch & Schmidbauer, 2018).

The shared variance between the two signals is quantified through cross-wavelet power, which measures the intensity of common oscillations at different time scales and periods.

The phase angle further indicates whether the two series are in phase or in anti-phase, as well as which one leads the other. This is represented by the orientation of the arrows in the graphs, according to the convention shown in Figure 3.2 (Roesch & Schmidbauer, 2018). For simplification, phase angles are expressed in degrees (°) rather than radians, and classified according to the following convention as also shown in Figure 3.3:

- *in phase*: $0° < \theta < 90°$ and $270° < \theta < 360°$ (when one increases, the other does too);
- *out of phase*: $90° < \theta < 270°$ (when one increases the other decreases);
- *X leading Y*: $90° < \theta < 180°$ and $270° < \theta < 360°$;
- *Y leading X*: $0° < \theta < 90°$ and $180° < \theta < 270°$.

To convert this phase angle into an interpretable time delay, the following formula needs to be applied:

$$\text{Delay [days]} = \frac{\theta}{360°} \times T[days] \tag{3.1}$$

with phase angle ϑ and period T.

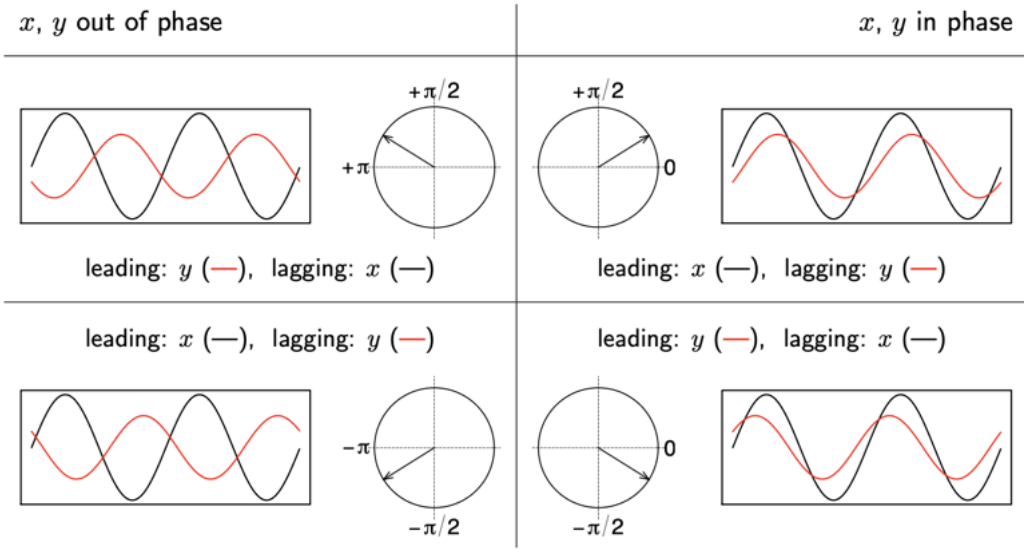


Figure 3.2. Wavelet phase description (Roesch & Schmidbauer, 2018)

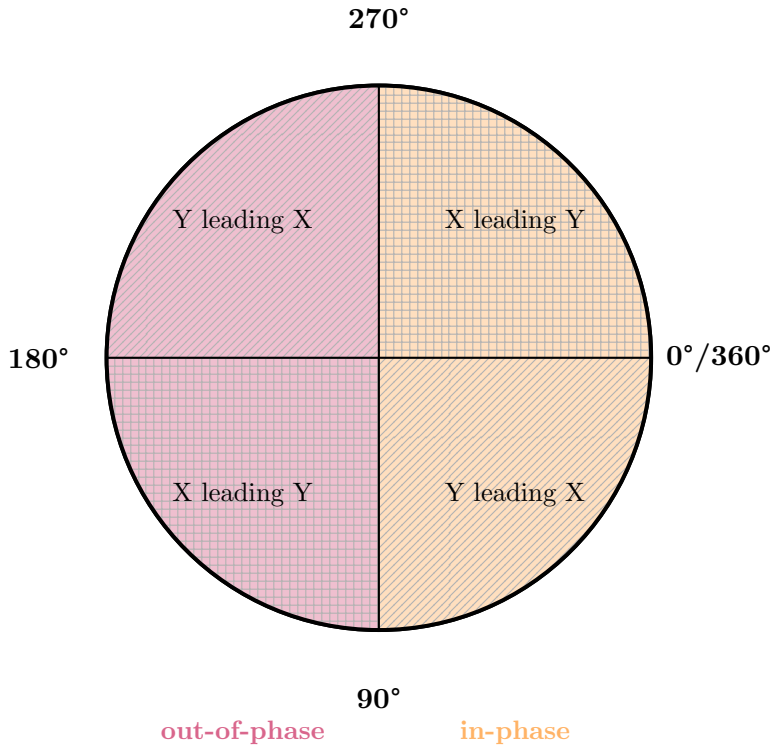


Figure 3.3. Wavelet phase angle interpretation

Chapter 4

Case study 1: the Grangesises landslide

4.1 Data gathering

4.1.1 EGMS

The datasets downloaded from EGMS for the area concerning the GS landslide are:

- *EGMS_L3_E40N24_100km_E_2019_2024*;
- *EGMS_L3_E40N24_100km_U_2019_2024*;
- *EGMS_L2b_161_0263_IW3_VV_2019_2024*;
- *EGMS_L2b_161_0264_IW3_VV_2019_2024*;
- *EGMS_L2b_066_0808_IW3_VV_2019_2024*;
- *EGMS_L2b_066_0809_IW3_VV_2019_2024*;
- *EGMS_L3_E40N24_100km_E_2015_2022*;
- *EGMS_L3_E40N24_100km_U_2015_2022*;
- *EGMS_L2b_161_0263_IW3_VV_2015_2022*;
- *EGMS_L2b_161_0264_IW3_VV_2015_2022*;
- *EGMS_L2b_066_0808_IW3_VV_2015_2022*;

- *EGMS_L2b_066_0809_IW3_VV_2015_2022*.

The datasets' name format stands for:*EGMS_level_relative_orbit_burst_cycle_swath _polarisation_years* in the case of the *calibrated* files and *EGMS_level_tile_name_resolution _direction* for the *ortho* ones. The datasets belonging to the same track but to different bursts were joined and the files obtained were renamed as shown in Figure 4.1.



Figure 4.1. GS datasets' names conversion

4.1.2 ReRCoMF

Due to its significant extent and the impact on urban settlements and roads, the Grangesises landslide is characterised by an extensive ReRCoMF monitoring network, as shown in Figure 4.2.

Table 4.1 lists the instruments for which data are available, along with their main characteristics.

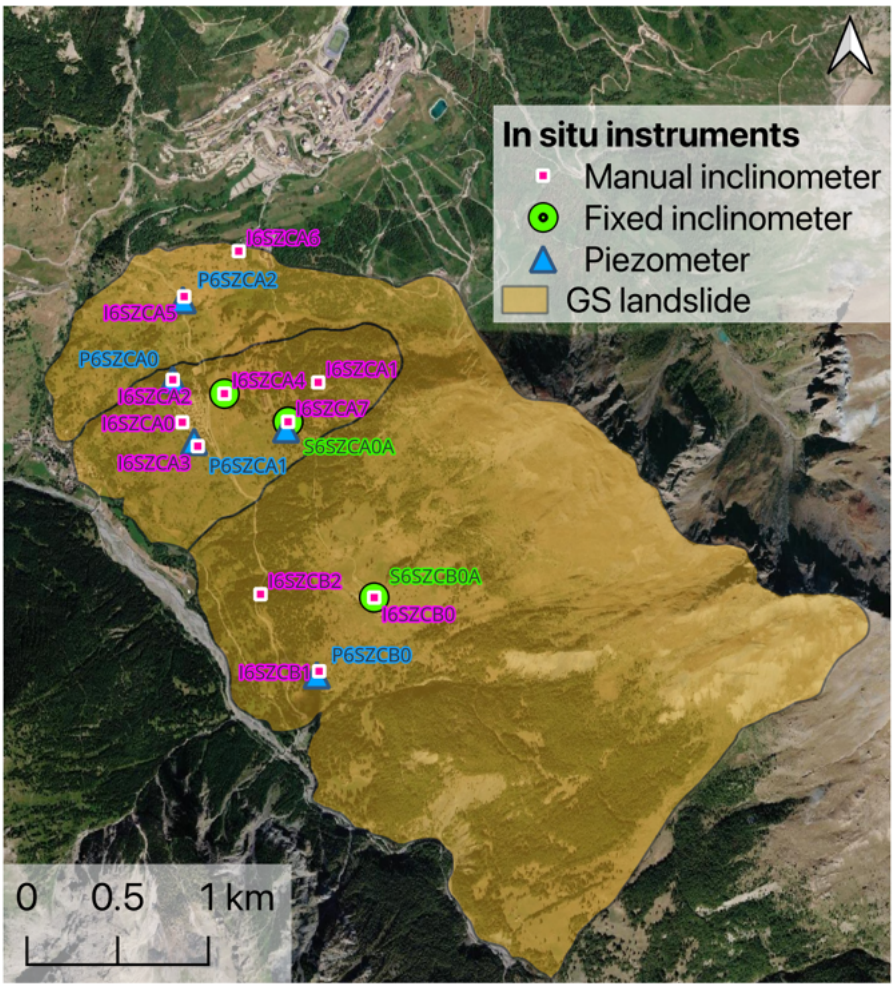


Figure 4.2. GS ReRCoMF instruments

Table 4.1. GS ReRCoMF instruments

Instrument type	Instrument code	First reading available	Last reading available	Depth [m]	Total length [m]	Average reading frequency	Active
Manual inclinometer	I6SZCA0	28/09/89	03/11/25	/	54	2/year	yes
Manual inclinometer	I6SZCA1	22/08/90	04/11/25	/	72.5	2/year	yes
Manual inclinometer	I6SZCA2	30/05/00	17/07/14	/	57.5	2/year	no
Manual inclinometer	I6SZCA3	09/05/07	29/10/19	/	88.5	2/year	no
Manual inclinometer	I6SZCA4	15/05/06	29/06/21	/	118	2/year	yes
Manual inclinometer	I6SZCA5	15/05/06	28/10/19	/	121	2/year	no
Manual inclinometer	I6SZCA6	15/05/06	09/06/25	/	51.5	2/year	yes
Manual inclinometer	I6SZCA7	15/05/06	04/11/25	/	106	2/year	yes
Manual inclinometer	I6SZCB0	03/05/01	10/11/09	/	80	2/year	no
Manual inclinometer	I6SZCB1	15/05/06	03/11/25	/	90	2/year	yes
Manual inclinometer	I6SZCB2	06/04/07	03/11/25	/	91	2/year	yes
Fixed inclinometer	S6SZCA0A	22/12/08	09/11/25	18.5	/	1/day	no
Fixed inclinometer	S6SZCA0B	04/08/10	16/11/15	25.5	/	1/day	no
Fixed inclinometer	S6SZCA0C	04/08/10	16/11/15	35.5	/	1/day	no
Fixed inclinometer	S6SZCA1A	18/11/15	23/03/26	29.5	/	1/day	yes
Piezometer	P6SZCA1	03/05/05	14/11/22	/	/	1/day	no
Piezometer	P6SZCA2	29/07/14	10/11/25	/	/	1/day	yes
Piezometer	P6SZCB0	01/10/09	10/11/25	/	/	1/day	yes

Green rows indicate active instruments, while the orange one highlights a manual inclinometer reported as active but whose last available reading date is in 2021.

4.1.3 Arpa weather stations

Figure 4.3 shows Arpa weather stations near the Grangesises landslide.

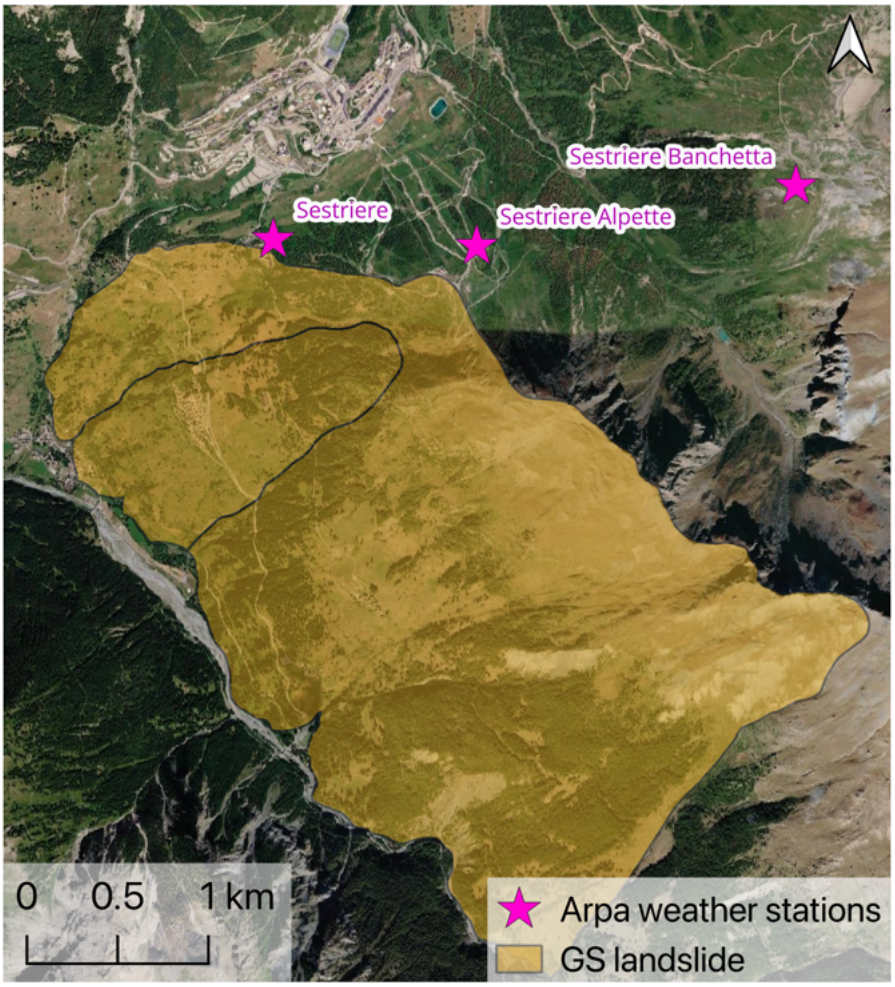


Figure 4.3. GS Arpa weather stations

Table 4.2 reports the details of the three closest Arpa weather stations to the Grangesises landslide. Among these, the *Sestriere* station was selected as the most representative for the study area, based on its altitude, aspect and proximity to the landslide.

Table 4.2. GS Arpa weather stations' details

Name	E (WGS84, 32N)	N (WGS84, 32N)	Elevation (m a.s.l)	Aspect
Sestriere	332352.916	4979716.586	2016	W
Sestriere Alpette	333473.662	4979680.63	2235	NE
Sestriere Banchetta	335232.981	4980011.888	2473	SW

4.2 Data analysis

4.2.1 EGMS data validation

EGMS horizontal displacements are validated by comparison with the horizontally projected displacements recorded by manual inclinometers. This comparison is bounded to those inclinometers recording data in at least one of the two EGMS datasets. For *I6SZCA3*, *I6SZCA5*, *I6SZCA7 (2019-2024)*, and *I6SZCB1 (2015-2022)*, a filtering of the first measurements is applied, as shown in Appendix A, given the large discrepancies with the EGMS data, interpreting these as anomalies caused by the initial instrumental adjustments

As Table 4.3 shows, there are three extents of agreement between the EGMS and inclinometers average velocities: highly coherent mean velocities (± 2 *mm/year*, green), coherent recordings with a difference in mean velocity up to *4.5 mm/year, orange*, and extremely incoherent mean velocities with large difference in values or opposed signs (red). The mean velocities are also displayed in Figure 4.4.

The incoherences between the EGMS and inclinometer data are primarily caused by the deeply localised nature of inclinometer measurements and the spatial distribution of PS, which are generally offset from the inclinometer locations within a buffer zone. The overall agreement between the mean velocities obtained by the datasets validates the use of EGMS horizontal data for analysing the study area.

Table 4.3. GS: EGMS and manual inclinometer average velocities

EGMS dataset	Manual inclinometer	Label	v_{EGMS} [mm/year]	v_{incl} [mm/year]	$v_{\text{EGMS}} - v_{\text{incl}}$ [mm/year]
GS_2015_2022_H	I6SZCA0	CA0_15	6.17	7.12	-0.95
GS_2019_2024_H	I6SZCA0	CA0_19	4.49	1.02	3.47
GS_2015_2022_H	I6SZCA1	CA1_15	5.55	-2.6	8.15
GS_2019_2024_H	I6SZCA1	CA1_19	5.54	17.79	-12.25
GS_2015_2022_H	I6SZCA3	CA3_15	7.31	3.03	4.28
GS_2015_2022_H	I6SZCA4	CA4_15	5.2	1.01	4.19
GS_2015_2022_H	I6SZCA5	CA5_15	1.43	3.45	-2.02
GS_2015_2022_H	I6SZCA6	CA6_15	-0.37	4.39	-4.76
GS_2019_2024_H	I6SZCA6	CA6_19	4.61	3.69	0.92
GS_2015_2022_H	I6SZCA7	CA7_15	5.98	3.95	2.03
GS_2019_2024_H	I6SZCA7	CA7_19	6.26	5.66	0.6
GS_2015_2022_H	I6SZCB1	CB1_15	7.41	4.16	3.25
GS_2019_2024_H	I6SZCB1	CB1_19	6.82	8.01	-1.19
GS_2015_2022_H	I6SZCB2	CB2_15	-0.88	8.14	-9.02
GS_2019_2024_H	I6SZCB2	CB2_19	0.22	9.04	-8.82

4.2.2 Inclinometers

Fixed inclinometers

Figure 4.5 shows the fixed inclinometers installed in the Grangesises landslide area, while Figure 4.6 presents the four graphs of cumulative displacement and cumulative precipitation over time corresponding to these instruments.

The four fixed inclinometer profiles suggest a heterogeneous deformation pattern within the monitored slope. *S6SZCA0A*, *S6SZCA0B* and *S6SZCA0C* are installed in the same location but at different depths: *18.5 m*, *25.5 m* and *35.5 m* respectively and therefore provide a vertical comparison of the deformation pattern for the same location.

Their profiles show an overall progressive increase in cumulative displacement, yet they differ in temporal behaviours. *S6SZCA0A* shows several short oscillations and a marked step-like pattern, suggesting a deformation process that is active yet not uniform over time, with phases of acceleration followed by relative stabilisation, consistent with its lower depth compared to the others. These increments appear to recur annually, with accelerations occurring roughly around mid-year.. *S6SZCA0B* shows a relatively regular increase in displacement with a few subtle accelerations, yet a clear step-like pattern is still visible, suggesting a similar deformation process compared to the one detected for *S6SZCA0A*. Finally, *S6SZCA0C* presents the most linear behaviour, with a steady and almost continuous growth of cumulative displacement, which indicates a more constant displacement regime. In this case too, a slight annual cyclicality can be detected, although of smaller magnitude compared to the rest of the data. The graphs show a weak correlation between precipitation and displacement, suggesting that this external factor has only a

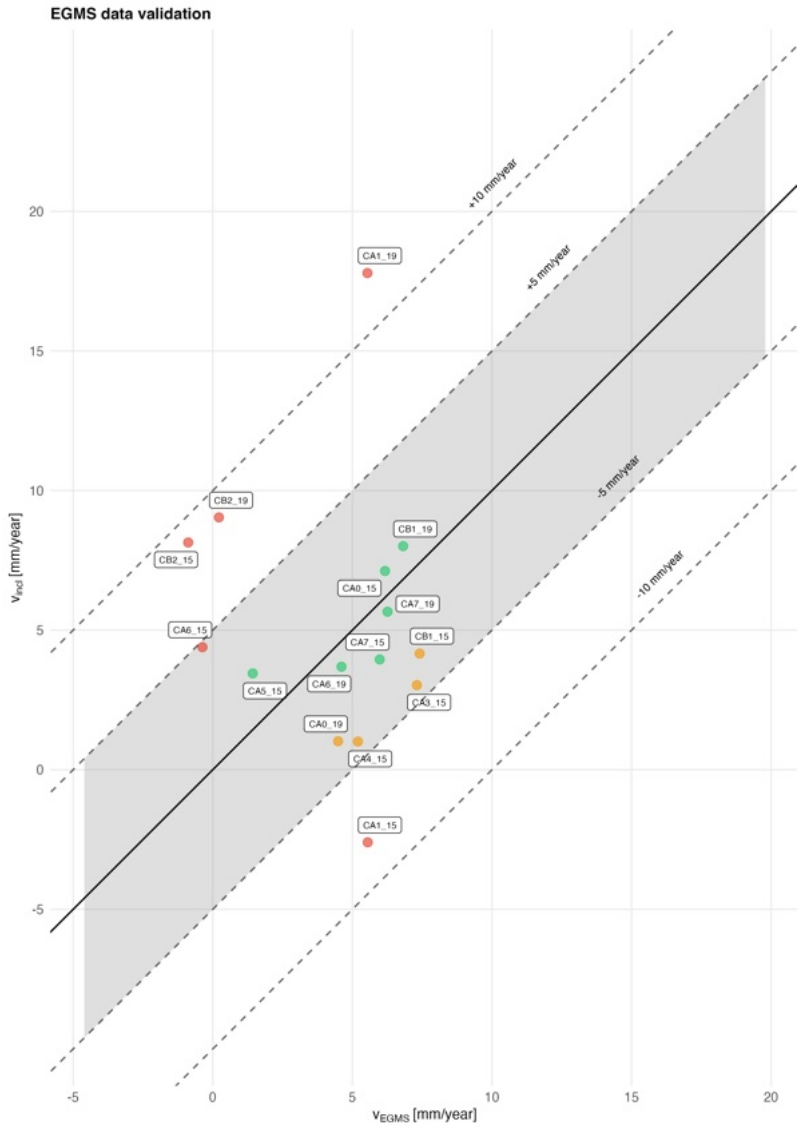


Figure 4.4. GS EGMS data validation

subtle effect on the landslide motion.

S6SZCA1A is installed at a depth of *29.5 m* and is located approximately *383* m to the north-east and about *100 m* lower than the other three inclinometers. It reaches the highest cumulative displacement and shows the most pronounced step-like increments, with well-defined phases of acceleration recurring at an approximately annual frequency, roughly around mid-year, except for the period from around 2020 to 2024, during which the trend appears to be more stable. These sudden changes may correspond to phases of acceleration and could be linked to external factors.

Overall, the four profiles suggest that the slope does not deform uniformly, but rather shows different displacement rates depending on depth, with more significative

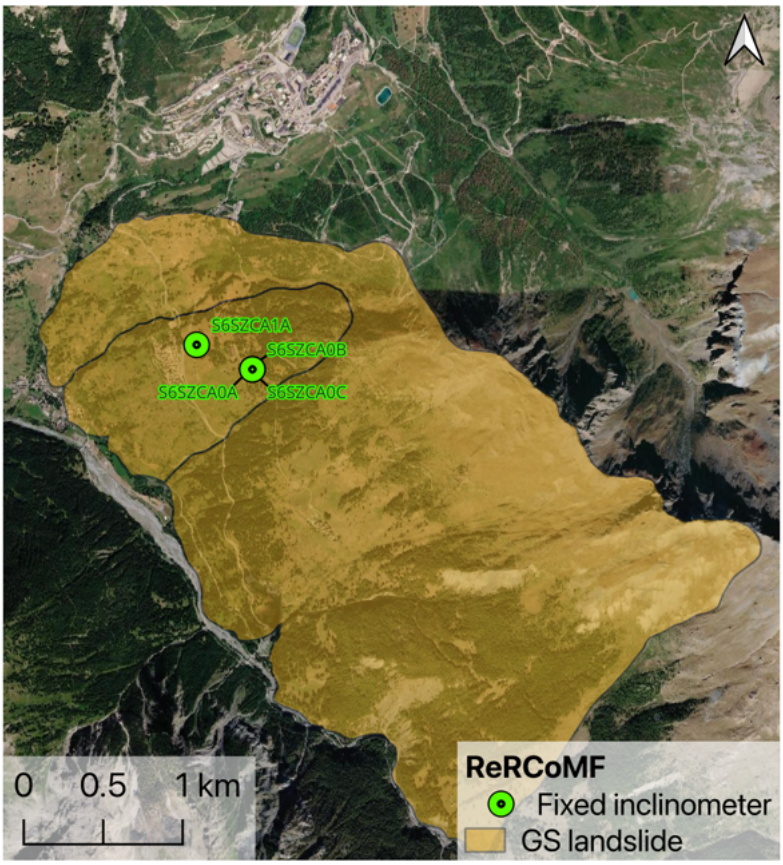


Figure 4.5. GS fixed inclinometers location

movements detected at around *25 to 30 m*. Furthermore, the recurring step-like pattern observed in most instruments, particularly *S6SZCA0A* and *S6SZCA1A*, points to a cyclical deformation behaviour with an approximately annual periodicity, potentially driven by seasonal external factors.

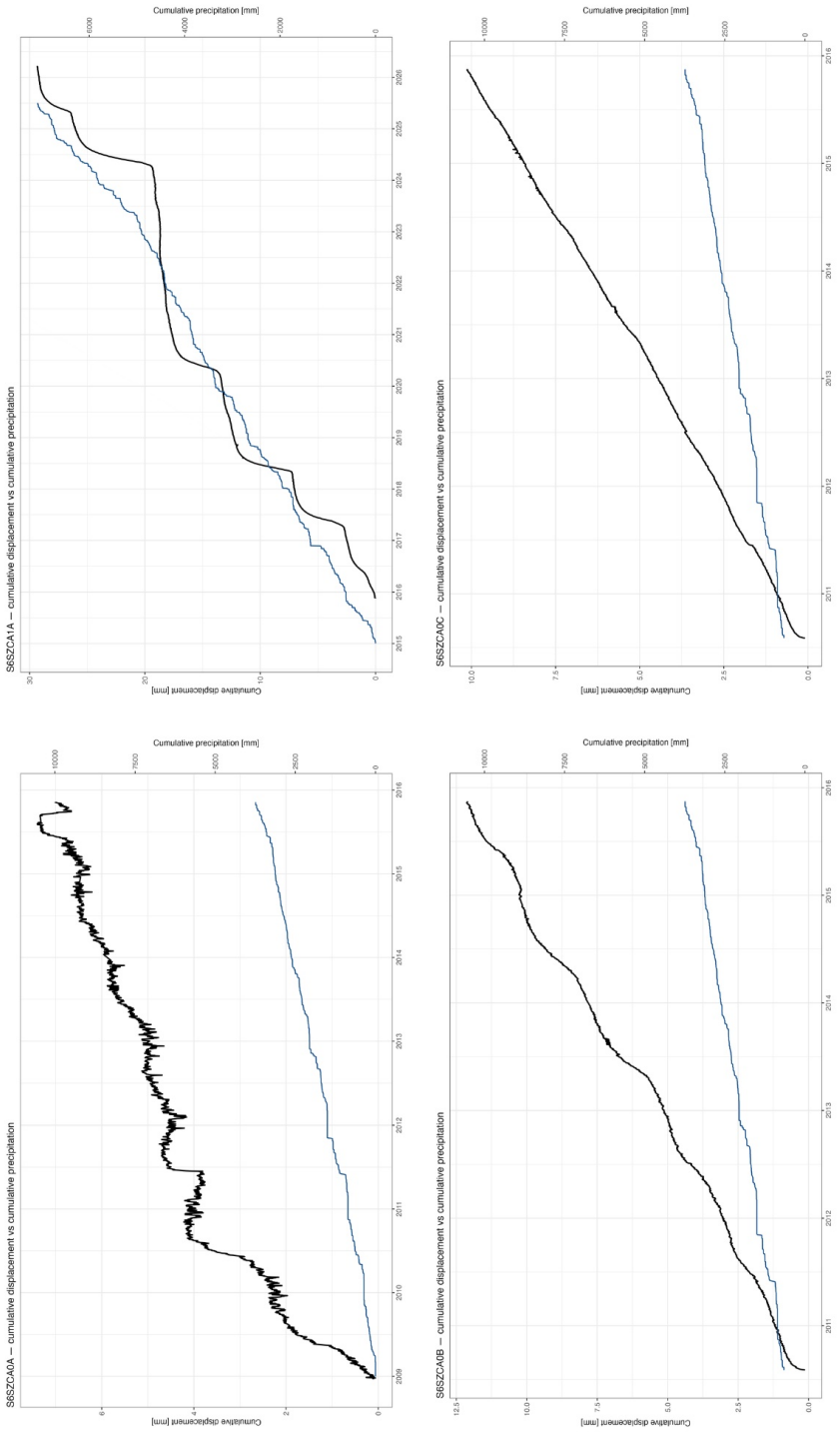


Figure 4.6. GS fixed inclinometers: Cumulative displacement vs cumulative precipitation

Manual inclinometers

Figure 4.7 displays the manual inclinometers installed in the Grangesises landslide area, while the corresponding cumulative displacement profiles as a function of depth are shown in Appendix A.

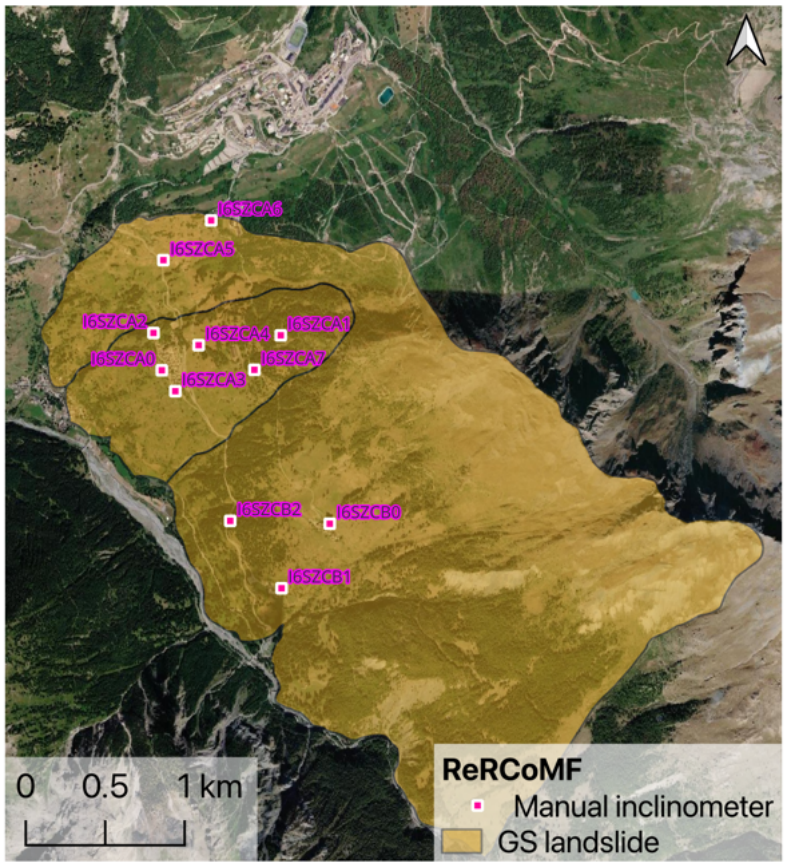


Figure 4.7. GS manual inclinometers location

The data derived from manual inclinometers was first organised into three spatially coherent groups as shown in Figure 4.8, based on the location of the boreholes, under the assumption that instruments within each group should exhibit comparable deformation patterns.

The displacement profiles were then examined to identify depths showing characteristic changes in deformation, which were interpreted as possible shear surfaces. On the basis of these observed critical depths, a set of potential failure surfaces was manually defined and subsequently interpolated to reconstruct their likely geometry in depth.

An initial set of plots was generated to visualise the identified points where the inclinometers intersect possible shear surfaces within each group (Figure 4.9). Subsequently, a trial-and-error procedure was used to interpolate these intersection points and construct

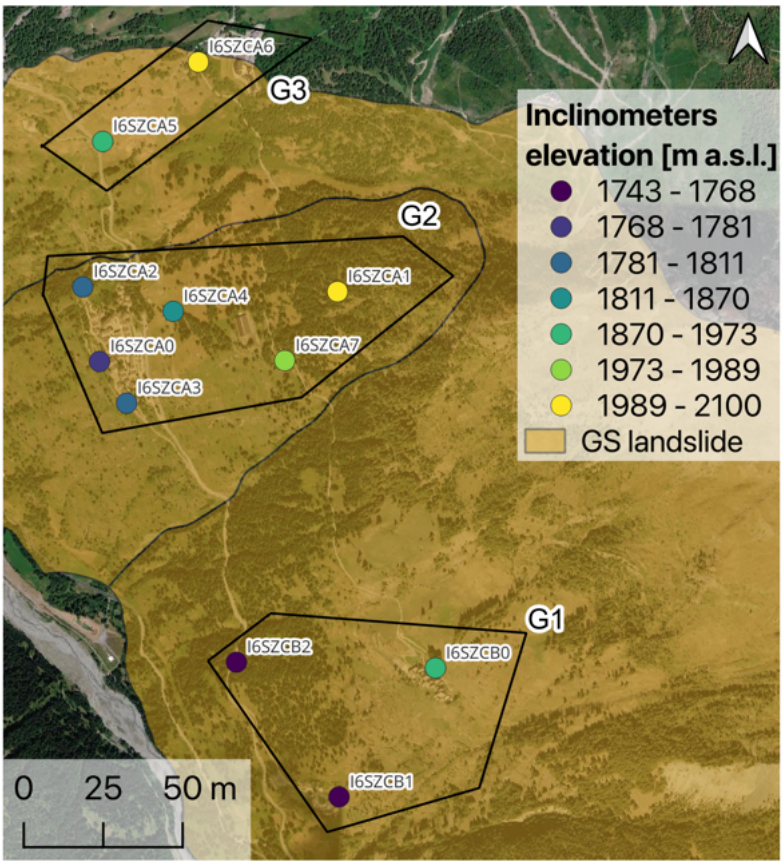


Figure 4.8. GS manual inclinometers elevation and group division

possible shear surface profiles along elevation as shown in Figure 4.10.

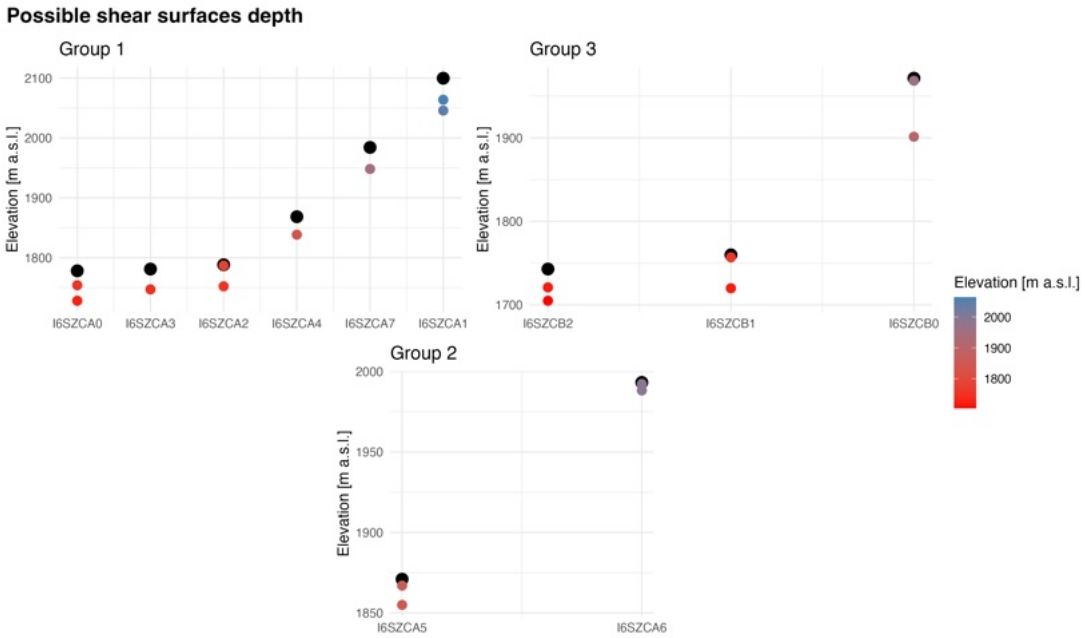


Figure 4.9. GS manual inclinometers: possible shear surfaces depths

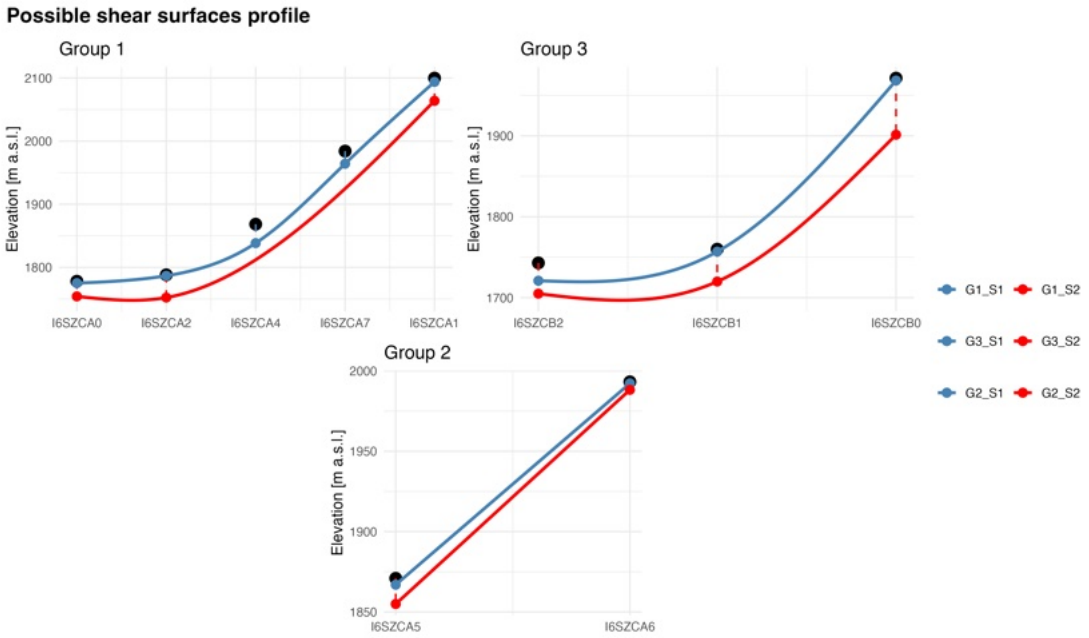


Figure 4.10. GS manual inclinometers: possible shear surfaces profiles

The presence of two distinct sets of points in each group may indicate multiple shear surfaces, or a vertically complex deformation zone. The interpolated profiles further suggest that the shear surfaces are not perfectly planar, but rather exhibit a gentle curvature, implying a progressive variation in depth along the slope.

Figure 4.11 and 4.12 show the cumulative azimuth and resultant displacement of the eleven manual inclinometers monitoring the Grangesises landslide at a 0.5 m depth.

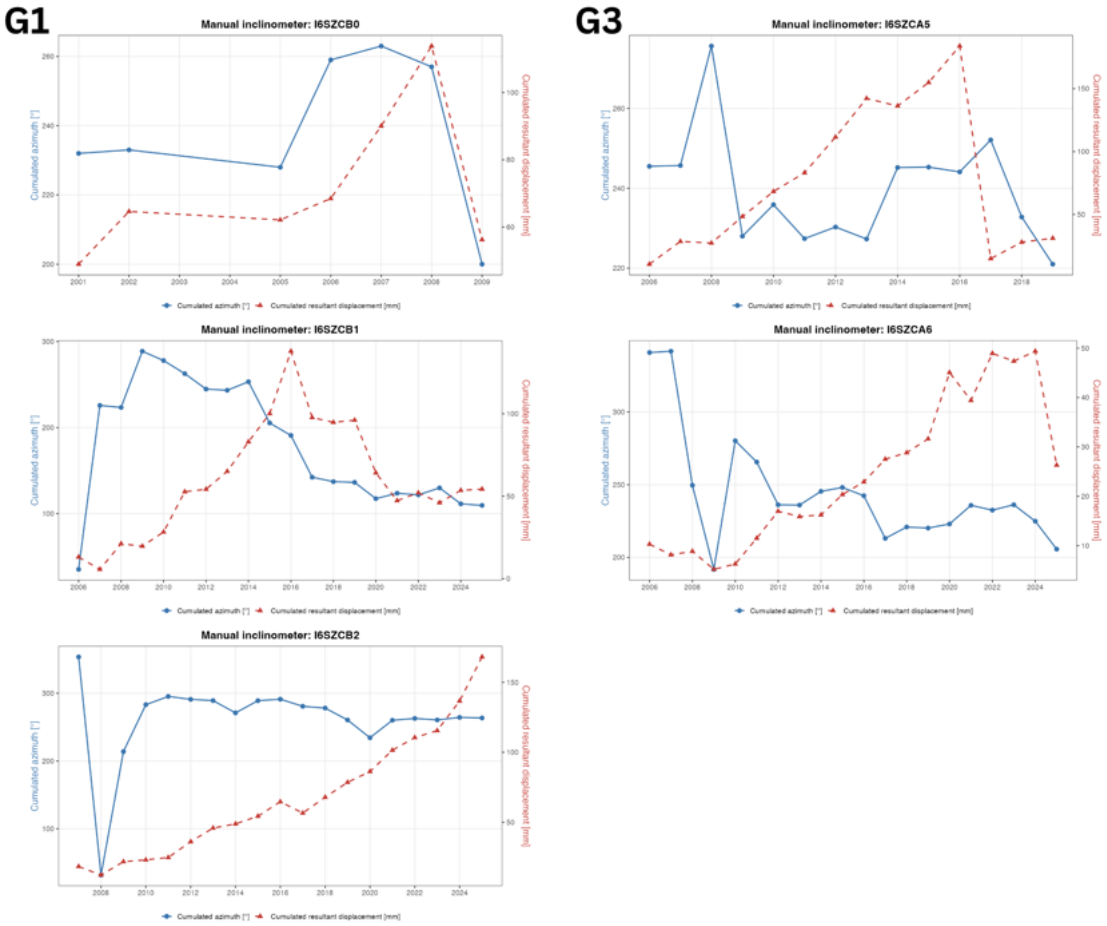


Figure 4.11. GS manual inclinometers, Group 1 and 3: cumulative azimuth and resultant displacement

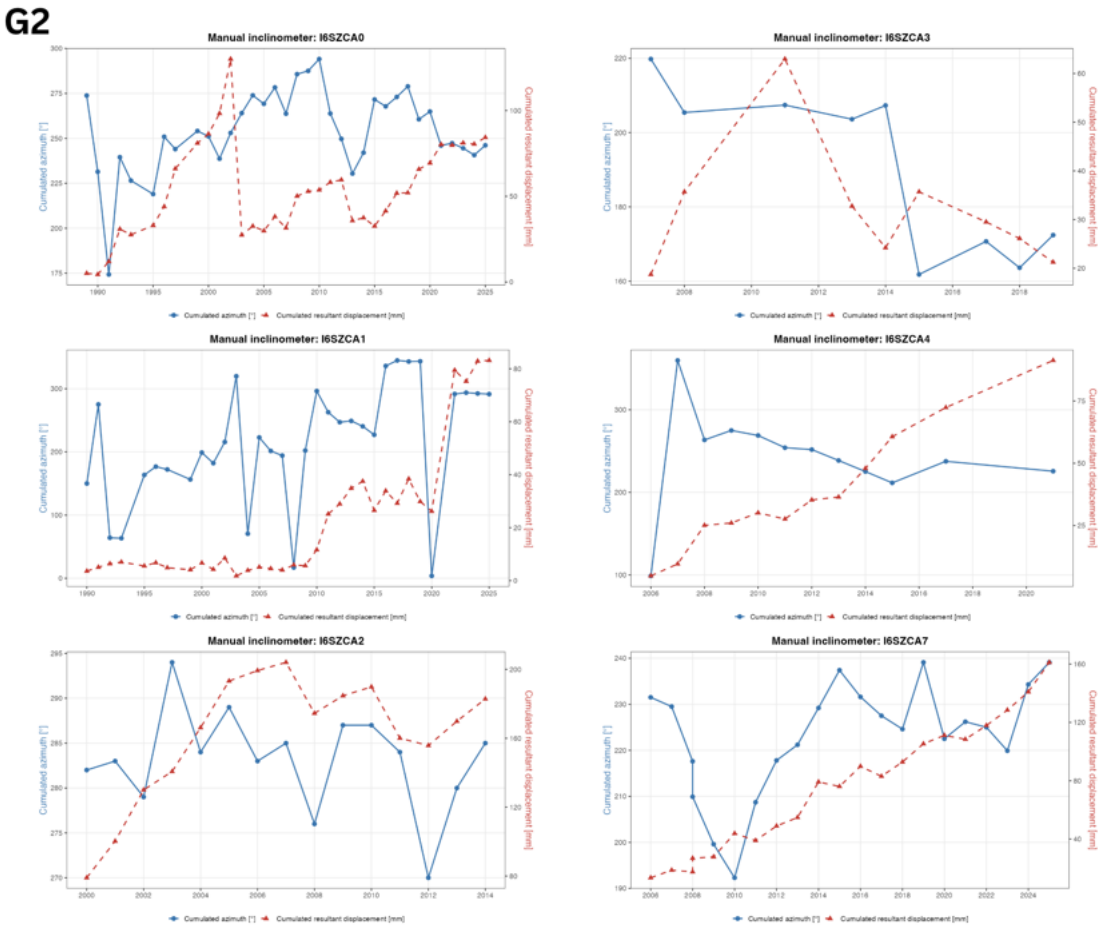


Figure 4.12. GS manual inclinometers, Group 2: cumulative azimuth and resultant displacement

The three instruments belonging to Group 1 show a progressive and sustained displacement trend reflecting an ongoing slow-moving phenomenon. *I6SZCB0* records a stable azimuth around *200–220°* (SSW) with displacements approximately reaching *90 mm*. *I6SZCB1* portrays a more complex directional behaviour although it shows a recent stabilisation toward ESE. A peak in displacement is recorder in 2015-2016, yet followed by a declining trend, suggesting a phase of kinematic deceleration. *I6SZCB2* is the most active instrument of the group, with an almost monotonous growth of displacement, exceeding *150 mm* and an azimuth converging on *270–290°* (WNW). The monitoring data collected by this instrument represents a clear indicator of an active and coherent deformation process.

Group 2 is characterised by a complex kinematic setting as it entails the greatest number of instruments, some of which have recorded data over an extremely long time span. *I6SZCA0* reflects a long, moderate, non-accelerating displacement stabilised around *80–90 mm*, while *I6SZCA1* shows an extreme directional variability throughout

most of its record, possibly reflecting low-magnitude movements susceptible to instrumental noise, before showing a marked acceleration from 2018 onward, reaching 80 mm by 2024. *I6SZCA2*, though its series ends in 2014, recorded the highest displacements in the entire dataset (*120–200 mm*) with a coherent WNW azimuth. *I6SZCA3* displays a non-monotonic displacement trend, peaking around *60 mm* in 2010–2011 and then declining, stepping in a stabilisation period. *I6SZCA4* exhibits a persistent displacement increase beyond *75 mm* with no signs of deceleration, despite a highly variable azimuth gradually stabilising in recent years. Finally, *I6SZCA7* shows a nearly linear displacement increase from around *40* to over *155 mm* with a consistently SSW-oriented azimuth of *200–230°*, highlighting the behaviour of a stable, long-term sliding mechanism.

For what it concerns Group 3, the two instruments share a coherent kinematic pattern, with displacement steadily growing and azimuths consistently pointing toward the SW–W direction, suggesting an homogeneous movement along the slope. *I6SZCA5* records cumulated displacements approaching *150 mm*, with a notable acceleration from 2016–2018 onward. *I6SZCA6* shows a similar displacement trend, reaching about *50 mm* in the most recent readings with no evidence of stabilisation, confirming that the movements in this sector remain active.

Across all three groups, the predominant displacement direction consistently falls within the W–SSW sector, coherently with the expected downslope orientation of the Grangesises landslide. While certain instruments document phases of deceleration or stabilisation, several others show no sign of deceleration, confirming the persistence of active deformation. The acceleration phases observed across multiple instruments from approximately 2016–2018 onward suggest the possible influence of a common reactivating mechanism.

In order to provide a spatial overview of the kinematics of the landslide, Figure 4.13 represents for every manual inclinometer the cumulative displacement vector corresponding to the latest available reading at 0.5 m depth. This is shown as an arrow whose orientation reflects the cumulative azimuth of movement and whose colour indicates the displacement magnitude (Figure 4.13).

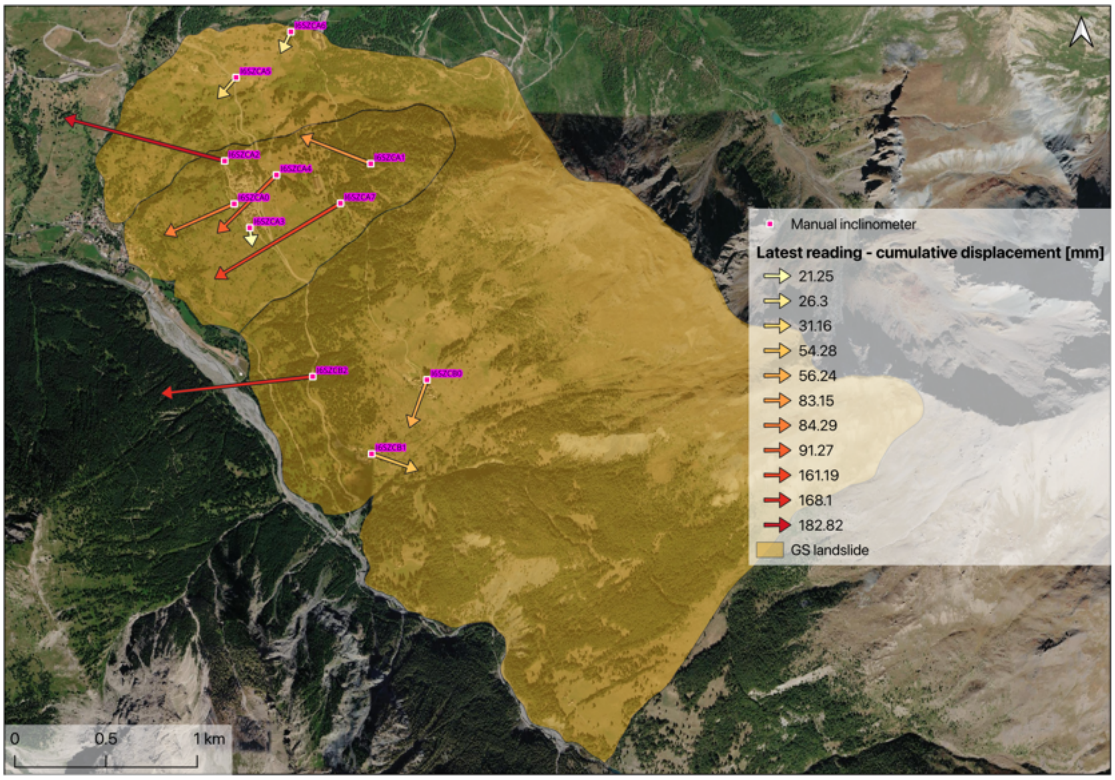


Figure 4.13. GS manual inclinometers - latest cumulative displacement and azimuth

The map reveals an overall coherent spatial pattern within the landslide body. The inclinometers belonging to Group 2 and 3, thus in the upper and central-western sector, record cumulative displacements ranging from approximately 21 *to* 91 *mm*, with arrows predominantly oriented towards the west and southwest, consistently with the downslope direction towards the valley. Three instruments, *I6SZCA2*, *I6SZCA7* and *I6SZCB2*, stand out with significantly higher cumulative displacements, reaching 161 *to* 182 *mm*, suggesting a more active kinematic behaviour in this sector. The Group 1 manual inclinometers, which are found in the low-eastern portion of the landslide, show more incoherent displacement directions, with significantly lower values ranging from approximately 54 *to* 84 *mm*.

The majority of the inclinometers recorded their last reading in 2025, providing an up-to-date picture of the current kinematics of the landslide. However, *I6SZCB0* has not been active since 2009, meaning its cumulative displacement is likely a significant underestimate of the actual total deformation, and should therefore be interpreted with caution. *I6SZCA4* and *I6SZCA5* recorded their last readings in 2019. It is possible to assume that the former would have continued accumulating displacement had it remained active, while the latter can be considered reasonably representative of the current conditions, as its behaviour does not differ significantly from the nearby *I6SZCA6*. Finally, *I6SZCA2* ceased operating in 2014 due to excessive deformation, which itself is indicative

of particularly intense kinematic activity in that sector of the landslide.

Overall, all the instruments showing lower cumulative displacement rates are also the ones whose cumulative azimuth is incoherent with the others, thus suggesting that in these cases the movement direction may be less clearly defined or more influenced by local factors. From a general point of view, the spatial distribution of the vectors confirms a predominant W-SW displacement across the landslide body, with higher rates focused in the central-western sector.

4.2.3 EGMS

The standard deviations of the velocities measured by EGMS for the PS located downslope of the study area are calculated for each dataset, as such points are considered not affected by active instability processes. The maximum value obtained across all datasets is then rounded up and used as a conservative estimate of measurement uncertainty. A stability threshold of $\pm 2\sigma$ is applied, obtaining a stability interval of ± 3 *mm/year*, applied to all datasets and components. PS with velocities falling within this range are classified as *stable*, while those positively or negatively exceeding it are considered indicative of ground movement.

Figures 4.14 and 4.15 show the spatial distribution of PS within and around the Grangesises landslide, classified according to their velocity ranges, for the 2015 - 2022 and 2019 - 2024 datasets respectively, across their four components: *horizontal, vertical, ascending, and descending* LOS.

The interpretation of the velocity patterns detected within the different datasets must be carried out considering the land cover where the PS lie, as different surface types may lead to significantly different readings of the detected signals. In urbanised sectors, PS located on buildings or infrastructure may show, especially in the vertical and horizontal components, misleading velocity signals driven by seasonal thermal expansion and contraction of structures rather than actual ground deformation. In vegetated areas, the PS density is generally lower, as vegetation reduces coherence and limits the availability of stable scatterers. In contrast, in non-urbanised and poorly vegetated areas, thus those natural targets as bare rock outcrops or agricultural lands, such artefacts are negligible and the velocities can be more confidently attributed to real ground movements. As the Grangesises landslide body is largely characterised by the latter land cover type, a geomorphological interpretation of the detected signals is considered appropriate.

For the 2015 - 2022 datasets (Figure 4.14), the *horizontal* component shows PS with negative velocities predominantly between -9 *and* -3 *mm/year* distributed across the

landslide body, with isolated points reaching -15 *to* -9 *mm/year*. The *vertical* component is characterised by a more homogeneous pattern, with most PS belonging to the stability threshold, suggesting a predominantly slope-parallel displacement vector with a limited vertical projection. The *ascending* data shows mean velocities mostly within -3 *and* 3 *mm/year*, while the *descending* track highlights an overall negative mean velocity ranging from -9 *and* -3 *mm/year* with points reaching significative negative values in the central and eastern sectors, confirming the kinematic activity of the area during this period.

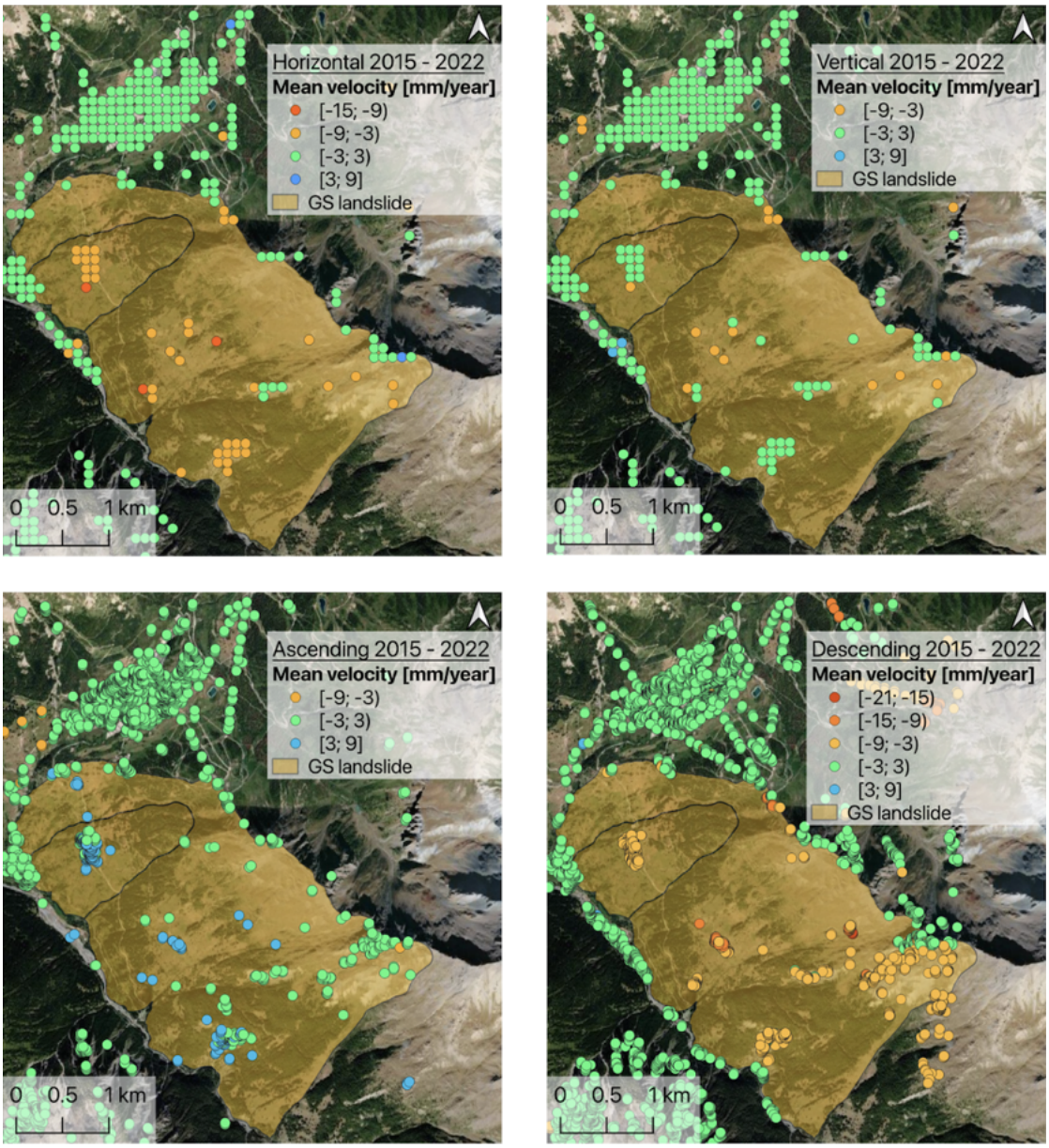


Figure 4.14. GS 2015 - 2022: EGMS PS, mean velocity distribution

For the 2019 - 2024 period (Figure 4.15), the observed velocity spatial distribution is coherent with the earlier dataset, though with generally higher values. The *horizontal* component shows the majority of PS within the landslide body to negatively exceed the

stability threshold, with values predominantly ranging between -9 *and* -3 *mm/year* and some isolated points reaching rates of -15 *to* -21 *mm/year*. The *vertical* set of points reflects a rather homogeneous behaviour, with many *PS* found in the stable range, but with a significant percentage recording velocities between -9 *and* -3 *mm/year* , especially in the north-eastern sector of the landslide, characterised by bare rocks. The *ascending* track does not show particularly unstable points, whereas the *descending* one is characterised by significant negative velocities across the majority of the landslide, reflecting an overall movement of the area. The orbital asymmetry found in both timeseries suggests a downslope displacement vector whose orientation is more sensitive to the *descending* LOS direction.

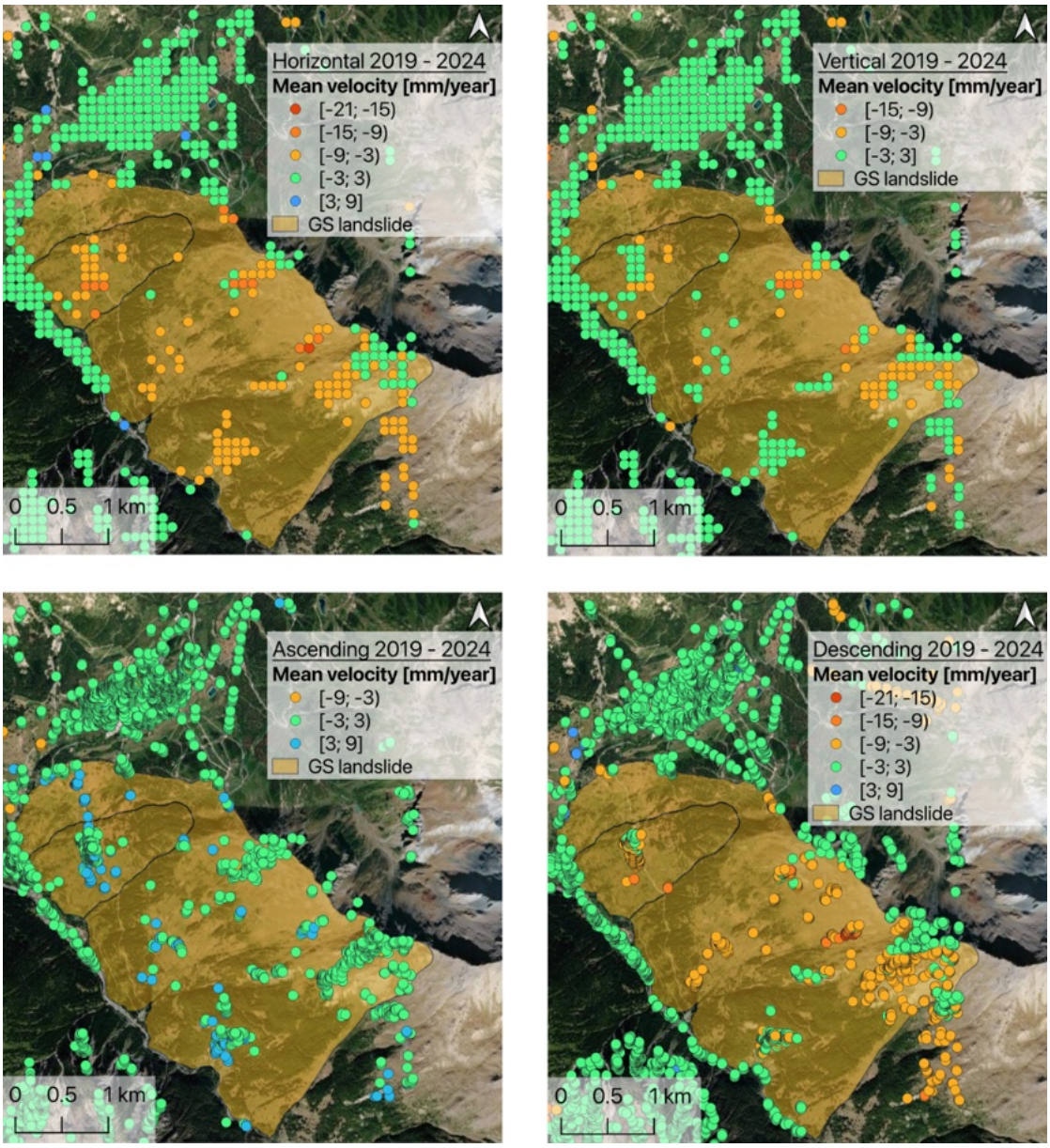


Figure 4.15. GS 2019 - 2024: EGMS PS, mean velocity distribution

Table 4.4 reports the PS density expressed in PS/km^2 for each land cover class and component, relatively for the 2015 - 2022 and 2019 - 2024 datasets. As expected, the *urbanised* areas have the highest PS density across all components and both time periods, reflecting the higher availability of stable reflectors such as buildings and infrastructure in urban environments. *Exposed soil* areas show intermediate density values, with the *ascending* and *descending* components recording the highest numbers. Coherently with the theory, *forested* areas show the lowest PS density across all components and both datasets, confirming that dense vegetation significantly reduces interferometric coherence and limits the availability of reliable scatterers. Nevertheless, some PS are still detected within forested areas, particularly in the *ascending* and *descending* tracks.

Table 4.4. GS - PS density (PS/km^2) based on land cover class and EGMS component

PS/km^2	**2015–2022**			**2019–2024**			**% increase**		
	U	**ES**	**F**	**U**	**ES**	**F**	**U**	**ES**	**F**
H	40	9	3	50	21	8	25%	133%	167%
V	40	9	3	50	21	8	25%	133%	167%
A	2018	52	15	2656	139	19	32%	167%	27%
D	2013	118	6	2184	189	15	8%	60%	150%

Consequently, the Norton, Modified Lomnitz and Aydan creep models are fitted to all the dataset components (*U, ES, F*) in order to determine which better applies to the EGMS time series (Appendix A). Both the Norton and the modified Lomnitz laws show a good degree of fitting, both having an average R^2 of 0.88. The former linear creep model is chosen to carry out further analysis. For each dataset, an average curve deriving from the models of the three land cover fits is computed to compare the displacement rates and to evaluate whether these remained consistent across the two acquisition periods as shown in Figure 4.16 and 4.17.

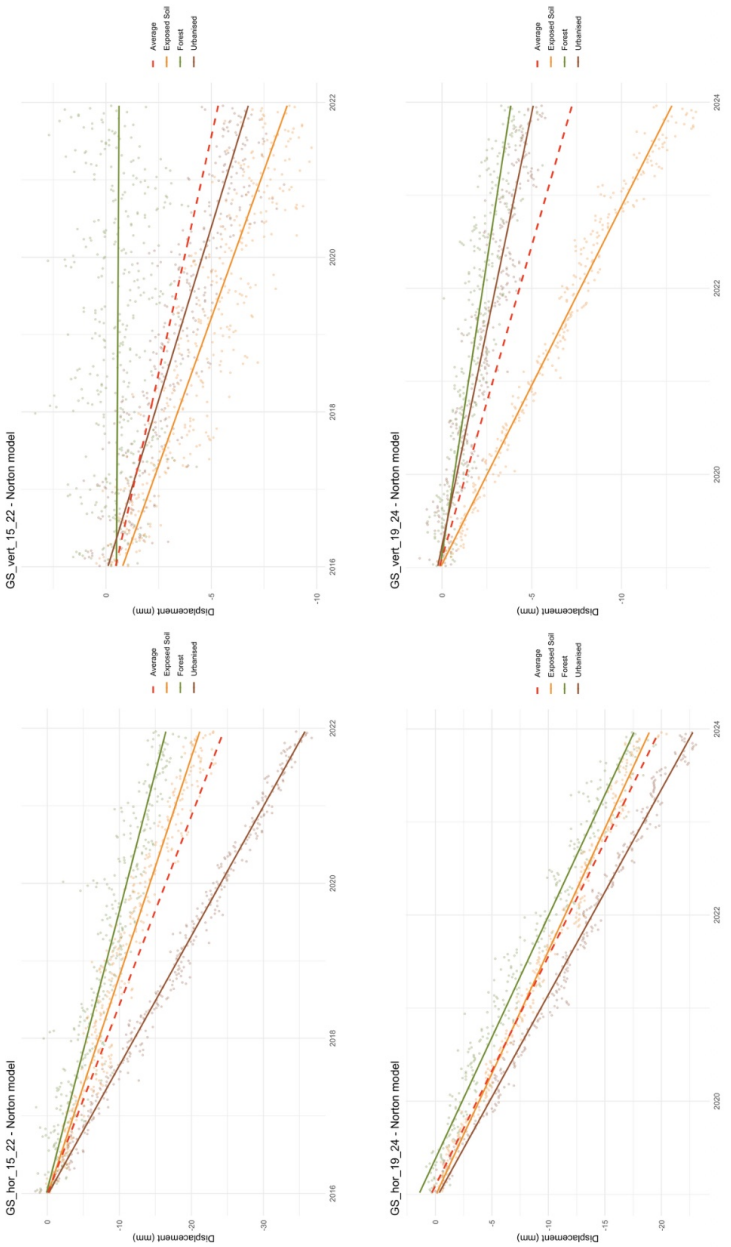


Figure 4.16. GS: Norton model applied to *horizontal* and *vertical* datasets

The *horizontal* time series record negative displacement values, consistently with the W-SW direction of the landslide. For both time periods, the U areas show the steepest displacement curves, followed by the ES and then the F areas. This suggests an increased superficial stability ensured by the vegetation cover and an acceleration in urbanised areas possibly caused by the additional loading of infrastructures.

The *vertical* components show negative displacements, suggesting a downward displacement. ES exhibits the highest displacement rate in both periods, followed by U and F. The F class in the 2015-2022 dataset is characterised by a high level of noise,

thus does not provide reliable information. The consistent displacement trends across the two periods suggest a stable deformation pattern, with *U* areas displaying lower rates compared to *ES*. This could be explained by the impermeability of urban surfaces which limits water infiltration and therefore reduce the impact of wetting and drying cycles on vertical deformation. In the contrary, *ES* is directly subject to water permeation and therefore is more susceptible to volumetric changes that enhance vertical displacement.

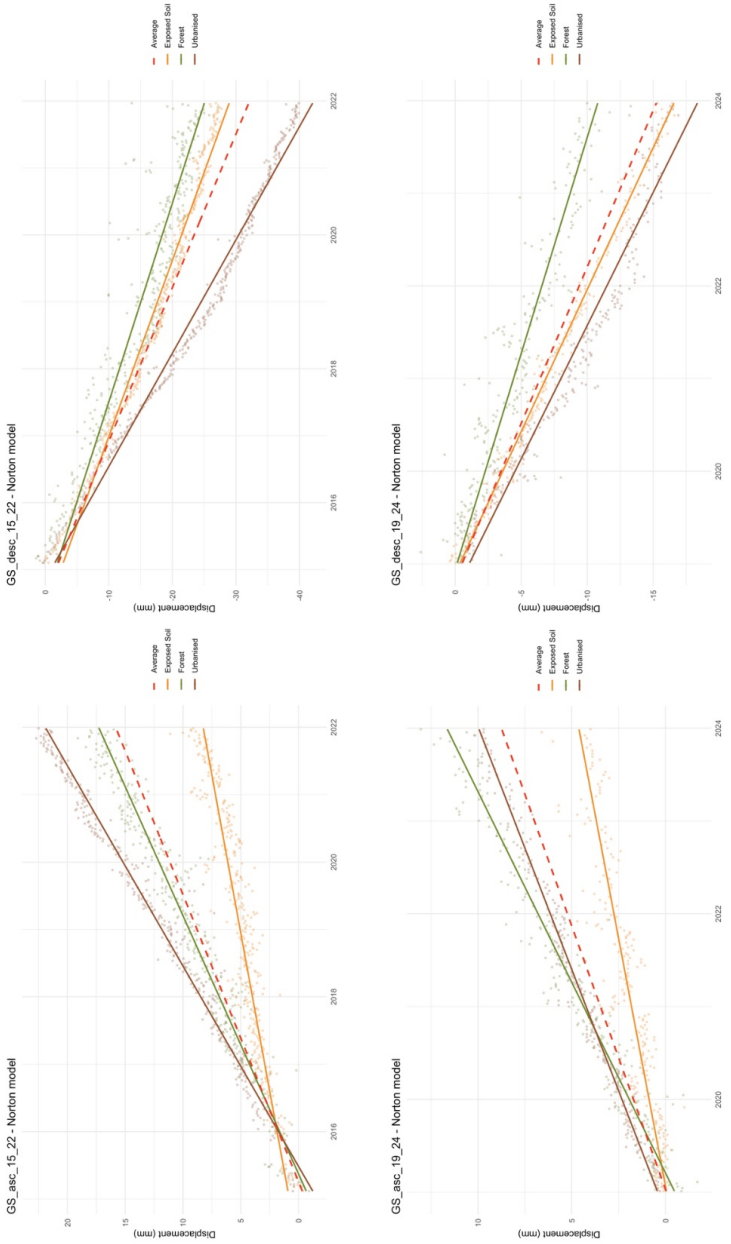


Figure 4.17. Norton model applied to *ascending* and *descending* datasets

The *ascending* tracks record positive displacement values, consistent with the downslope direction of the GS landslide. *ES* displays a much higher displacement rate

compared to the other two for both time periods, making it the most active land cover class, being highly susceptible to both vertical and horizontal movements. *U* and *F* rates have similar *ascending* trends: *U* areas show high lateral displacement, partially offset by a lower downward displacement, while *F* areas reflect overall slower rates, potentially underestimated to low PS density.

The *descending* components display negative displacement rates, coherently with the *ascending* values. Since the LOS of this track is roughly aligned with the GS movement direction, it successfully captures the horizontal component of displacement and therefore shows coherent behaviours compared to the horizontal graphs.

Comparing the two acquisition periods, the graphs show an overall convergence between *U* and *ES* trends which may reflect a change in the main deformation mechanisms. Given the increased PS density in the more recent time period, the trends deduced by the relative graphs are assumed to be more accurate. The deceleration in *U* areas in the *horizontal* component potentially highlights a stabilisation of lateral deformation, while the acceleration of *ES* in the *vertical* component may reflect an increased susceptibility to downward displacement, possibly related to recent changes in hydrological conditions. This ultimately shows that the contribution of land cover may not remain constant but rather evolve over time.

4.2.4 Triggering factors analysis

A comparison between potential triggering factors and EGMS displacement time series identifies seasonal oscillations that are added to the landslide's intrinsic creep motion previously modelled with Norton's equation. To identify potential triggering factors for displacement, the 24 EGMS subsets obtained (*horizontal, vertical, ascending* and *descending* divided in *U, ES, F* for both 2015-2022 and 2019-2024) are analysed for coherence with: *depth to groundwater [m], precipitation [mm], temperature [°C]*, and *snow depth [cm]*. Groundwater depth is obtained by three piezometers located in the GS landslide area (*P6SZCA1*, *P6SZCA2*, *P6SZCB0*, as shown in Figure 4.2), while precipitation, temperature, and snow depth are collected from Arpa's Sestriere weather station (Figure 4.3).

Initially, graphs comparing the displacement and triggering factors time series (e.g. Figure 4.18; see Appendix A) are produced to visually localise coherence. However, the significant noise in the EGMS data hides any clear pattern. Consequently, a wavelet cross-coherence analysis is applied to all couples of time series to quantify coherence and 72 graphs are produced for each time period considered (see Appendix A).

Preliminary analysis showed that wavelet coherence yielded consistently high val-

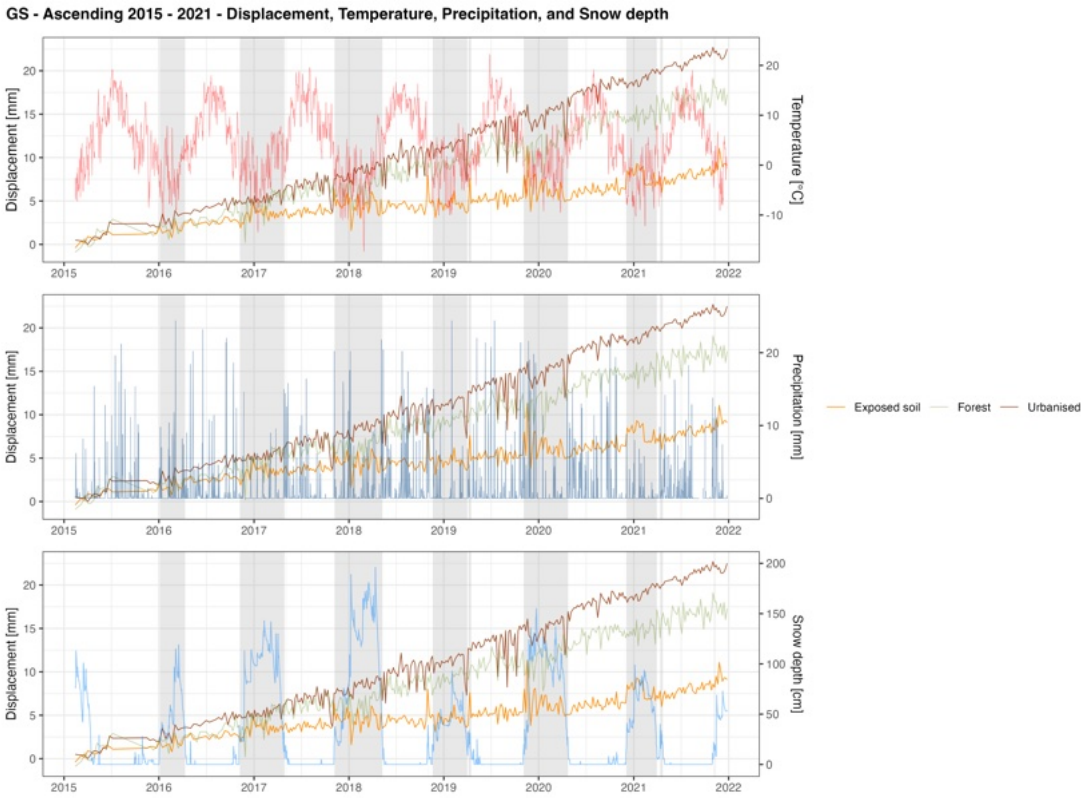


Figure 4.18. Example: GS 2015 - 2022, EGMS and triggering factors

ues across all time scales and periods, probably because the continuous fluctuations of both signals. For this reason, cross-wavelet power was selected to identify areas representing meaningful interaction between displacement and the selected triggering factor. Cross-wavelet power can be considered as a non-normalised measure of covariance and it thus depends on the amplitudes of both signals. In order to have comparable graphs, all cross-wavelet power plots have a uniform colour scale based on the global maximum calculated across the displacement–forcing factor combinations for both case studies (24 for the first one), excluding few outliers from forested regions.

All graphs are computed with displacement as input X and the environmental factor as input Y. Consequently, the phase angle between the two signals is to be interpret as follows: positive phase values indicate Y preceding X, while negative values indicate the opposite. The wavelet cross-coherence graphs computed show an heterogeneous behaviour across the different datasets. To synthesise the results, the dominant periods identified across all displacement–environmental variable combinations are first examined.

Figure 4.19 shows the distribution of dominant periods across the 2015–2022 and the 2019-2024 ranges. All histograms highlight that the dominant period across every land cover type and displacement component is 365 days, reflecting regular seasonal cycles of

temperature, precipitation, snow accumulation, and coupled groundwater response. Secondary periods are sporadically present in all combinations, likely corresponding to individual events or sub-seasonal meteorological fluctuations. Forested areas are characterised by the highest level of variation of periods, potentially due to the reduced PS density and thus recorded noise.

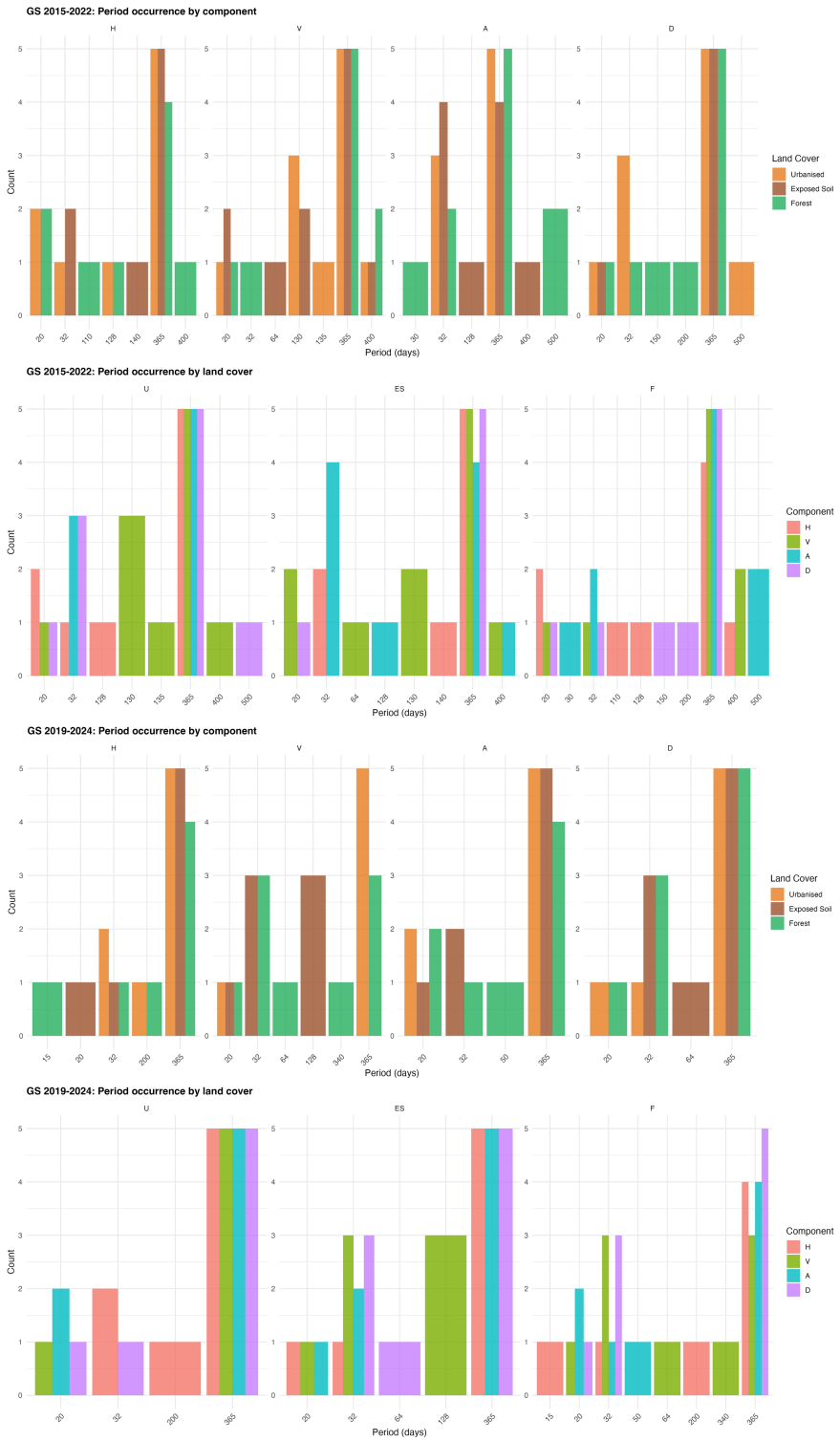


Figure 4.19. GS - triggering factors period occurrence

For this reason, the interpretation of phase angles and delays focuses on the annual

cycle. While phase angles and delays are computed for all identified periods (provided in Appendix A), only the results at T=365 d are presented. Precipitation is not part of this analysis as it never exhibits a 365-day periodicity, but is rather characterised by episodic variability with periods of 20 - 32 days. Both phase angles and periods are determined qualitatively aiming at identifying dominant temporal relationships rather than providing precise quantitative predictions.

Tables 4.5 and 4.6 show the average cross-wavelet power for all the pairings analysed at the 365-d period.

Table 4.5. GS 2015–2022: Average cross-wavelet power at period=365 d

2015-2022	**Average cross-wavelet power**			
	H	**V**	**A**	**D**
P6SZCA1				
U	0.4	0.3	0.3	0.3
ES	0.5	0.4	0	0.8
F	0.3	0.5	0.5	0.5
P6SZCA2				
U	0.3	0.3	0.3	0.3
ES	0.4	0.3	0.4	0.6
F	0.3	0.4	0.5	0.4
P6SZCB0				
U	0.7	0.6	0.5	0.5
ES	0.8	0.6	0.9	0.9
F	0.4	0.7	0.7	0.7
Temperature				
U	0.7	0.6	0.6	0.6
ES	0.8	0.6	0.7	1.1
F	0.4	0.8	0.8	0.8
Snow depth				
U	0.7	0.6	0.6	0.6
ES	0.8	0.8	0.7	1.2
F	0.4	0.8	0.8	0.7

In the 2015-2022 range, piezometric data shows moderate intensity (0.4 - 0.5) for *P6SZCA1* and *P6SZCA2*, located in the north-western part of the landslide, while piezometer *P6SZCB0*, found further south, shows overall higher values around 0.7 - 0.9, with higher correlations found in ES areas. Temperature and snow depth highlight con-

Table 4.6. GS 2019–2024: Average cross-wavelet power at period=365 d

2019-2024	**Average cross-wavelet power**			
	H	**V**	**A**	**D**
P6SZCA1				
U	0.3	0.5	0.4	0.5
ES	0.4	0	0.5	0.3
F	0	0	0	0.4
P6SZCA2				
U	0.5	0.7	0.7	0.7
ES	0.6	0	0.8	0.6
F	0.4	0.3	0.4	0.6
P6SZCB0				
U	0.4	0.9	0.7	0.8
ES	0.8	0	0.8	0.7
F	0.4	0.7	0.6	0.8
Temperature				
U	0.6	0.9	0.8	0.8
ES	0.8	0	0.9	0.8
F	0.6	0.5	0.6	0.8
Snow depth				
U	0.8	0.9	0.8	0.8
ES	0.8	0	0.9	0.8
F	0.4	0.5	0.6	0.8

sistent and coherent power across all displacement components and land cover classes (0.7 - 0.9). During the 2019-2024 interval, a strengthening in the correlation between these two weather factors is noticeable, combined with a weakening of response to piezometric fluctuations, especially in the ascending and descending components over forested areas. Such shift suggests a change in the triggering mechanisms, with recent displacements being more significantly driven by atmospheric forcing rather than subsurface water content.

Shifting to the phase angles observed on the wavelet graphs, they are characterised by different degrees of stability. Where they show small fluctuations, a mean angle is considered, while where they significantly change direction, indicating weak or unstable coherence, no reliable angle and delay estimate is reported. Table 4.7 shows the phase angles identified only for those combinations that have a cross-wavelet power equal or greater to 0.7 to limit noise. Additionally, the analysis focuses on the 2019-2024 time period given the significant increase in PS density shown in Table 4.4, especially in ES areas with increases ranging from 130 to 160 % thanks to improvements in data processing and elaboration and to the five-year moving window approach adopted since 2020 (EGMS, 2025a, 2025b). This enables a more consistent and less noisy data collection. Finally, given the complexity of the interpretation regarding the *ascending* and *descending* components due to slope geometry (slope and aspect), satellite acquisition geometry (LOS and view angle), and local topography, the main interpretation solely focuses on *horizontal* and *vertical* displacement components.

Pore pressure variations affect vertical consolidation and soil rebound through effective stress changes and soil compressibility. A decrease in groundwater depth, thus a lowering of the water table level, physically entails an increase in effective stress, causing soil consolidation and subsidence, detectable in the *vertical* component of EGMS datasets (Terzaghi et al., 1967). *P6SZCA1* and *P6SZCA2* hardly show any coherence with *horizontal* or *vertical* components. This can partially derive from *P6SZCA1* limited recordings as it was deactivated in December 2022. Beyond this date, the final measured value is extended as a constant through December 2024, so that its lack of oscillation causes the detection of no meaningful correlations. Vertical displacements in urbanised areas are characterised by an in-phase coherence with the groundwater depth variations detected by *P6SZCA2*, entailing a sinking of the ground when the water table level is lower and viceversa. *P6SZCB0* shows a higher degree of correlation with the displacement components, especially for the *vertical* one, as they are again in-phase and thus coherent with theory. It also shows an in-phase horizontal response in ES areas, suggesting a lateral pore pressure-driven mobilisation.

Freeze-thaw cycles are the primary periodic weathering mechanisms found in alpine environments (H. Chen et al., 2025). These cycles are driven by the phase transition

Table 4.7. GS 2019–2024: Phase angles at period=365 d (filtered by power ≥ 0.7)

2019-2024	**Phase angle [°]**	
	H	**V**
P6SZCA1		
U		
ES		
F		
P6SZCA2		
U		50
ES		
F		
P6SZCB0		
U		40
ES	15	
F		350
Temperature		
U		5
ES	355	
F		
Snow depth		
U	155	180
ES	165	
F		

of water in soil pores and fractures: when water freezes, it undergoes a 9% volumetric expansion, causing displacements and further pressure on the soil structure (M. Chen et al., 2026; Yang et al., 2026; Ye et al., 2026). The freeze-thaw mechanism is represented in Figure 4.20. This process can be detected by EGMS displacement observations through characteristic temperature-displacement correlations, yet the specific phase relationship varies by land cover class and displacement component.

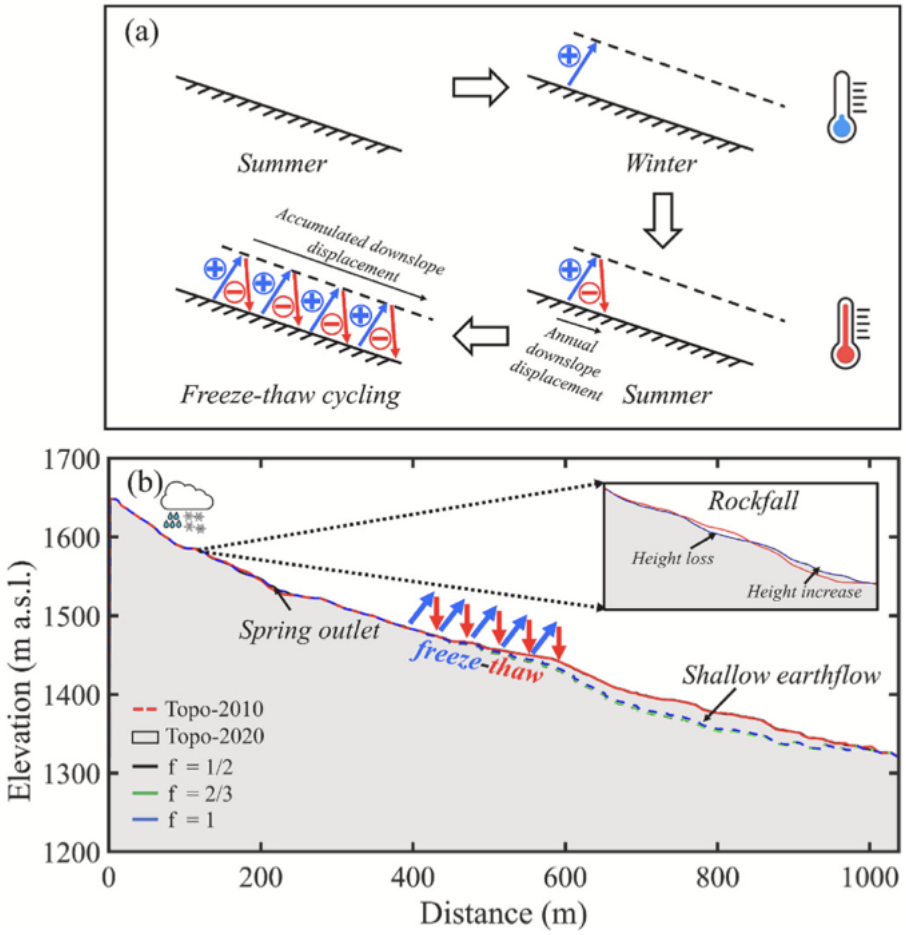


Figure 4.20. Freeze-thaw mechanism: uplift values (blue) caused by freezing and subsidence values (red) caused by thaw process (H. Chen et al., 2025)

In exposed soil areas, freeze-thaw cycles define seasonal motions as negative temperatures cause the water present in soil pores to freeze, thus increasing its volume and causing an overall movement that can be divided in a vertical uplift and a horizontal negative displacement (westward for local geometry). Spring/summer thaw enables elastic recovery and positive (eastward) *horizontal* displacement. Consequently, an in-phase correlation is expected between temperature and *horizontal* displacements and an out-of-phase correlation with *vertical* ones. As a matter of fact, the phase angle observed when combining temperatures and displacements shows a perfectly in-phase correlation with

horizontal displacements.

In urbanised areas, the dominant mechanism is the thermo-mechanical response of infrastructure materials to temperature shifts. These tend to thermally expand when temperatures rise, and contract when they decrease, respectively generating an almost immediate vertical uplift or sinking and an overall horizontal expansion or contraction. Consequently, elevated temperatures are expected to show in-phase correlation with *vertical* displacement and an in-phase or out-of-phase correlation with *horizontal* displacement depending on whether the thermal stress induces expansion toward or away from the satellite LOS. The correlation detected between the *vertical* displacement detected in urbanised areas and temperature is in fact perfectly in-phase.

Snow depth is directly proportional to the static load that the accumulated snow mass exerts. Unlike temperature, snow accumulation persists over months and exerts prolonged stress: high snow depths cause compression (negative *vertical* displacement) and when the stress decreases because of snow melting, the underlying material recovers, generating positive *vertical* displacement. Similarly, snow load induces *horizontal* displacements consistently with the landslide direction. The out-of-phase behaviour reflects the inverse relationship between temperature and snow depth. In urbanised areas, snow depth shows an almost perfectly out-of-phase correlation with *vertical* displacement as the snow load causes infrastructures compression (negative values). Both urbanised and exposed soil areas are characterised too by an out-of-phase correlation between snow depth and *horizontal* displacement, as a consequence to the snow load inducing a downward movement along the landslide westward direction (negative values).

Table 4.8 defines the delays calculated for every phase angle detected for the 365 days period. Phase delays obtained for the different phase angles observed for piezometric and temperature variables are very small or almost equal to a full year, likely representing measurement noise or instrumental resolution rather than physically meaningful lags. This behaviour is consistent with the immediate response that these factors trigger. Differently, snow depth exhibits consistent delays of approximately 170–180 days, which aligns with the phase lag between the raise in temperatures and the subsequent snowmelt-driven hydrological response.

Table 4.8. GS 2019–2024: Phase delays at period=365 d (filtered by power ≥ 0.7)

2019-2024	**Delay [d]**	
	H	**V**
P6SZCA1		
U		
ES		
F		
P6SZCA2		
U		51
ES		
F		
P6SZCB0		
U		41
ES	15	
F		353
Temperature		
U		5
ES	360	
F		
Snow depth		
U	157	183
ES	167	
F		

Chapter 5

Case study 2: the Thuras landslide

5.1 Data gathering

5.1.1 EGMS

The datasets downloaded from EGMS for the area concerning the T landslide coincide with the ones used for the GS landslide. The datasets' updated names are:

- T_2015_2022_H;
- T_2015_2022_V;
- T_2015_2022_A;
- T_2015_2022_D;
- T_2019_2024_H;
- T_2019_2024_V;
- T_2019_2024_A;
- T_2019_2024_D.

5.1.2 ReRCoMF

The Thuras landslide is characterised by a much smaller ReRCoMF monitoring network, having only one piezometer, one manual inclinometer and two fixed inclinometers as shown in Figure 5.1.

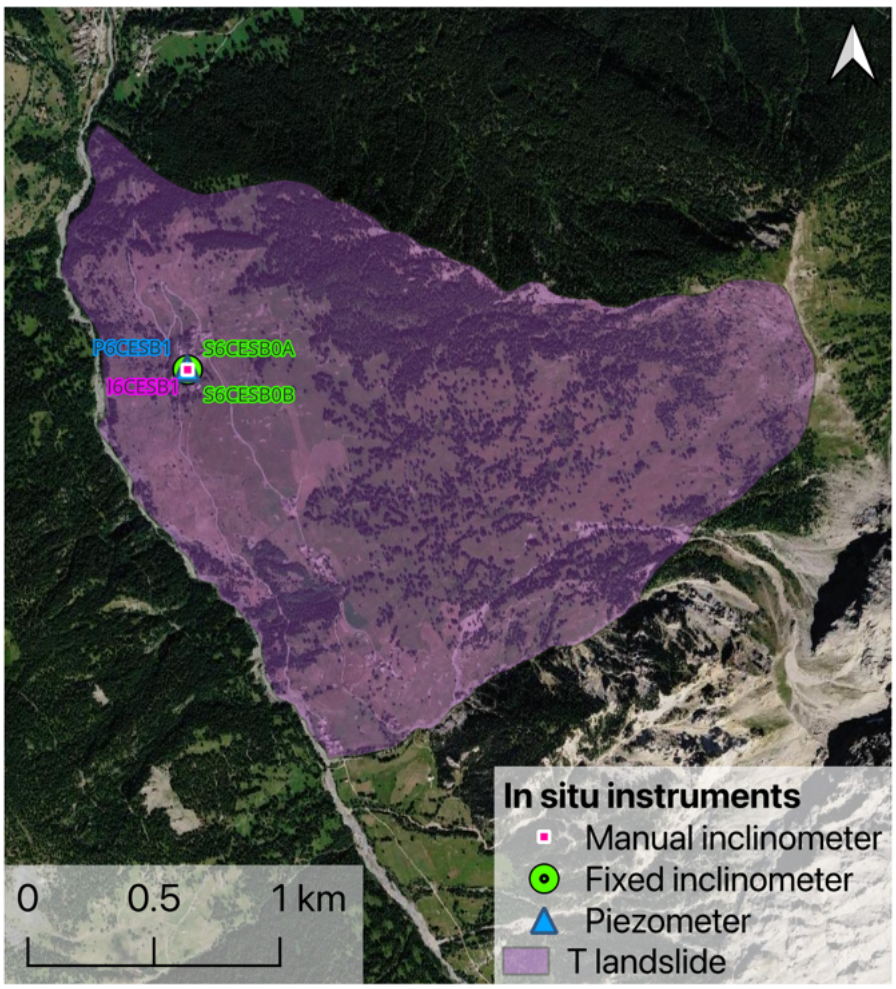


Figure 5.1. T ReRCoMF instruments

Table 5.1 lists the instruments for which data are available, along with their main characteristics.

Table 5.1. GS ReRCoMF instruments

Instrument type	Instrument code	First reading available	Last reading available	Depth [m]	Total length [m]	Average reading frequency	Active
Manual inclinometer	I6CESB1	17/07/13	15/06/21	/	80.5	1/year	yes
Fixed inclinometer	S6CESB0A	11/03/14	23/03/26	22.5	/	1/day	yes
Fixed inclinometer	S6CESB0B	11/03/14	23/03/26	25.5	/	1/day	yes
Piezometer	P6CESB1	16/10/20	23/03/26	/	/	1/day	yes

Green rows indicate active instruments, while the orange one highlights the only manual inclinometer present that is reported as active but whose last available reading date is in 2021.

5.1.3 Arpa weather stations

The Arpa weather station chosen to retrieve the data from to conduct the T landslide analysis is the *Sestriere* station, as for the GS landslide analysis. This choice is based on its high level of representativeness given its altitude, aspect, and proximity to the landslide body.

5.2 Data analysis

5.2.1 EGMS data validation

EGMS horizontal displacements are validated by comparison with the horizontally projected displacements recorded by the only manual inclinometer present. This can only be done with the EGMS data ranging from 2015 to 2022 as the inclinometer's last recording is June 2021. Figure B4 shows the comparison between the two datasets and the average velocities measured are: $v_{EGMS} = 14.79$ *mm/year* and $v_{incl} = 11.69$ *mm/year*. A difference of *2.10 mm/year* reflects a good coherence between the displacements detected by the two sensors.

5.2.2 Inclinometers

Fixed inclinometers

Figure 5.3 represents the graphs of cumulative displacement and cumulative precipitation over time corresponding to the two fixed inclinometers *S6CESB0A* and *S6CESB0B*. The two instruments share the same location but they are installed at two different depths, thus enabling a vertical comparison of deformation for the same area: *S6CESB0A* reaches *22.5 m* while *S6CESB0B* reaches *25.5 m*. The two graphs show a shared increasing trend, characterised by a step-like pattern, suggesting seasonal periods of accelerations and stabilisation, potentially driven by external factors. Overall, the accelerations occur around

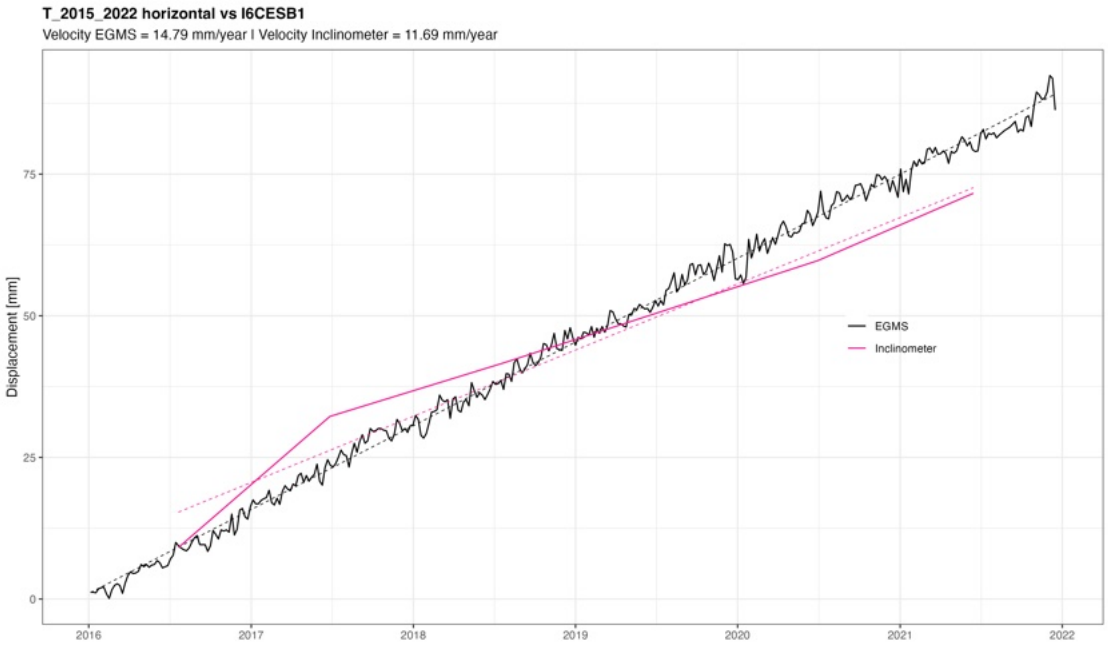


Figure 5.2. T EGMS data validation

mid-year. There is no sign of strong correlation between precipitation and displacement, thus this external factor has limited effect on the landslide motion. From 2021 to 2024, the trend appears more stable in both graphs, but this period is then followed by a sharp increase around May 2024. *S6CESB0B* records displacements that measure around double the value measured by *S6CESB0A*, which entails a larger displacement occurring at higher depths.

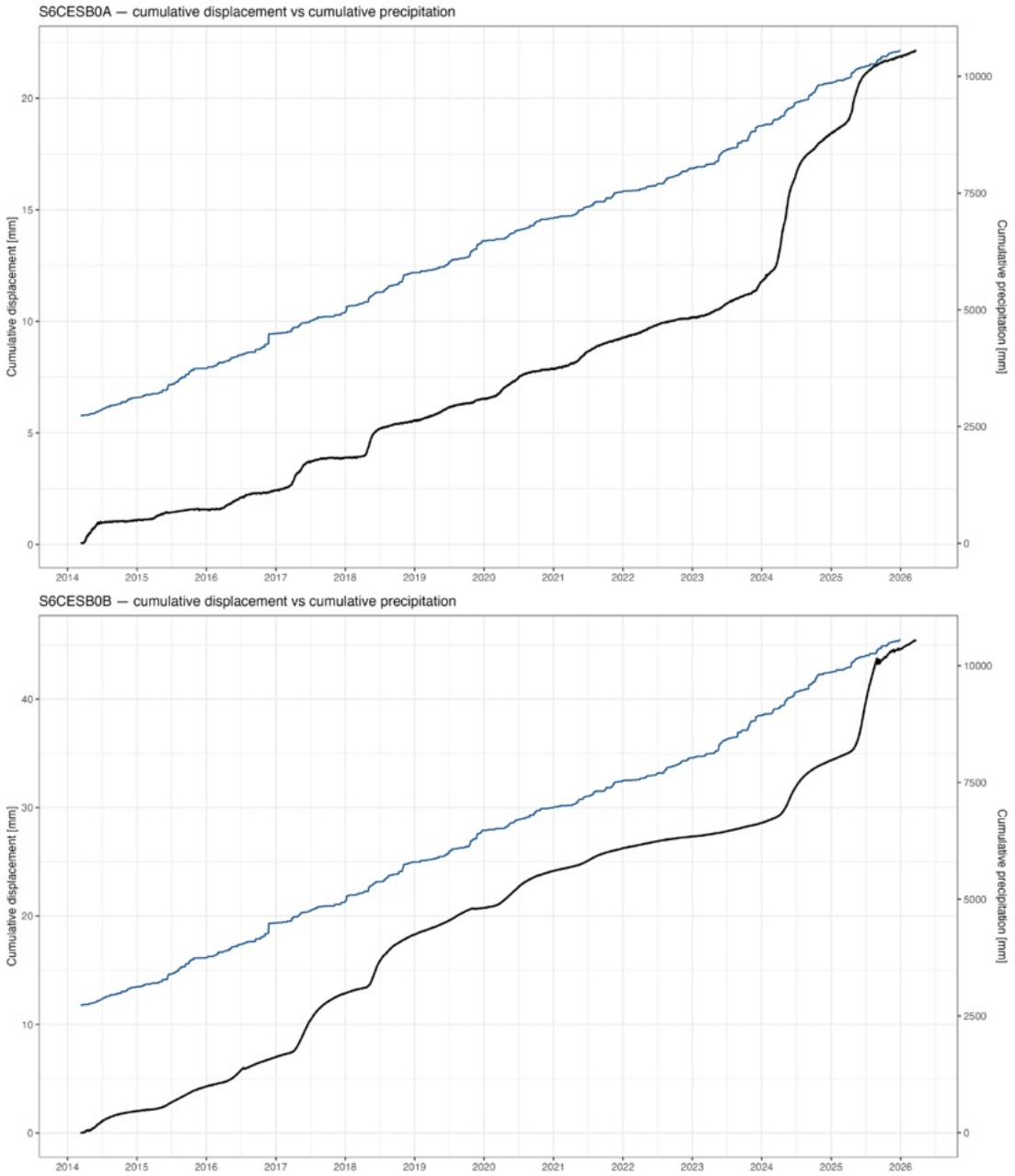


Figure 5.3. T fixed inclinometers: Cumulative displacement vs cumulative precipitation

Manual inclinometers

Figure 5.4 displays the cumulative displacement profiles detected by the manual inclinometer *I6CESB1* installed in the Thuras landslide area as a function of depth. The displacement profile highlights two critical depths where possible shear surfaces occur: a first one at around 22.5 m and a second one at around 25.5 m, coinciding with the depths at which the fixed inclinometers are installed to monitor displacements. It is not possible to construct possible shear surface profiles along elevation as there is only one available

instrument, yet the data confirms the presence of two critical depths.

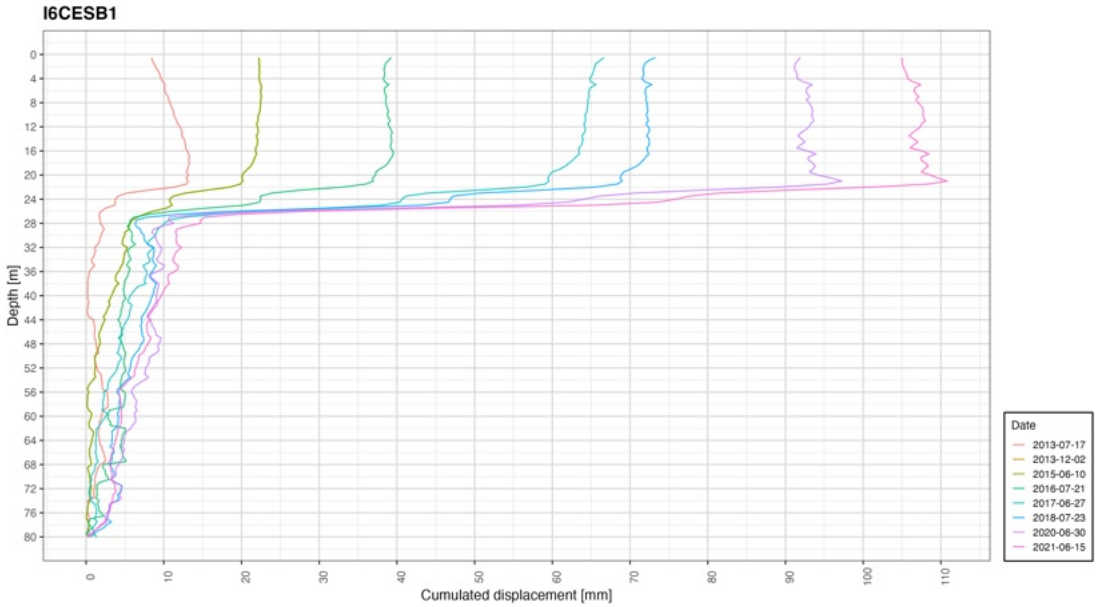


Figure 5.4. T manual inclinometer: cumulative displacement vs depth

Figure 5.5 shows the cumulative azimuth and resultant displacement recorded by the inclinometer.

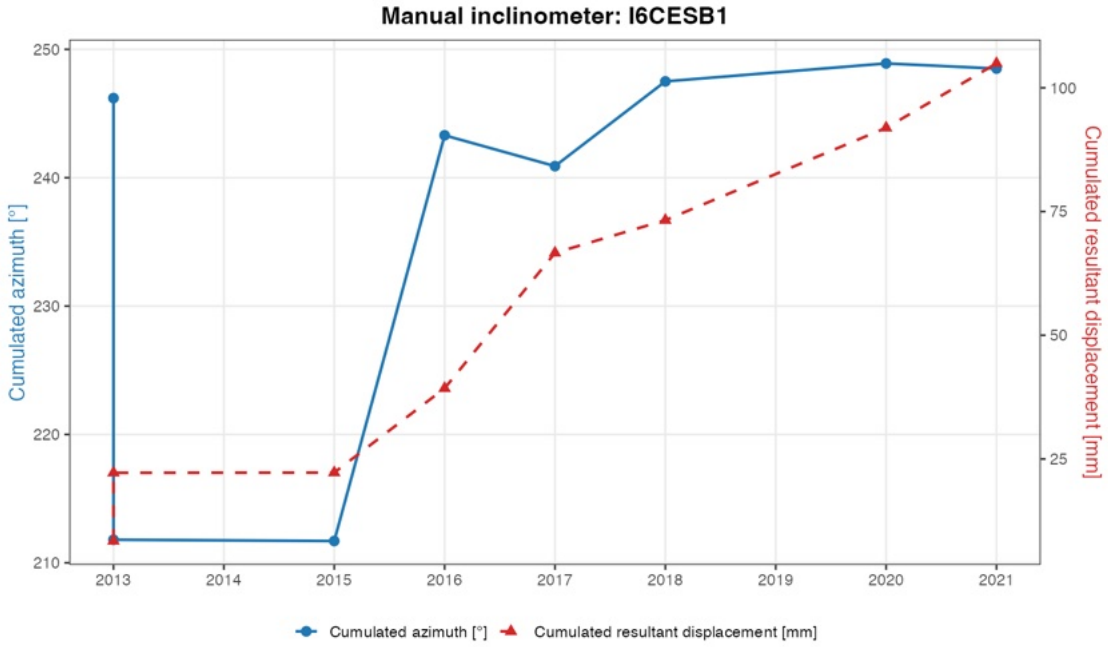


Figure 5.5. T manual inclinometer: cumulative azimuth and resultant displacement

The graph shows a progressive and sustained displacement trend reflecting an

ongoing movement. The first readings seem to be affected by the instrument's adjustment. The cumulative azimuth stabilises from 2016, reaching angles of around *247°*, thus pointing south-west, coherently with the expected downslope orientation of the Thuras landslide. The cumulative displacements grow steadily from 2015, reaching a peak of around *105 mm* in 2021. The data collected by the manual inclinometer *I6CESB1* is consistent with an active and coherent deformation process.

5.2.3 EGMS

The stability threshold of the EGMS components concerning the Thuras landslide area is defined as in the previous case study: a range of $\pm 2\sigma$ is applied, obtaining a stability interval of ± 3 *mm/year*, applied to all datasets and components. Figures 5.6 and 5.7 spatially represent the PS within and around the Thuras landslide, classified according to their velocity ranges, for the 2015 - 2022 and 2019 - 2024 datasets respectively, across their four components.

PS in the 2015-2022 datasets (Figure 5.6) are mainly located in urbanised areas. In all components, the southern section of the landslide belongs to the stable interval. The *horizontal* component shows PS with negative velocities between -9 *and* -21 *mm/year* coherently with the landslide's slope, while the vertical one is characterised by points with lower velocities ranging from -9 *mm/year* and reaching the stable interval, suggesting a limited vertical movement. The *ascending* data is entirely characterised by PS with positive velocities, while the *descending* track reflects an overall negative mean velocity, reaching values up to -27 *mm/year*, proving the landslide's on-going activity.

The 2019 - 2024 period (Figure 5.7) has a clear increased number of PS (a part from the forested areas) which show an overall velocity spatial distribution coherent with the earlier dataset. In this time range too, the southern part of the T landslide appears to be the most stable. The *horizontal* track shows negative velocities, reaching up to -27 *mm/year*, while the *vertical* one shows lower velocities, belonging to the -3 *to* -9 *mm/year* range. The *ascending* component is characterised by only positive velocities, coherently with the landslide's slope. On the opposite, the *descending* one overall shows PS with negative velocities, mainly between -9 *and* -21 *mm/year*. The asymmetry in PS density found in both timeseries suggests a downslope displacement vector whose orientation is more sensitive to the *descending* LOS direction.

Table 5.2 reports the PS density expressed in PS/km^2 for each land cover class and component, relatively for the 2015 - 2022 and 2019 - 2024 datasets. As expected, the *urbanised* areas entail the highest PS density across all components and both time periods, given the higher reflectivity of points it covers. *Exposed soils* show intermediate density

values, while extremely few points belong to *forested* areas. There is a clear difference in PS density between the *ascending* and *descending* tracks, as the latter shows much higher values, probably due to the landslide movement being more sensitive to this LOS. There is a decrease in the PS density in forested areas in both *ascending* and *descending* components, inherent of the low coherence of forested areas and potentially caused by an increase in vegetation density or caused by the temporal decommissioning of Sentinel-1 B.

Table 5.2. T - PS density (PS/km^2) based on land cover class and EGMS component

PS/km^2	**2015–2022**			**2019–2024**			**% increase**		
	U	**ES**	**F**	**U**	**ES**	**F**	**U**	**ES**	**F**
H	62	4	1	82	12	3	32%	200%	200%
V	62	4	1	82	12	3	32%	200%	200%
A	924	18	6	1355	30	5	47%	67%	−17%
D	4168	63	6	4886	116	3	17%	84%	−50%

Subsequently, the Norton, Modified Lomnitz and Aydan creep models are fitted to every dataset component to determine which better applies to the EGMS time series (Appendix B). As in the previous case study, the Norton and the modified Lomnitz laws successfully fit the datasets, with an average of about R^2 of 0.75. The Norton linear creep model is chosen to analyse the displacement trends. As shown in Figure 5.8 and 5.9, average displacement curves are computed for each dataset using the three land cover models to assess displacement behaviours and changes across the two periods.

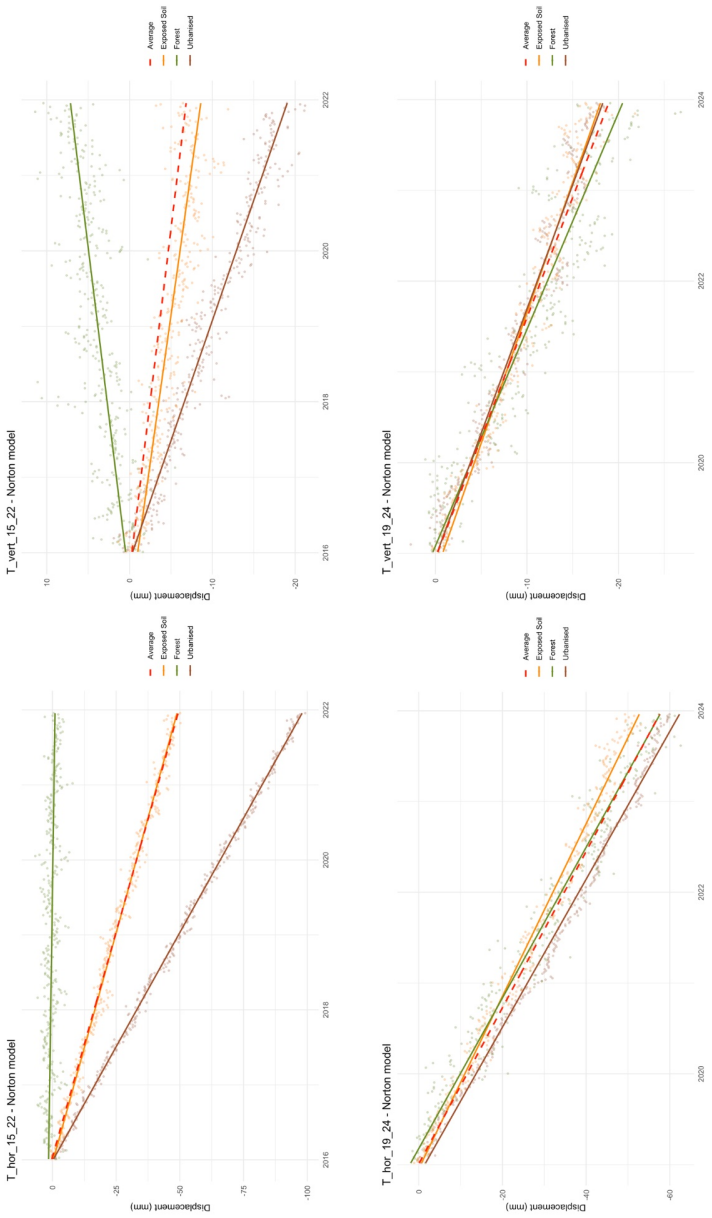


Figure 5.8. T: Norton model applied to *horizontal* and *vertical* datasets

The *horizontal* time series are characterised by negative displacement values, coherently to the W-SW direction of the T landslide. Both time ranges show the U areas as the ones with the steepest displacement curves. During 2015-2022 the F areas appear to be entirely stable, probably due to the very low PS density which lacks significance. While ES areas appear to have a stable trend between the two time ranges and U ones show decreasing displacement rates, all three land components share similar rates in the 2019-2024 period.

The *vertical* components show negative displacements apart from the F areas in

2015-2022. Such recordings define a subtle but downward displacement. *U* areas keep a constant trend over time, while a higher displacement rate is recorded in the latter time range for *ES* areas. This could be caused by the higher sensitivity of exposed soils to water permeation that ultimately affect the vertical response of soil. On the contrary, *urbanised* areas tend to have rather impermeable surfaces that limit water infiltration and thus reduce the effect of wetting and drying cycles on vertical deformation. The *F* class in the 2015-2022 dataset, as for the *horizontal* component, has a high level of noise and records an unexpected positive displacement rate. Overall, the *vertical* components is characterised by a stable deformation pattern.

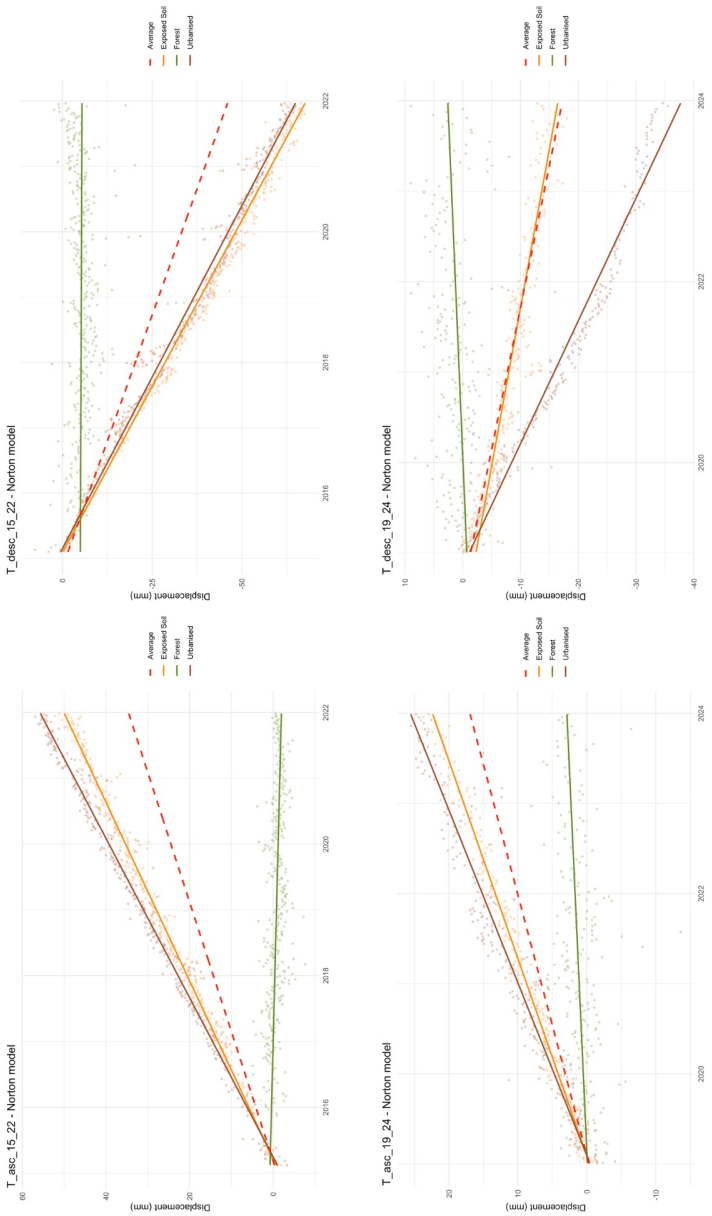


Figure 5.9. T: Norton model applied to *ascending* and *descending* datasets

The *ascending* tracks record positive displacement values, consistent with the downslope direction of the T landslide. *F* areas show an almost horizontal trend, providing further evidence of its lack of significance given the very low PS density. *U* and *ES* share a similar trend across both time periods, with the former having slightly faster rates. They are both affected by a significant decrease in displacement in 2019-2024, suggesting a change towards a slower landslide motion.

The *descending* components show an almost horizontal trend for *F* areas, consistent with the *ascending* observations. In the first time range, *U* and *ES* share almost identical negative trends, coherently with the *ascending* values. The second time period is characterised by lower displacement rates for both land cover types, with *ES* areas recording a drastic decrease. This is potentially explained by the improved observations given the 84% increase in PS density and possible ground stabilisation through drainage and consolidation processes.

Overall, the analysis of the creep models applied to the Thuras landslide reveals consistent downslope (W-SW) kinematics with land-cover-dependent displacement rates. *Urbanised* areas have the fastest trends in almost every EGMS component, while *exposed soils* have an intermediate one, possibly reflecting not only different mechanisms but also due to the large difference in PS density. All three land cover classes show a convergence towards lower displacement rates in the 2019–2024 period, suggesting a transition towards a more stable creep kinematics. This change in trends is also thought to be the effect of the higher accuracy induced by the increased PS denisty.

5.2.4 Triggering factors analysis

The potential triggering factors affecting the Thuras landslide seasonal oscillations, superimposed to the intrinsic creep motion, are analysed through the comparison with EGMS displacement time series. The 24 EGMS subsets obtained (*horizontal, vertical, ascending* and *descending* divided in *U, ES, F* for both 2015-2022 and 2019-2024) are subject to a coherence analysis with: *depth to groundwater [m], precipitation [mm], temperature [°C]*, and *snow depth [cm]*. Groundwater depth data is gathered by the piezometer located in the Thuras lanslide area (*P6CESB1*), while the other datasets coincide with the ones used for the first case study, thus collected by Arpa's Sestriere weather station (Figure 4.3).

The graphs obtained to compare EGMS displacement and the potential triggering factors time series are show in Appendix B. Due to high noise levels, a wavelet cross-coherence analysis is carried out to quantify the extent of signal coherence between the different pairings. A cross-wavelet power approach is adopted rather than a coherence

analysis to detect meaningful interactions between displacement and the selected triggering factor. Preliminary coherence analysis showed misleading high values across all time scales and periods, probably caused by the signals' continuous fluctuations.

Cross-wavelet power represents a non-normalised measure of covariance between two signals and thus depends on the amplitude of both signals. To ensure comparability across the graphs, all the plots have a uniform colour scale, based on the global maximum value calculated across the 16 displacement–forcing factor pairings of this case study and the 24 of the first one, excluding few outliers from forested regions with inherent data noise. Consistently with the first case study, all graphs are computed with displacement as X and environmental factor as Y.

Firstly, the dominant periods detected across all the different parings are analysed. Figure 5.10 represents the occurrence of the dominant periods detected across the 2015-2022 and 2019-2024 time periods. All histograms highlight the 365-day period as the most recurrent across all land cover types, suggesting regular seasonal cycles of temperature, precipitation, snow accumulation, and coupled groundwater response. There are some secondary periods, especially around 30-32 days, that are sporadically present across the different combinations, which likely correspond to sub-seasonal meteorological fluctuations or individual events. As in the first case study, forested areas show the broadest variation of observed periods, likely due to the few PS belonging to this land cover category found in the landslide area.

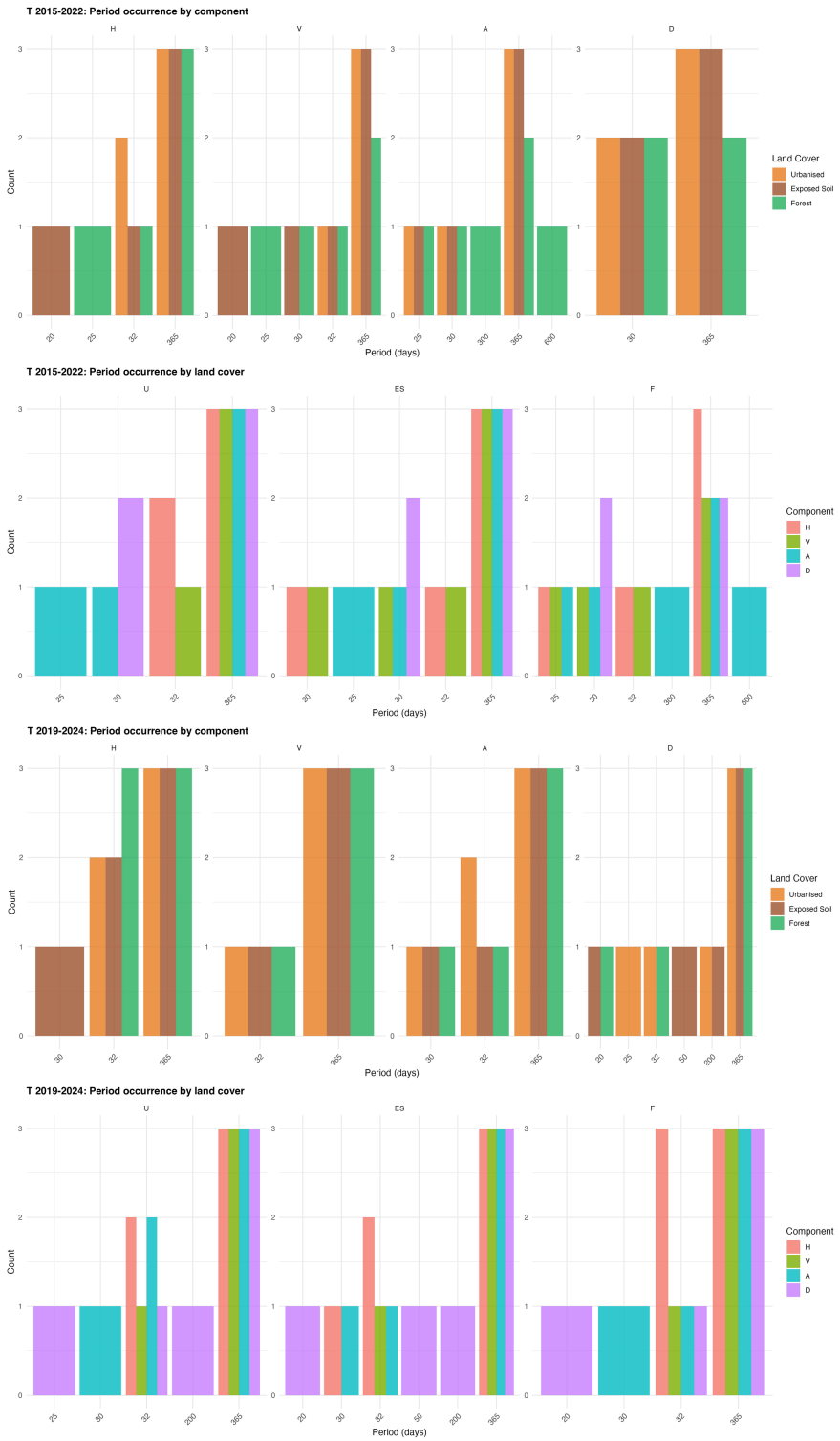


Figure 5.10. T - triggering factors period occurrence

Given the importance of the 365-day cycle, phase angles and delays are analysed

at this period. This section examines only the annual component (T = 365 d), yet the overall phase angles and delays for all detected periodicities are found in Appendix B. Precipitation is excluded from the interpretation as it lacks annual coherence, while it only shows a coherent short timescale (20-32 days) response to events.

The qualitatively-obtained phase angles and delays are analysed at the 365-day period, as it dominates the wavelet power across all pairings. This section examines only the annual component (T = 365 d), while results for all detected periodicities are available in Appendix B. Precipitation is excluded from the interpretation as it lacks annual coherence, displaying instead a monthly response to individual events.

Tables 5.3 and 5.4 report the average cross-wavelet power for all the combinations analysed. When the wavelet plots had

Table 5.3. T 2015–2022: Average cross-wavelet power at period=365 d

2015-2022	**Average cross-wavelet power**			
	H	**V**	**A**	**D**
P6CESB1				
U	0.3	0.4	0.7	0.7
ES	0.4	0.5	0.7	0.7
F	0.4	0	0.3	0
Temperature				
U	0.7	0.3	0.8	0.8
ES	0.4	0.3	0.8	0.8
F	0.8	0.6	0.7	0.4
Snow depth				
U	0.7	0.3	0.8	0.8
ES	0.4	0.3	0.8	0.8
F	0.8	0.6	0.7	0.5

The 2015-2022 period is characterised by low intensity for the piezometric forcing except for the *ascending* and *descending* tracks for the U and ES areas. Temperature and snow depth show higher and coherent power values, suggesting strong coupling between these two intertwined factors and the detected displacement. Across all forcing variables, the *vertical* component exhibits significantly lower values compared to the others. Overall, the *ascending* and *descending* tracks highlight higher power than the *ortho* ones, possibly reflecting better sensitivity to oblique slope movements.

In the 2019-2024 range, *horizontal* and *vertical* components display increased cross-wavelet power with the analysed triggers, possibly reflecting the 200% increase in

Table 5.4. T 2019–2024: Average cross-wavelet power at period=365 d

2019-2024	Average cross-wavelet power			
	H	V	A	D
P6CESB1				
U	0.6	1.1	0.7	0.7
ES	0.5	0.3	0.5	0.7
F	0.4	0.6	0.5	0.5
Temperature				
U	0.8	1.2	0.7	0.6
ES	0.7	0.4	0.5	0.6
F	0.4	0.6	0.5	0.5
Snow depth				
U	1.0	1.0	0.7	0.6
ES	0.7	0.4	0.5	0.6
F	0.4	0.6	0.5	0.5

PS density. Conversely, the *ascending* and *descending* tracks show weakened values, coherently with the decreased PS density.

Phase angles are considered stable when fluctuations are small and thus a reasonable mean can be calculated. When these significantly oscillate, indicating poor coherence, the relationship is considered unreliable and not reported. Table 5.5 presents phase angles only for those combinations with cross-wavelet power equal to or greater than 0.7, to limit noise. Moreover, the analysis focuses on the 2019-2024 period and is limited to the *horizontal* and *vertical* components, which exhibit a 200% increase in PS density. Finally, the interpretation excludes the *ascending* and *descending* tracks due to their inherent complexity related to slope geometry and acquisition effects on these viewing geometries, combined with the decreased PS density. These methodological choices ensure more robust and less noisy findings.

The phase angles obtained for the urbanised areas show an in-phase coherence between the depth to groundwater and *vertical* displacements. This reflects a sinking of the ground when the water table level lowers and vice versa. Such behaviour is a probable effect of pore pressure fluctuations that cause effective stress and soil compressibility to change (Terzaghi et al., 1967).

In urbanised areas, temperature shows a perfectly in-phase coherence with both the *horizontal* and *vertical* components. This likely reflects the thermo-mechanical response of infrastructure materials to temperature shifts. In fact, high temperatures cause

Table 5.5. T 2019–2024: Phase angles at period=365 d (filtered by power ≥ 0.7)

2019-2024	Phase angle [°]	
	H	V
P6CESB1		
U		315
ES		
F		
Temperature		
U	0	0
ES	0	
F		
Snow depth		
U	180	170
ES	180	
F		

infrastructure to expand, while low ones cause contraction. The phase of the correlation between temperature and the *horizontal* component changes depending on whether the thermal stress induces expansion toward or away from the satellite LOS. In this case, higher temperatures dictate positive displacement (away from the LOS), opposite to downslope motion. The perfectly in-phase correlation detected with *vertical* displacement defines an immediate vertical uplift when temperatures are higher, consistently with the underlying physical mechanism.

Exposed soil areas also show an in-phase correlation between temperature and *horizontal* displacement. This likely reflects the effect of freeze-thaw cycles that affect alpine environments. This cycle entails negative *horizontal* displacements (westward for local geometry) when temperatures lower, caused by the increase in volume due to the freezing of the water present in soil pores.

Snow depth defines a proportional static load exerting on the ground. Such load induces an overall compression on the ground which can cause *horizontal* displacements aligned with downslope motion and negative *vertical* displacement. On the contrary, when snow melts and the load decreases, the underlying material is able to recover and exhibits positive *vertical* displacement. Both urbanised and exposed soil areas show an out-of-phase correlation between snow depth and *horizontal* displacement, due to downward movement induced by snow load (negative values). Additionally, urbanised areas are characterised by an almost perfectly out-of-phase correlation with *vertical* displacement as the snow load

causes infrastructure compression (negative values).

Table 5.6 shows the delays calculated for every phase angle detected for the 365-day period. The delay detected for the *P6CESB1* piezometer is nearly a full year, likely

Table 5.6. T 2019–2024: Phase delays at period=365 d (filtered by power ≥ 0.7)

2019-2024	**Delay [d]**	
	H	**V**
P6CESB1		
U		319
ES		
F		
Temperature		
U	0	0
ES	0	
F		
Snow depth		
U	183	172
ES	183	
F		

representing measurement noise or instrumental resolution and can thus be interpreted as an immediate response of *vertical* displacement to changes in groundwater depth. *Horizontal* displacements show an immediate response to temperature changes in both urbanised and exposed soil areas. Similarly, the *vertical* component shows an equal response to temperature. Finally, snow depth exhibits nearly perfect out-of-phase delays, which align with the phase lag between the rise in temperatures and the subsequent snowmelt-driven hydrological response.

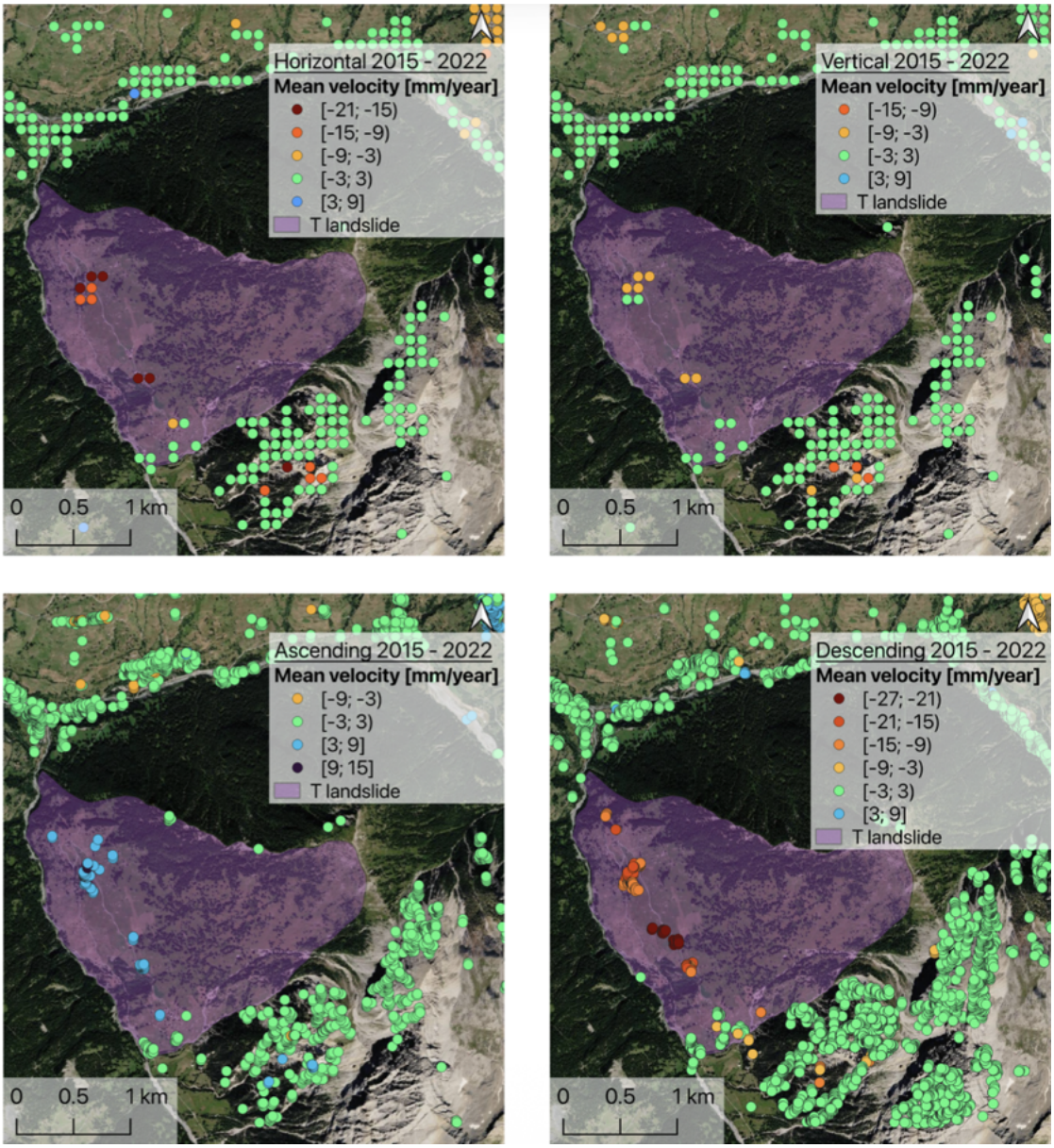


Figure 5.6. T 2015 - 2022: EGMS PS, mean velocity distribution

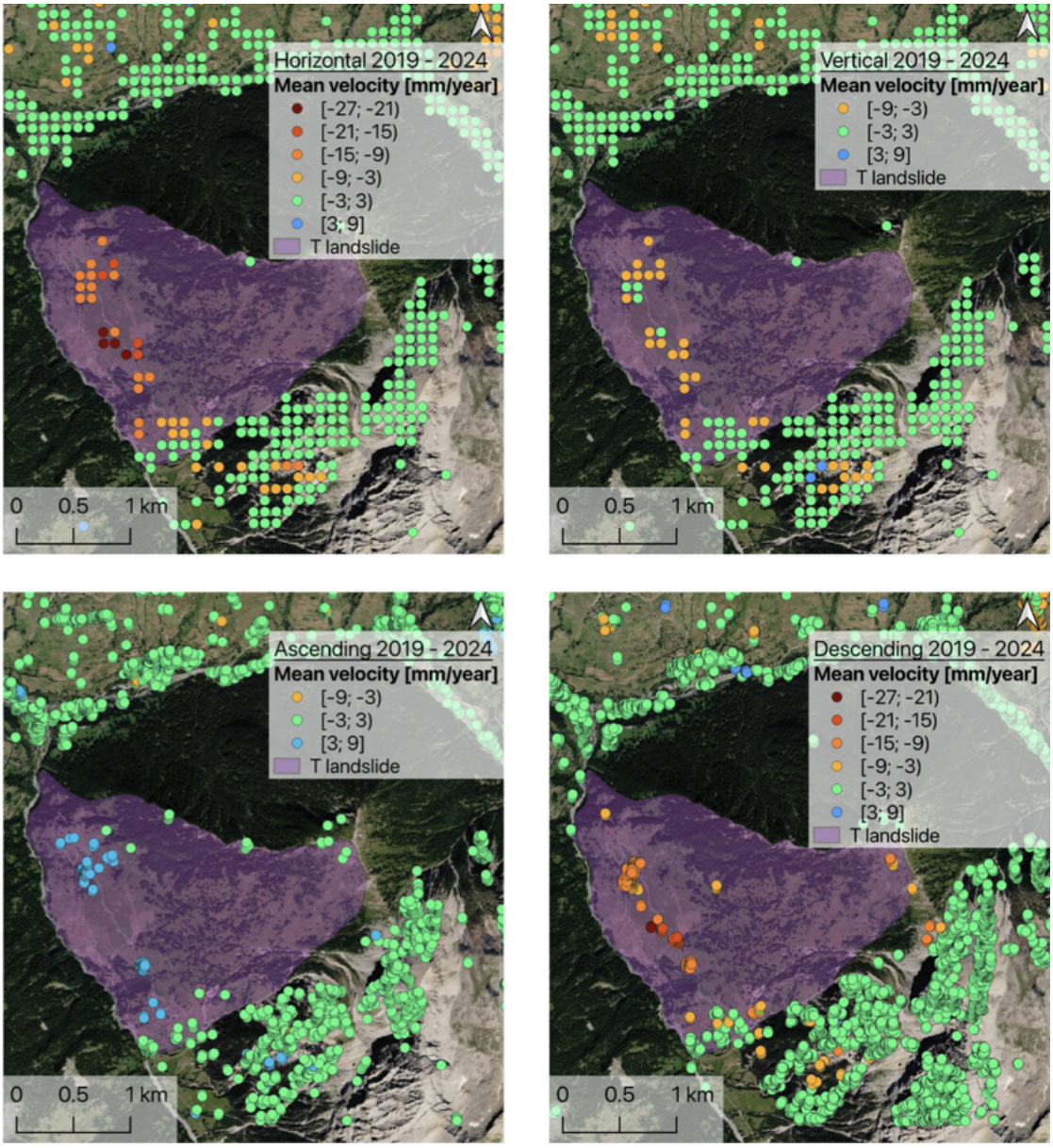


Figure 5.7. T 2019 - 2024: EGMS PS, mean velocity distribution

Chapter 6

Conclusions

This thesis analyses the movement of two Deep-seated Gravitational Slope Deformations (DsGSDs): the Grangesises and Thuras landslides, located in the Susa Valley, in Piedmont, Italy. The methodology entails an analysis of both *in-situ* and remote sensing data, to gather a global view of the two movements and determine the coherence between the two types of data. Initially, the data collected by the *in-situ* instruments is revised and interpreted, consequently the analyses covers the datasets derived from the European Ground Motion Service (EGMS).

The Grangesises and Thuras case studies share many similarities given their close location, similar geological and meteorological environment, and almost identical downslope direction as shown in Chapter 2.1. The two analyses carried out demonstrate agreement between satellite-derived displacement and ground-based inclinometer kinematics, supporting the use of EGMS for detecting slow-motion landslide deformation in the analysed areas (Section 4.2.1 and 5.2.1).

The analysis of the Grangesises landslide gives a spatial overview of the landslide movement given the distributed instruments (as shown in Figure 4.2), while Thuras, with limited instruments (Figure 5.1), cannot capture such complexity. However, the monitoring network density covering the Grangesises area reflects the larger extent of the landslide and higher exposure of settlements and infrastructure. The difference between the extent of the two *in-situ* monitoring networks highlights the the difference between exposure level and site characteristics of the two DsGSDs.

Both landslides exhibit long-term creep rates consistently modelled by Norton linear theory (Section 4.2.3 and 5.2.3), which functions as the two landslides' intrinsic motion mechanism. For both case studies, the baseline creep is summed to oscillatory displacement patterns connected to seasonal meteorological cycles as detected by the cross-wavelet

analysis. Both landslides move dominantly downslope in a southwest direction. Consequently, phase angles and delays derived from the cross-wavelet analysis are consistent across both sites (Sections 4.2.4 and 5.2.4). The observed consistency across the two independent case studies suggests that the methodology followed successfully captures the landslide kinematics.

As shown in Tables 4.6 and 5.4, the cross-wavelet power between meteorological variables and displacement components is moderate, suggesting that meteorological forcing mainly modulates the surface/near-surface displacement signal rather than controlling the long-term deep-seated motion. The observed displacement patterns differ by land cover. In exposed soil areas, freeze–thaw cycles are the main effects on displacement, while urbanised areas are rather affected by thermal effects that cause materials expansion and contraction. This shows that the same forcing generates different responses depending on land cover.

The analysis carried out encounters a number of limitations. Firstly, the meteorological data is gathered only from the Sestriere Arpa weather station (Figure 4.3). While this station was selected as the most representative for both study areas, it might hide some site-specific variations. Secondly, the monitoring *in-situ* instruments have some temporal gaps in data recording which interrupt continuous measurement. Additionally, the time periods covered by the various instruments are variable and not always comparable with the datasets provided by EGMS. For EGMS data, the decommissioning of Sentinel-1B in January 2022 doubled the revisit time (from 6 to 12 days), reducing temporal sampling.

The land cover classification adopted (*Urbanised, Exposed Soil, Forest*) represents a categorisation intended to detect different ground behaviours. However, different classifications could potentially reveal additional heterogeneity in forcing-response relationships. Additionally, case studies are found in largely forested areas which results in low interferometric coherence and sparse PS density in the EGMS datasets. These areas cannot be well characterised through remote sensing technologies as they are subject to elevated noise and extremely low PS density that significantly limits the spatial resolution of displacement detection in these areas. Moreover, the localised monitoring of the Thuras landslide prevents the assessment of the overall landslide kinematics.

Finally, the cross-wavelet phase and delay estimates are interpreted qualitatively on the basis of visual inspection of the computed graphs. The analysis is carried out applying a number of simplifications: it focuses on the *horizontal* and *vertical* displacement components and the temporal windows for phase analysis are restricted to periods of sufficient power and stability, potentially missing secondary behaviours, limiting the completeness of the full kinematic picture.

The methodology developed in the thesis, combining EGMS satellite data with

ground-based in-situ monitoring instruments, has proven effective in characterising both Grangesises and Thuras landslide kinematics and provides a more complete overview, better than either technique alone. The dual approach used enables the validation of satellite-derived displacement through independent inclinometer records, while revealing extensive long-term displacement trends that would not be achievable by *in-situ* instruments alone. The analysis carried out was successful in decoupling the two landslides' movements into a baseline creep and oscillatory motions, and clarified how environmental triggers interact with the landslide structure and land cover.

On one hand, the Grangesises landslide is characterised by a large number of active sectors that result in a great spatial heterogeneity and a more representative monitoring network. On the other hand, the Thuras landslide is defined by a more localised and less characterisable behaviour, yet showing strong cross-wavelet power values, suggesting a more clearly defined coherence with environmental forcing. Overall, the comparison between the two case studies shows that EGMS products are particularly effective in identifying the spatial distribution and temporal persistence of slow-moving deformation, especially where sufficient PS density is available. However, the interpretation of EGMS-derived displacement remains strongly dependent on land cover, satellite viewing geometry, and the availability of independent ground-based measurements. For this reason, EGMS should not be considered a replacement for in-situ monitoring, but rather a complementary tool capable of extending the spatial and temporal interpretation of landslide activity. Future analyses could improve both methodological and temporal resolution by reducing the simplifications adopted in the wavelet analysis and extending the temporal coverage through historical radar data as Cosmo and Envisat to obtain a more global overview of the two landslides' evolution.

Appendix

Appendix A

Chapter 4 appendix



Figure A1. GS data validation 1

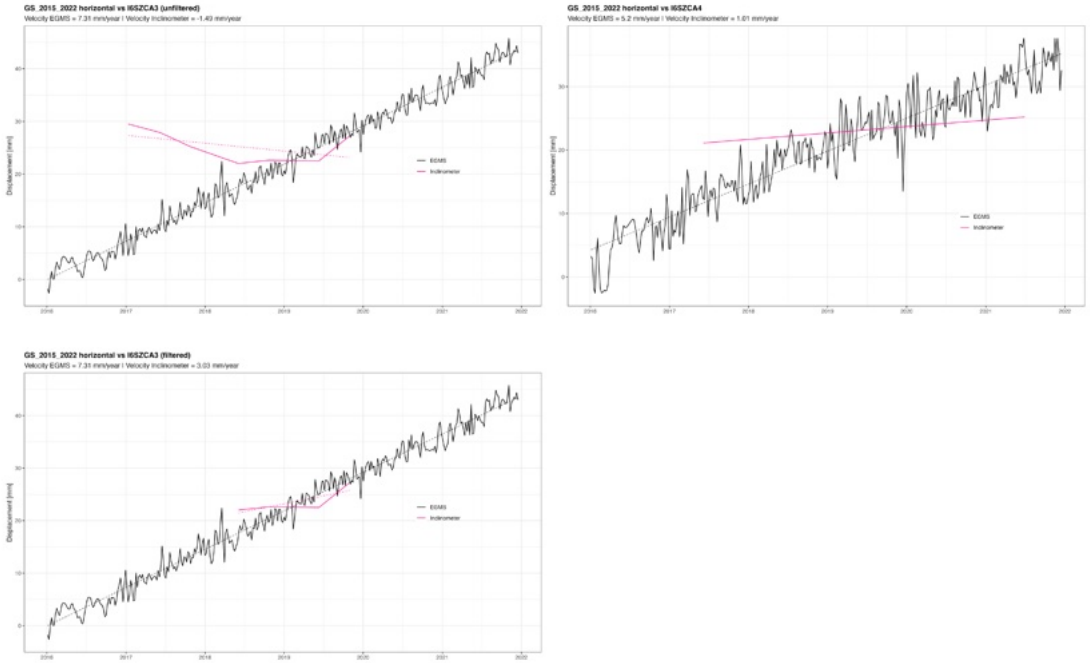


Figure A2. GS data validation 2

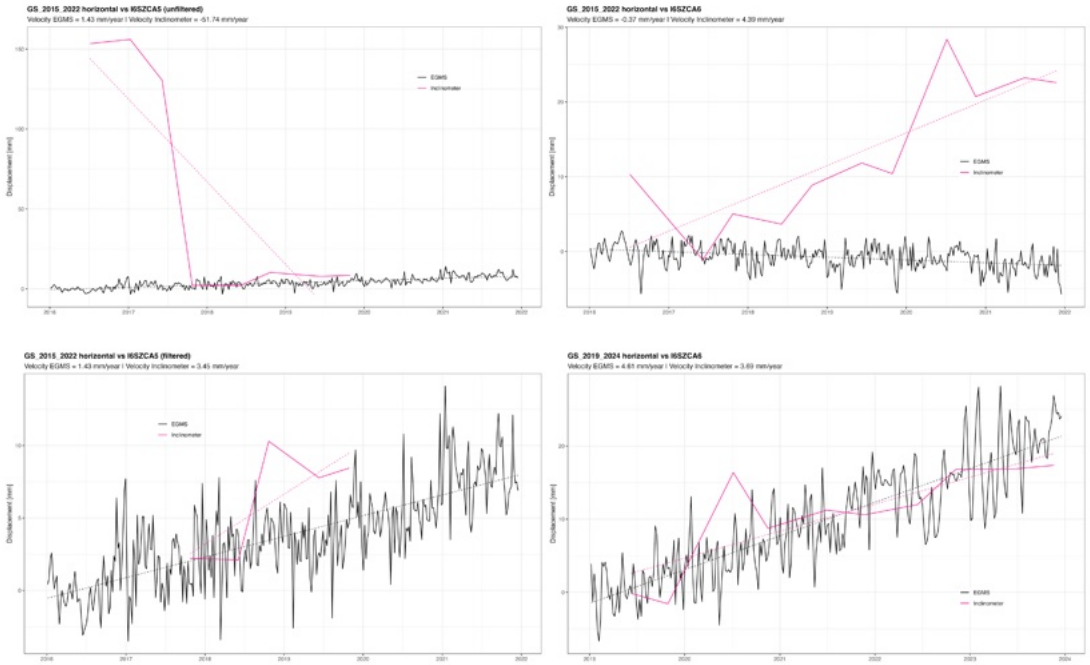


Figure A3. GS data validation 3

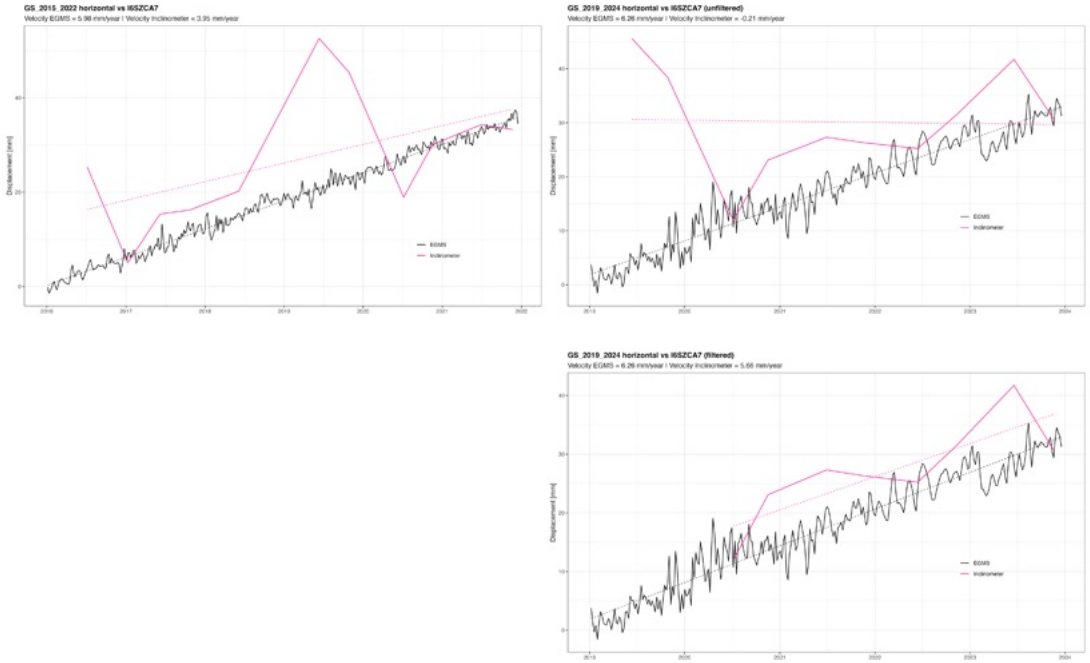


Figure A4. GS data validation 4

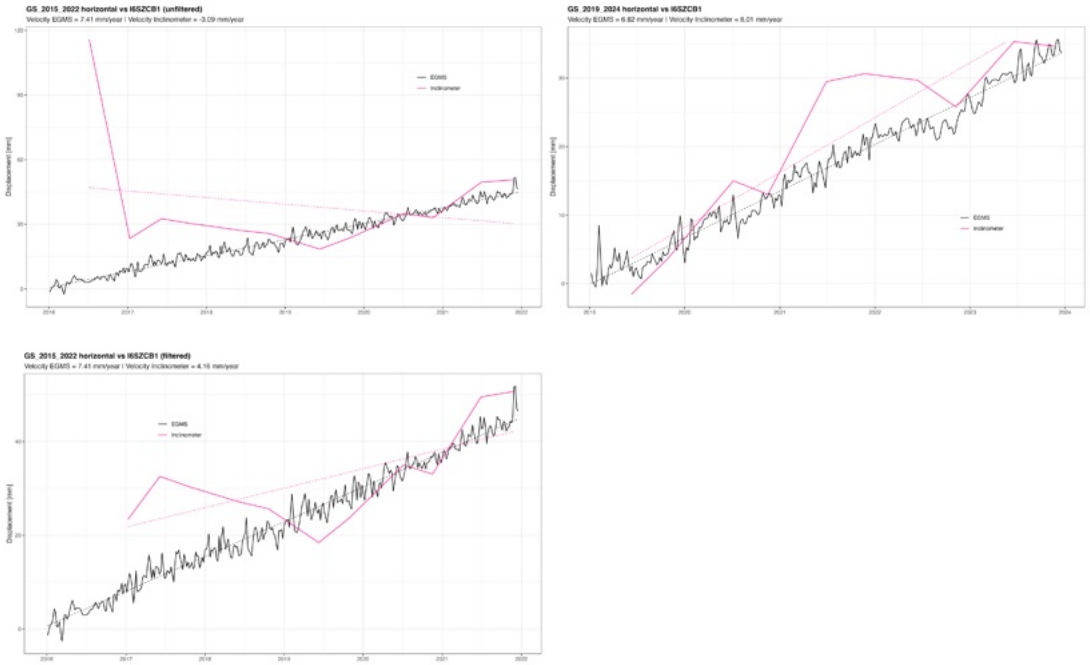


Figure A5. GS data validation 5

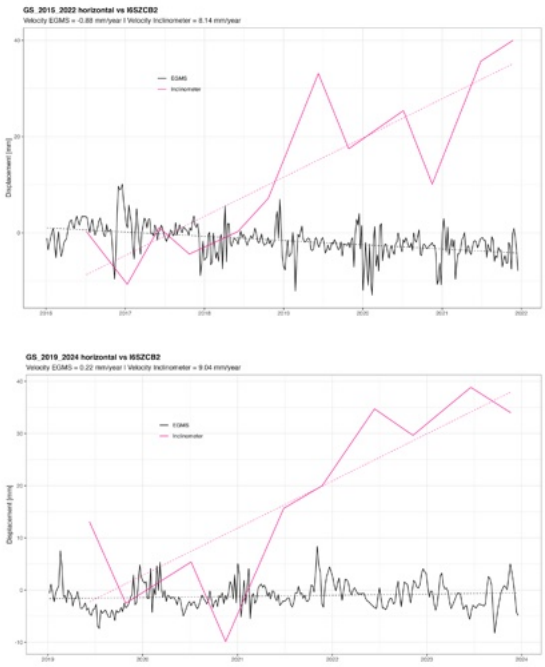


Figure A6. GS data validation 6

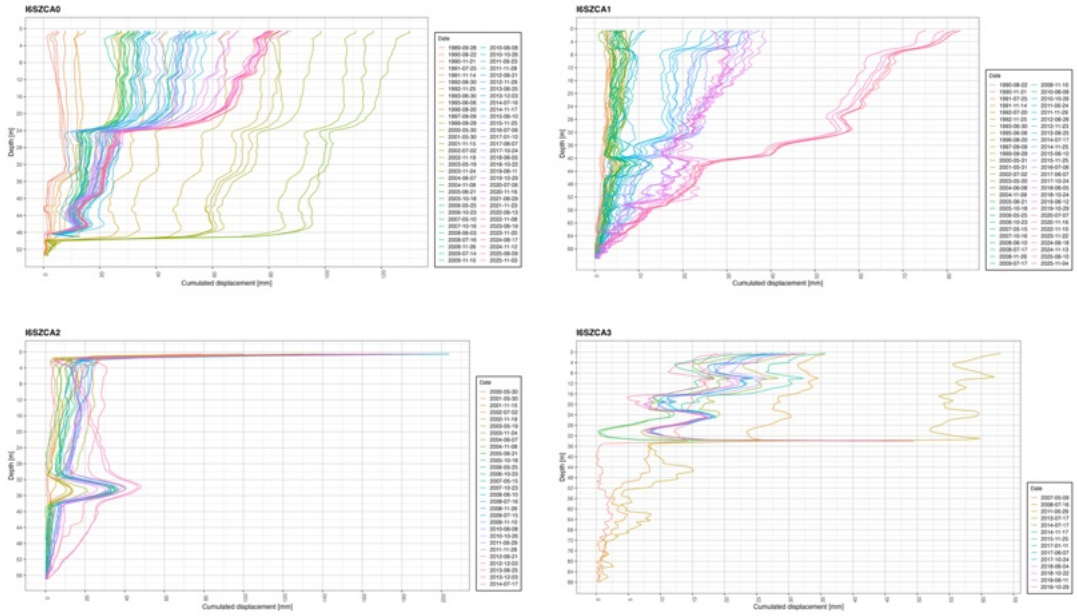


Figure A7. GS manual inclinometers 1

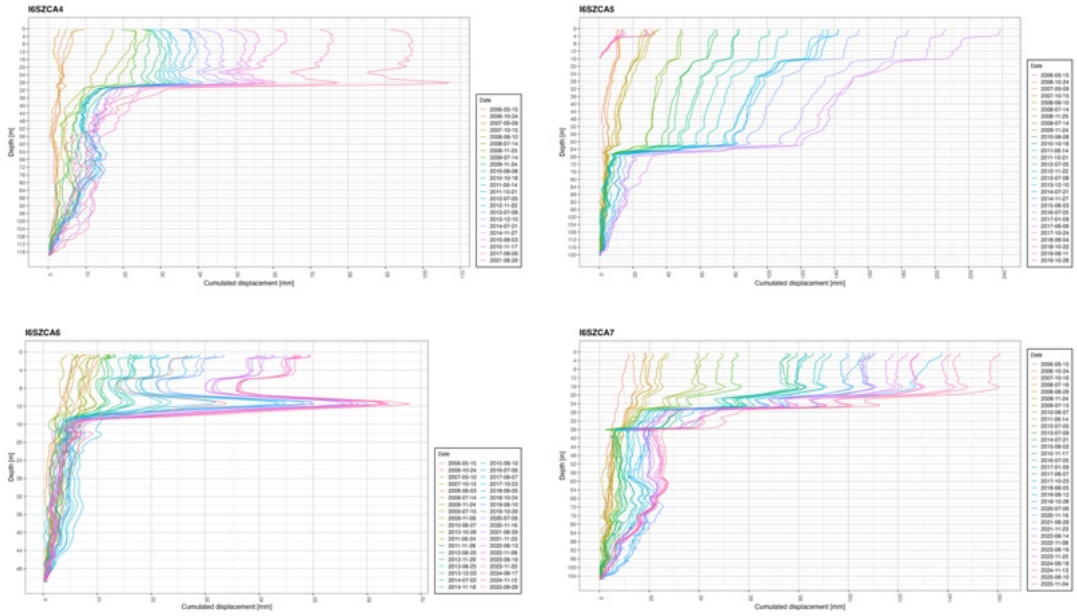


Figure A8. GS manual inclinometers 2

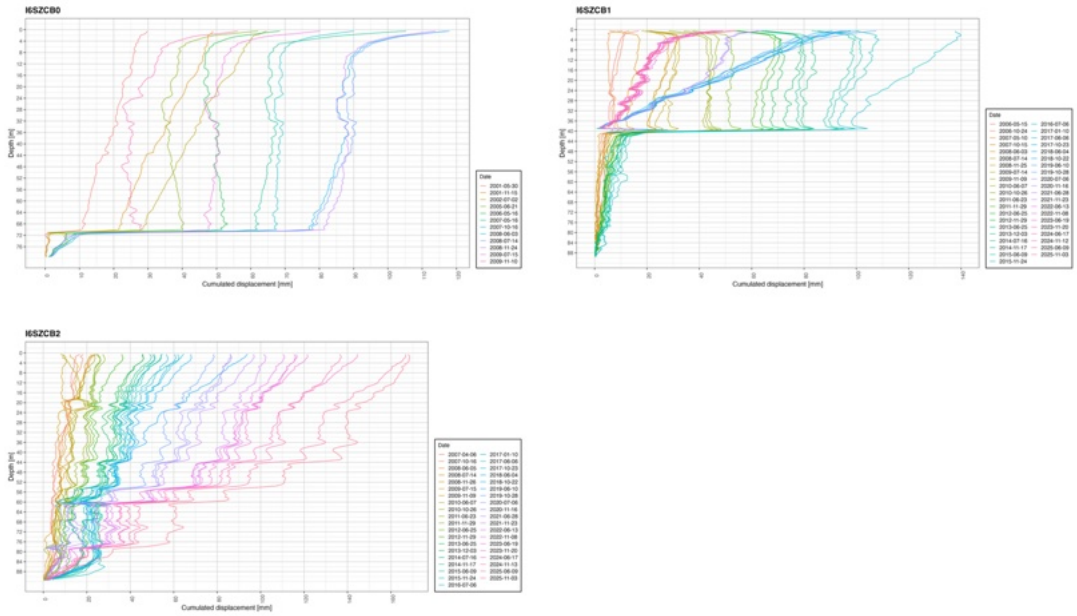


Figure A9. GS manual inclinometers 3

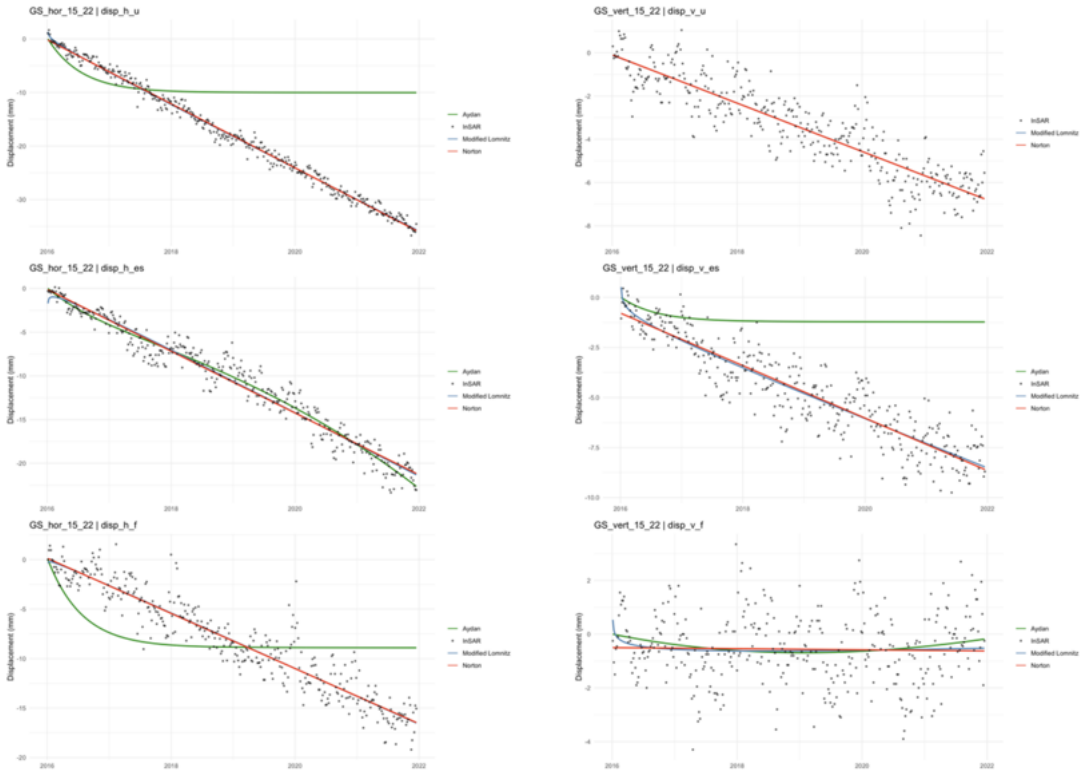


Figure A10. GS creep models 1

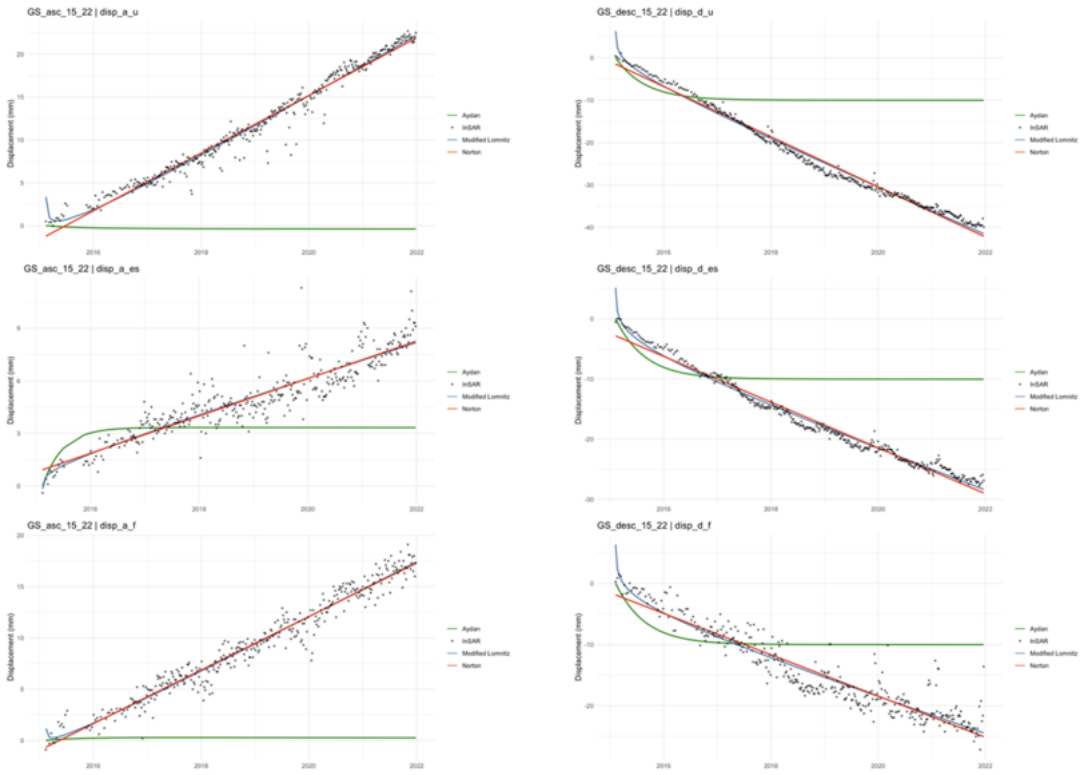


Figure A11. GS creep models 2

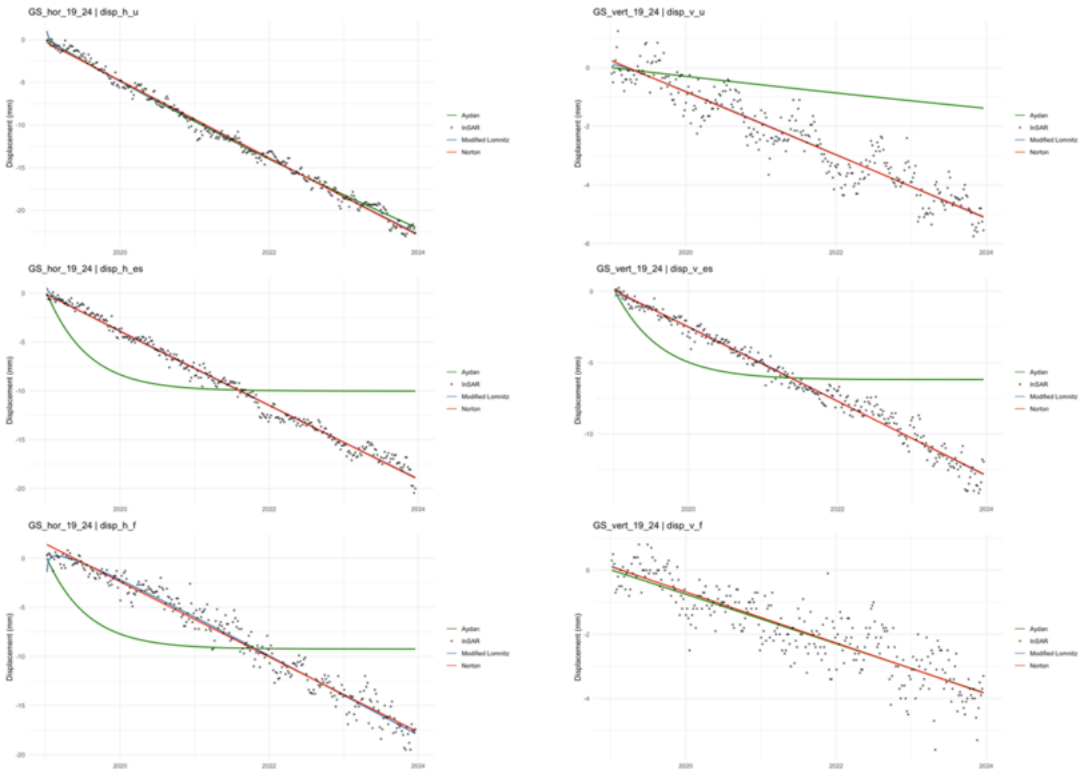


Figure A12. GS creep models 3

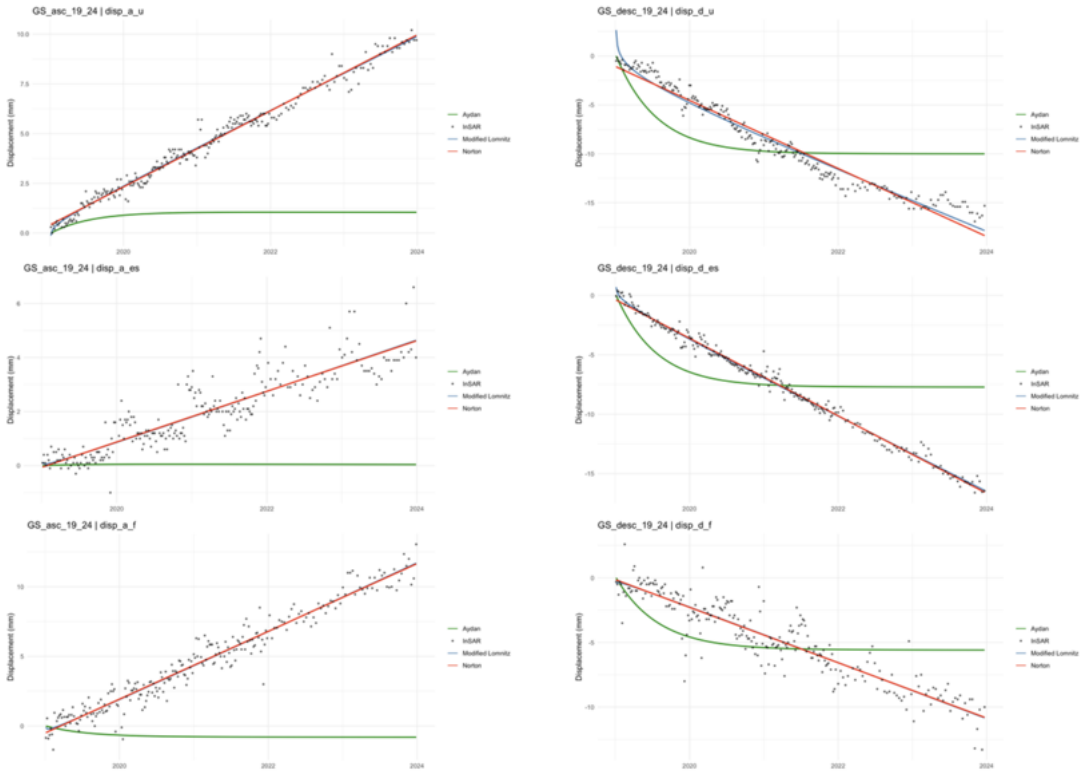


Figure A13. GS creep models 4

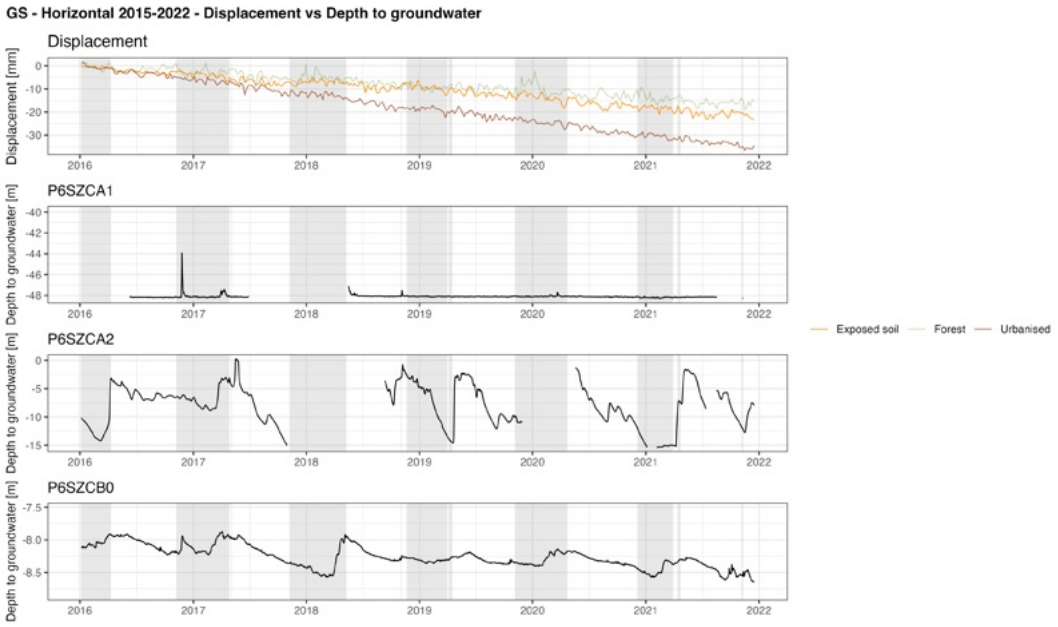


Figure A14. GS triggers 1

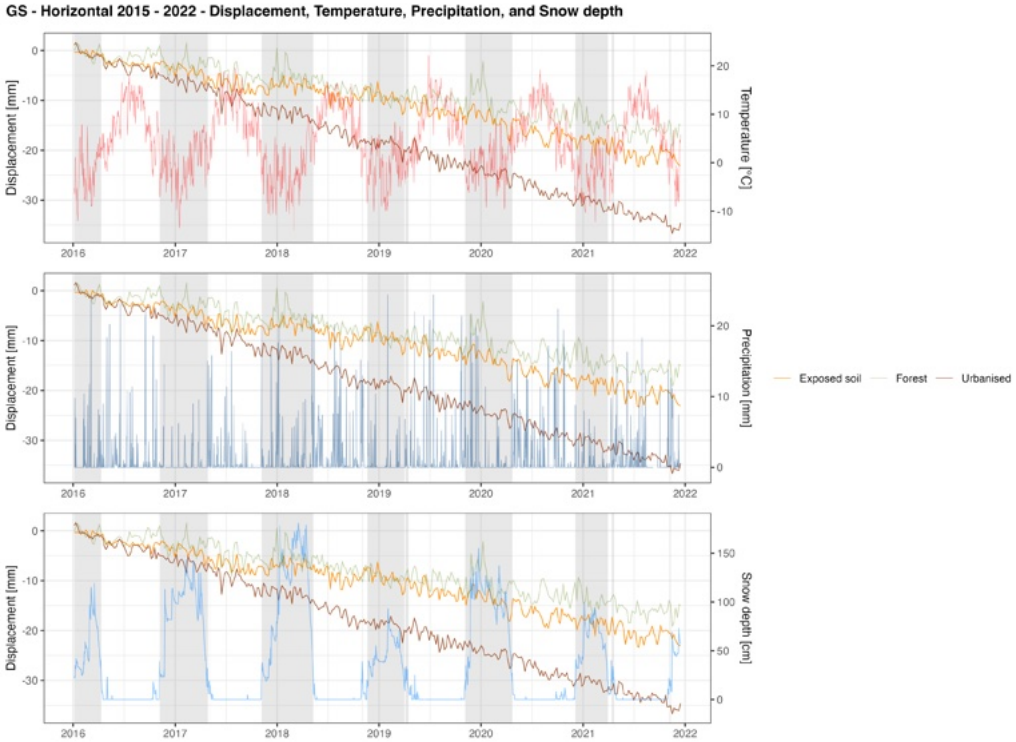


Figure A15. GS triggers 2

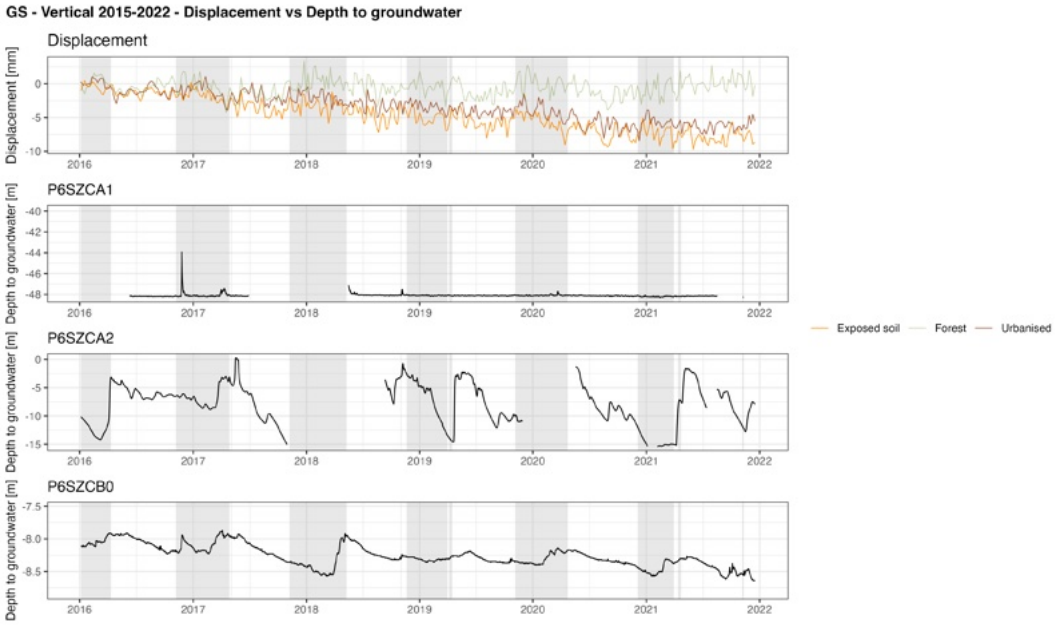


Figure A16. GS triggers 3

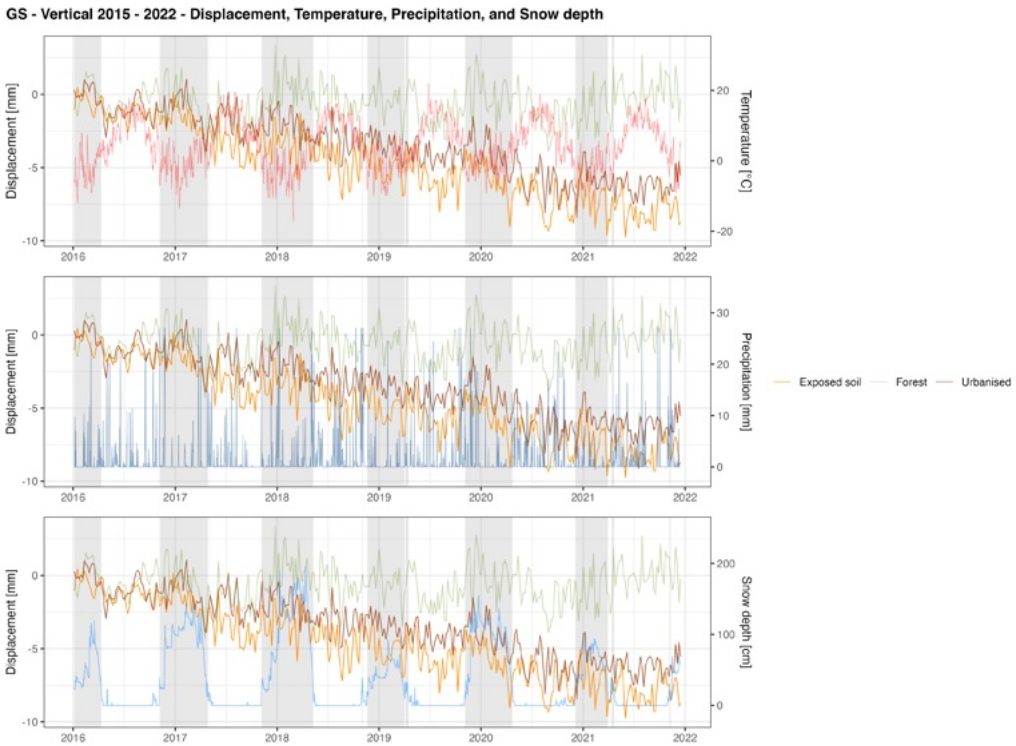


Figure A17. GS triggers 4

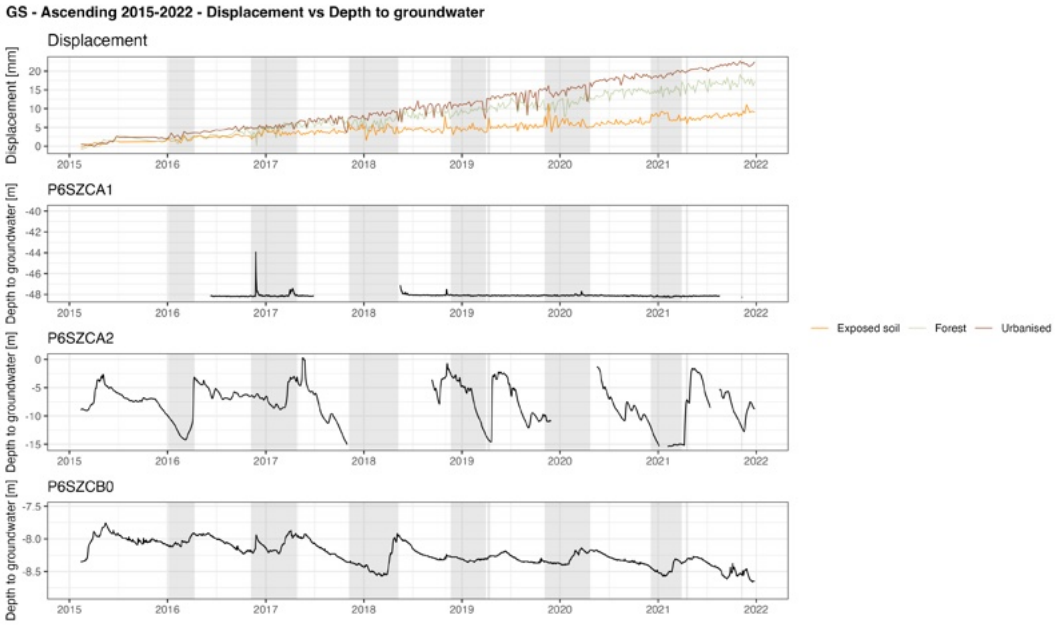


Figure A18. GS triggers 5

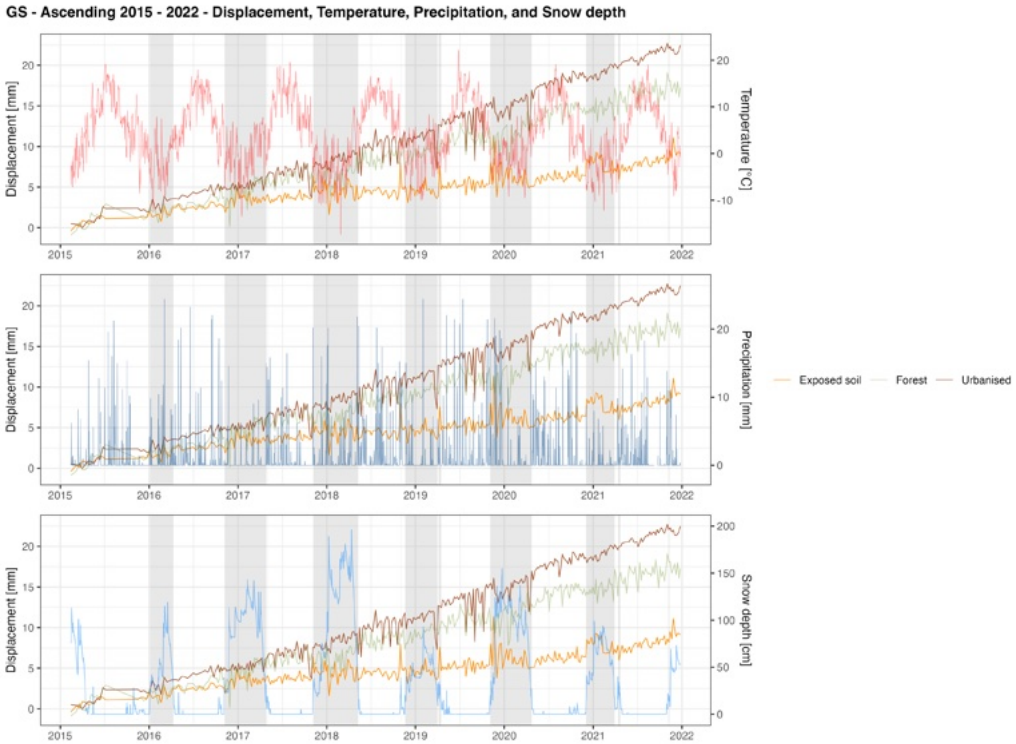


Figure A19. GS triggers 6

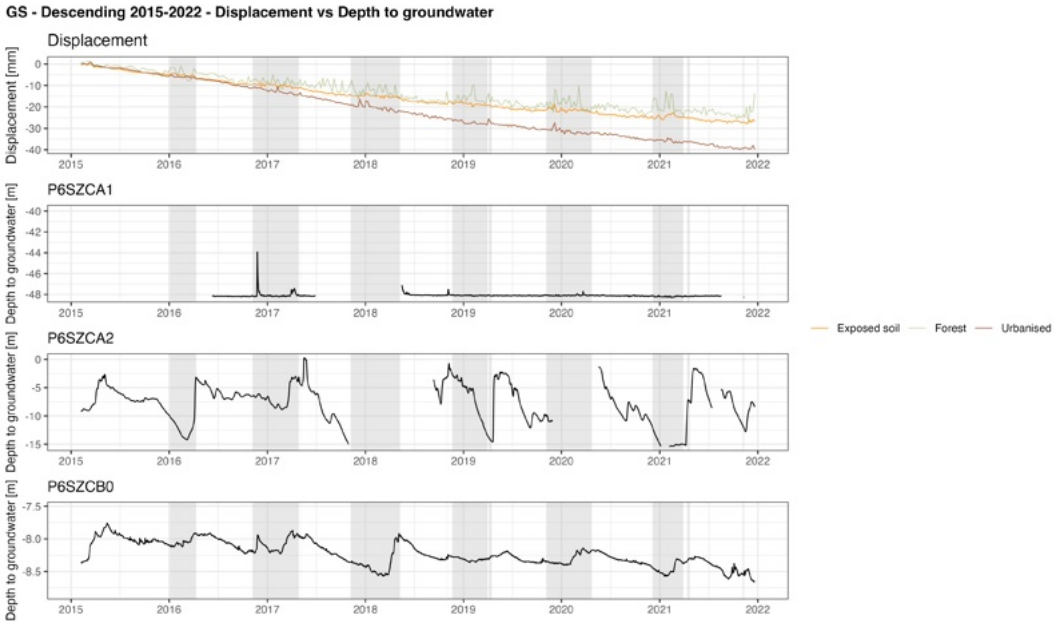


Figure A20. GS triggers 7

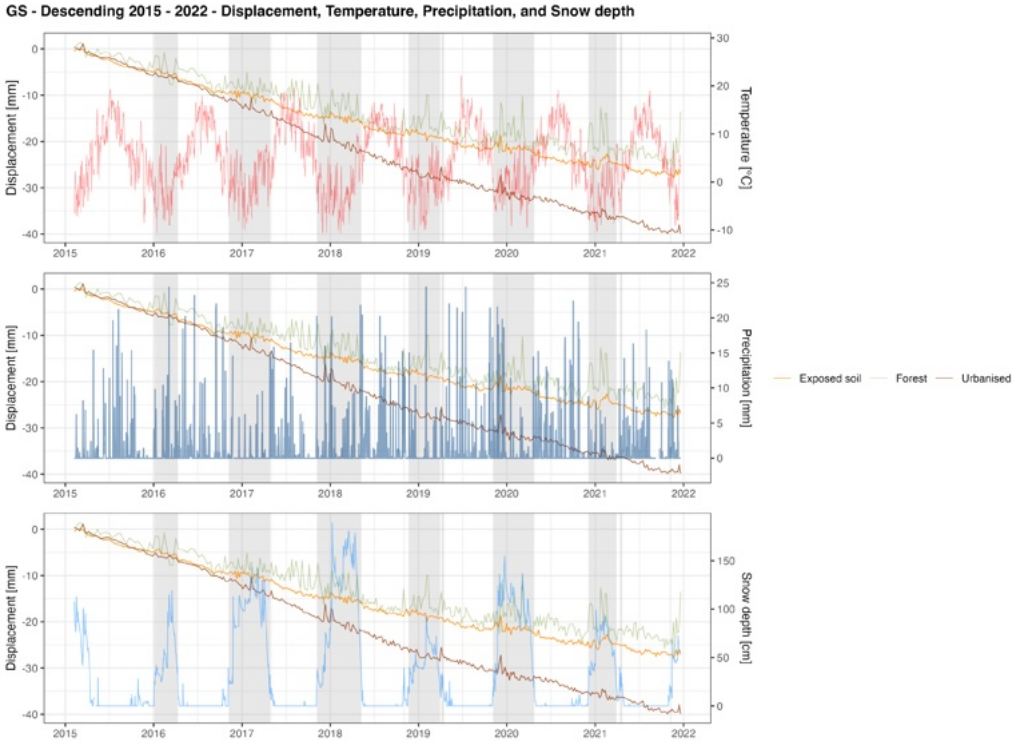


Figure A21. GS triggers 8

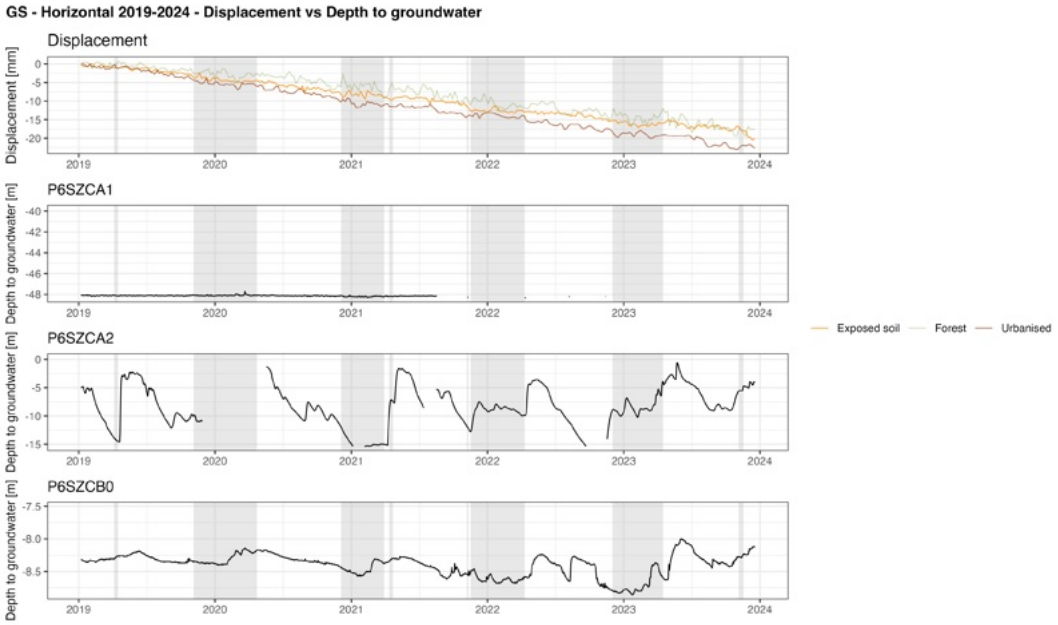


Figure A22. GS triggers 9

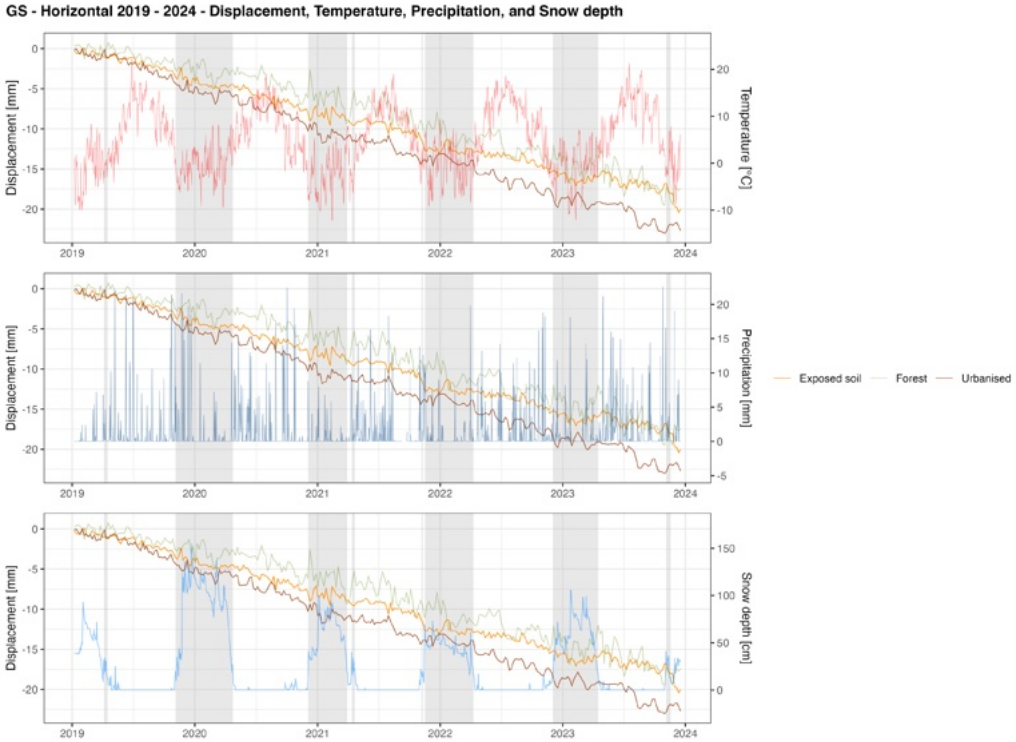


Figure A23. GS triggers 10

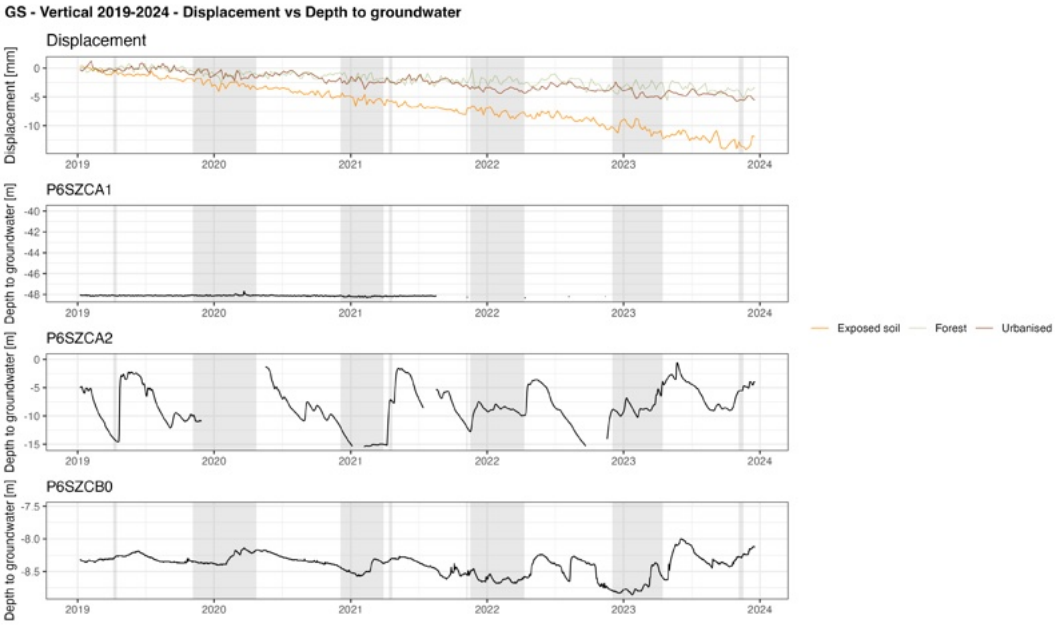


Figure A24. GS triggers 11

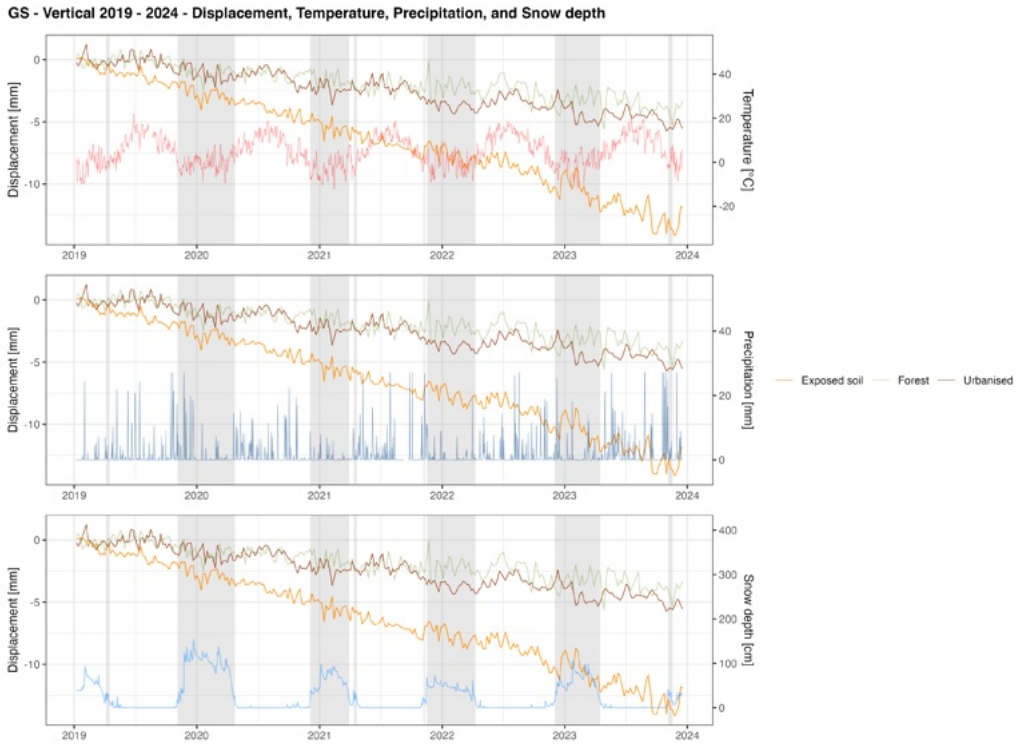


Figure A25. GS triggers 12

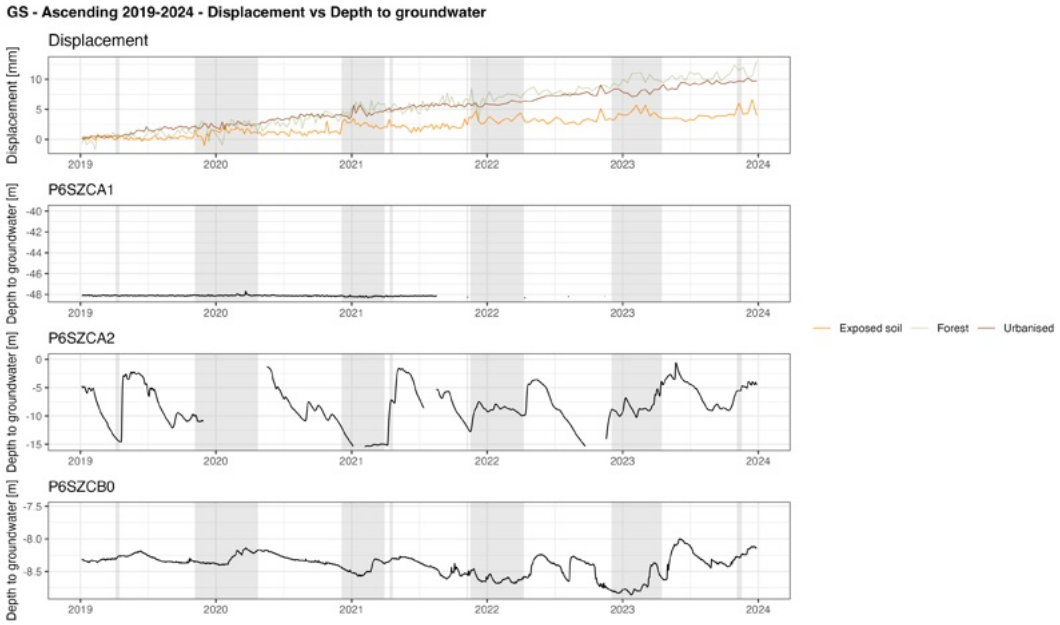


Figure A26. GS triggers 13

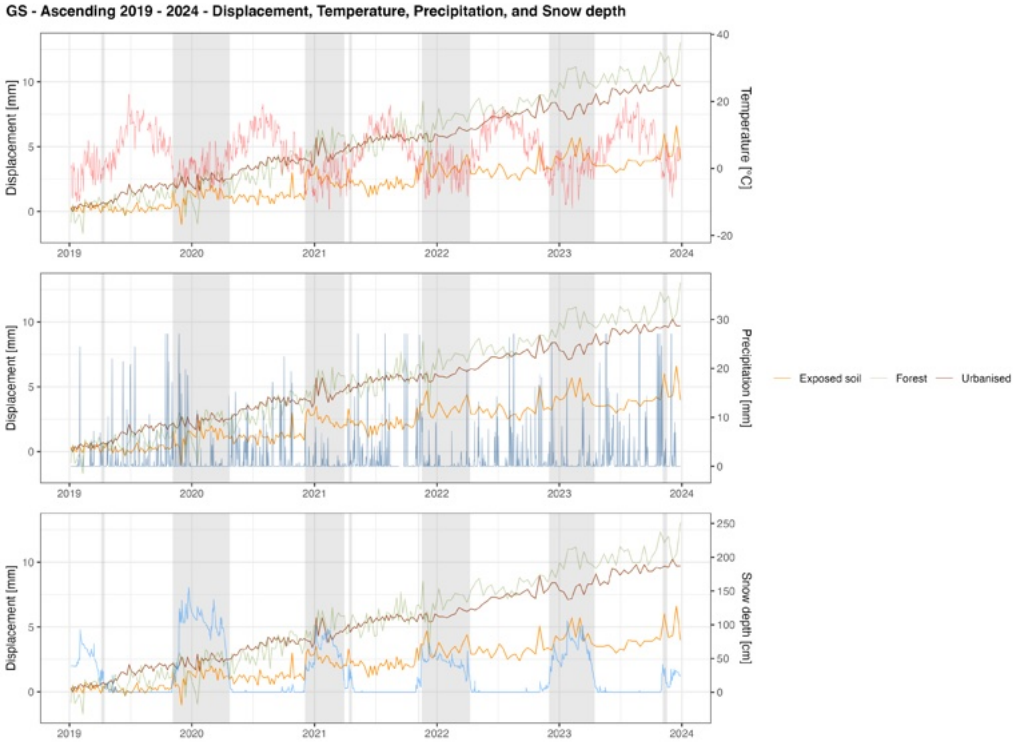


Figure A27. GS triggers 14

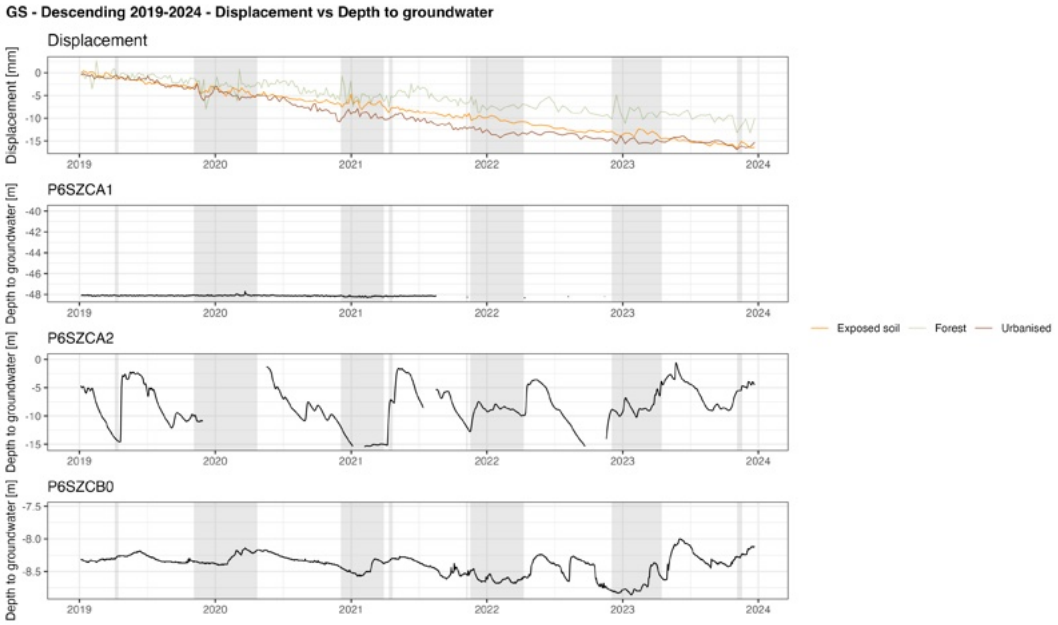


Figure A28. GS triggers 15

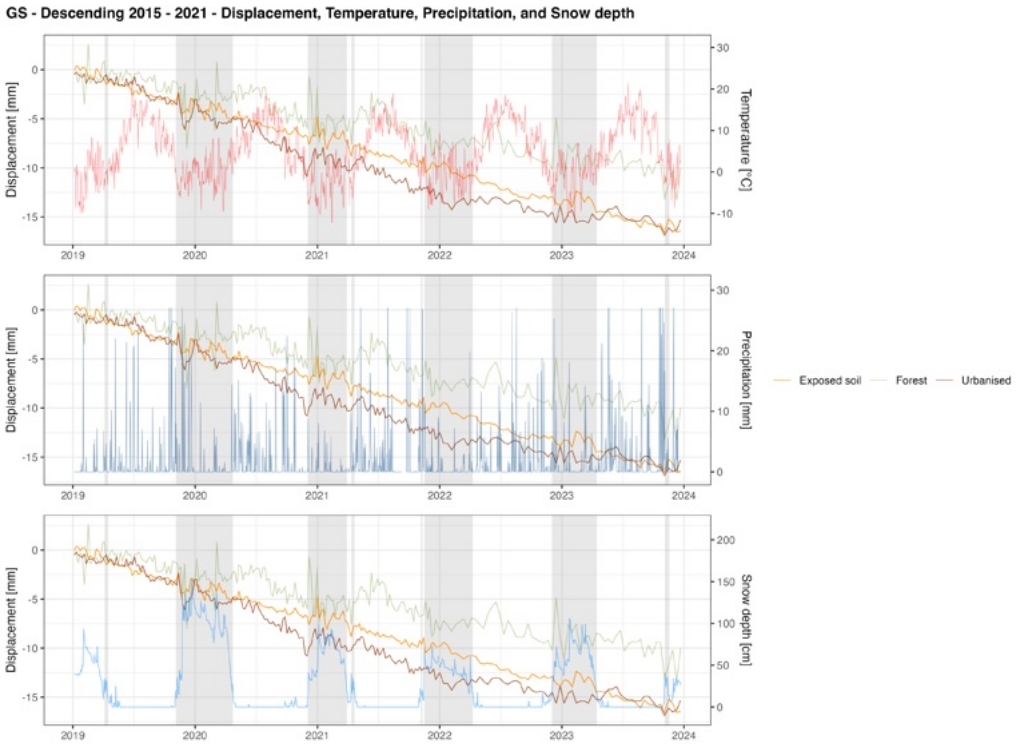


Figure A29. GS triggers 16

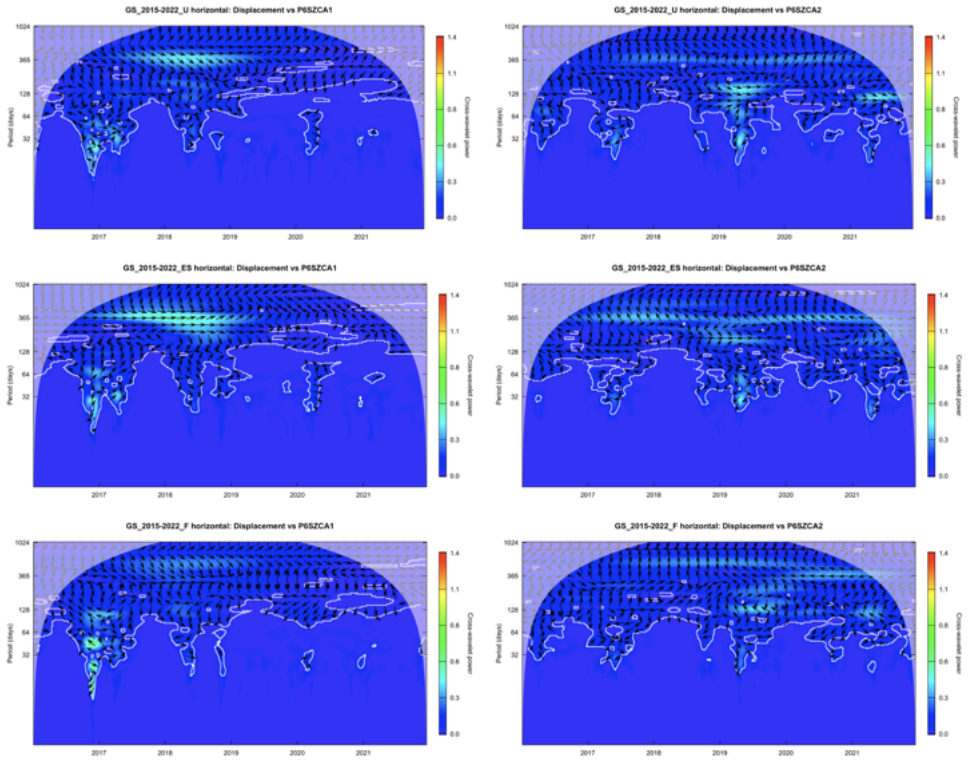


Figure A30. GS wavelet analysis 1

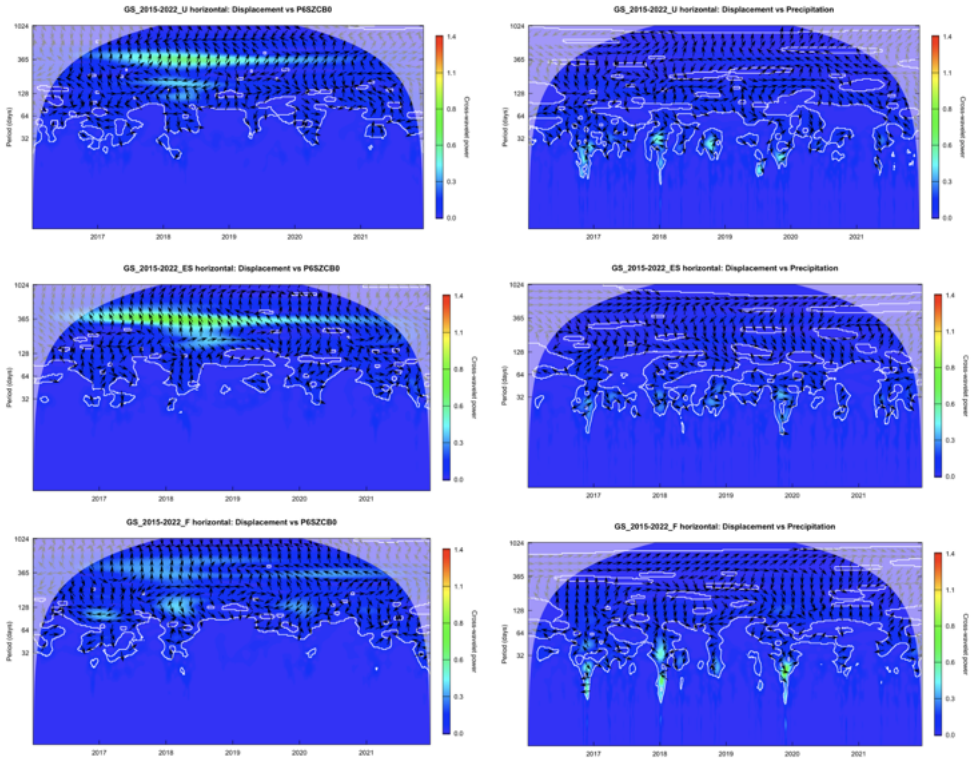


Figure A31. GS wavelet analysis 2

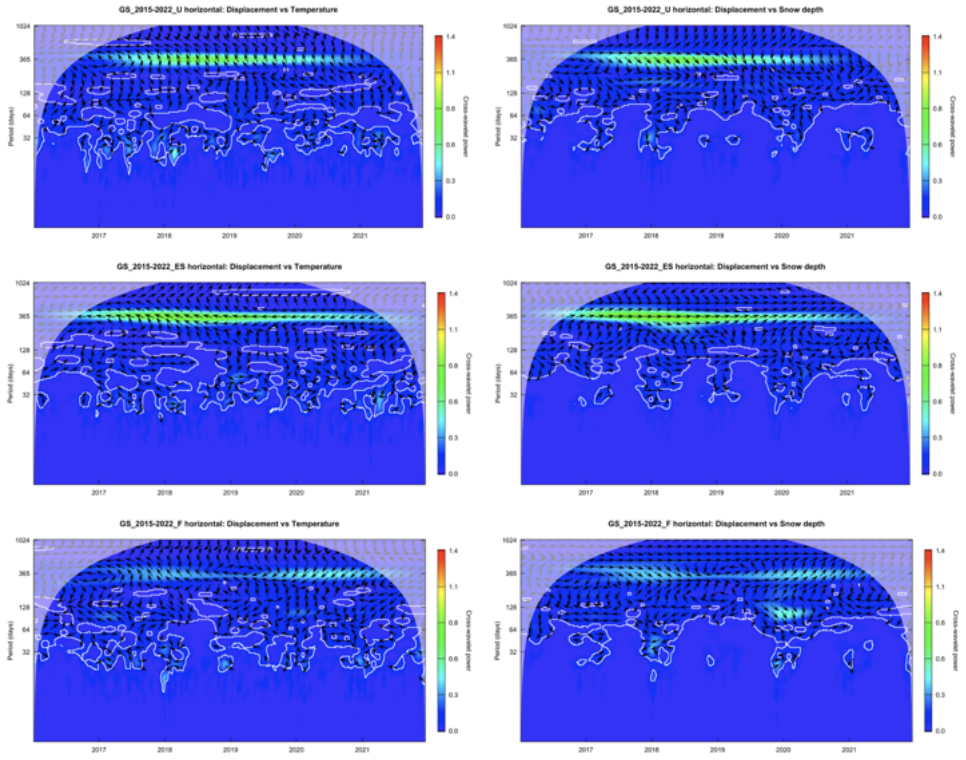


Figure A32. GS wavelet analysis 3

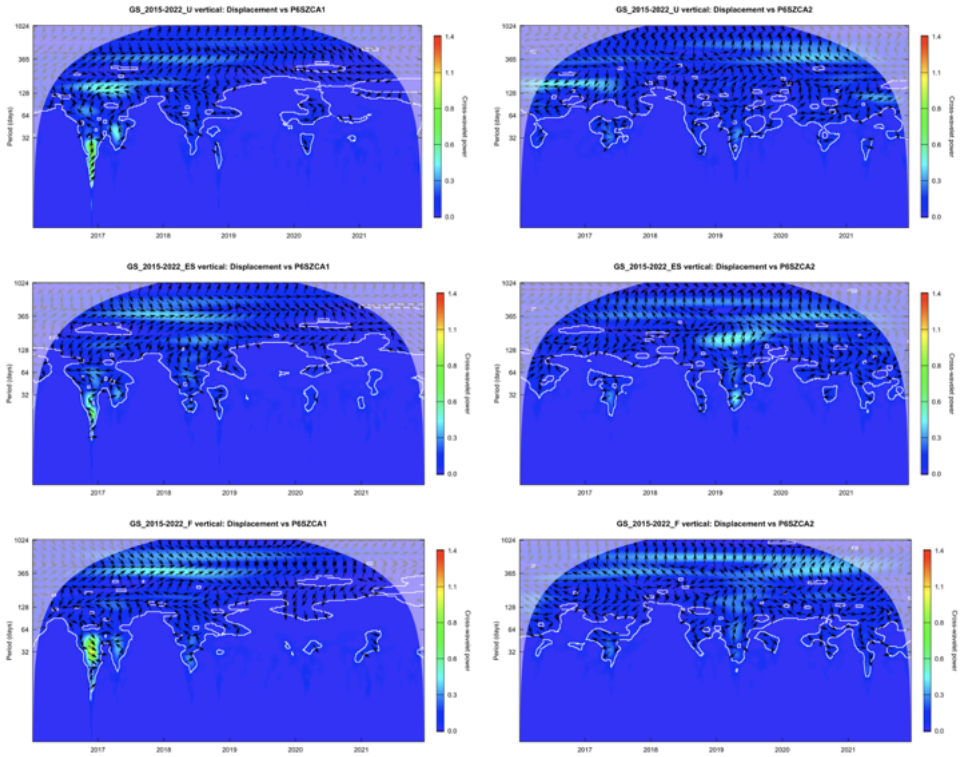


Figure A33. GS wavelet analysis 4

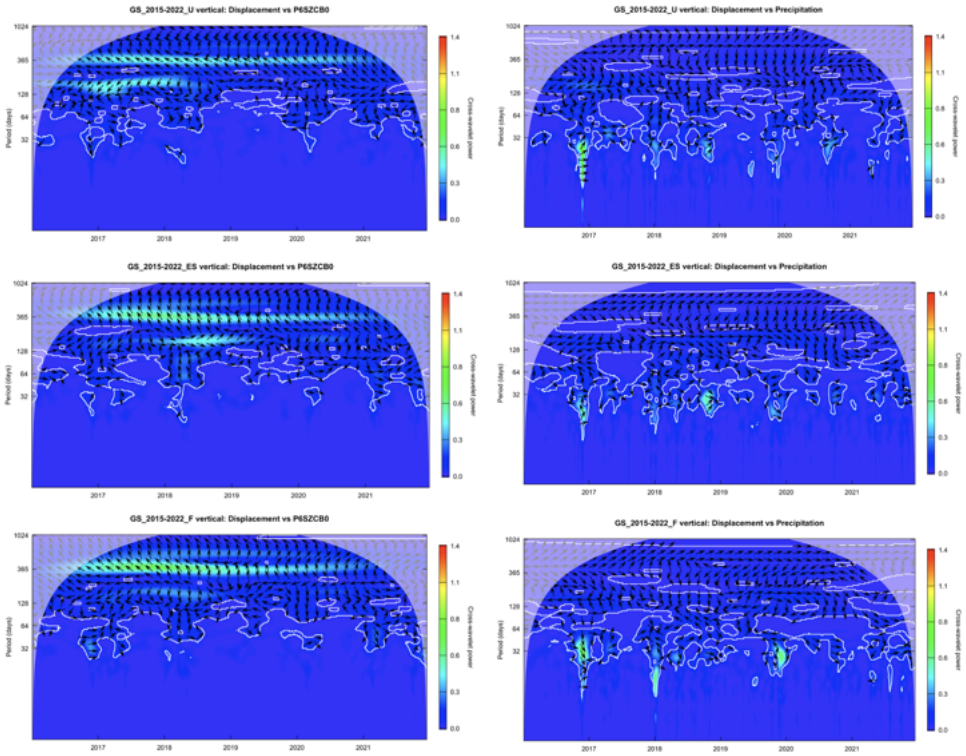


Figure A34. GS wavelet analysis 5

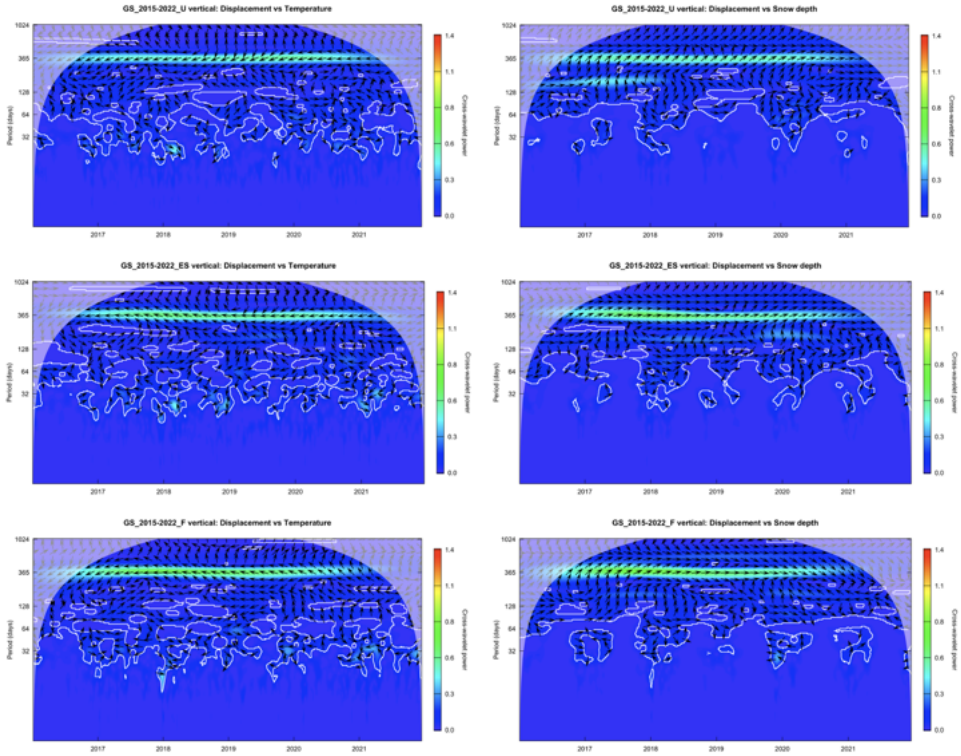


Figure A35. GS wavelet analysis 6

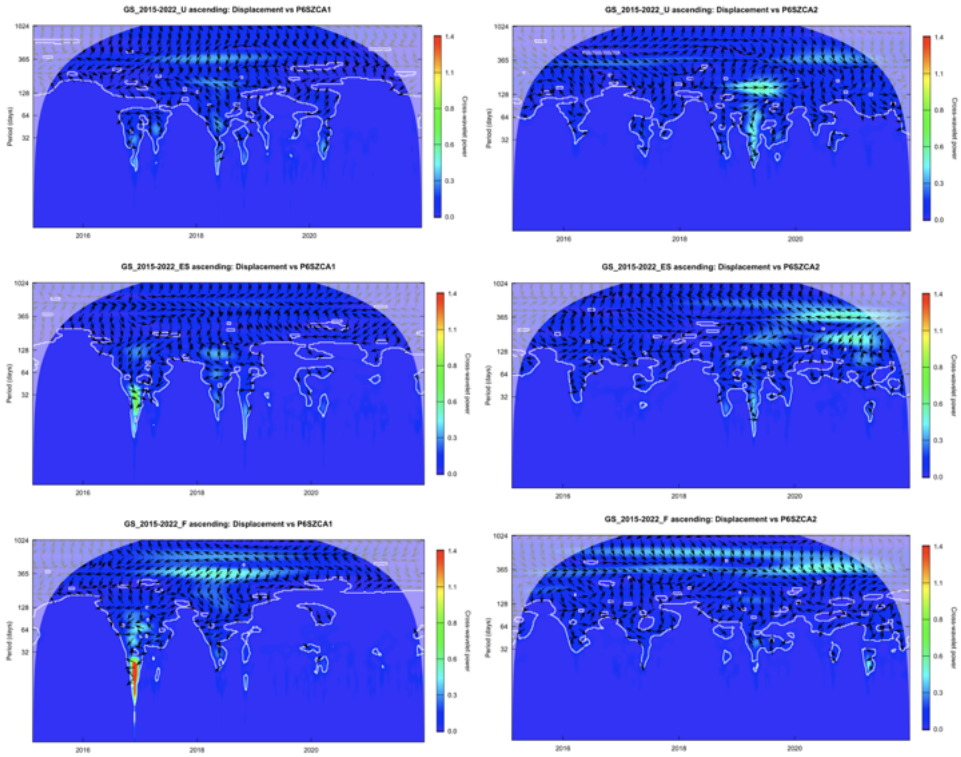


Figure A36. GS wavelet analysis 7

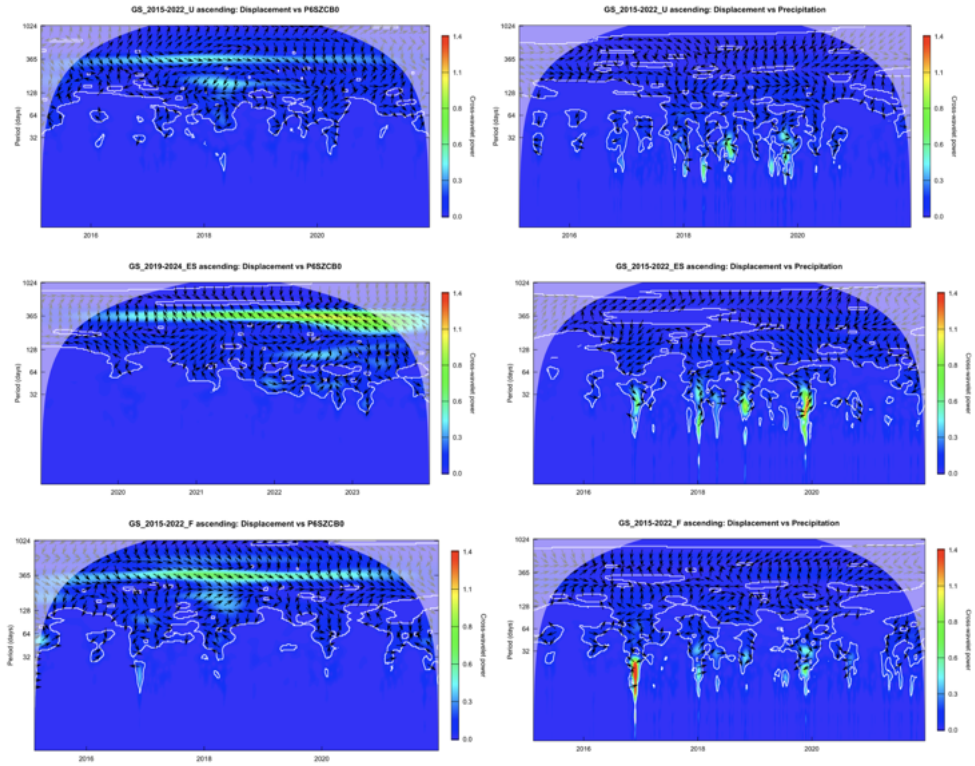


Figure A37. GS wavelet analysis 8

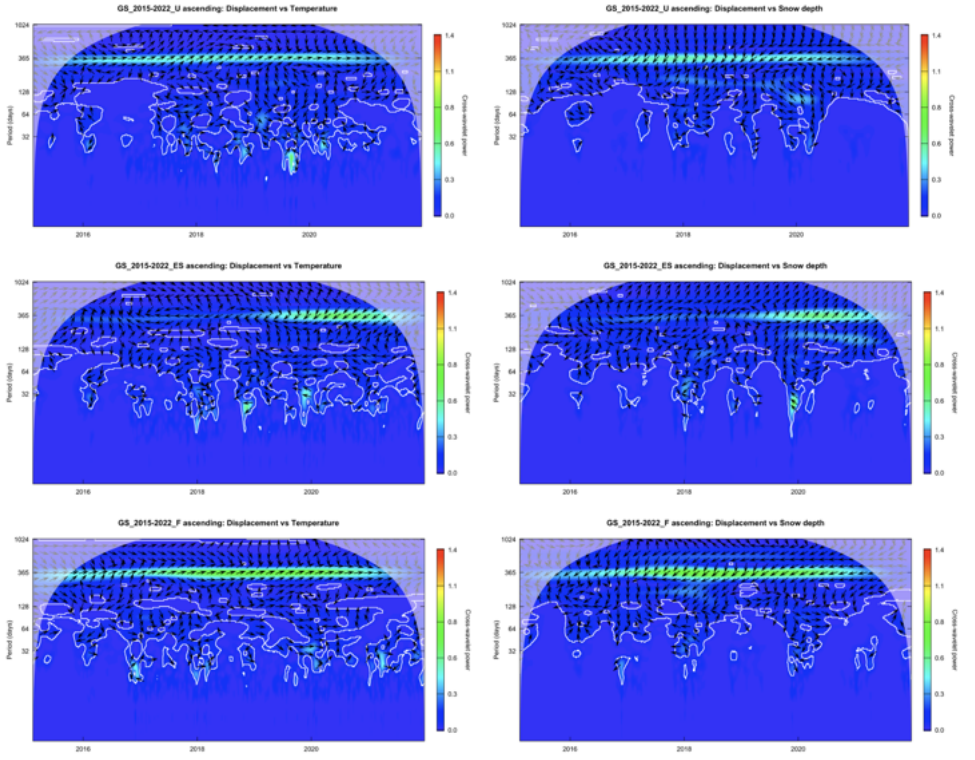


Figure A38. GS wavelet analysis 9

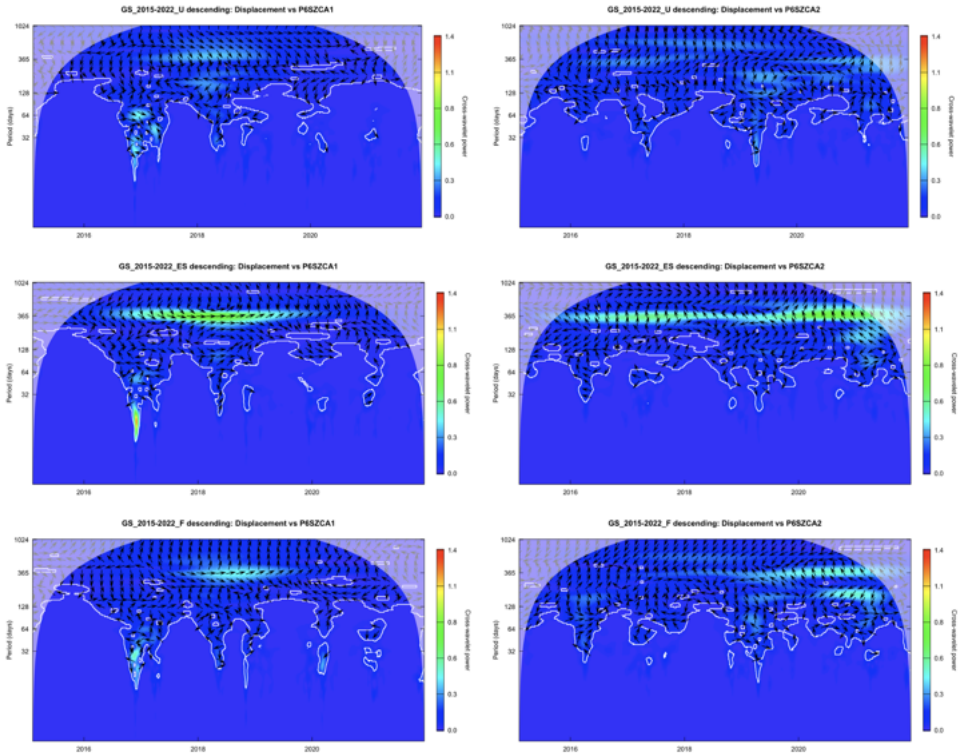


Figure A39. GS wavelet analysis 10

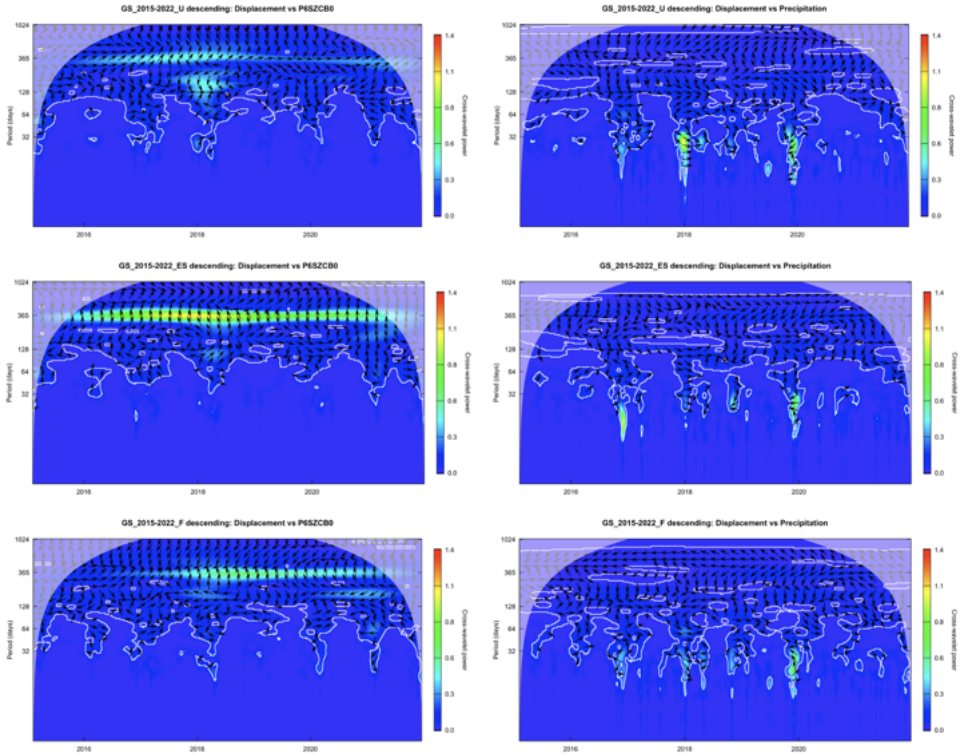


Figure A40. GS wavelet analysis 11

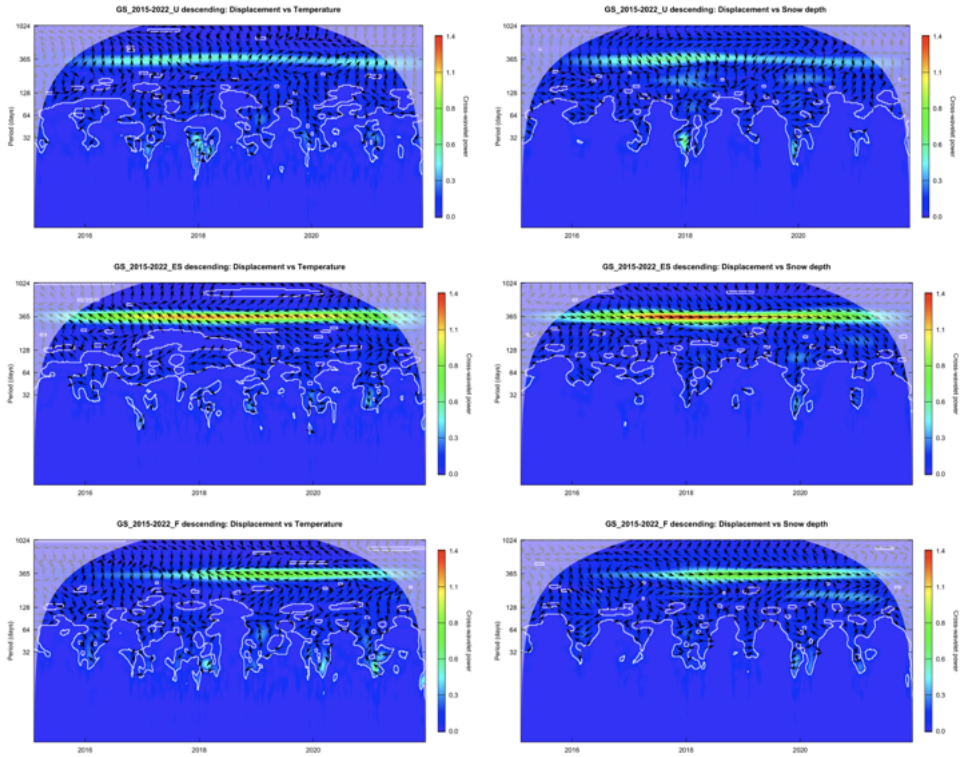


Figure A41. GS wavelet analysis 12

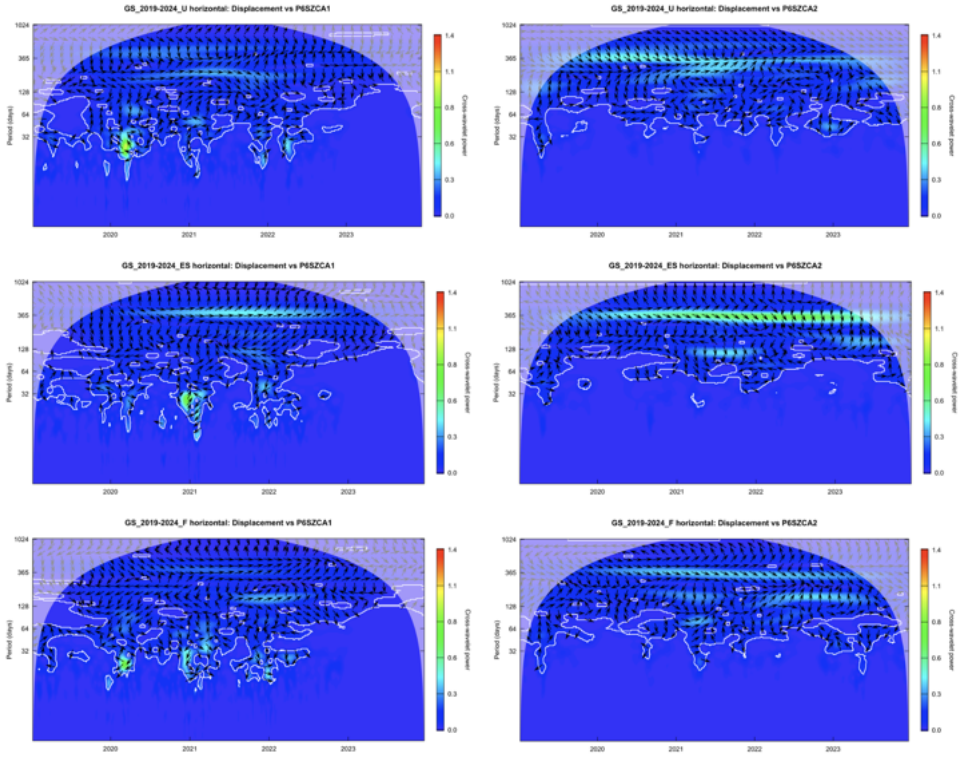


Figure A42. GS wavelet analysis 13

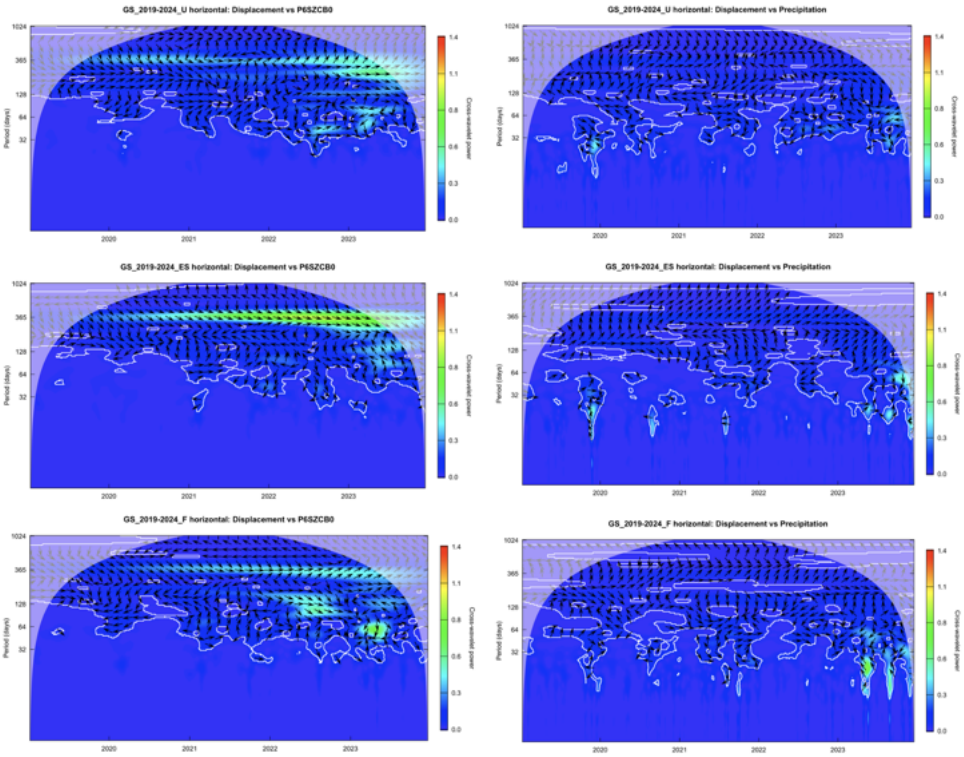


Figure A43. GS wavelet analysis 14

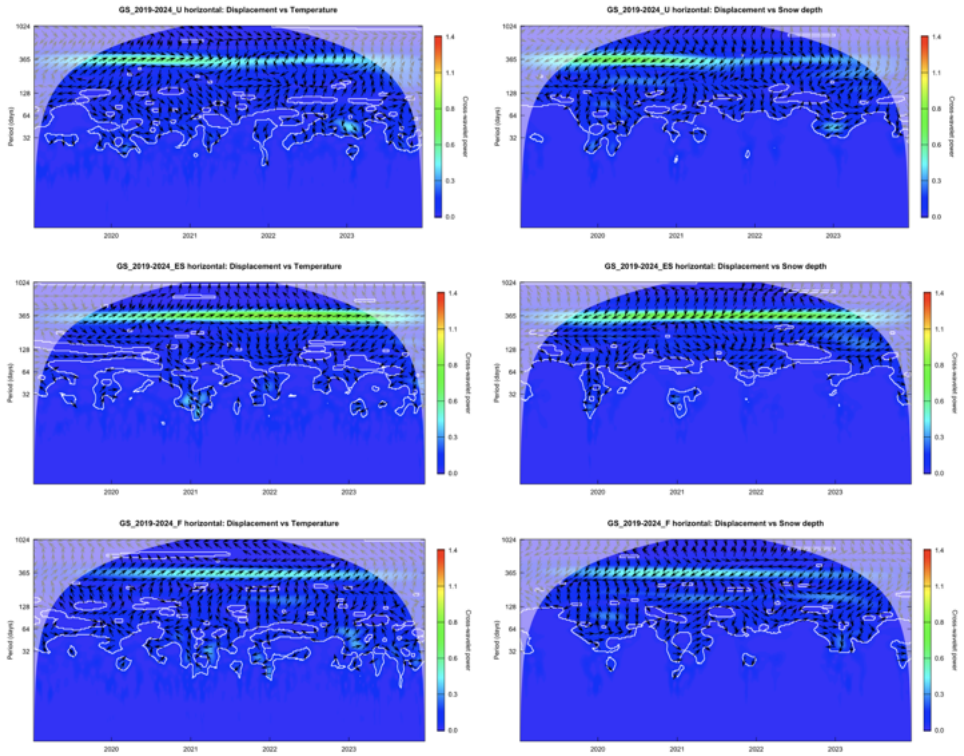


Figure A44. GS wavelet analysis 15

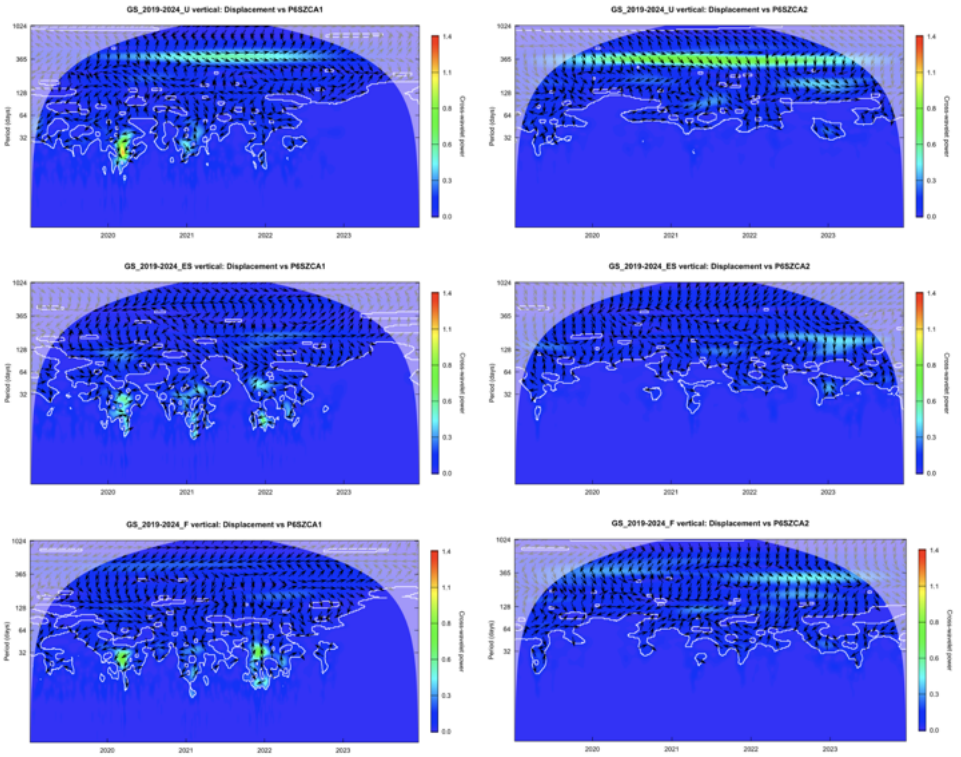


Figure A45. GS wavelet analysis 16

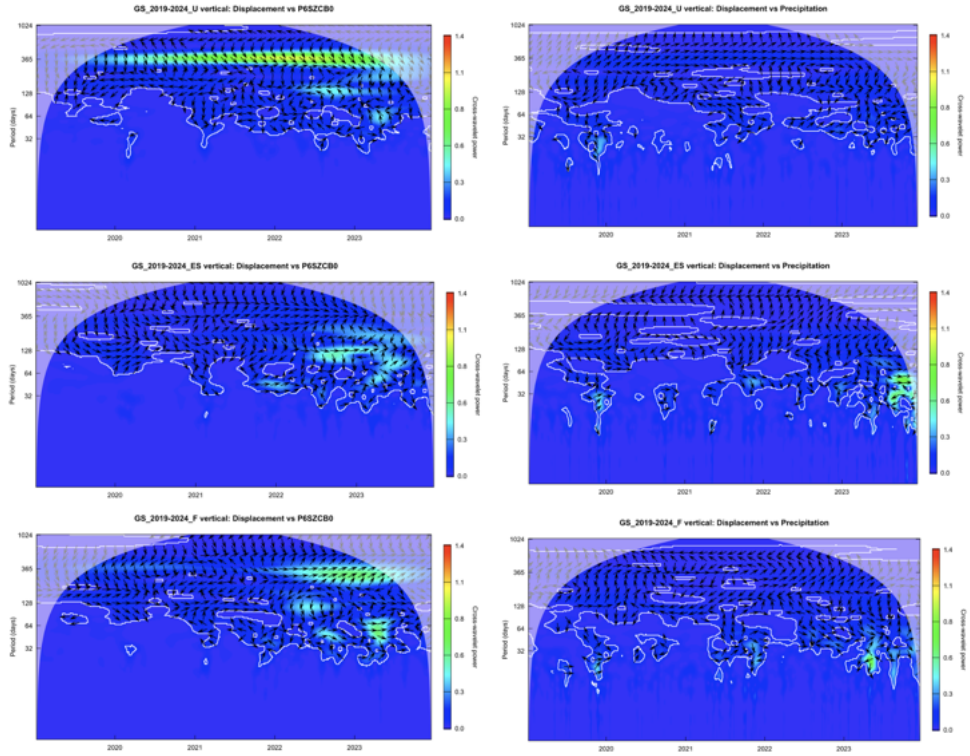


Figure A46. GS wavelet analysis 17

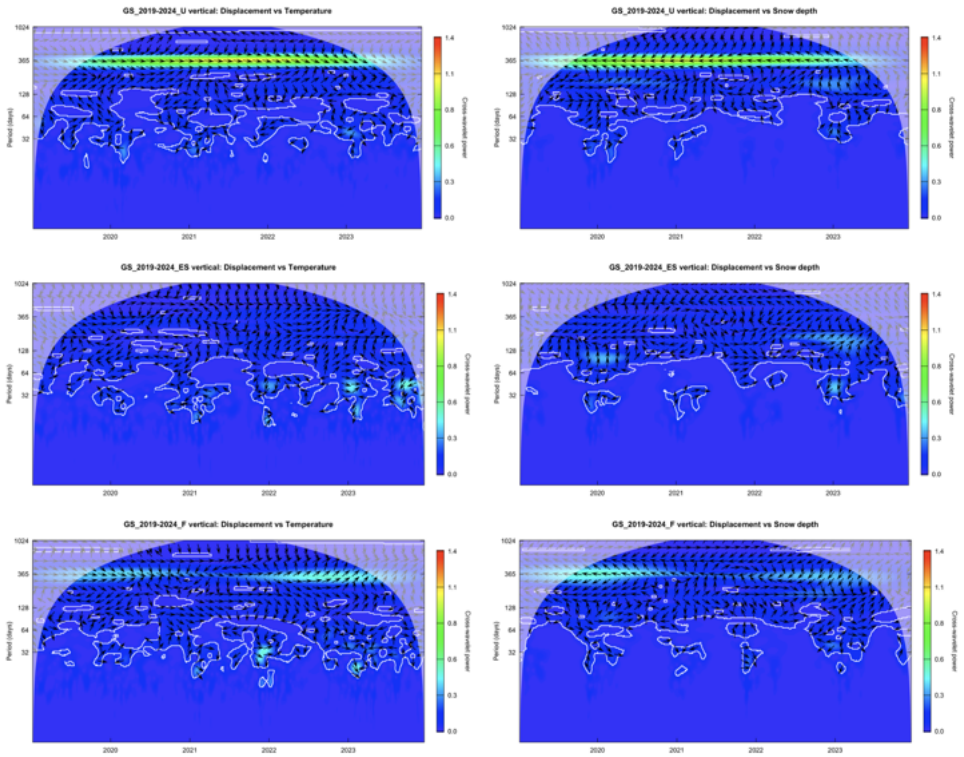


Figure A47. GS wavelet analysis 18

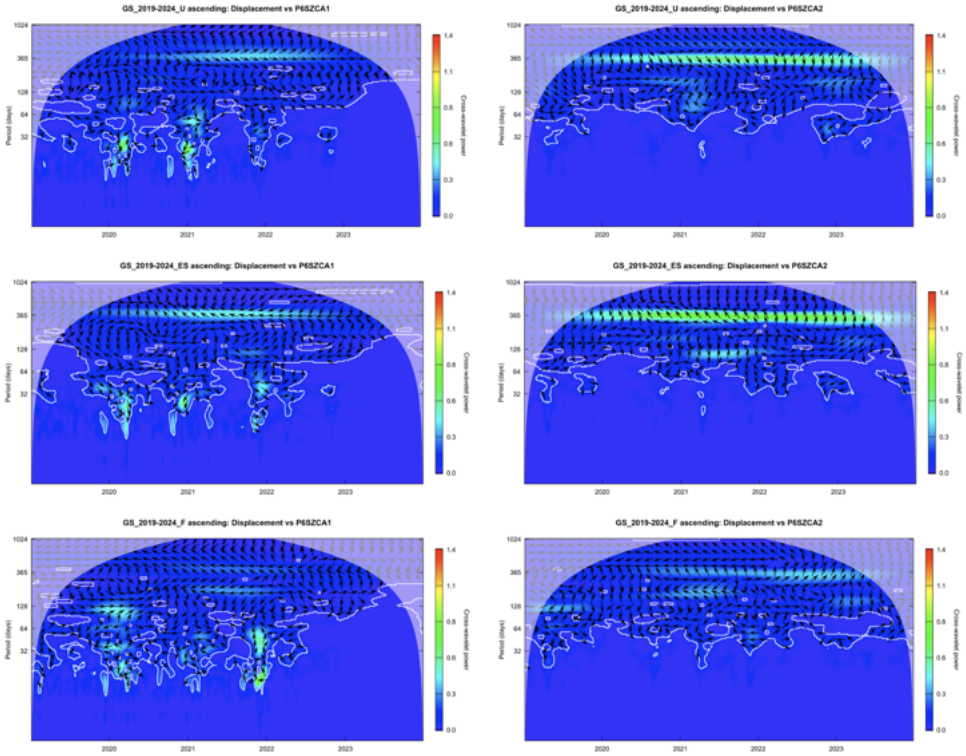


Figure A48. GS wavelet analysis 19

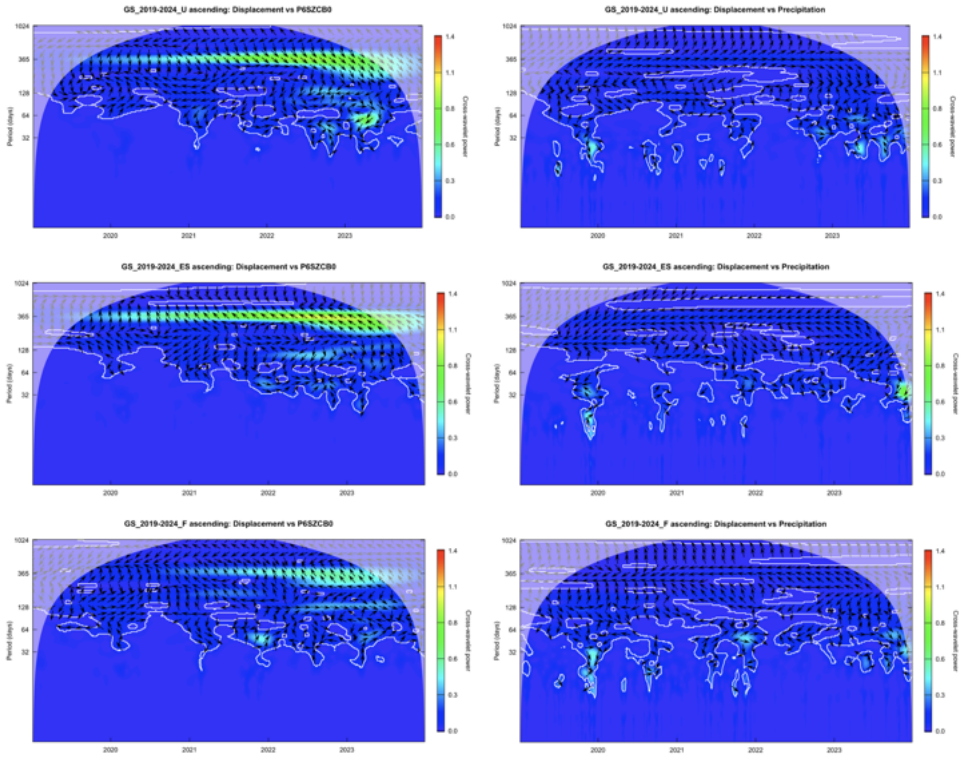


Figure A49. GS wavelet analysis 20

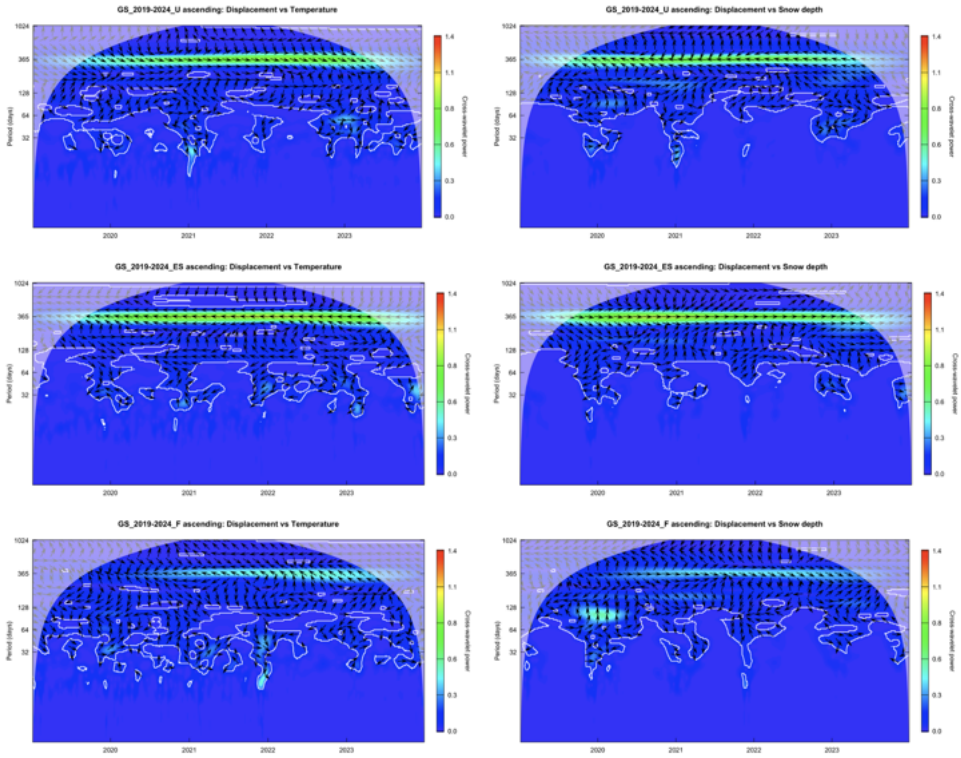


Figure A50. GS wavelet analysis 21

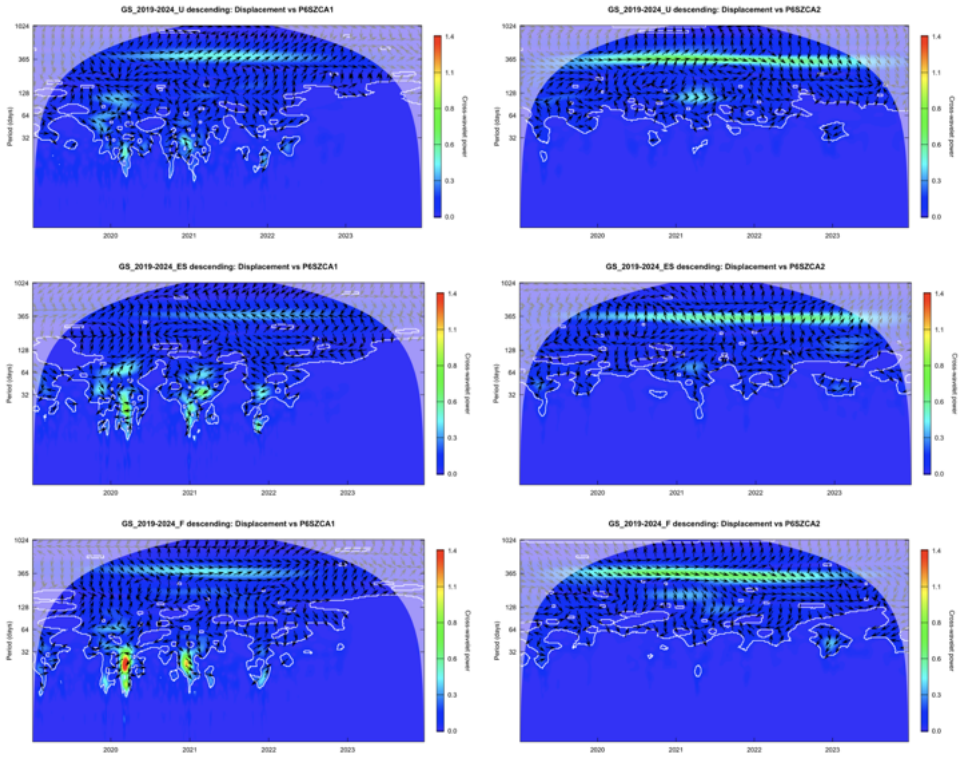


Figure A51. GS wavelet analysis 22

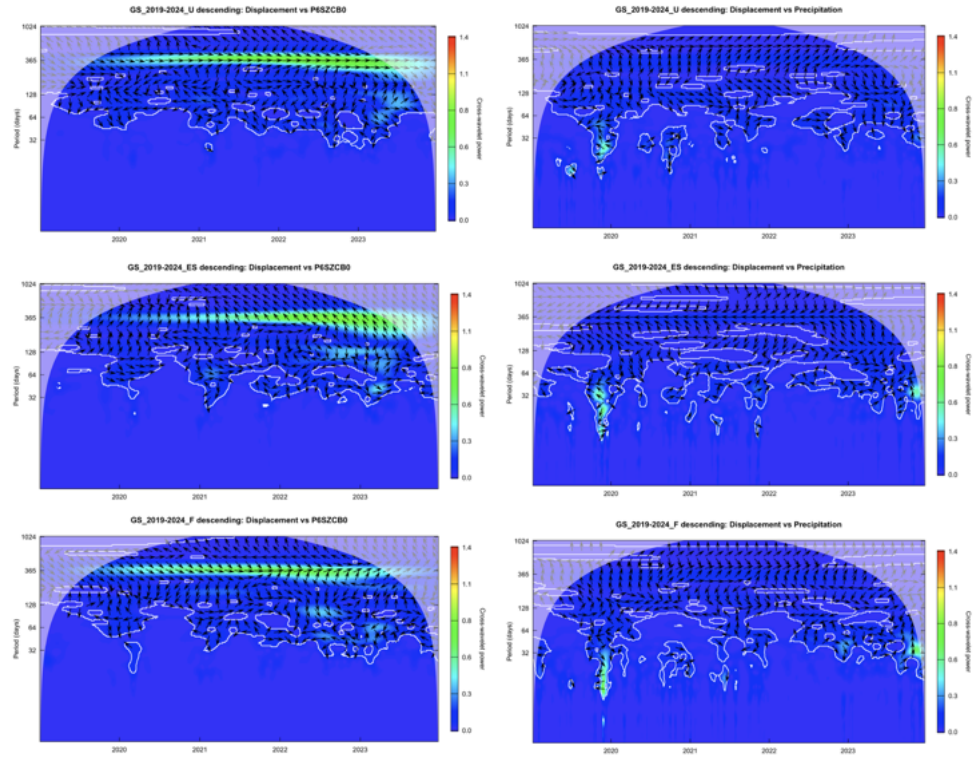


Figure A52. GS wavelet analysis 23

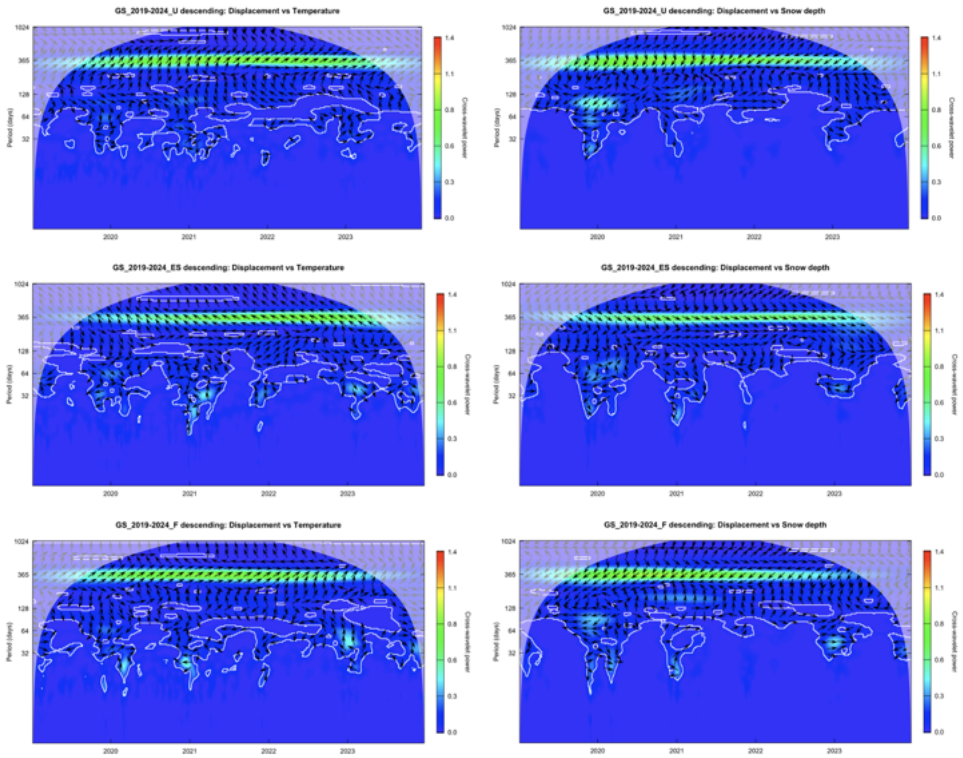


Figure A53. GS wavelet analysis 24

Table A1. GS 2015-2022 wavelet analysis: periods, phase angles, and phase delays

		2015_2022_H			**2015_2022_V**			**2015_2022_A**			**2015_2022_D**		
		U	**ES**	**F**	**U**	**ES**	**F**	**U**	**ES**	**F**	**U**	**ES**	**F**
P6SZCA1	**Period 1**	365	365		130	64	32	32	32	365	32	365	32
	Period 2				365	365	365	365	128	500	365		365
	Period 3						400						
	Angle 1	20	0		165	180			20	140		180	
	Angle 2				315	350	335	120		200	60		180
	Angle 3						30						
	Delay 1	20	0		60	32			2	142		183	
	Delay 2				319	355	340	122		278	61		183
	Delay 3						33						
P6SZCA2	**Period 1**	32	32	110	130	130	365	365	365	365	365	365	200
	Period 2	128	140	365	365	365	400		400	500	500		365
	Period 3	365	365	400	400	400							
	Angle 1						215	20	185	15	330	260	
	Angle 2	20	0	200	200	235	270		240	65	255		230
	Angle 3	280	240	270	275	270							
	Delay 1						218	20	188	15	335	264	
	Delay 2	7	0	203	203	238	300		267	90	354		233
	Delay 3	284	243	300	306	300							
P6SZCB0	**Period 1**	365	365	128	130	130	365	365	365	365	365	365	150
	Period 2			365	365	365							365
	Angle 1	290	240				230	25	210	30	335	265	
	Angle 2			245	210	240							260
	Delay 1	294	243				233	25	213	30	340	269	
	Delay 2			248	213	243							264
Precipitation	**Period**	20	32	20	20	20	20	32	32	32	20	20	20
	Angle												
	Delay												
Temperature	**Period 1**	20	365	20	365	20	365	32	32	30	32	365	365
	Period 2	365		365		365		365	365	365	365		
	Angle 1		180		170		180		180			210	200
	Angle 2	255		180		180		350	140	355	275		
	Delay 1		183		172		183		16			213	203
	Delay 2	259		183		183		355	142	360	279		
Snow depth	**Period 1**	365	365	365	135	365	365	365	32	32	32	365	365
	Period 2				365				365	365	365		
	Angle 1	40	0	0		0	350	140				0	10
	Angle 2				325				290	145	85		
	Delay 1	41	0	0		0	355	142				0	10
	Delay 2				330				294	147	86		

Table A2. GS 2019-2024 wavelet analysis: periods, phase angles, and phase delays

		2019_2024_H			**2019_2024_V**			**2019_2024_A**			**2019_2024_D**		
		U	**ES**	**F**	**U**	**ES**	**F**	**U**	**ES**	**F**	**U**	**ES**	**F**
P6SZCA1	**Period 1**	32	32	32	20	20	20	20	20	20	20	32	20
	Period 2	200	365		365	32	32	365	365	50	365	64	365
	Period 3	365										365	
	Angle 1			140								135	
	Angle 2	0	0		15	330		20	215		335		0
	Angle 3											215	
	Delay 1			12								12	
	Delay 2	0	0		15	29		20	218		340		0
	Delay 3											218	
P6SZCA2	**Period 1**	365	365	200	365	128	340	365	365	365	365	365	365
	Period 2			365									
	Angle 1	20	35		50		50	55	235	235	10	265	15
	Angle 2			20									
	Angle 3												
	Delay 1	20	35		51		47	56	238	238	10	269	15
	Delay 2			20									
P6SZCB0	**Period 1**	365	365	365	365	128	64	365	365	365	365	365	365
	Period 2						365						
	Angle 1		15	5	40			55	230	240	0	230	0
	Angle 2						350						
	Delay 1		15	5	41			56	233	243	0	233	0
	Delay 2						355						
Precipitation	**Period**	32	20	15		32	32	20	32	20	32	32	32
	Angle												
	Delay												
Temperature	**Period 1**	365	365	365	365	32	32	365	32	32	365	32	32
	Period 2						365		365	365		365	365
	Angle 1	340	355	340	5			8			325		
	Angle 2						0		180	200		210	325
	Delay 1	345	360	345	5			8			330		
	Delay 2						0		183	203		213	330
Snow depth	**Period 1**	365	365	365	365	128	365	365	365	365	365	365	32
	Period 2												365
	Angle 1	155	165	150	180		180	185	0	20	130	20	
	Angle 2												155
	Delay 1	157	167	152	183		183	188	0	20	132	20	
	Delay 2												157

Appendix B

Chapter 5 appendix

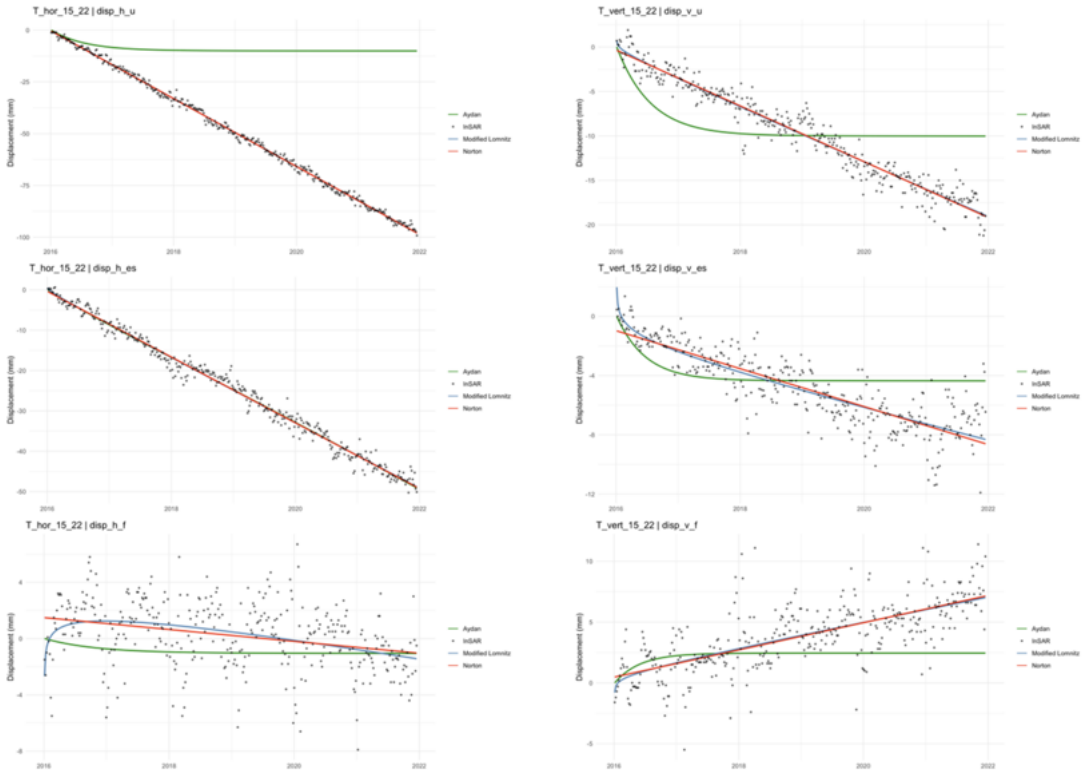


Figure B1. T creep models 1

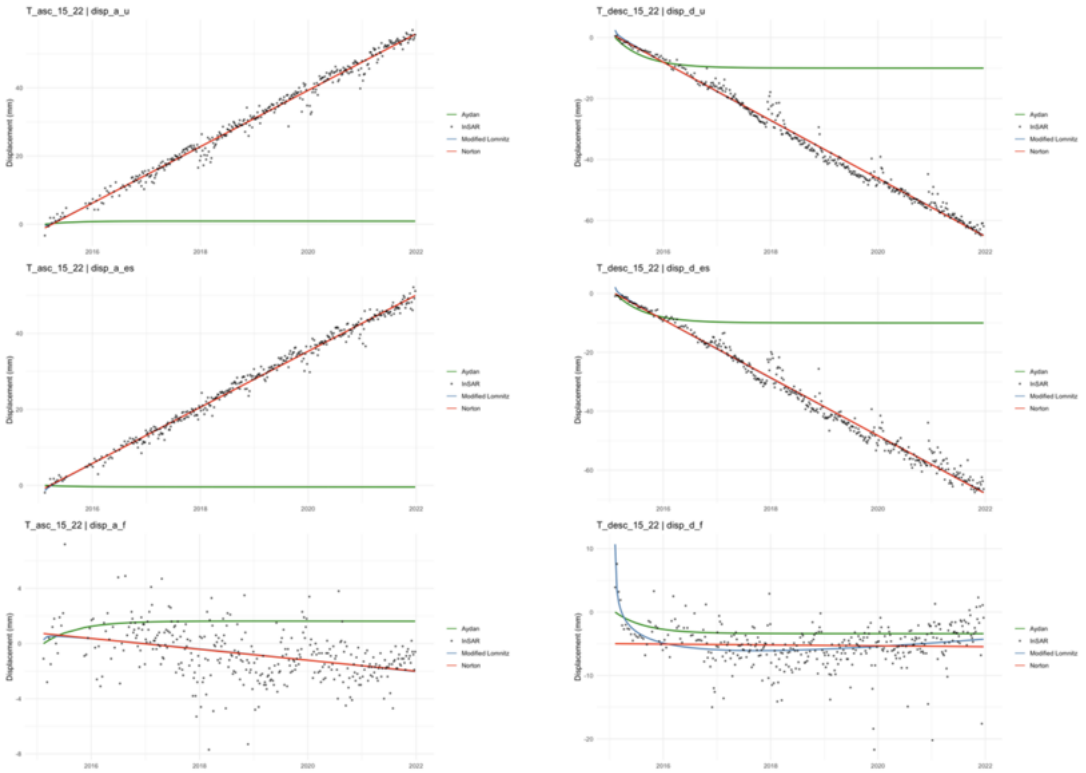


Figure B2. T creep models 2

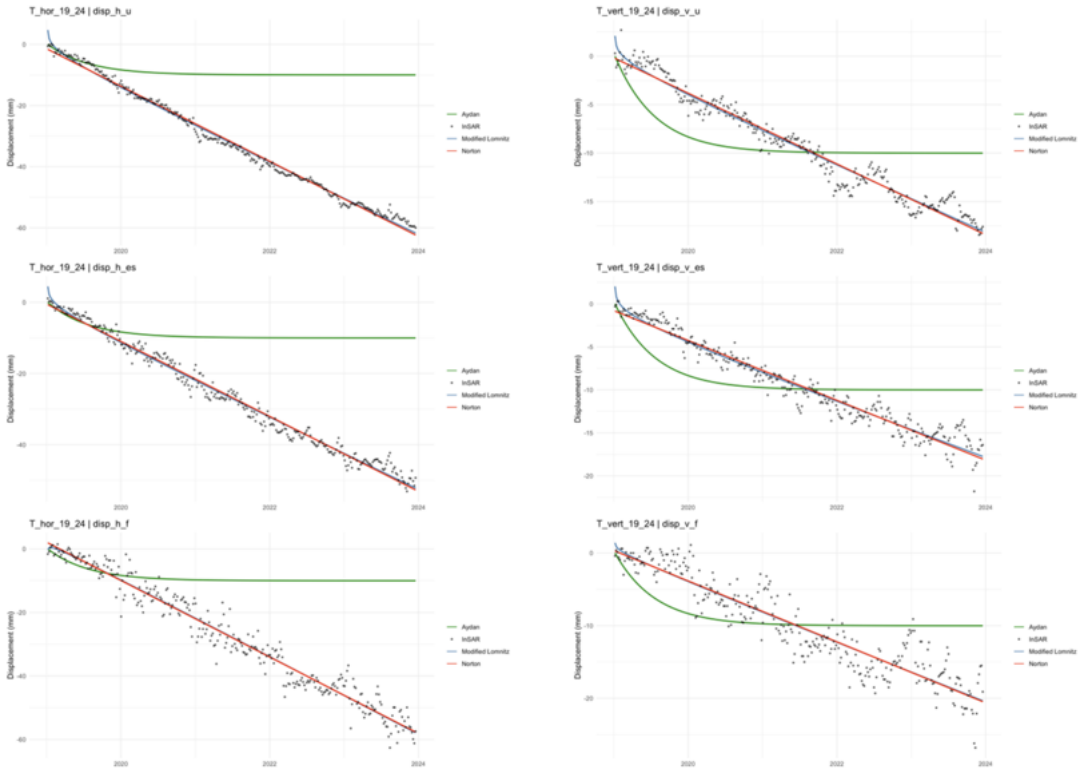


Figure B3. T creep models 3

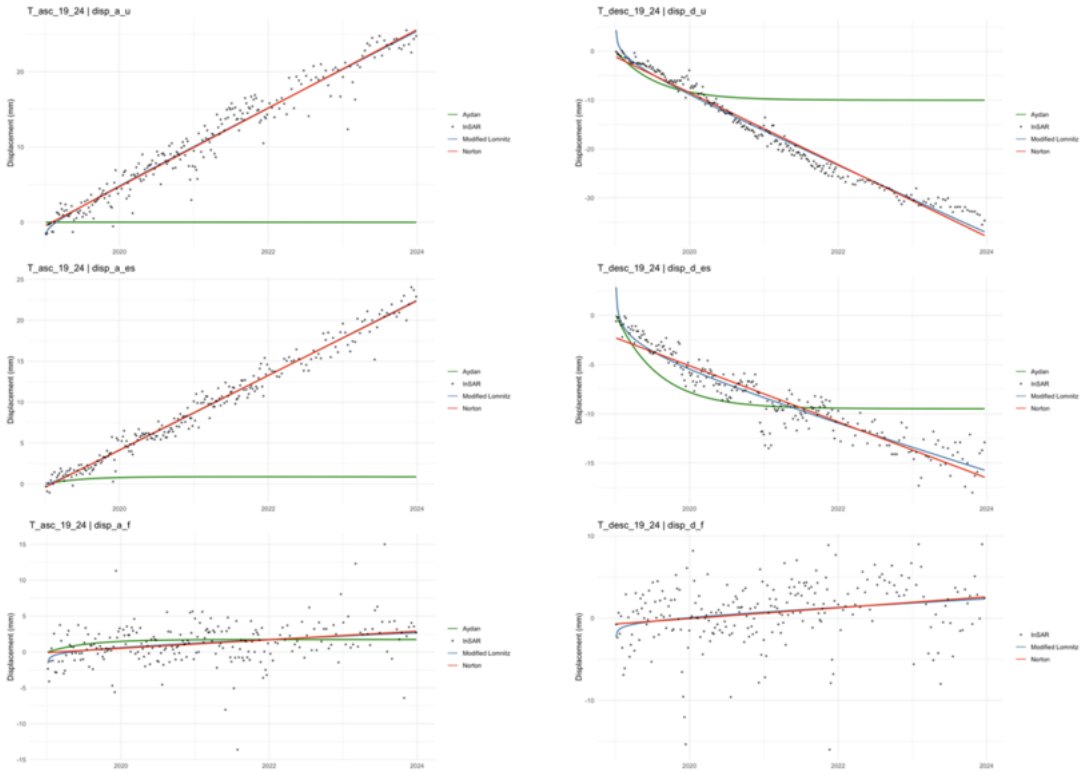


Figure B4. T creep models 4

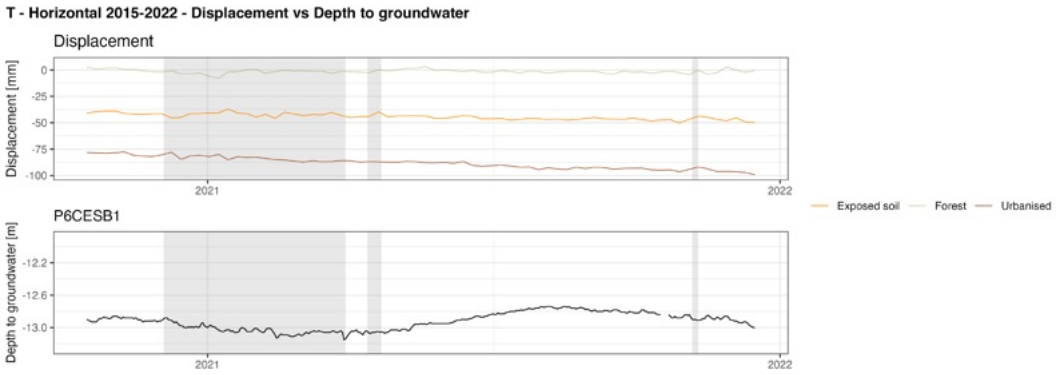


Figure B5. T triggers 1

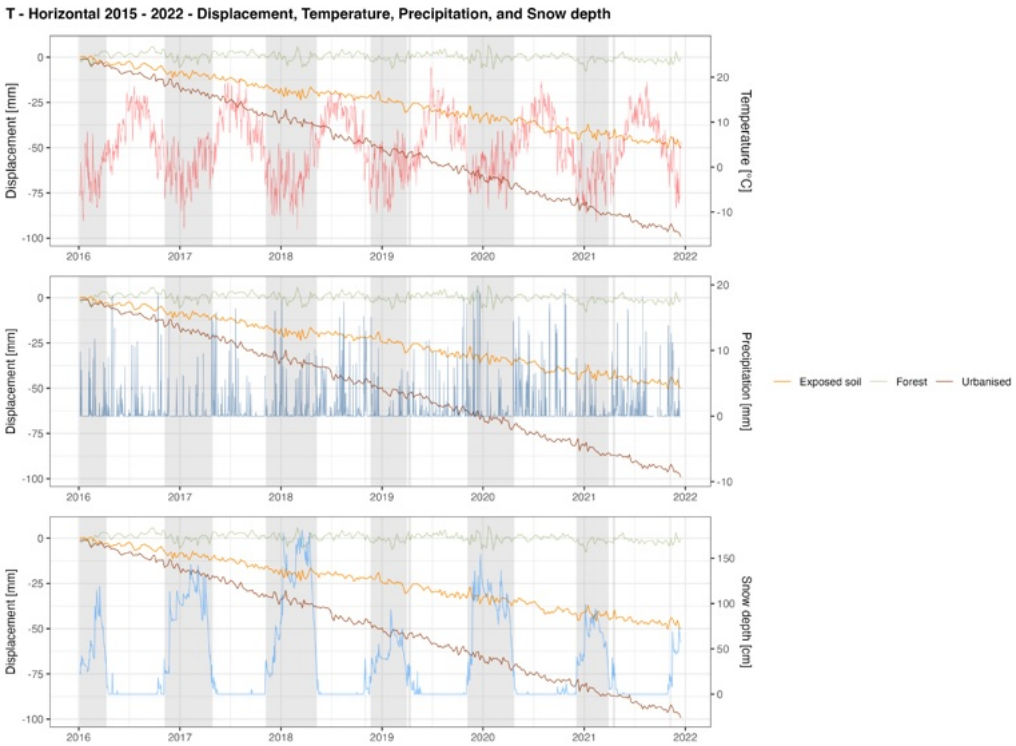


Figure B6. T triggers 2

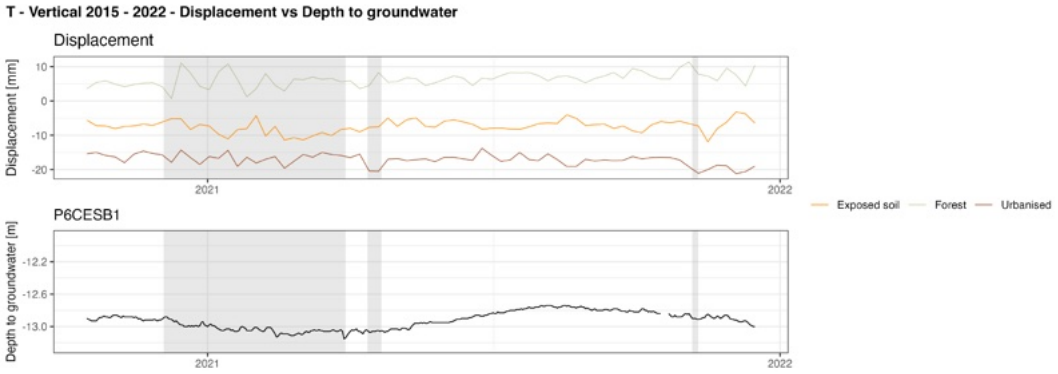


Figure B7. T triggers 3

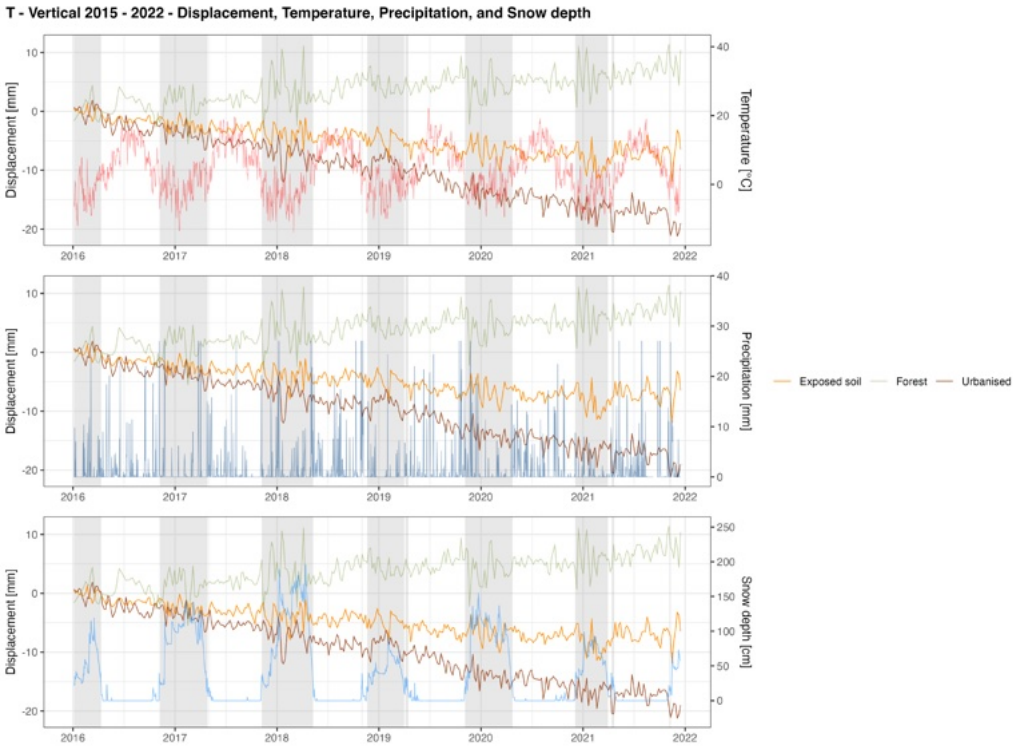


Figure B8. T triggers 4

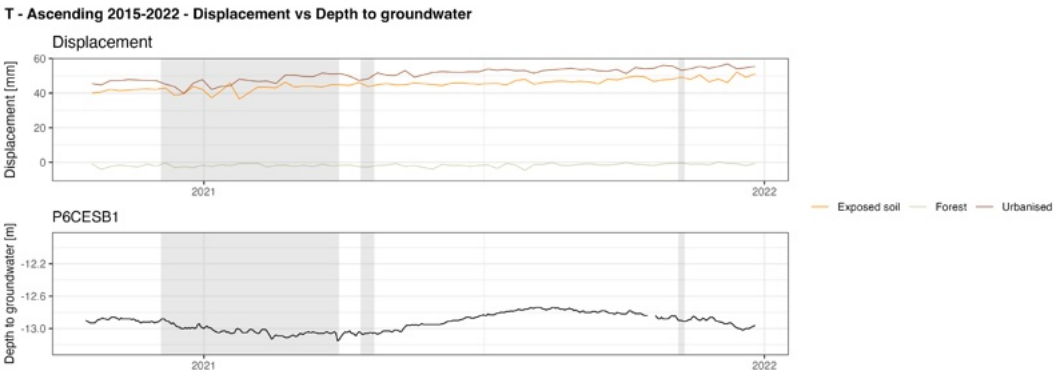


Figure B9. T triggers 5

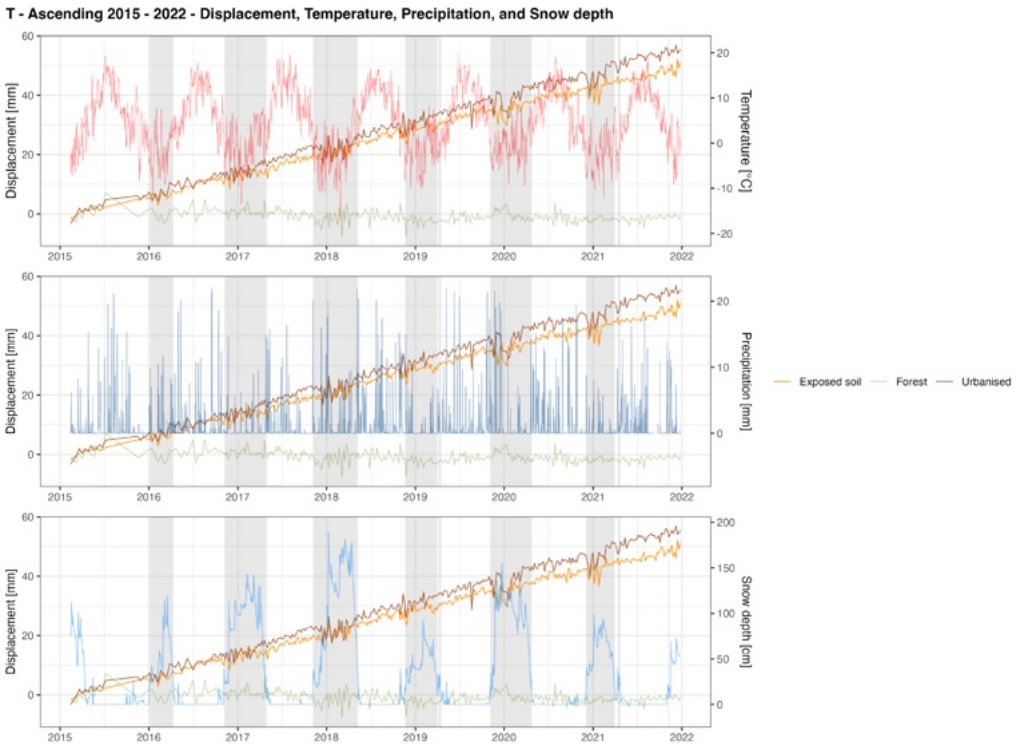


Figure B10. T triggers 6

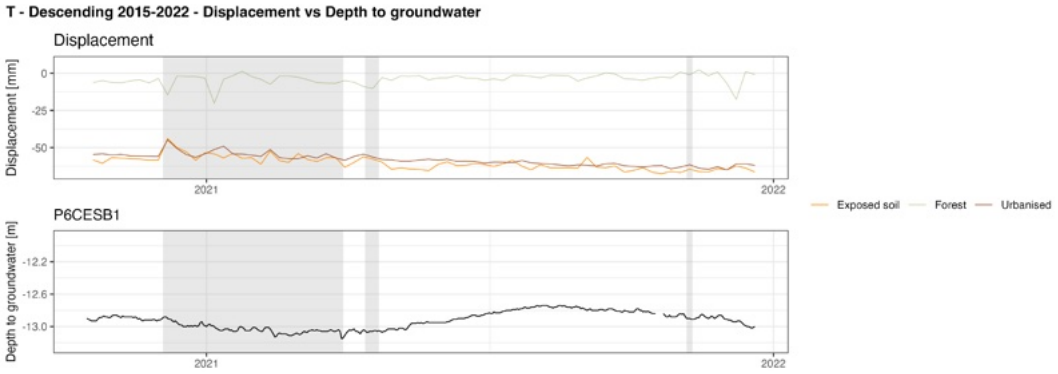


Figure B11. T triggers 7

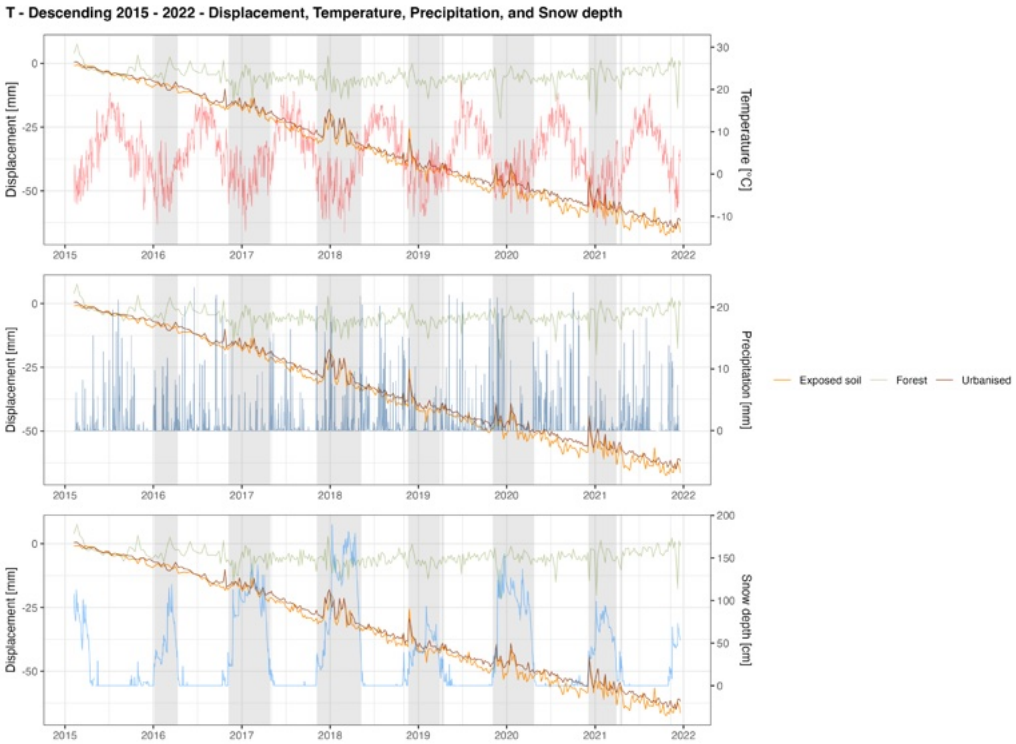


Figure B12. T triggers 8

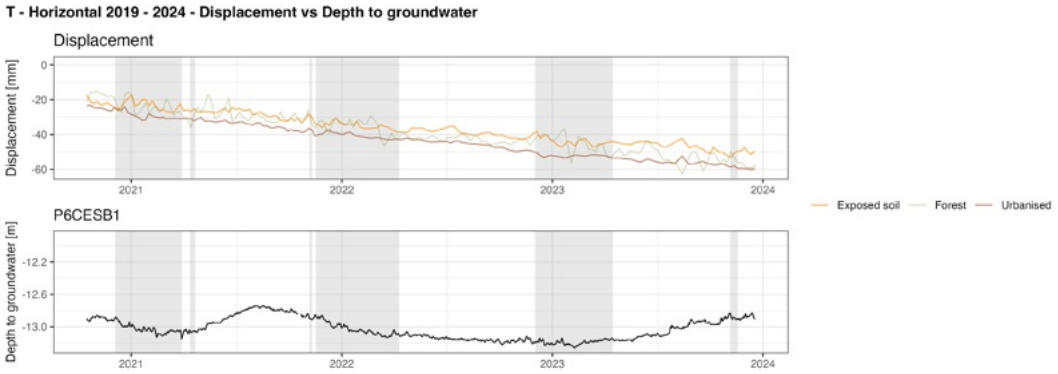


Figure B13. T triggers 9

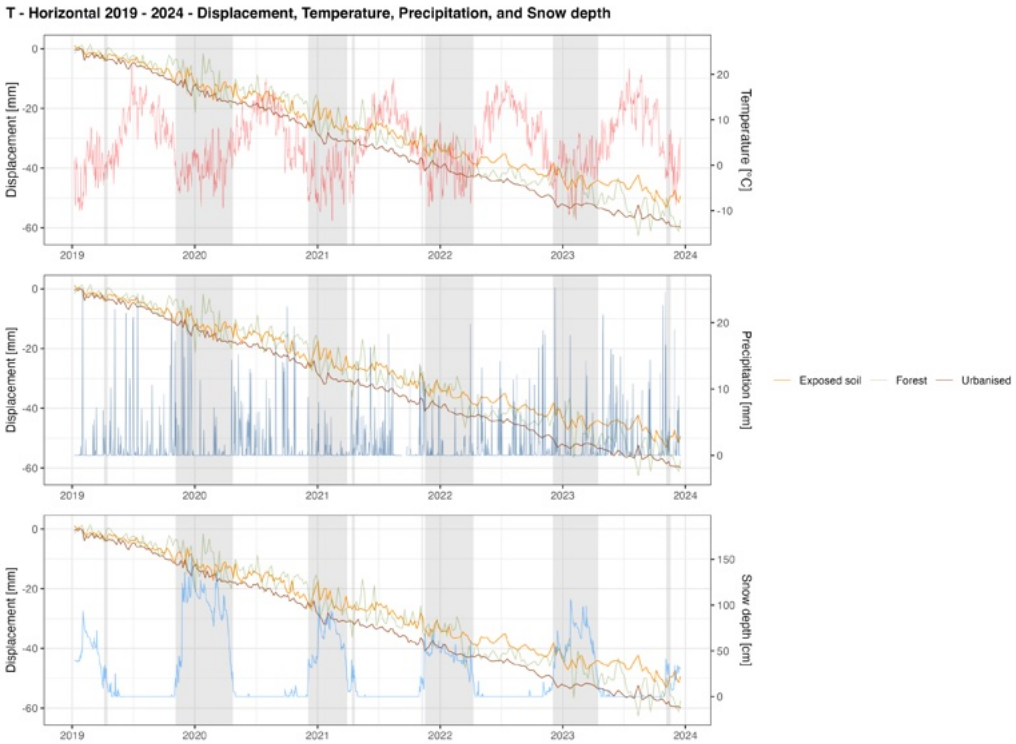


Figure B14. T triggers 10

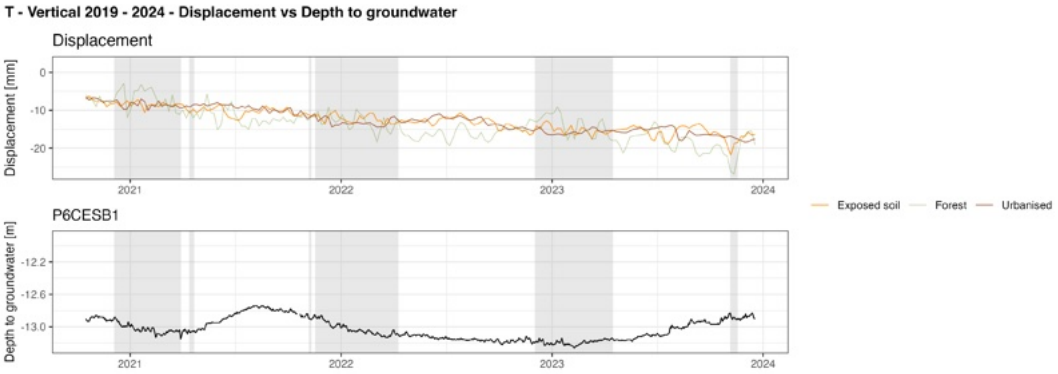


Figure B15. T triggers 11

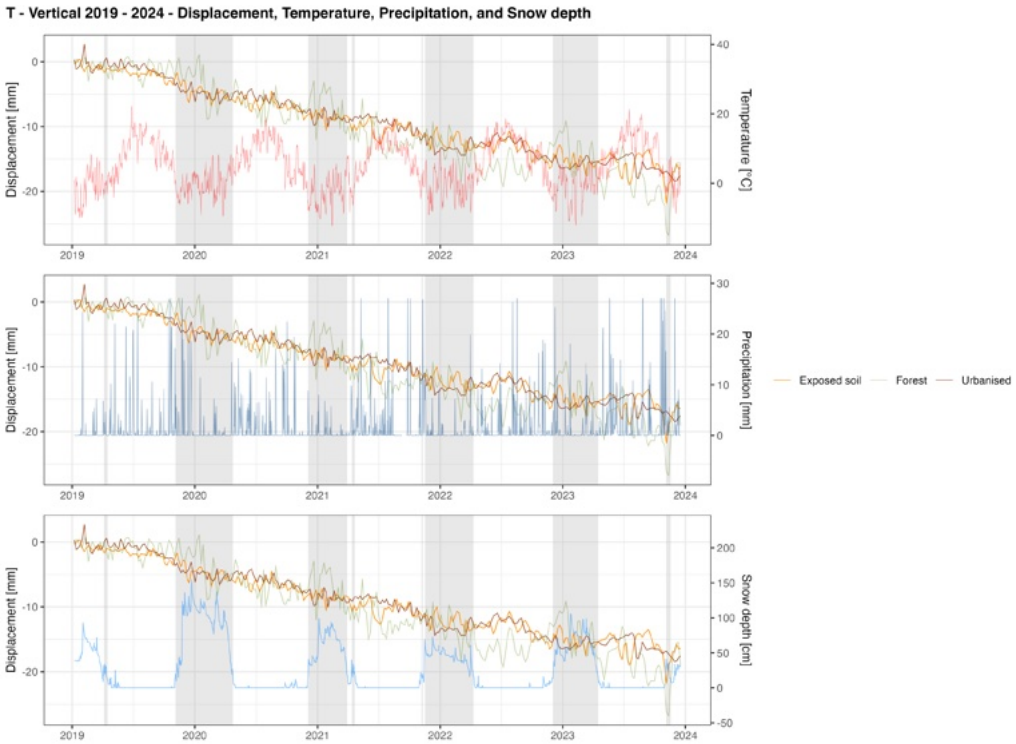


Figure B16. T triggers 12

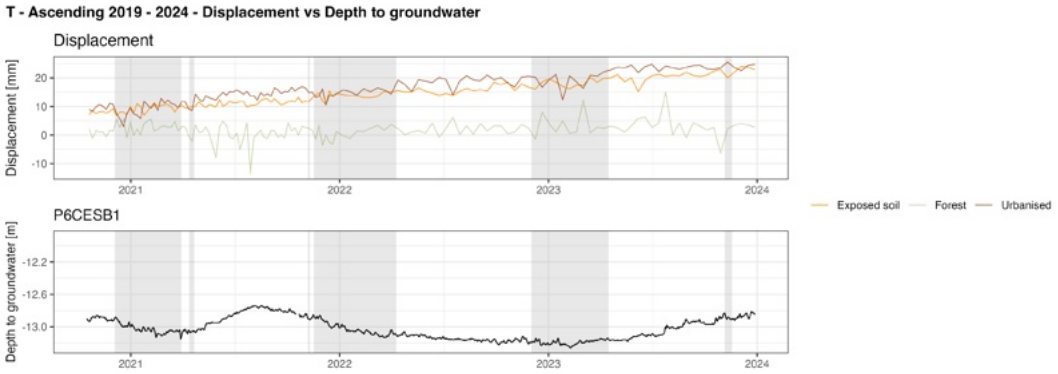


Figure B17. T triggers 13

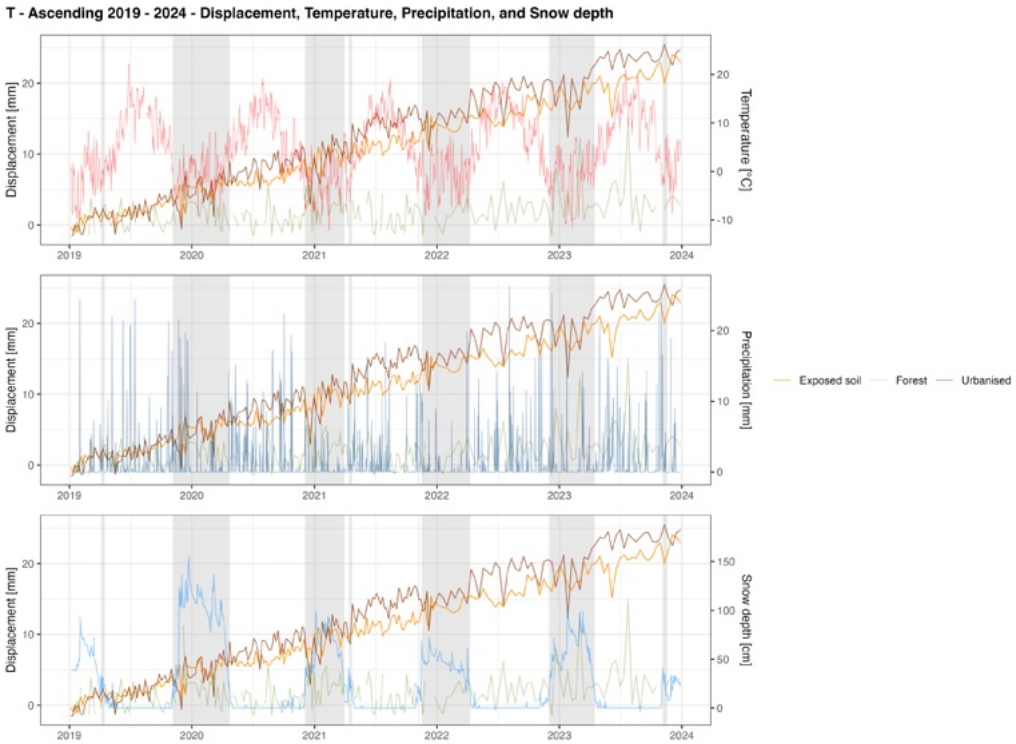


Figure B18. T triggers 14

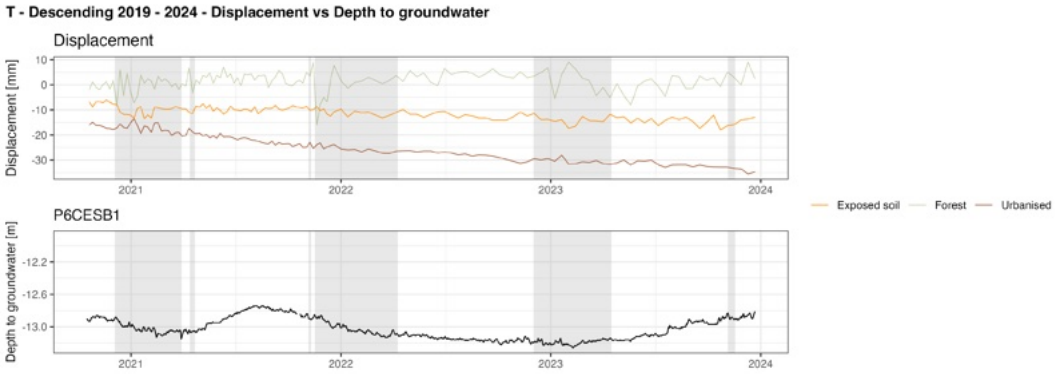


Figure B19. T triggers 15

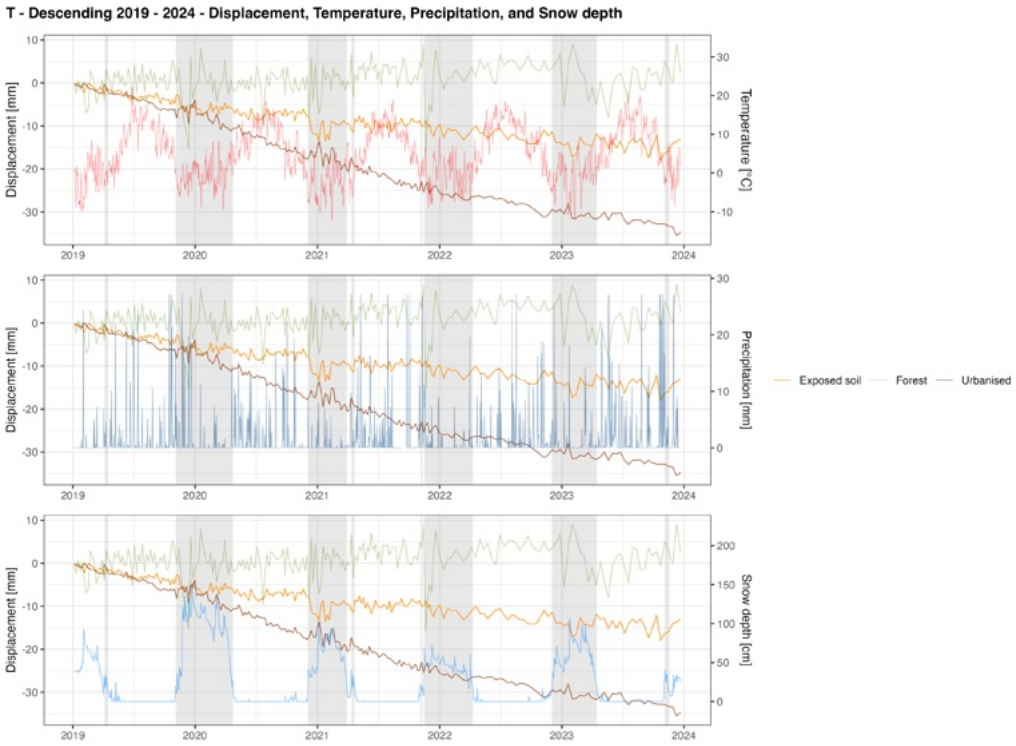


Figure B20. T triggers 16

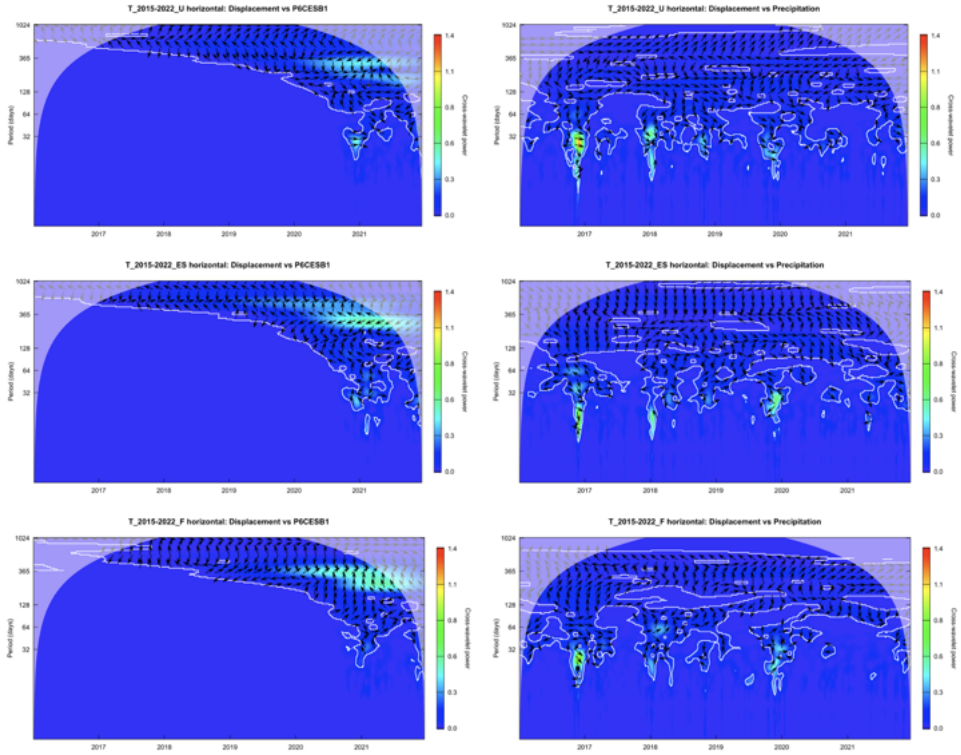


Figure B21. T wavelet analysis 1

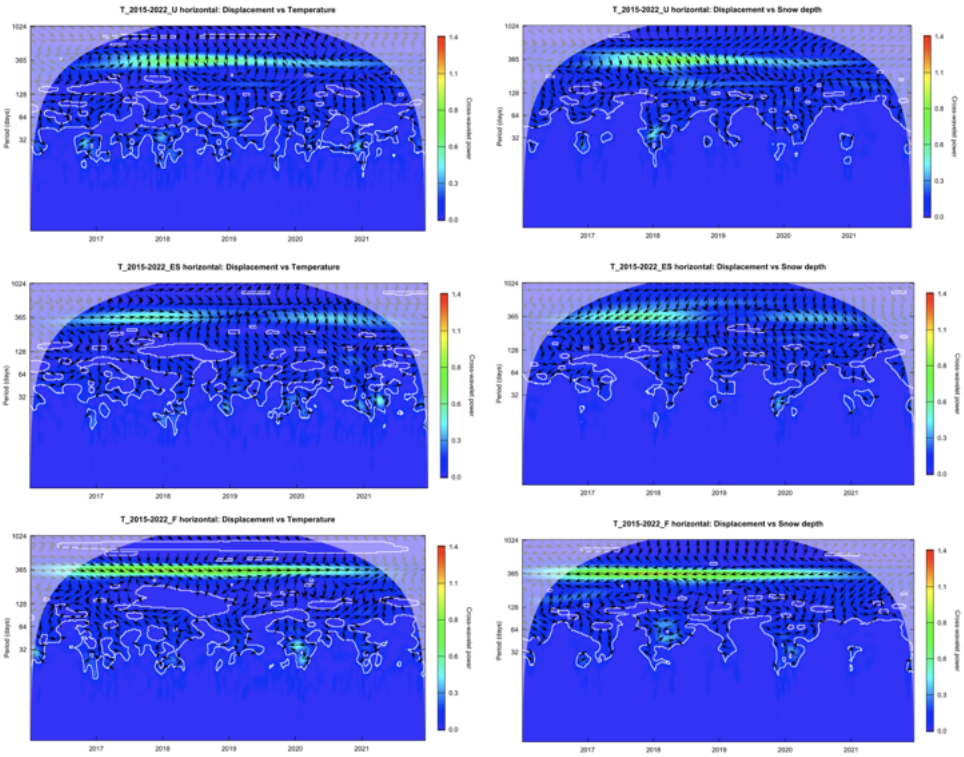


Figure B22. T wavelet analysis 2

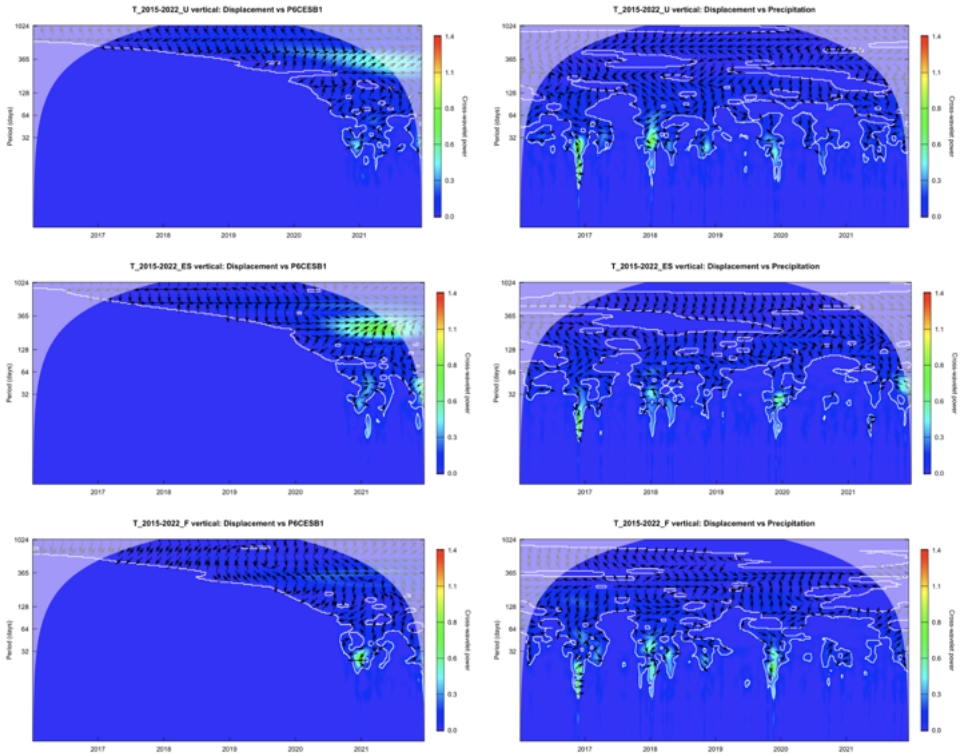


Figure B23. T wavelet analysis 3

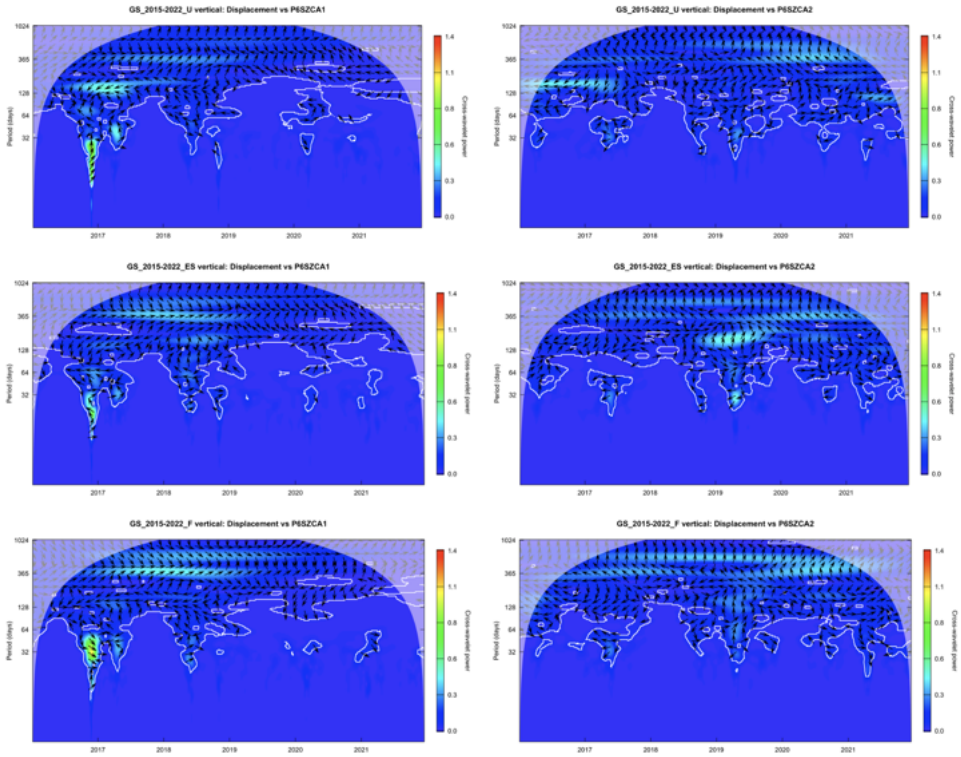


Figure B24. T wavelet analysis 4

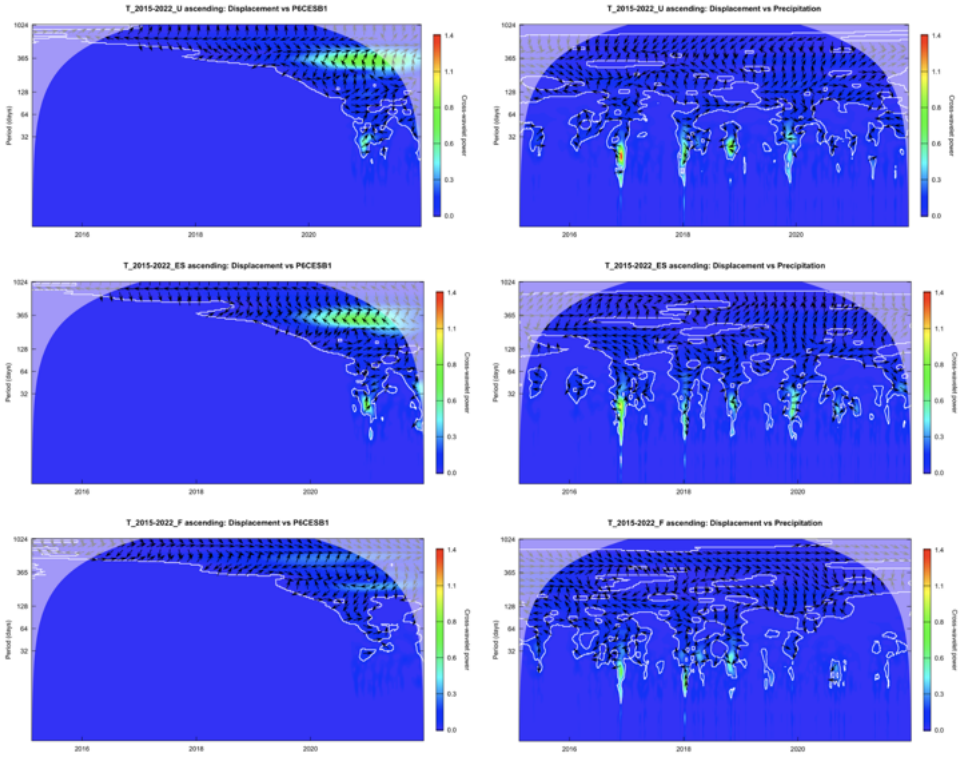


Figure B25. T wavelet analysis 5

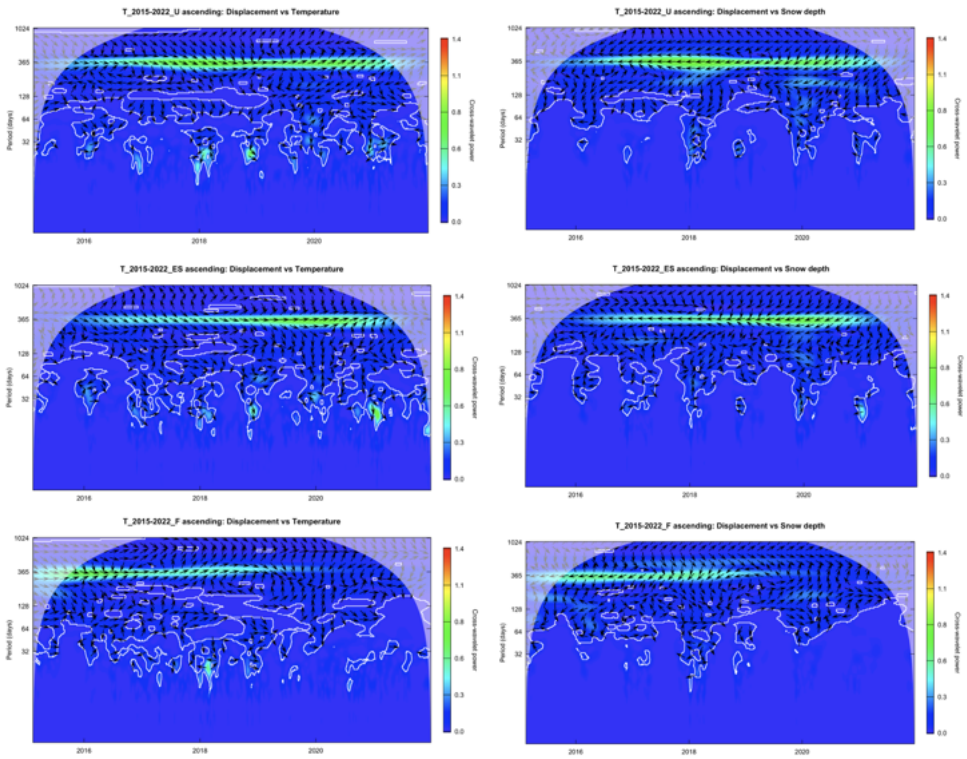


Figure B26. T wavelet analysis 6

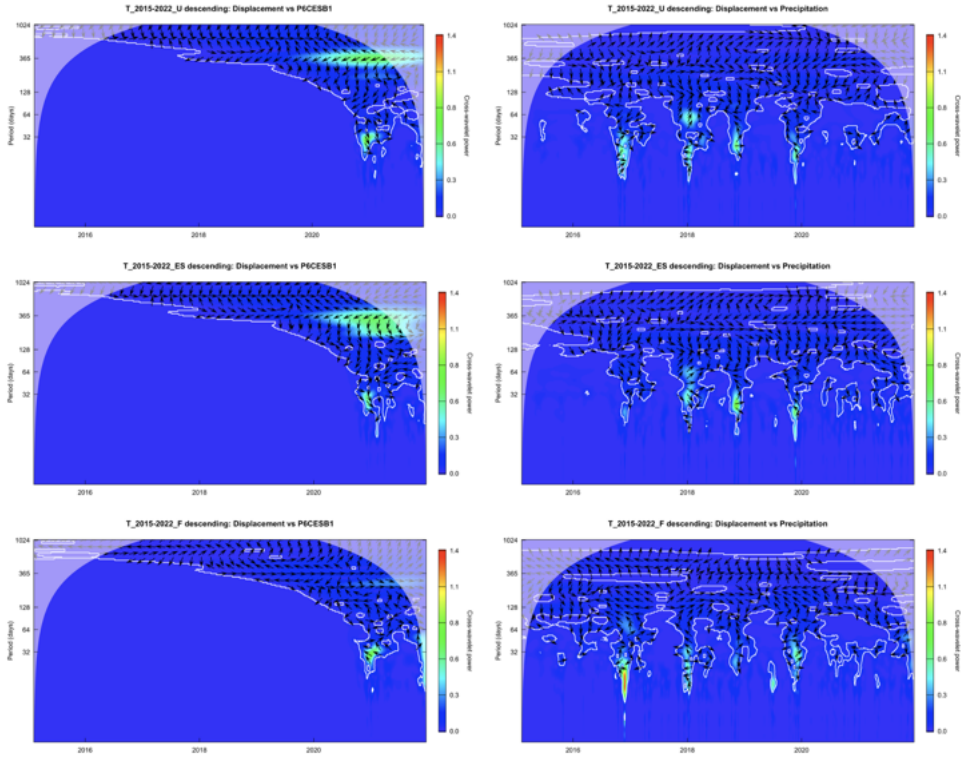


Figure B27. T wavelet analysis 7

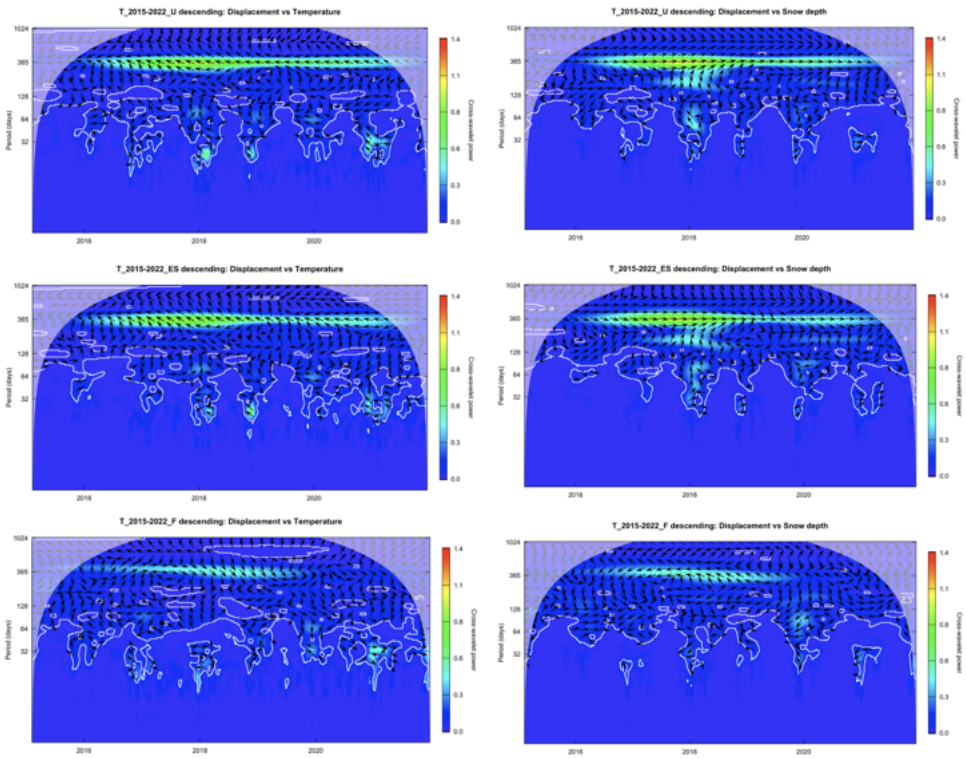


Figure B28. T wavelet analysis 8

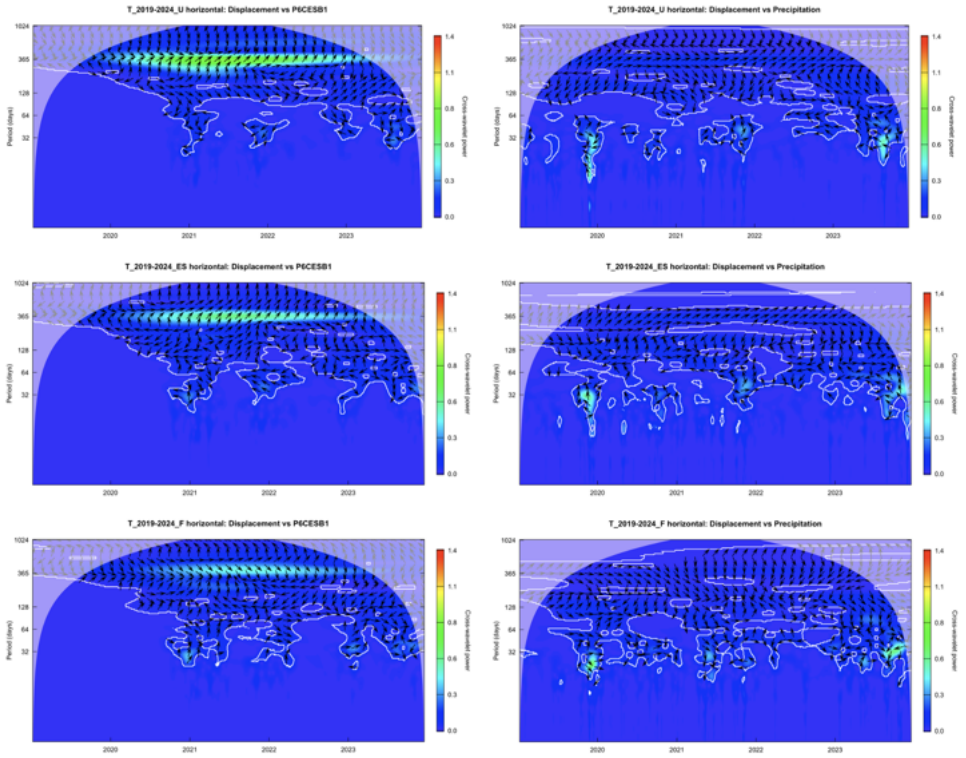


Figure B29. T wavelet analysis 9

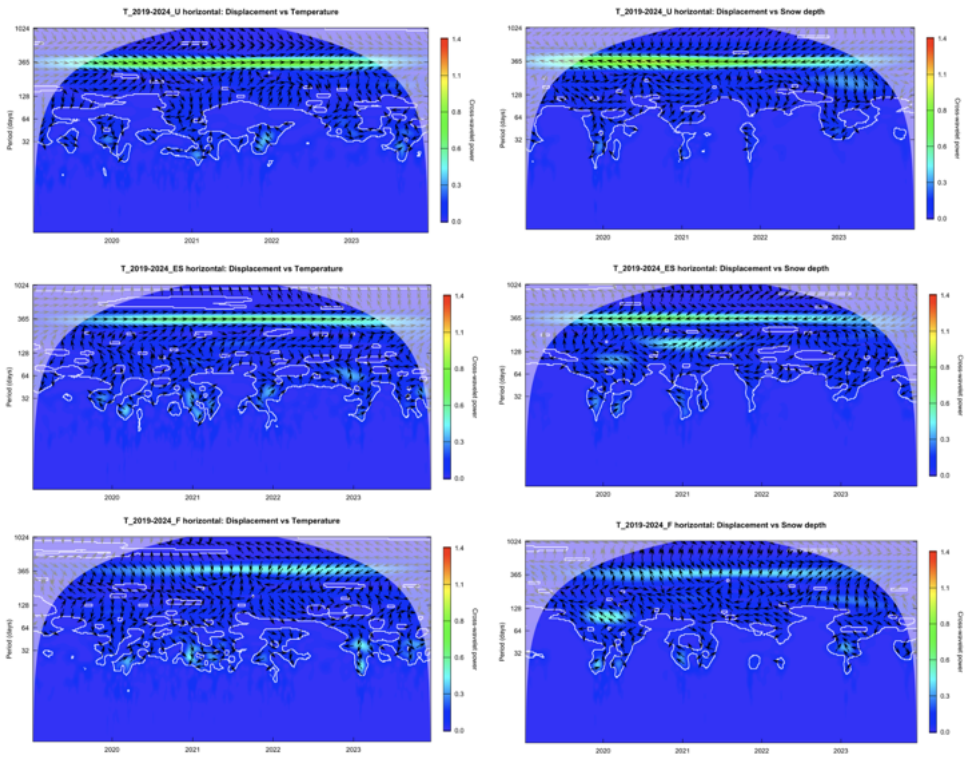


Figure B30. T wavelet analysis 10

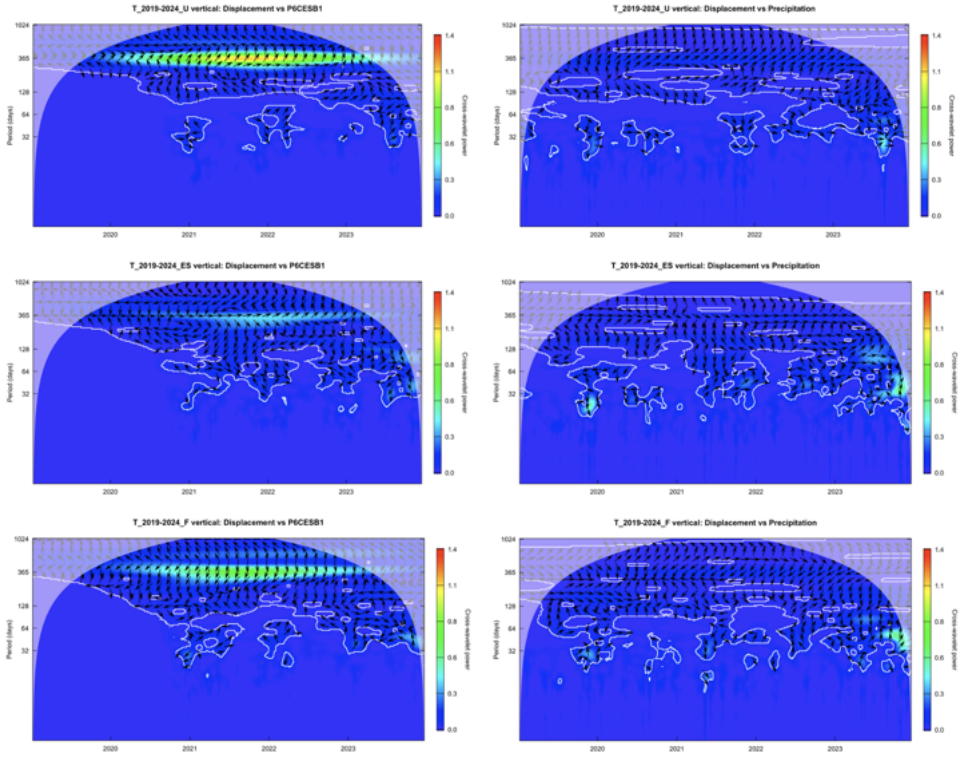


Figure B31. T wavelet analysis 11

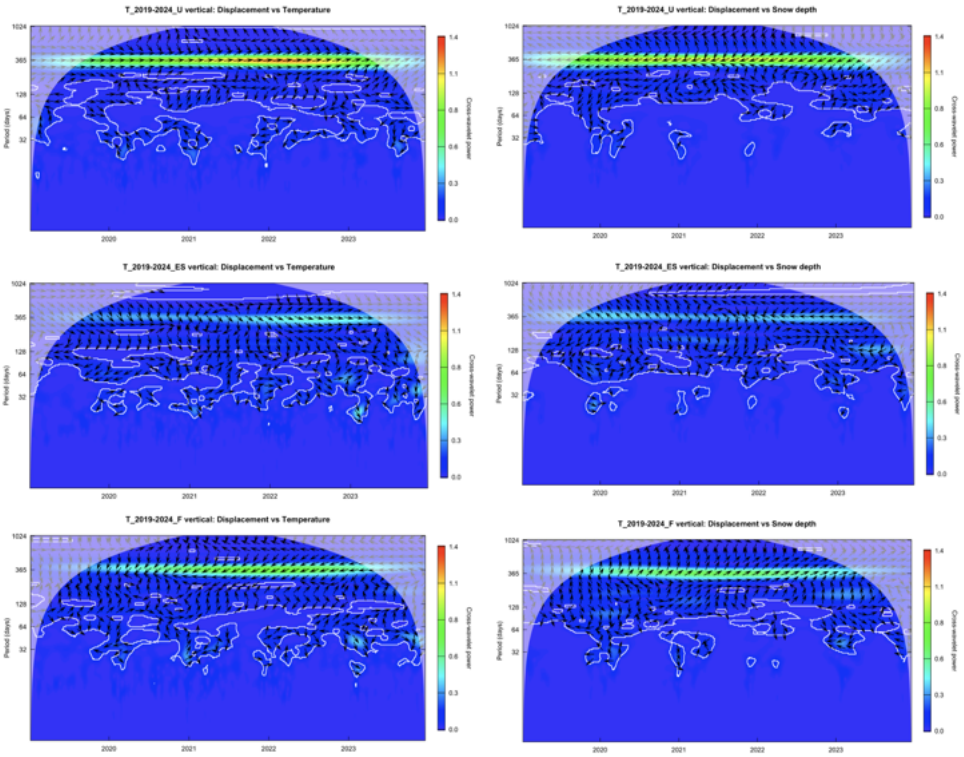


Figure B32. T wavelet analysis 12

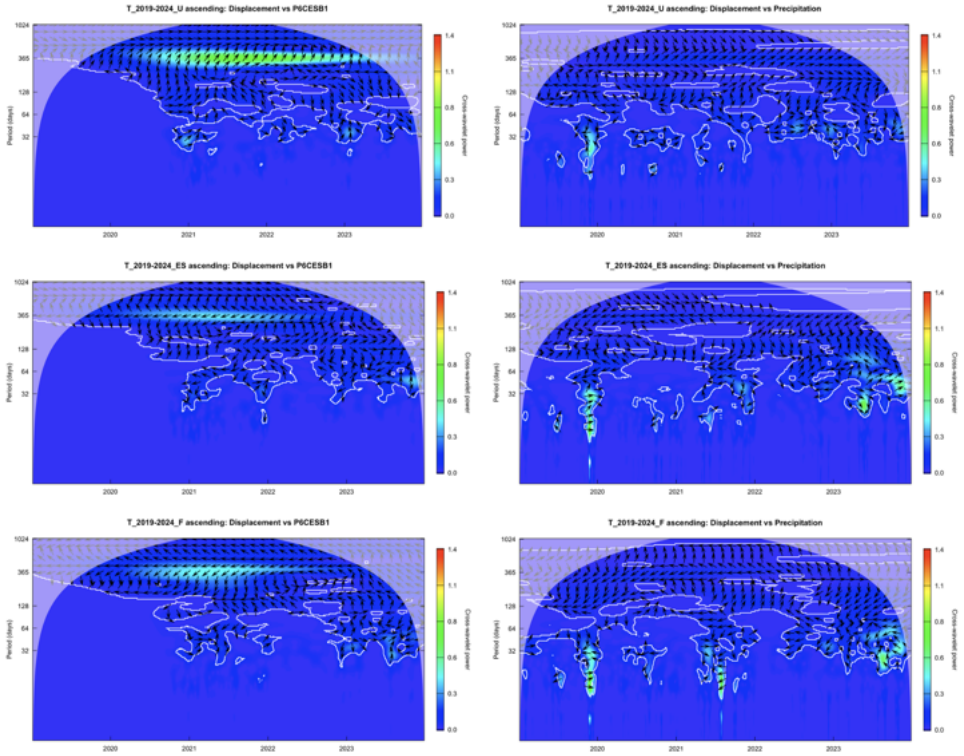


Figure B33. T wavelet analysis 13

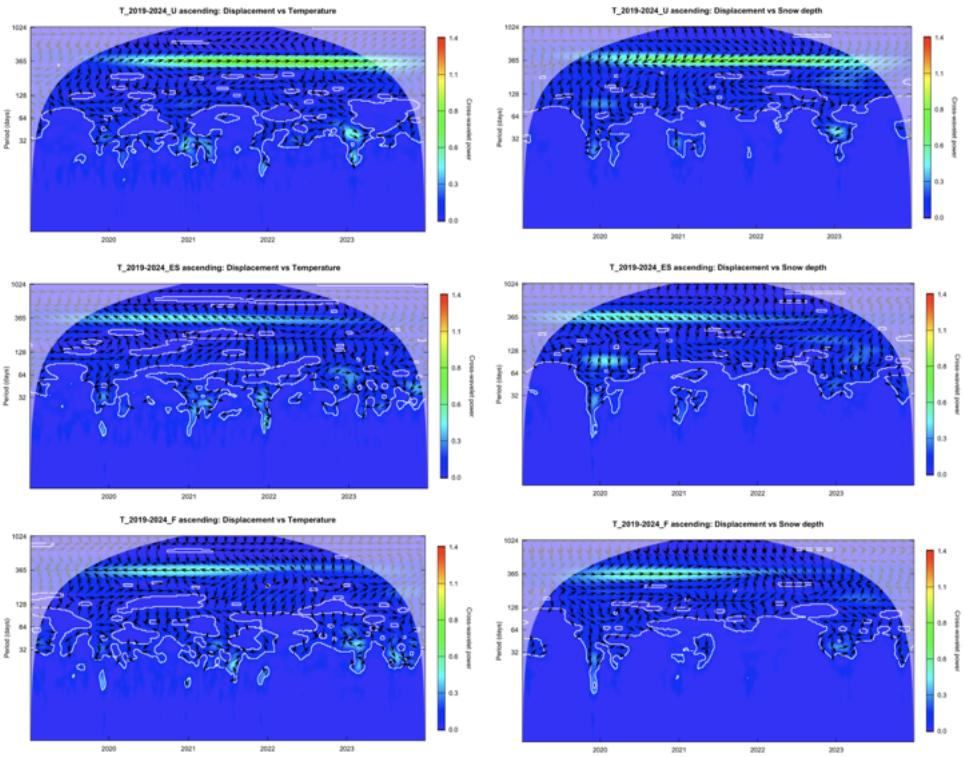


Figure B34. T wavelet analysis 14

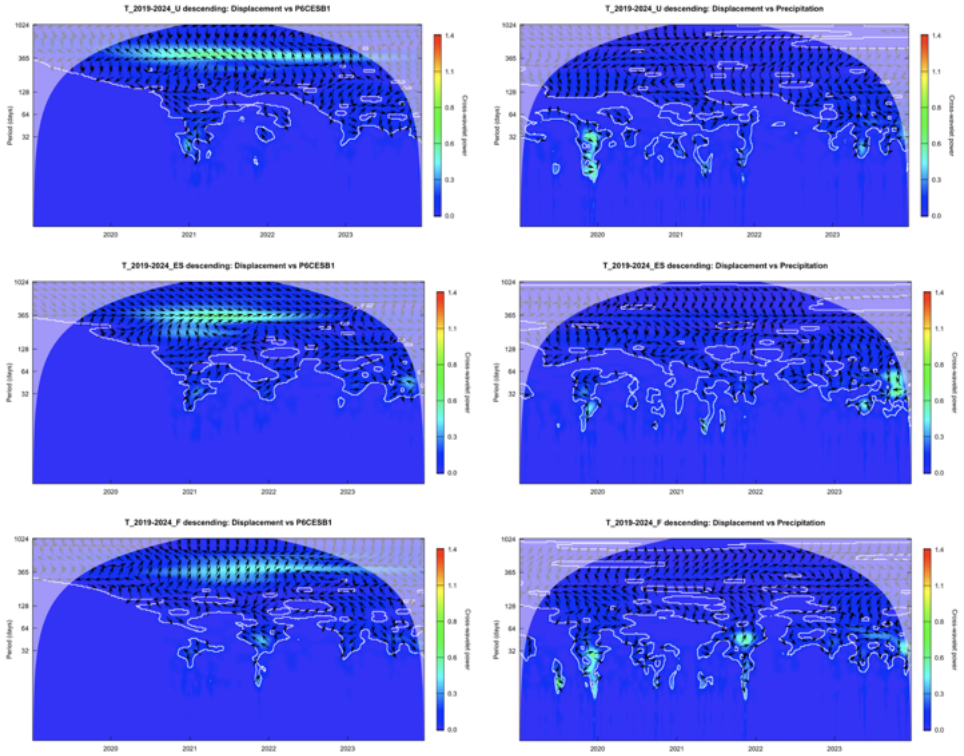


Figure B35. T wavelet analysis 15

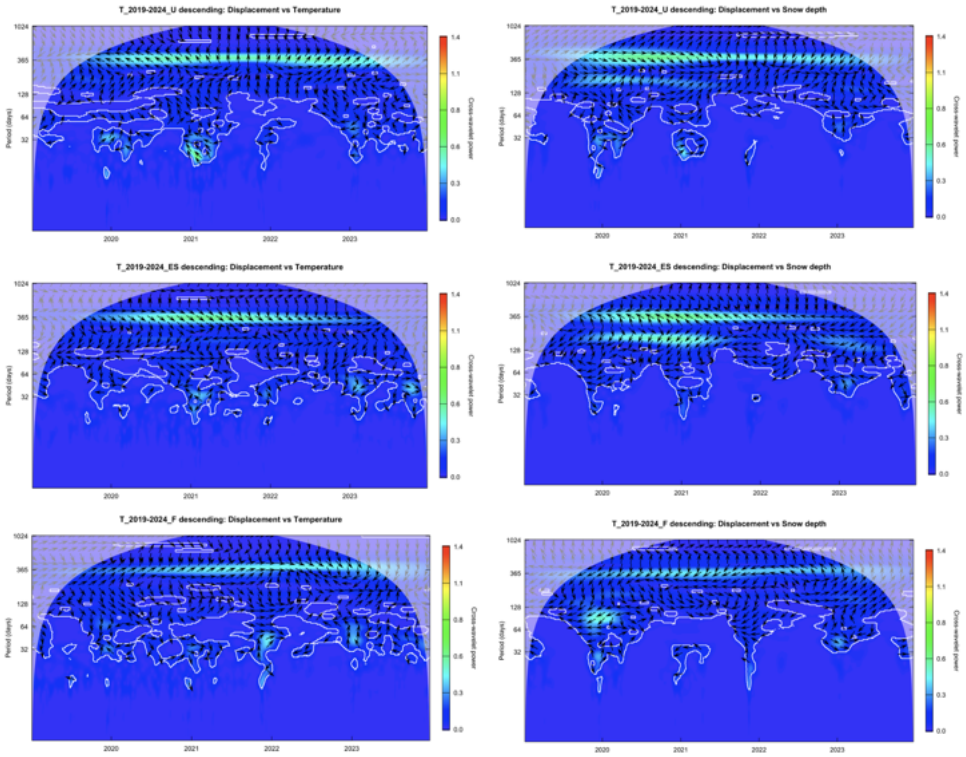


Figure B36. T wavelet analysis 16

Table B1. T 2015-2022 wavelet analysis: periods, phase angles, and phase delays

		2015_2022_H			**2015_2022_V**			**2015_2022_A**			**2015_2022_D**		
		U	**ES**	**F**	**U**	**ES**	**F**	**U**	**ES**	**F**	**U**	**ES**	**F**
P6CESB1	**Period 1**	365	365	365	365	365		365	365	300	365	365	
	Period 2									600			
	Angle 1	140	180	300	315	350		270	270	300	180	150	
	Angle 2									180			
	Delay 1	142	183	304	319	355		274	274	250	183	152	
	Delay 2									300			
Precipitation	**Period**	32	20	25	32	20	25	25	25	25	30	30	30
	Angle												
	Delay												
Temperature	**Period 1**	32	32	32	365	32	32	30	30	30	30	30	30
	Period 2	365	365	365		365	365	365	365	365	365	365	365
	Angle 1				270								
	Angle 2	260	0	5		90	90	0	0	0	200	210	45
	Delay 1		0		274								
	Delay 2	264	0	5		91	91	0	0	0	203	213	46
Snow depth	**Period 1**	365	365	365	365	30	30	365	365	365	365	365	365
	Period 2					365	365						
	Angle 1	60	150	180				180	180	140	0	0	265
	Angle 2					270	270						
	Delay 1	61	152	183		0	0	183	183	142	0	0	269
	Delay 2				0	274	274						

Table B2. T 2019-2024 wavelet analysis: periods, phase angles, and phase delays

		2019_2024_H			**2019_2024_V**			**2019_2024_A**			**2019_2024_D**		
		U	**ES**	**F**	**U**	**ES**	**F**	**U**	**ES**	**F**	**U**	**ES**	**F**
	Period 1	365	365	365	365	365	365	365	365	365	365	365	365
	Angle 1	330	315	140	315	345	110	310	170	145	210	350	290
P6CESB1	**Delay 1**	335	319	142	319	350	112	314	172	147	213	355	294
	Period	32	32	32	32	32	32	30	30	30	25	20	20
Precipitation	**Angle**												
	Delay												
	Period 1	32	32	32	365	365	365	32	32	32	32	50	32
	Period 2	365	365	365				365	365	365	365	365	365
	Angle 1				0	135	155						
	Angle 2	0	0	90				0	215	180	270	30	350
	Delay 1				0	137	157						
Temperature	**Delay 2**	0	0	91				0	218	183	274	30	355
	Period 1	365	30	32	365	365	365	32	365	365	200	200	365
	Period 2		365	365				365			365	365	
	Angle 1	180			170	220	320		25	0	315	115	150
	Angle 2		180	270				160			40	210	
Snow depth	**Delay 1**	183			172	223	324		25	0	175	64	152
	Delay 2		183	274				162			41	213	

Bibliography

Agenzia Regionale per la Protezione dell'Ambiente del Piemonte. (2012). Scheda descrittiva di dettaglio iii livello di approfondimento. *SISTEMA INFORMATIVO FRANE IN PIEMONTE*.

Agenzia Regionale per la Protezione dell'Ambiente del Piemonte. (2015). *Sifrap - sistema informativo frane in piemonte*. https://www.geoportale.piemonte.it/geonetwork/srv/api/records/arlpa_to:07.04.02-D_2011-03-24-11:43

Agenzia Regionale per la Protezione dell'Ambiente del Piemonte. (2025a). *Carta geologica, geopiemonte map*. https://www.geoportale.piemonte.it/geonetwork/srv/ita/catalog.search#/metadata/arlpa_to:07-11-00-D_2017-05-22-12:00

Agenzia Regionale per la Protezione dell'Ambiente del Piemonte. (2025b, June). *Rete regionale di controllo sui movimenti franosi (rercomf)*. https://www.arpa.piemonte.it/scheda-informativa/rete-regionale-controllo-sui-movimenti-franosi-rercomf

Agliardi, F., Crosta, G., & Zanchi, A. (2001). Structural constraints on deep-seated slope deformation kinematics. *Engineering Geology*, *59*(1–2), 83–102. https://doi.org/10.1016/s0013-7952(00)00066-1

Agliardi, F., Crosta, G., & Frattini, P. (2012). Landslides: Types, mechanisms and modeling. Cambridge University Press.

Agliardi, F., Crosta, G. B., Frattini, P., & Malusà, M. G. (2013). Giant non-catastrophic landslides and the long-term exhumation of the european alps. *Earth and Planetary Science Letters*, *365*, 263–274. https://doi.org/10.1016/j.epsl.2013.01.030

Agliardi, F., Scuderi, M. M., Fusi, N., & Collettini, C. (2020). Slow-to-fast transition of giant creeping rockslides modulated by undrained loading in basal shear zones. *Nature Communications*, *11*(1). https://doi.org/10.1038/s41467-020-15093-3

Albano, M., Saroli, M., Beccaro, L., Moro, M., Doumaz, F., Discenza, M. E., Del Rio, L., & Rompato, M. (2023). Multi-source data analysis to assess the past and present kinematics of the pisciotta deep-seated gravitational slope deformation (southern italy). *Remote Sensing of Environment*, *296*, 113751. https://doi.org/10.1016/j.rse.2023.113751

Alberto, W., Carraro, F., & Giardino, M. (2008). Specificità e implicazioni applicative dell'evoluzione del fenomeno gravitativo di cima bosco (alta valle di susa, alpi occidentali). *Giornale di Geologia Applicata*, *8*(2), 233–244.

Alte Valli - Hautes Vallées. (2026). Val di susa. Retrieved 2026, from https://altevalli.eu/it/territoires-2/valle-di-susa-val-sangone/#:~:text=La%20Val%20di%20Susa%20%C3%A8,e%20pi%C3%B9%20popolata%20del%20Piemonte

Ambrosi, C., & Crosta, G. (2006). Large sackung along major tectonic features in the central italian alps. *Engineering Geology*, *83*(1–3), 183–200. https://doi.org/10.1016/j.enggeo.2005.06.031

Aydan, O., Ito, T., Ozbay, U., Kwasniewski, M., Shariar, K., Okuno, T., Ozgenoglu, A., Malan, D., & Okada, T. (2014). Isrm suggested methods for determining the creep characteristics of rock. *Rock Mechanics and Rock Engineering*, *47*(1), 275–290.

Ballantyne, C. K., Sandeman, G. F., Stone, J. O., & Wilson, P. (2014). Rock-slope failure following late pleistocene deglaciation on tectonically stable mountainous terrain. *Quaternary Science Reviews*, *86*, 144–157. https://doi.org/10.1016/j.quascirev.2013.12.021

Barla, G., Antolini, F., Barla, M., Mensi, E., & Piovano, G. (2010). Monitoring of the beauregard landslide (aosta valley, italy) using advanced and conventional techniques. *Engineering Geology*, *116*(3–4), 218–235. https://doi.org/10.1016/j.enggeo.2010.09.004

Baumgartner, S. V., & Krieger, G. (2014). Multi-channel sar for ground moving target indication. In *Academic press library in signal processing: Volume 2 - communications and radar signal processing* (pp. 911–986). Elsevier. https://doi.org/10.1016/b978-0-12-396500-4.00018-1

Bovenga, F., Belmonte, A., Refice, A., Pasquariello, G., Nutricato, R., Nitti, D. O., & Chiaradia, M. T. (2018). Performance analysis of satellite missions for multi-temporal sar interferometry. *Sensors*, *18*(5), 1359. https://doi.org/10.3390/s18051359

Cannarozzi, M. (2023). *Mapping,geological characterization and analysis of activity of deep-seated gravitational slope derformation in the poqueira basin (sierra nevada, spain)* [Doctoral dissertation, Università degli Studi di Milano-Bicocca].

Chan, Y. K., & Koo, V. C. (2008). An introduction to synthetic aperture radar (sar). *Progress In Electromagnetics Research B*, *2*, 27–60. https://doi.org/10.2528/pierb07110101

Chen, H., Zhao, C., Tomás, R., Reyes-Carmona, C., & Kang, Y. (2025). Integrating insar and non-rigid optical pixel offsets to explore the kinematic behaviors of the lanuza complex landslide. *Remote Sensing of Environment*, *320*, 114651. https://doi.org/10.1016/j.rse.2025.114651

Chen, M., Chang, M., Zhou, W., Gan, W., Xiong, J., & Yin, H. (2026). Rainfall-meltwater synergy and freeze-thaw cycles enhance the activities of low-frequency debris flows: Unraveling the 2024 catastrophic event in the ridi catchment on the eastern margin of the tibetan plateau. *CATENA*, *271*, 110233. https://doi.org/10.1016/j.catena.2026.110233

Chigira, M. (1992). Long-term gravitational deformation of rocks by mass rock creep. *Engineering Geology*, *32*(3), 157–184. https://doi.org/10.1016/0013-7952(92)90043-x

Cignetti, M., Godone, D., Zucca, F., Bertolo, D., & Giordan, D. (2020). Impact of deep-seated gravitational slope deformation on urban areas and large infrastructures in the italian western alps. *Science of The Total Environment*, *740*, 140360. https://doi.org/10.1016/j.scitotenv.2020.140360

Crippa, C. (2021). *Regional and local scale analysis of very slow rock slope deformations integrating insar and morpho-structural data.* [Doctoral dissertation, Università degli Studi di Milano-Bicocca].

Crosetto, M., Crippa, B., Mróz, M., Cuevas-González, M., & Shahbazi, S. (2025). Applications based on egms products: A review. *Remote Sensing Applications: Society and Environment*, *37*, 101452. https://doi.org/10.1016/j.rsase.2025.101452

Crosetto, M., Cuevas-González, M., Mróz, M., Moldestad, D., Raspini, F., Casagli, N., Bateson, L., Novellino, A., Motagh, M., Guerrieri, L., & Comerci, V. (2026). Euro-

pean ground motion service: A decade of sentinel-1 observations. *Remote Sensing of Environment*, *339*, 115389. https://doi.org/10.1016/j.rse.2026.115389

Crosetto, M., Solari, L., Balasis-Levinsen, J., Bateson, L., Casagli, N., Frei, M., Oyen, A., Moldestad, D. A., & Mróz, M. (2021). Deformation monitoring at european scale: The copernicus ground motion service. *The International Archives of the Photogrammetry, Remote Sensing and Spatial Information Sciences*, *XLIII-B3-2021*, 141–146. https://doi.org/10.5194/isprs-archives-xliii-b3-2021-141-2021

Crosetto, M., Monserrat, O., Cuevas-González, M., Devanthéry, N., & Crippa, B. (2016). Persistent scatterer interferometry: A review. *ISPRS Journal of Photogrammetry and Remote Sensing*, *115*, 78–89. https://doi.org/10.1016/j.isprsjprs.2015.10.011

Crosta, G., Frattini, P., & Agliardi, F. (2013). Deep seated gravitational slope deformations in the european alps. *Tectonophysics*, *605*, 13–33. https://doi.org/10.1016/j.tecto.2013.04.028

Cruden, D. M., & Varnes, D. J. (1996). Landslides: Investigation and mitigation. Transportation Research board special report 247.

Dramis, F., & Sorriso-Valvo, M. (1994). Deep-seated gravitational slope deformations, related landslides and tectonics. *Engineering Geology*, *38*(3–4), 231–243. https://doi.org/10.1016/0013-7952(94)90040-x

EGMS. (2022, May). *End-to-end implementation and operation of the european ground motion service (egms)* (1.6). Consortium ORIGINAL (OpeRatIonal Groundmotion INsar ALliance).

EGMS. (2025a, August). *European ground motion service (egms) - algorithm theoretical basis document*. Retrieved 2025, from https://library.land.copernicus.eu/products/European_Ground_Motion_Service_Algorithm_Theoretical_Basis_Document_v4.html

EGMS. (2025b). *Product user manual* (2nd ed.). https://land.copernicus.eu/en/technical-library/guidelines-european-ground-motion-service-product-analysis-in-qgis/@@download/file

EGMS. (2025c, January). *Validation white paper* (3.0). European Ground Motion Service.

EGMS. (2026a). *European ground motion service*. Retrieved 2026, from https://land.copernicus.eu/en/products/european-ground-motion-service?tab=overview

EGMS. (2026b). *European ground motion service*. https://egms.land.copernicus.eu

Ferretti, A., Monti-Guarnieri, A., Prati, C., Rocca, F., & Massonnet, D. (2007, February). *Insar principles: Guidelines for sar interferometry processing and interpretation* (Monti-Guarnieri, Ed.). ESA Publications.

Ferretti, A., Prati, C., & Rocca, F. (2001). Permanent scatterers in sar interferometry. *IEEE Transactions on Geoscience and Remote Sensing*, *39*(1), 8–20. https://doi.org/10.1109/36.898661

Fioraso, G., & Mosca, P. (2014). Note illustrative della carta geologica d'italia alla scala 1:50.000 f. 171 cesana torinese, servizio geologico d'italia - ispra. https://doi.org/10.15161/OAR.IT/143175

Frattini, P., Crosta, G., & Allievi, J. (2013). Damage to buildings in large slope rock instabilities monitored with the psinsar™ technique. *Remote Sensing*, *5*(10), 4753–4773. https://doi.org/10.3390/rs5104753

Grämiger, L. M., Moore, J. R., Gischig, V. S., Ivy-Ochs, S., & Loew, S. (2017). Beyond debuttressing: Mechanics of paraglacial rock slope damage during repeat glacial cycles. *Journal of Geophysical Research: Earth Surface*, *122*(4), 1004–1036. https://doi.org/10.1002/2016jf003967

ISTAT. (2023, August). *Csr 2023-2027 – classificazione e ripar!zione del territorio regionale per zone al!metriche (montagna, collina e pianura)* (tech. rep.). ISTAT.

Jaboyedoff, M., Penna, I., Pedrazzini, A., Baroň, I., & Crosta, G. B. (2013). An introductory review on gravitational-deformation induced structures, fabrics and modeling. *Tectonophysics*, *605*, 1–12. https://doi.org/10.1016/j.tecto.2013.06.027

Materazzi, M., Aringoli, D., Pambianchi, G., Gentili, B., & Giacopetti, M. (2014). Deep seated gravitational slope deformations and large landslides interferring with fluvial dynamics; examples from central apennines (italy). https://doi.org/10.13140/2.1.2873.6001

Meyer, F. (2019). Spaceborne synthetic aperture radar: Principles, data access, and basic processing techniques. https://doi.org/10.25966/EZ4F-MG98

NASA. (2026). *Synthetic aperture radar (sar)*. Retrieved 2026, from https://www.earthdata.nasa.gov/learn/earth-observation-data-basics/sar

Pánek, T., & Klimeš, J. (2016). Temporal behavior of deep-seated gravitational slope deformations: A review. *Earth-Science Reviews*, *156*, 14–38. https://doi.org/10.1016/j.earscirev.2016.02.007

Pánek, T., Lenart, J., Hradecký, J., Hercman, H., Braucher, R., Šilhán, K., & Škarpich, V. (2018). Coastal cliffs, rock-slope failures and late quaternary transgressions of the black sea along southern crimea. *Quaternary Science Reviews*, *181*, 76–92. https://doi.org/10.1016/j.quascirev.2017.12.004

Perissin, D., & Ferretti, A. (2007). Urban-target recognition by means of repeated spaceborne sar images. *IEEE Transactions on Geoscience and Remote Sensing*, *45*(12), 4043–4058. https://doi.org/10.1109/tgrs.2007.906092

Regione Piemonte. (2024, September). *Land cover piemonte: Classificazione di uso e copertura del suolo*. https://www.geoportale.piemonte.it/geonetwork/srv/ita/catalog.search;jsessionid=1907C77A00157E43A595F9A5DD20956C.clu001node01_tc1-catalogo-gnosreg?node=srv#/metadata/r_piemon:35df8a16-5d89-461f-a0f2-abc2180713d2

Regione Piemonte. (2026). *Il bosco e le sue funzioni*. https://www.regione.piemonte.it/web/temi/ambiente-territorio/foreste/foreste-piemonte-economia-ambiente/bosco-sue-funzioni

Riva, F. (2017). *Damage-based long-term modelling of paraglacial to postglacial evolution of alpine rock slopes* [Doctoral dissertation, Università degli Studi di Milano-Bicocca].

Riva, F., Agliardi, F., Amitrano, D., & Crosta, G. B. (2018). Damage-based time-dependent modeling of paraglacial to postglacial progressive failure of large rock slopes. *Journal of Geophysical Research: Earth Surface*, *123*(1), 124–141. https://doi.org/10.1002/2017jf004423

Roesch, A., & Schmidbauer, H. (2018). *Waveletcomp: Computational wavelet analysis* (R package version 1.1). https://CRAN.R-project.org/package=WaveletComp

Shahbazi, S., Barra, A., Navarro, J. A., & Crosetto, M. (2024). From egms data to a differential deformation map for buildings at continent level. *Procedia Computer Science*, *239*, 2150–2157. https://doi.org/10.1016/j.procs.2024.06.403

Terzaghi, K., Peck, R. B., & Mesri, G. (1967). *Soil mechanics in engineering practice* (3rd ed.). Wiley-Interscience.

TREAltamira. (2026). *Insar at a glance*. Retrieved 2016, from https://site.tre-altamira.com/insar/

Varnes, D. J. (1978). Slope movement types and processes.

Wempen, J. M., & McCarter, M. K. (2017). Comparison of l-band and x-band differential interferometric synthetic aperture radar for mine subsidence monitoring in central utah. *International Journal of Mining Science and Technology*, *27*(1), 159–163. https://doi.org/10.1016/j.ijmst.2016.11.012

Yang, Y., Mei, G., Ma, Z., Xu, N., & Peng, J. (2026). Impact of freeze-thaw on landslide activity under diverse topographies using geospatial data mining: Insights from qilian permafrost region, tibetan plateau. *CATENA*, *268*, 110024. https://doi.org/10.1016/j.catena.2026.110024

Ye, J., Jiang, R., Xiao, S., Han, Y., Ju, L., Lu, W., Bai, R., Yao, T., & Zhang, L. (2026). Freeze–thaw cycles control successive glacier landslide hazards in amney machen mountain. *Landslides*, *23*(7), 2117–2134. https://doi.org/10.1007/s10346-026-02700-5